



UNIVERSITÀ DEGLI STUDI
DI TRENTO

DEPARTMENT OF INFORMATION ENGINEERING AND COMPUTER SCIENCE
ICT International Doctoral School

ADVANCED METHODS FOR
SIMULATION-BASED PERFORMANCE
ASSESSMENT AND ANALYSIS OF RADAR
SOUNDER DATA

Elena Donini

Advisor

Dr. Francesca Bovolo

Fondazione Bruno Kessler

Co-Advisor

Prof. Lorenzo Bruzzone

Università degli Studi di Trento

April 2021

Dedicated to my mother, Giusi.

Abstract

Radar Sounders (RSs) are active sensors that transmit in the nadir electromagnetic (EM) waves with a low frequency in the range of High-Frequency and Very-High-Frequency and relatively wide bandwidth. Such a signal penetrates the surface and propagates in the subsurface, interacting with dielectric interfaces. This interaction yields to backscattered echoes detectable by the antenna that are coherently summed and stored in radargrams. RSs are used for planetary exploration and Earth observation for their value in investigating subsurface geological structures and processes, which reveal the past geomorphological history and possible future evolution. RS instruments have several parameter configurations that have to be designed to achieve the mission science goals. On Mars, radargram visual analyses revealed the icy layered deposits and liquid water evidence in the poles. On the Earth, RSs showed relevant structures and processes in the cryosphere and the arid areas that help to monitor the subsurface geological evolution, which is critical for climate change. Despite the valuable results, visual analysis is subjective and not feasible for processing a large amount of data. Therefore, a need emerges for automatic methods extracting fast and reliable information from radargrams. The thesis addresses two main open issues of the radar-sounding literature: i) assessing target detectability in simulated orbiting radargrams to guide the design of RS instruments, and ii) designing automatic methods for information extraction from RS data. The RS design is based on assessing the performance of a given instrument parameter configuration in achieving the mission science goals and detecting critical targets. The assessment guides the parameter selection by determining the appropriate trade-off between the achievable performance and technical limitations. We propose assessing the detectability of subsurface targets (e.g., englacial layering and basal interface) from satellite radar sounders with novel performance metrics. This performance assessment strategy can be applied to guide the design of the SNR budget at the surface, which can further support the selection of the main EORS instrument parameters. The second contribution is designing automatic methods for analyzing radargrams based on fuzzy logic and deep learning. The first method aims at identifying buried cavities, such as lava tubes, exploiting their geometric and EM models. A fuzzy system is built on the model that detects candidate reflections from the surface and the lava tube boundary. The second and third proposed methods are based on deep learning, as they showed groundbreaking results in several applications. We contributed with an automatic technique for analyzing radargram acquired in icy areas to investigate the basal layer. To this end, radargrams are segmented with a deep learning network into literature classes, including englacial layers, bedrock, echo-free zone (EFZ) and thermal noise,

as well as new classes of basal ice and signal perturbation. The third method proposes an unsupervised segmentation of radargrams with deep learning for detecting subsurface features. Qualitative and quantitative experimental results obtained on planetary and terrestrial radargrams confirm the effectiveness of the proposed methods, which investigate new subsurface targets and allow an improvement in terms of accuracy when compared to other state-of-the-art methods.

Keywords [Radar sounder, Cryosphere, Arid Areas, Planetary Exploration, Earth Observation, Performance Assessment, Automatic Data Analysis, Deep Learning, Fuzzy Logic]

Acknowledgements

This thesis reflects the results of the efforts, support, and contributions of many to whom I am extremely grateful. There is a lot to be thankful for since the last few years have been full of amazing experiences, collaborations, and discoveries that resulted in academic and personal growth. My Ph.D. completion would not have been possible without the support of family, friends, and colleagues to whom I would like to express my gratitude. Most importantly, I am thankful to Dr. Francesca Bovolo for the opportunity to work on such a stimulating and interesting topic and for the advice and constant encouragement, and motivation. I thank Prof. Lorenzo Bruzzone for his support, advice, and understanding throughout my research. I also would like to thank prof. Avik Bhattacharya and prof. Alessandra Budillon for reviewing the thesis and helping to significantly improve it. The research presented in the thesis is a collaborative effort with my RSLab colleagues and all the course project and bachelor's thesis students who worked with me. I am particularly grateful to Milad Niroumand, who spent his precious time proofreading the thesis. A special thank goes to all the past and current RSLab and RSDE members who provided moments of joy and hope. I also would like to thank the Ph.D. colleagues and friends who started and walked this journey with me. At last but certainly not least, my greatest and hearty thanks to my lovely family and my friends, who made my life more enjoyable.

I acknowledge the use of data and data products from CReSIS generated with support from the University of Kansas, NASA Operation IceBridge grant NNX16AH54G, NSF grants ACI-1443054, OPP-1739003, and IIS-1838230, Lilly Endowment Incorporated, and Indiana METACyt Initiative; and the use of HiCARS lines, funded as part of NSF's International Polar Year activities (grant ANT-0733025) to the University of Texas at Austin, and the UK's NERC grant NE/D003733/1 to the University of Edinburgh. I also acknowledge the Principal Investigators G. Picardi (Università di Roma 'La Sapienza', Rome, Italy), R. Orosei (IAPS, Rome, Italy), and J. Plaut (JPL, Pasadena, USA) of the MARSIS instrument onboard the Mars Express mission. Datasets of the uncalibrated MARSIS data have been downloaded from the Zenodo repository. I also thank the SELENE (KAGUYA) LRS team and the SELENE Data Archive for providing the SELENE (KAGUYA) data. SELENE is a Japanese mission developed and operated by JAXA.

Elena

The works in this thesis was partially supported by the Italian Space Agency under (1) contract ASI/INAF n. 2013-056-R.O "Partecipazione Italiana alla fase A/B1 della mis-

sione JUICE”; (2) grant No ASI 2018-25-HH.0 in the framework of “Attività scientifiche per JUICE fase C/D”; and (3) contract ASI n. 2016-14-U.O “SaTellite Radar sounder for eArTh sUb-surface Sensing (STRATUS)”; and (4) contract “Attività scientifiche per il radar sounder di EnVision fase A” n.2019-25-HH.0.

Contents

1	Introduction	1
1.1	Background	1
1.2	Problem definition and motivations	3
1.3	Novel contributions	8
1.3.1	Performance assessment of future radar sounder missions	9
1.3.2	Automatic analysis of radar sounder data with fuzzy logic and deep learning	10
1.4	Structure of the thesis	11
	Part I: Background on radar sounder	15
2	Radar Sounders	15
2.1	Introduction	15
2.2	Principles of radar sounding	16
2.2.1	Propagation of the wave	18
2.2.2	Geometric resolution	20
2.2.3	Interaction with subsurface targets	22
2.3	Radar sounder instruments	23
2.3.1	Exploration of Mars subsurface	25
2.3.2	Exploration of the Moon subsurface	27
2.3.3	Exploration of comet 67P subsurface	27
2.3.4	Exploration of the Jovian Moon subsurface	28
2.3.5	Exploration of the Venus subsurface	29
2.3.6	Exploration of the Earth subsurface	29
2.4	Conclusion	31

Part II: Performance assessment of future radar sounder missions **35**

3 An approach to the assessment of detectability of subsurface targets in polar ice from satellite radar sounders **35**

- 3.1 Introduction 36
- 3.2 Challenges of orbital sounding of the Earth 38
 - 3.2.1 Propagation through Ionosphere 39
 - 3.2.2 Surface and firn scattering 40
 - 3.2.3 Volume scattering losses 41
 - 3.2.4 Ability to resolve the target signal from noise 41
 - 3.2.5 Complex structure of the target 42
- 3.3 Methodology 43
 - 3.3.1 Limitations in the previous studies 43
 - 3.3.2 Science goals of orbital sounding: a hierarchical approach to the performance analysis 44
 - 3.3.3 Proposed approach 45
 - 3.3.4 Assumptions 48
 - 3.3.5 Orbital data simulation approach 50
 - 3.3.6 Primary performance assessment 52
 - 3.3.7 Secondary performance assessment 54
- 3.4 Experimental Results 56
 - 3.4.1 Definition of the data set 56
 - 3.4.2 Simulated orbital radargrams 59
 - 3.4.3 IRH detection performance 60
 - 3.4.4 Basal interface detection performance 63
 - 3.4.5 Subglacial lakes detection performance 64
- 3.5 Discussions and Conclusions 65
- 3.6 Appendix A: SNR margin calculations 69
- 3.7 Appendix B: Comparison of simulated orbital RS performance obtained from different airborne radargrams 70

Part III: Automatic analysis of radar sounder data with fuzzy logic and deep learning **77**

4 An unsupervised fuzzy system for the automatic detection of candidate lava tubes in radar sounder data **77**

- 4.1 Introduction 78
- 4.2 Lava Tube Model 81

4.3	Proposed Approach to Detect Candidate Lava tubes	85
4.3.1	Detection of the Reflections	87
4.3.2	Characterization of the Reflections	89
4.3.3	Fuzzy Detection Approach	92
4.4	Description of the Datasets and Experimental Results	98
4.4.1	Simulated Dataset	98
4.4.2	LRS Dataset	102
4.5	Discussion	108
4.6	Conclusions	109
5	A method based on deep learning for the automatic semantic segmentation of radar sounder data	111
5.1	Introduction	112
5.2	Formulation of the problem	114
5.3	Proposed deep learning-based method	116
5.3.1	Deep network architecture	117
5.3.2	Unsupervised pre-training of the network	121
5.3.3	Generation of the segmentation map	121
5.4	Description of the dataset and experimental results	123
5.4.1	Pre-processing of the datasets	125
5.4.2	Setup of the neural network	125
5.4.3	Evaluation criteria	126
5.4.4	Dataset 1: North Greenland	126
5.4.5	Dataset 2: West Antarctica	128
5.5	Conclusions and future works	130
6	An unsupervised deep learning method for subsurface target detection in radar sounder data	133
6.1	Introduction	134
6.2	Proposed deep learning method	135
6.2.1	Candidate label assignment	136
6.2.2	Label refinement for target reflection detection	137
6.2.3	Extraction and analysis of deep features	139
6.3	Description of the dataset and experimental results	141
6.4	Conclusions and future works	143
6.5	Appendix: Statistical analysis	144
7	Conclusions	147

7.1 Summary and discussion of the novel contributions	147
7.2 Future works	150
Bibliography	153
Appendix A: List of Abbreviations	176
Appendix B: List of Symbols	177

Chapter 1

Introduction

This chapter elaborates on the background of radar sounding, defines the problems addressed in the thesis and the motivations. Then, we summarize the novel contributions proposed in this thesis. Finally, the structure of the thesis is provided.

1.1 Background

Radar sounders (RSs) are active sensors cable of probing the subsurface in a non-intrusive way, and thus, without digging nor coming in contact with the observed body. RSs transmit electromagnetic (EM) waves in the nadir direction that can penetrate the surface and propagate in the subsurface. This is because the signal has a low frequency in the range of High-Frequency (3-30 MHz) or Very-High-Frequency (30-300 MHz) and a wide bandwidth that reaches up to 100 MHz. The subsurface is the outcome of geological processes that slowly generate irregular structures with different chemical compositions, creating dielectric discontinuities. The discontinuities are visible to the radar waves because of the high contrast of the material dielectric properties. Interacting with the EM signal, the discontinuities generate reflected echoes detectable by the radar antenna. These echoes are coherently summed together and then stored in radargrams. The radar profiles (radargrams) are the direct measurements of the subsurface geometrical and dielectric properties. Radargrams can be exploited to derive valuable products, supporting scientific research, with automatic and manual analyses.

In the last decades, radar sounders have been widely adopted for planetary exploration, including Mars and the Moon, and Earth observation. Sounding the subsurface of the Earth and other planets of the Solar System has been of great scientific interest for the ability to acquire direct subsurface measurements of inaccessible places. Direct measurements on the dielectric and geometric structure can reveal the subsurface geological and geophysical characteristics. Radar sounding enabled the investigation of the present and past subsurface geological processes and the accurate modeling of the surface elevation,

thereby immensely contributing to planetary science. Mars was probed by two orbiting RSs: the Mars Advanced Radar for Subsurface and Ionosphere Sounding (MARSIS) radar on the ESA Mars Express [1], and the SHallow RADAR sounder (SHARAD) on the NASA Mars Reconnaissance Orbiter [2]. They jointly provided information about subsurface water and ice, surface elevation and roughness, the interaction of the Martian atmosphere with the solar wind, and ice layers in the shallowest subsurface. Another example is the Lunar Radar Sounder (LRS) mounted on the Kaguya spacecraft by the Japan Aerospace Exploration Agency (JAXA) [3]. Its objectives were to acquire lunar plasma waves and to study the geological evolution of the Moon. Currently, two sounders are under development for the exploration of the Jovian Moons, i.e., the RIME (Radar for Icy Moon Exploration) on-board of the ESA JUperiter Icy Moons Explorer (JUICE) spacecraft [4], and REASON (Europa Clipper mission) by NASA. RIME will probe Ganymede for i) characterizing the subsurface and identifying possible habitats, ii) exploring Europa recent active zones, and ii) studying Callisto as an early Jovian system remnant. REASON will acquire data of Europa to define the ice crust in the near-surface up to the ocean, looking for water pockets.

In Earth observation, radar sounders are mostly mounted on airborne platforms and have been widely employed to probe the cryosphere. The cryosphere represents all the regions containing a certain percentage of water in the frozen state (e.g., snow cover, ice sheets, glaciers, permafrost, and floating ice), including Antarctica and Greenland. The objectives of airborne mounted RSs are to map the structure and processes of ice-sheets and ice-shelves up to the basal interface for extracting information to monitor the terrestrial climate. The cryosphere represents about 20% of the terrestrial continental surface and exhibits different responses to climatic stresses that remain largely unquantified [5]. Ice sheets evolve in response to climate change [6], and thus, it is a significant component affecting the climate system (e.g., the melting of Antarctica and Greenland ice shelves can raise the sea level to 62 m and 7.2 m, respectively [7]). The decisive role of the cryosphere dynamics in the context of global climate evolution has been often highlighted by the World Climate Research Programme (WCRP)¹, the Scientific Research Programmes (SRPs) of the Scientific Committee on Antarctic Research (SCAR)², and the ESA's Living Planet Programme³ [5, 8]. Locally, information about ice and climate history over long timescales can be derived with relatively good precision from ice core data [9]. However, ice coring implies extremely high logistic costs and is unfeasible for the large-scale analysis of the ice sheet dynamics. A more spatially detailed view can be

¹World Climate Research Programme (WCRP) website: <https://www.wcrp-climate.org/>

²Committee on Antarctic Research (SCAR) Scientific Research Programmes (SRPs) website: <https://www.scar.org/science/srp/>

³ESA's Living Planet Programme website: https://www.esa.int/Applications/Observing_the_Earth/The_Living_Planet_Programme/ESA_s_Living_Planet_Programme

obtained using radar sounding, which provides observations of the surface and subsurface. RSs support the investigations of the subglacial environment, providing insights into the interaction between the polar ice and the climate system [10, 11]. Modeling the behavior of grounded ice sheets and the coastal floating ice remains a technical and scientific challenge [12, 13, 8, 14], given the size of the domains (Antarctica and Greenland) and the numerous physical processes that can be addressed with radar sounding.

The rest of this chapter is structured as follows: Section 1.2 defines the main open issues of radar sounding related to the work proposed and describes the thesis motivations. Section 1.3 describes the novel contributions proposed by this thesis. Finally, Section 1.4 describes structure of the thesis.

1.2 Problem definition and motivations

The design of RS instruments is based on assessing the performance of a given configuration in achieving the mission science goals and detecting critical targets. These assessments are used to guide the selection of the instrument parameters by determining the appropriate trade-off between the achievable performance and the technical and physical limitations [4]. In the literature, there are several analysis on the impact of the Earth's ionosphere [15, 16, 17], the surface clutter [18, 19], and the penetration capability (assuming homogeneous dielectric properties) [20]. However, most of these studies lack a performance assessment that considers the target properties, which are a performance-limiting factor (e.g., in terms of subsurface scattering and attenuation losses) and a detection objective of the instrument. Hence, target detectability can be assessed by modeling the radar response (i.e., simulating) of the expected acquisition scenario and the target properties. Simulations can be done with traditional 3D approaches that coarsely model the subsurface dielectric and geometric properties [21, 22, 23], or with the analog-based strategy that extracts the target geometry and dielectric properties from existing radargrams [24]. The simulation approach choice depends on several mission-specific factors, e.g., the uncertainty degree of the dielectric profile, the acquisition challenges, and the mission requirements during the instrument development. The main difference between the two types of simulators is in the modeling of the subsurface. In traditional 3D approaches, the subsurface is modeled according to prior knowledge of the investigated targets, which is hard to achieve, and thus, the simulations are based on coarse models. The analog-based method considers the target-specific properties extracted from radargrams, and it realistically simulates the response of a given RS parameter configuration. For a more detailed description of the literature and the simulation approaches, we refer to the introduction of Chapter 3. The target detectability is assessed in simulations generated by varying the RS parameters with data processing techniques. Therefore, analyzing the

simulations provides information on the target detectability, which gives insights into a given RS configuration performance and can guide the RS design.

Currently, the most common approach for extracting information from radargrams is visual interpretation. This approach enabled the understanding and characterization of the subsurface geology of other planets of the Solar System, terrestrial cryosphere, and arid areas. SHARAD and MARSIS sounders lead to the analysis of the global martian subsurface geology. One of the ground-breaking scientific discoveries from RS data is the identification and characterization of the icy layered deposit in the polar caps (i.e., North and South Pole layered deposits) [25, 26]. At the base of the layered deposit of the South Pole, some strong bright reflections have been recently interpreted as a film of water that generates a subglacial lake [26]. On the Moon, the LRS identified volcanic features and structures, such as the Maria stratification, that give critical insights on the volcanic evolution [27]. Airborne-mounted RSs profile the Earth's subsurface in the cryosphere [28, 29] and in arid areas [30]. In the cryosphere (mainly Greenland and Antarctica), radargrams can image the ice column down to the bedrock in the continent and down to the ice-water interface for the floating ice. Radargrams helped in characterizing the ice thickness overall Greenland [31, 32] and the Antarctica [33], mapping subglacial lakes at the basal interface [34], and the characterization of the ice stratigraphy [35, 36]. Recently, widespread deformation of the internal ice column was discovered related to super-cooling phenomena, enhancing the understanding of the ice-sheet basal boundary conditions and dynamics [37, 38]. Although visual interpretation provided a tremendous scientific return, it is a heavily time-demanding approach and is not suitable for analyzing many radargrams. This is a limiting factor for visual analysis since the amount of available data is significantly large and expected to grow with the planned future RS mission for planetary exploration and the Earth's airborne campaigns. Moreover, visual interpretation is a subjective task that can lead to severe misinterpretations. Hence, a need emerges for novel methods that can address these limitations and automatically and systematically extract information on subsurface geological targets and processes from radargrams.

In the literature, automatic methods for analyzing radargrams focus on extracting information at different levels of the data processing chain (see Fig. 1.2). The data processing chain considers three levels of extracting information and generating products at a different level of complexity and abstraction. Raw data are normally ground processed with methods, such as the range compression and Doppler focusing, to obtain Level 1 products. Level 1 products are further processed with data analysis techniques to retrieve Level 2 products (e.g., detecting linear reflections and clutter). Finally, Level 2 products are further analyzed to obtain Level 3 products (e.g., the map of basal units and buried cavities). Rradargram automatic analysis methods in the literature are mainly dedicated

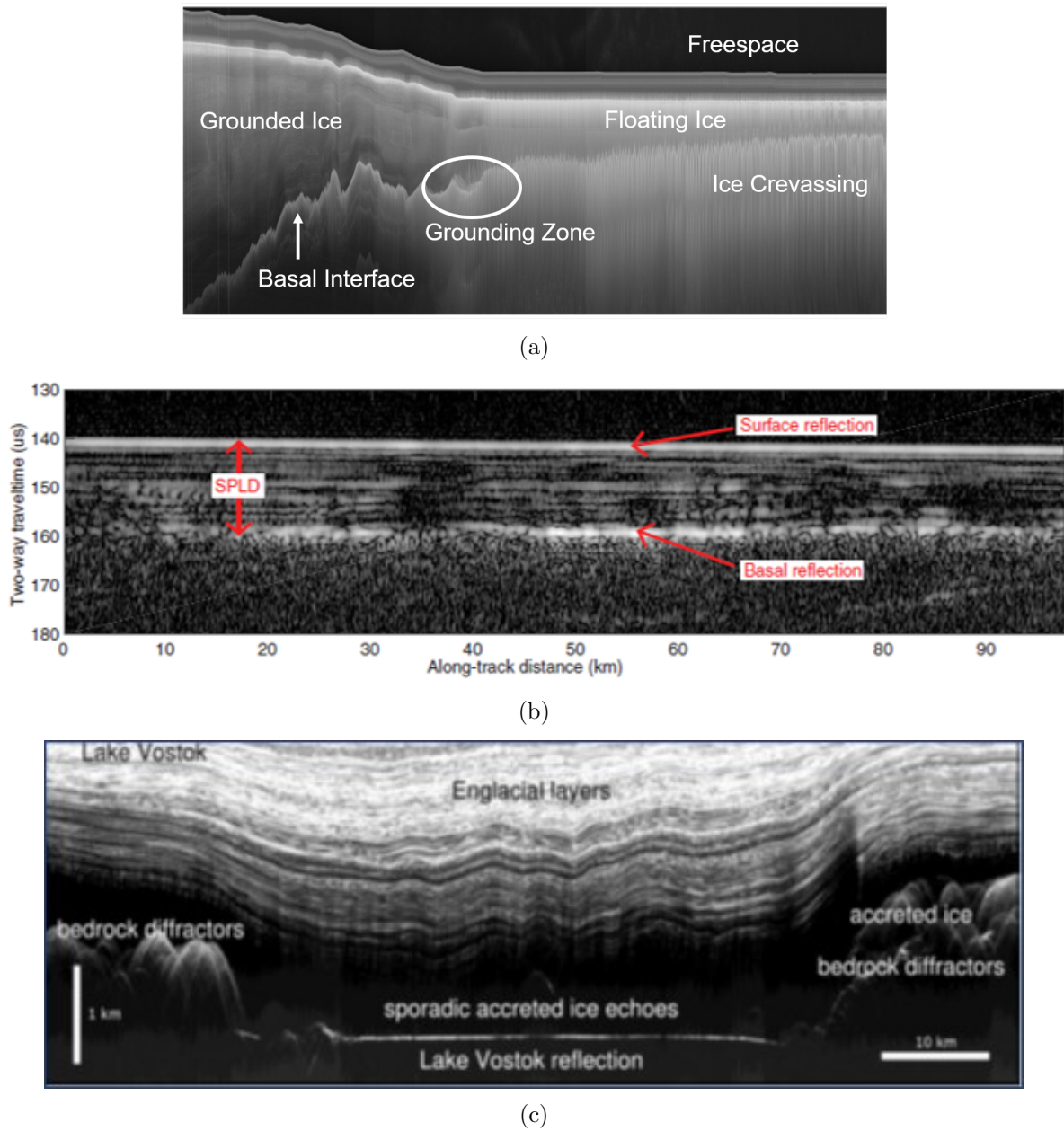


Figure 1.1: Examples of radargrams: (a) radargram imaging floating ice in Antarctica by MCoRDS [29], (b) radargram imaging the Layered South Pole Deposit (SPLD) of Mars by MARSIS [1], and (c) radargram imaging lake Vostok in East Antarctica acquired by HiCARS radar sounder [39].

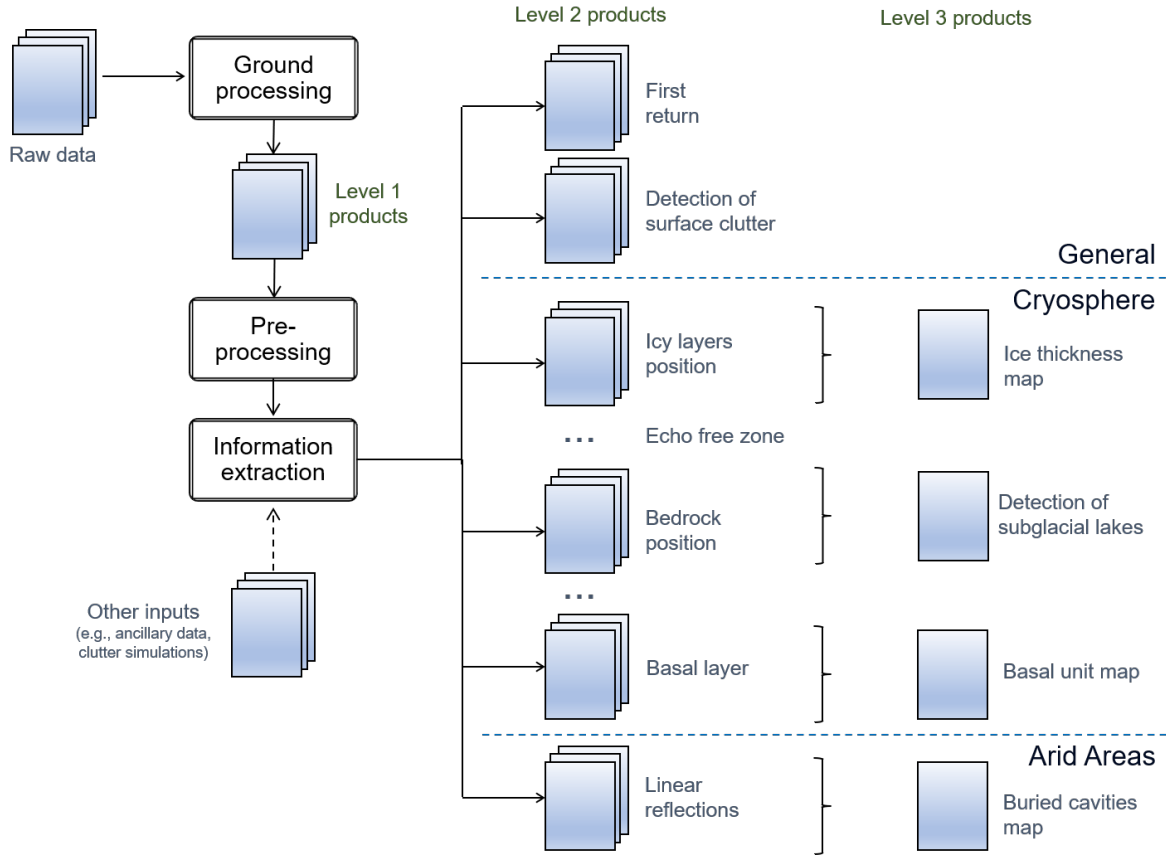


Figure 1.2: Schematic representation of the data processing chain.

to level 2 product generation, while few generate level 3 products. These methods can be divided into supervised and unsupervised depending on whether they require reference data. Supervised algorithms learn from available pairs of input and the output labeled data. In the unsupervised training, the algorithms infer the mapping function from the data without having any reference. This is relevant since reference data are hard to retrieve, especially on the subsurface images.

Literature methods focus on a limited number of targets in the subsurface, such as the detection of linear reflections (e.g., ice layering) [42, 43, 40], detection of subsurface features (e.g., ice layering and the last return) [44], segmentation for detecting important subsurface targets (e.g., layer pack, basal interface, echo-free zone and noise) [41, 45], the identification of subglacial lakes at the basal interface [46]. Linear reflection detector contributed to the detection and characterization of the ice stratigraphy, i.e., layers of ice characterized by variation in the dielectric properties of the polar caps of the Earth [43], and Mars [42, 40]. Algorithm in [43] detects with high accuracy horizontal layers. The method flattens the layers referring to the surface slope to decrease the effect of the

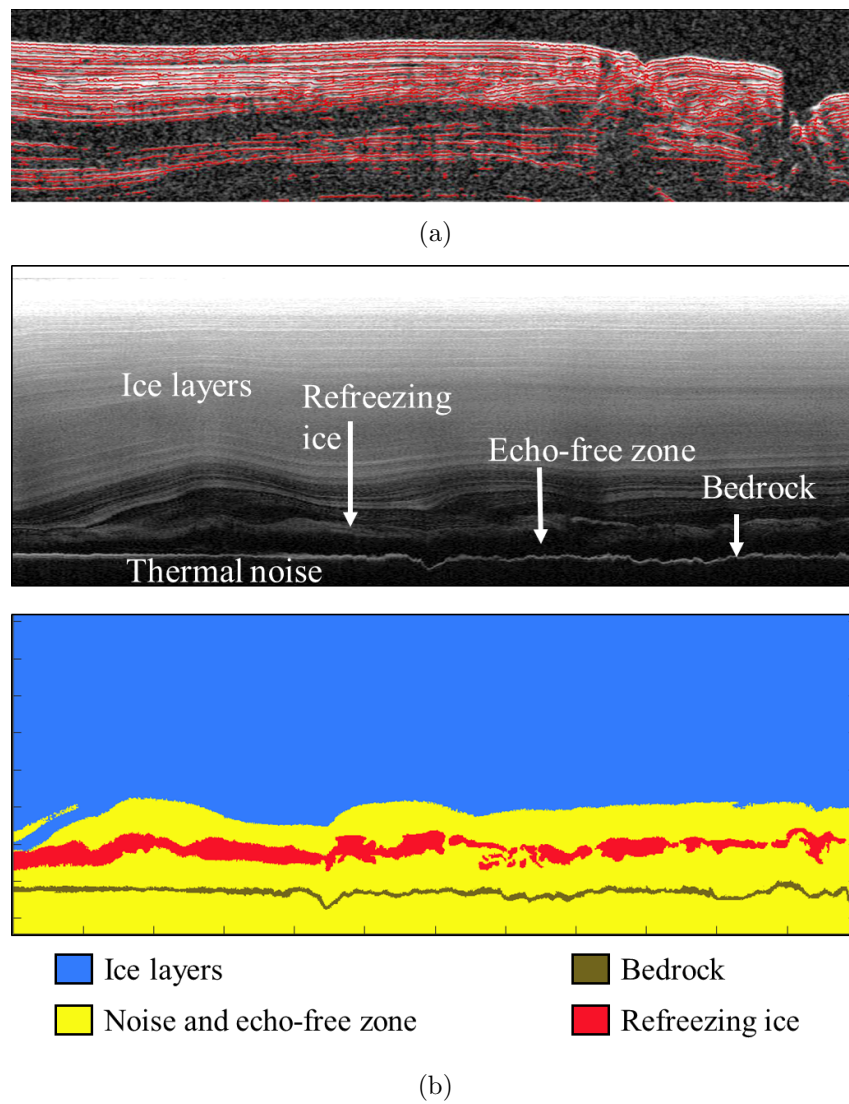


Figure 1.3: Examples of algorithms for automatic target detection in RS data. (a) Linear dielectric interface detection [40]. (b) Segmentation of ARS data into layers, bedrock, echo-free zone, thermal noise and refreezing ice [41].

local inclination. Then, filtering, thresholding, and morphological processing are applied to extract linear reflectors [43]. Ferro et al. extracted the horizontal reflection and their attributes (position, width, and radar contrast) with a Steger filter [42]. The linear reflection detection improved also for non-horizontal lines by using local scale hidden Markov model and the Viterbi algorithm [40] (see Fig. 1.3(a)). Subsurface feature extraction is based on the statistical analysis and allows for the characterization of bright reflections in the radargram [44]. The automatic segmentation permits the identification of subsurface targets, including layers, bedrock, basal ice, thermal noise, and Echo-Free Zone (EFZ) [45, 41]. The subglacial lake detection method provides for each sample of the bedrock a label indicating the presence of water or rock [46]. All the methods are based on the handcrafted design of geometric and statistical features representing the targets. Handcrafted features are then analyzed with a Super Vector Machine (SVM) classifier that predicts for each sample a label in the investigated classes (see Fig. 1.3(b)). However, SVM methods are based on the manual design of features, limiting the application of the technique to the modeled classes only with poor generalization capabilities. Adapting the system for new classes means designing new features based on the new target statistical and geometric properties. Moreover, SVM works in a supervised manner and requires a large amount of reference data labeled by experts. Reference data is seldom available in radar sounding as the knowledge on the subsurface structure can hardly be modeled realistically. For a more detailed description of the literature on data analysis, we refer to the introduction of Chapters 4, 5, and 6. From the literature analysis, a need emerges for developing automatic methods for detecting a wide variety of subsurface targets and dealing with the large number of radargrams planned to be acquired in complex scenarios, e.g., Venus and the Jovian Moons.

1.3 Novel contributions

The thesis novel contributions address two main open issues in the radar-sounding literature. On the one hand, we propose a novel approach for analyzing the detectability of subsurface targets in Earth observation simulated radargrams (EORS). On the other hand, the thesis contributes to the design and development of automatic methods for analyzing radar sounder data to obtain level 2 and 3 products (Fig. 1.2). For these two objectives, we studied the geological subsurface structure in arid areas and in the cryosphere to identify a list of possible targets detectable in airborne (ARS) and satellite radargrams. This analysis considered both the geometrical properties of the subsurface geological structures and the different RS sensor resolutions. The Ph.D. research is focused on a subset of those targets, selected by considering the related literature and available data. Selected targets are considered for the performance assessment of a given RS configuration and the design

of data analysis methods. This Ph.D. research work includes four main activities:

1. Assessment of detectability of subsurface targets in polar ice from a satellite radar sounder.
2. Development of an unsupervised fuzzy system for the automatic detection of candidate lava tubes in planetary radar sounder data.
3. Analysis of radargrams of icy areas with deep learning to model the boundary conditions and detect the basal layer and basal units.
4. Unsupervised segmentation of radargrams with deep learning for detecting subsurface features.

The rest of the Section briefly describes the novel contributions. Note that the proposed approaches can be adapted with few modifications to identify other subsurface structures and employed for processing radargrams from different missions.

1.3.1 Performance assessment of future radar sounder missions

A satellite mission with a radar sounder for Earth observation in polar regions can significantly support the monitoring cryosphere in the framework of climate change. Several studies are in progress to design and assess the performance of an Earth-orbiting radar sounder (EORS). However, one critical aspect of the cryospheric targets that are often ignored and simplified in these studies is the complex geo-electrical nature of the polar ice. Here, we adopt the analog simulation approach [24] based on reprocessing the ARS data to predict EORS performance. The ARS data are a rich source of information about the targets due to (1) the availability of vast archives of data from multiple campaigns [29, 47], (2) the widespread and full-depth coverage of the Antarctic and Arctic ice-sheets, and (3) the similarity with the actual radar signatures of complex cryospheric targets (principles of operation of the ARS and the EORS are similar). The input ARS data are selected to represent different regimes on Antarctica and Greenland, i.e., grounded ice, floating ice, and subglacial lakes. The performance assessment analyzes the achievability of the main objectives of an EORS mission: (1) detectability of englacial layering, (2) detectability of the basal interface, and (3) characterization of the nature of the basal interface. Assuming the range of central frequency and bandwidth in the literature, the proposed approach for performance assessment aims at revealing the required signal-to-noise (SNR) budget at the surface that maximizes the detectability of subsurface targets. The required SNR budget can guide the selection of main instrument parameters, such as the two-way antenna gain and the transmitted power. These parameters can support the optimization of the EORS sensor configuration, such as for the recently proposed distributed EORS architecture [48].

1.3.2 Automatic analysis of radar sounder data with fuzzy logic and deep learning

The first contribution for the automatic analysis of radar sounder data focuses on detecting cavities in the subsurface, including empty lava tubes. Lava tubes are buried channels that transport thermally insulated lava [49]. Nowadays, lava tubes on the Moon are believed to be empty and thus indicated as potential habitats for humans. In recent years, several studies investigated possible lava tube locations, considering the gravity anomaly distribution and surficial volcanic structures [50, 51]. Here, we propose a novel and unsupervised method to map candidate buried empty lava tubes in radar sounder data and extract their physical properties. The approach relies on a model that describes the geometrical and electromagnetic (EM) properties of lava tubes in radargrams. Considering the lava tube model, the method extracts reflections in radargrams and then analyzes them to identify those related to buried cavities and reject the others. The analysis consists of a fuzzy detection system based on the lava tube EM model that evaluates the properties of the reflections and the relation among them. The fuzzy rules consider the EM and geometrical properties of lava tubes, thus their appearance in radargrams. The proposed method can address the complex task of identifying candidate lava tubes on several radargrams in an automatic fast objective way. The final decision on candidate lava tubes should be taken in a post-processing step by expert planetologists. The effectiveness of the proposed method is demonstrated with experiments on two datasets: a dataset of simulated radargrams and a dataset of radargrams acquired on the Moon by the LRS. Identified candidate lava tubes are processed to extract geometrical parameters, such as the depth and the thickness of the crust (roof).

The second contribution on automatic data analysis proposes a deep learning-based method for the segmentation of radar sounder data. In the literature, radargram segmentation is based on handcrafted features, manually designed by considering target-specific properties [45, 41]. Note that handcrafted features strongly depend on the investigated targets, and thus, methods are not adaptable to other scenarios and classes. Recently, deep learning-based techniques automatically extracting features showed high performance in several domains. Here, we aim at automatically extracting information on basal boundary conditions given their substantial relevance for modeling the ice-sheet processes, such as the ice-sheet sliding. The method can be adapted with slight modifications to analyze other scenarios, such as the floating ice having different geometrical and dielectric properties. A novel automatic method based on deep learning is proposed to segment icy inland radargrams and locate meaningful geological targets for better understanding the ice-sheet and the basal boundary conditions processes. Radargrams are segmented into classes, including englacial layers, bedrock, echo-free zone (EFZ) and thermal noise

already considered in the literature, as well as new classes of basal ice and signal perturbation. The classes have a specific spatial distribution in the range and azimuth directions. Moreover, the proposed method can handle the large variability in the dimension and scale of the targets. The method effectiveness was tested on two datasets of radargrams by the MCoRDS3 radar sounder in the inland of Greenland and Antarctica with basal units in the basal layers.

The last contribution to radargram automatic analysis is the definition of an unsupervised method based on deep learning for segmenting planetary radar sounder data. Unsupervised segmentation does not require labeled data, which is an advantage with respect to supervised approaches. Supervised segmentation, especially those based on deep learning, relies on large labeled datasets that are hard to retrieve in the radar sounder domain. This paper proposes a novel and unsupervised method based on deep learning for extracting information on the subsurface targets in radargrams. The proposed method detects subsurface reflections in radargrams and analyzes the related deep features to distinguish buried targets. The technique is fully unsupervised and does not require any initial labeled data. We model radargrams with two main semantic classes: the background and the target. Background includes the no-signal areas and the thermal noise above the surface and below the basal return. The targets include the reflections from different dielectric interfaces in the subsurface, such as ice layers and basal return. Thus, the target class can be further divided into other subclasses. This hierarchical structure is exploited by the proposed method, which hierarchically segments the radargram. At first, we discriminate between the background and target to extract reflections in the radargram. The targets (i.e., radargram reflections) are segmented into subclasses by analyzing the deep features. We tested the proposed method on a dataset of MARSIS radargrams acquired near the South Pole of Mars to identify anomalies in the basal return that astrophysicists identified as subglacial lakes [26].

1.4 Structure of the thesis

This chapter described the context of the thesis, the motivation, and the novel contributions. The rest of the dissertation is organized into four main parts as follows.

Part I provides the theoretical background of RSs. Chapter 2 reviews the basic principles of radar sounding, analyzing the radar equation, the wave propagation and interaction with the subsurface targets, and the geometric resolution of radar images. Then, the present, past, and future radar sounder instruments are described.

Part II provides the proposed performance assessment approach for the target detectability in orbiting radar sounder data. Chapter 3 analyzes the performance assessment of target detectability in simulated EORS data.

In part III, the proposed novel approaches to radargram data analysis based on fuzzy logic and deep learning are presented in detail and supported by illustrative case studies. Chapter 4 proposes an unsupervised method for detecting candidate lava tube reflections in planetary radar sounder data. Chapter 5 presents a supervised deep learning-based method for segmenting inland radargrams and investigating the basal boundary conditions. Chapter 6 describes the proposed unsupervised deep learning-based method for the semantic segmentation of planetary radar sounder data.

Chapter 7 discusses the overall conclusions of the thesis and addresses possible future developments.

Finally, Appendix A lists all abbreviations used in the thesis, and Appendix B lists the mathematical symbols.

Part I: Background on radar sounder

Chapter 2

Radar Sounders

This chapter presents the technological background of radar sounding. We first describe the basic principles of radar sounding, analyzing the radar equation, the wave propagation and interaction with the subsurface targets, and the geometric resolution of radar images. We move then to the description of the past, present, and future radar sounder instruments.

2.1 Introduction

RADAR (RADio Detection And Ranging) refers to a group of active sensors used for a wide range of applications, from surveillance to imaging of the Earth surface and subsurface, in several remote sensing fields, including commercial, military, Earth observation, and planetary exploration [52]. Pulse-radar transmits an electromagnetic (EM) wave with high energy in the expected target direction and then collects the backscattered echoes. Measuring the time delay and power of the backscattered echoes enables estimating the target distance and backscattering coefficient. Imaging radars have a monostatic configuration and are equipped with an antenna for transmitting and receiving the signal. The radar-target distance is estimated by the two-way traveling time and the wave velocity in the medium. The backscattering coefficient stores the information on the target properties, including the composition and dimensions. Thus, it is of critical importance for characterizing the investigated targets [52, 53].

Radar Sounders (RSs) are a specific type of radar that image the subsurface of the Earth and planets of the Solar System, including Mars and the Moon. Mounted on airborne or spacecraft platforms, RSs are monostatic and transmit an EM at the nadir direction that probes the subsurface (see Fig. 2.1) and estimates the target depth and dielectric properties. Radar sounding plays a vital role in enhancing our understanding of geological targets and processes deep in the subsurface. This is while other remote sensing sensors (e.g., optical, SAR, and altimeter) cannot penetrate deep in the subsurface and reveal information about the surface targets only.

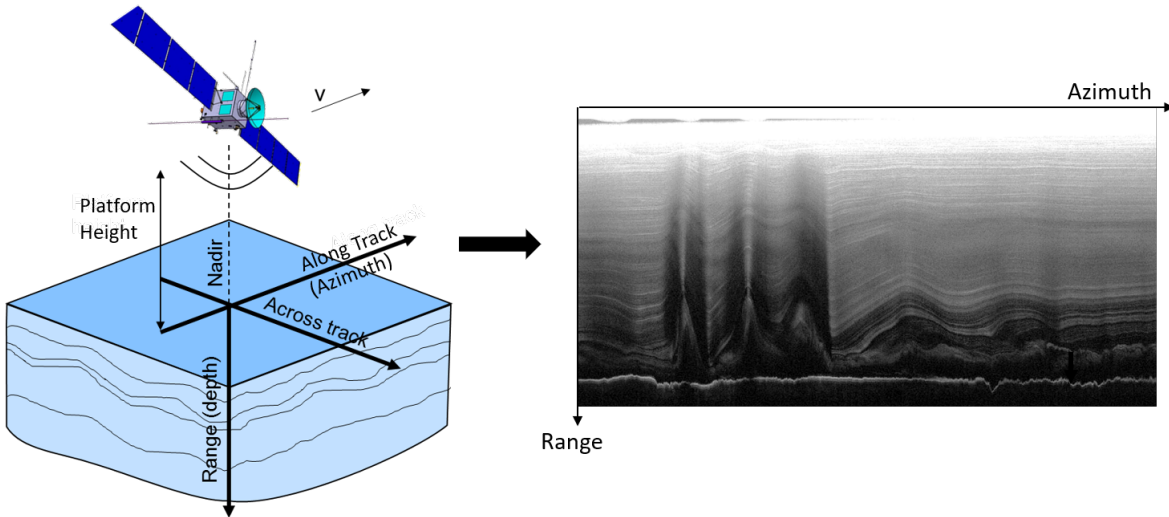


Figure 2.1: Working principles of radar sounder– on the left the acquisition geometry of a radar sounder, on the right an example of a radargram. Moving along-track, an RS transmits signal pulses at a time interval given by the pulse repetition interval (PRI) and illuminates the target region within the antenna footprint. The signal propagates through the subsurface, where it undergoes scattering, absorption, and transmission in its interaction with different types of dielectric interfaces. The time-varying signal received back at the antenna can then be interpreted to infer the target characteristics and depth.

This chapter briefly introduces the background and principles of radar sounding, citing examples of past, present, and future RS instruments. Section 2.2 presents the introduction and the principles of radar sounding, focusing on the radar equation, the wave propagation and interaction with the subsurface targets, and the geometric resolution of radar images. Section 2.3 lists and describes past and currently operating RSs and those under development for future satellite missions in the content Earth observation and planetary exploration.

2.2 Principles of radar sounding

The working principle is based on the backscattering of the transmitted EM wave by interfaces. Fig. 2.1 on the left illustrates the acquisition geometry of an RS instrument. RSs are mounted on a moving platform, typically a satellite or plane. The moving direction of the platform indicates the along-track or azimuth direction. The orthogonal direction to the along-track that points down toward is the nadir direction. Nadir represents the range of the radar and indicates the depth. The third direction is orthogonal to both the along-track and the nadir and is called across-track. The antenna transmits an electromagnetic signal at nadir direction at a low frequency that can penetrate the

surface and propagate in the subsurface. At each subsurface dielectric interface, a part is reflected in the radar antenna. Interacting with the interfaces reduces the wave energy so that the signal backscattered by deeper interfaces is not detectable by the radar receiver. The received echoes transport data about the depth and the specific dielectric properties of the target. The type of transducer for transmitting and receiving is a dipole. This is a critical issue as RS instruments require a low frequency to penetrate the surface, and the size of the dipole antenna is inversely proportional to the working frequency. Thereby, a low frequency corresponds to a large antenna that might be difficult to be carried by a moving platform (either satellite or airborne).

The signal received by the radar between the pulse transmission is called A-scan. The concatenation of several A-scans over multiple pulses generates the radar image, called radargram (Fig. 2.1 on the right). Radargrams are the coherent superposition of all the received echoes along the track of the moving platform. For each track point, an A-scan (i.e., a column of the radargram) can be estimated from the power and two-way traveling time of backscattered echoes. In summary, the radargram y-axis indicates the depth of the target or one-way delay, and the x-axis is the positions of the sensor along the track. Finally, the amplitude of each pixel corresponds to the power of the reflected wave.

Some of the radargram reflections are not backscattered from the subsurface. Some reflections are undesired and may completely mask the signal from desired subsurface targets, i.e., clutter [54]. The main clutter component is the off-nadir surface scattering received by the antenna concurrent with the nadir sub-surface reflections. The RS antenna is typically a dipole, having an omnidirectional radiation pattern and no directivity. The wave illuminates a large area of the surface, and echoes from the nadir subsurface and off-nadir surface simultaneously reach the RS antenna. This leads to difficulties in discriminating between the clutter and subsurface signals as the clutter intensity is usually higher than that of the subsurface signals. Many methods were proposed in the literature to mitigate clutter, mainly based on backscattering models and the statistical estimation of backscattering parameters of the surface [55, 56].

The time interval between the transmission of two pulses is the Pulse Repetition Interval (PRI), as shown in Fig. 2.2. PRI is inversely proportional to the Pulse Repetition Frequency (PRF). The fraction of time in which the radar transmits is called duty-cycle that is a measure of the radar power-rate consumption. The duty-cycle is a critical measurement for the design of a radar [53]. The pulse width depends on the modulation of the transmitted EM wave. RS signals are usually modulated linear frequency chirps with a narrower bandwidth (about a few MHz) than other modulations [52]. The main advantage of frequency modulation is that the waveform has a long duration and a large spectral width. The wide bandwidth helps to increase range resolution as the signal phase

is frequency depended. Moreover, the signal is long enough to have sufficient energy for detecting small and far objects. RS signals have a large fractional bandwidth (about 20-60% of the central frequency) to have the optimum trade-off between the maximum penetration and the range resolution [53]. The penetration increases by decreasing the central frequency, while the range resolution increases with the bandwidth decreasing.

2.2.1 Propagation of the wave

The electromagnetic wave propagation in a generic medium can be explained with Maxwell equations [57]. Snell's law describes the relationship between the incidence and refraction angles of the EM wave while passing through an interface between two media. At each interface, i.e., where there are two or more materials with different dielectric properties, the incident wave is divided proportionally to the media dielectric difference. The signal interacts with the interfaces so that the EM wave is backscattered, absorbed, and propagated.

Radar equation for subsurface sounding

The echo power P_r received by the radar antenna can be defined as in [58]:

$$P_r = \frac{P_t G^2 \lambda \sigma^0 A_{ill}}{(4\pi)^3 h^4} \quad (2.1)$$

where P_t is the power transmitted by the radar, and G is the radar system gain. h considers the height of the platform (in the range of 400 m - 500 km, depending on the platform type) from the surface and the depth of the target in the subsurface. σ^0 is the backscattered coefficient that is related to the dielectric properties of target, and A_{ill} indicates the geometric properties of the target. σ^0 and A_{ill} store the properties of the investigated media, but also provide insights into the propagation losses [52, 53].

The central frequency and the bandwidth of the transmitted signal are important parameters defining the sounder performance, including the penetration capabilities and the geometric resolution. The penetration capabilities depend on the frequency: the lower is the frequency, the higher the penetration, and the lower the attenuation. The wavelength, i.e., $\lambda = v_{medium}/f_c$, is directly proportional to the length of the antenna. This means that a large antenna corresponds to low frequencies. The dipole length is about 2-50 m, depending on the central frequency.

The bandwidth of the transmitted pulse influences the transmitting gain of the antenna and the range resolution. The vertical resolution depends inversely on the bandwidth. Increasing the bandwidth of the signal corresponds to a better range resolution. Combining frequency and bandwidth limitations, penetration capability in the subsurface is in contrast with the range resolution. Thus, increasing the penetration performance means

decreasing the resolution in the range direction and vice-versa. Therefore, a trade-off has to be found according to the specific requirement of the radar application [53].

The propagation in a dissipative and dispersive medium causes losses, including absorption and attenuation. Absorption and attenuation are due to the medium dispersive dissipative properties, respectively. Attenuation is related to the sounder penetration capabilities. Increasing the attenuation decreases the power of the backscattered echoes and penetration capability [53].

Wave velocity

Appropriate mapping of the subsurface from a radargram requires estimating the wave propagation velocity in the medium. The wave velocity strongly depends on the dielectric property of the medium. In the vacuum, the propagating velocity the speed of the light

$$c = \frac{1}{\sqrt{\epsilon_0 \mu_0}} \approx 3 \cdot 10^8 [m \cdot s^{-1}] \quad (2.2)$$

where $\epsilon_0 = 8.854 \times 10^{-12} [Fm^{-1}]$ and $\mu_0 = 4\pi \times 10^{-7} [NA^{-2}]$. In a medium, the propagation velocity depends on the medium dielectric properties:

$$v_{medium} = \frac{c}{\sqrt{\epsilon_r \mu_r}} = \frac{1}{\sqrt{\epsilon_0 \epsilon_r \mu_0 \mu_r}} \quad (2.3)$$

where ϵ_r and μ_r are the relative dielectric permittivity and permeability of the medium, respectively. Considering that ϵ_r and μ_r are always equal or greater than 1, the propagating velocity in a medium will be equal or smaller than c . Finally, we can estimate the distance of the target from the antenna (i.e., the depth) by considering the Round Trip Time (RTT). The RTT is defined as the time elapsed from the wave radiation to when the antenna receives the echo back. RTT indicates the time for propagating in the medium, hitting the target, and returning to the antenna. Assuming that the wave propagates in a homogeneous medium, and knowing the RTT and propagation velocity in the medium, it is possible to calculate the depth of the target (z) in the subsurface as:

$$z = \frac{v_{medium} \text{RTT}}{2} \quad (2.4)$$

Calculating the propagating wave velocity requires some information about the dielectric properties of the subsurface medium. Knowing the dielectric properties, it is not possible to relate echo delay with the target depth. However, in general, the reliable estimation of the relative dielectric properties is not possible from a single measurement. For this reason, prior knowledge of the investigated target is needed. Moreover, to extract information from a radargram, we should consider the whole sounding system characteristics. Collected data strongly depends on the medium dielectric properties and the expected geological dimension of the targets.

2.2.2 Geometric resolution

Radargram geometric resolutions depend on several factors, including the antenna radiation pattern, the surface roughness, and the altitude of the sounder [4]. For spaceborne acquisition, a resolution cell is defined by the first Fresnel zone on the surface (i.e., it corresponds to antenna footprint). In the along-track direction, the wave beam is formed by a single lobe. Hence, the wave footprint is limited by the antenna dimension (see Fig. 2.2 for the acquisition geometry). In the across-track direction, the footprint is larger due to the omnidirectional radiation pattern of the dipole. Resolution can be improved only

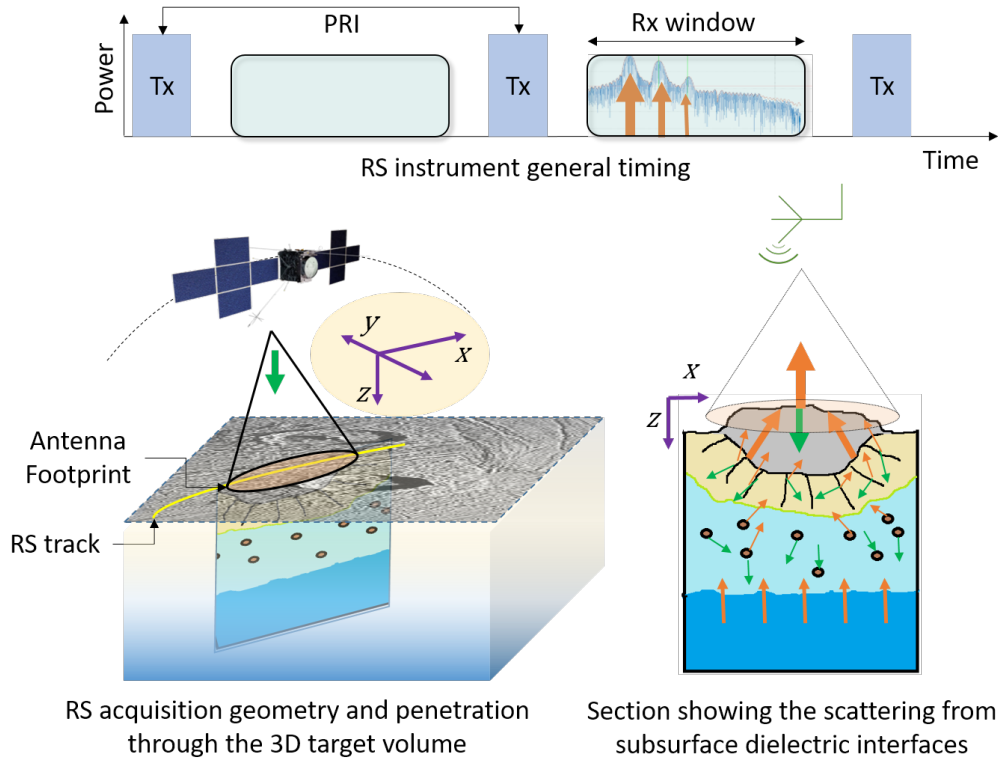


Figure 2.2: Schematic representation of the process of subsurface mapping using radar sounding. Moving along the track, an RS transmits pulses at a time interval PRI that illuminates the region within the antenna footprint. The signal propagates through the target subsurface, where it undergoes scattering, absorption, and transmission in its interaction with different types of dielectric interfaces. The time-varying signal received back at the antenna can then be interpreted to infer the target characteristics. The important direction vectors in the acquisition geometry are denoted by x (along-track), y (across-track) and z (range or depth).

in an along-track with a Doppler filtering, based on the synthetic aperture of the antenna developed by the moving platform. Doppler analysis also reduces the clutter reflections from the off-nadir surface and increases the Signal-To-Clutter-Ratio (SCR) parameter.

Along-track resolution

Doppler analysis consists of resolving the ground target position not only from amplitude processing but from its combination with the phase shift signal measured through coherent detectors. Hence, considering the processing of the data, two types of along-track resolutions can be defined, i.e., the focused resolution ρ_x^f and the unfocused resolution ρ_x^{uf} . The focused along-track resolution depends on the Doppler focusing of the data and has a higher resolution, but it implicates more onboard power consumption.

Focusing Algorithm. In the focused case, the history of the phase signal is fully exploited, and the maximum theoretical resolution is achievable ρ_x^f defined in (2.6). For the Doppler analysis, it is important to correctly sample the Doppler shifts by the Pulse Repetition Frequency (PRF) instrument. The lower limit of PRF is given by the Doppler Bandwidth B_D , which is defined as

$$B_D = 2 \frac{V_x^2}{h \lambda} T_i \quad (2.5)$$

where V_x is the velocity of the moving platform, and T_i is the integration time defined as the time interval that the radar illuminates a point on the ground. Hence, the along-track resolution is defined as:

$$\rho_x^f \approx \frac{V_x}{B_D} = \frac{h \lambda}{2 L_a} \quad (2.6)$$

where V_x is the velocity of the moving platform and B_D is the Doppler bandwidth defined in 2.5.

Unfocusing Algorithm. In the unfocused case, the phase signal is not exploited, and therefore, the along-track resolution is lower. However, the computational effort onboard is reduced by about 30%, and consequently, the platform power consumption. The basics assumption is that the objects produce a constant Doppler frequency over a time interval, called integration time T_i . Thus, the resolution value depends on the along-track space covered that is equal to the length of the synthetic aperture L_a , see (2.7).

$$\rho_x^{uf} = L_a = \sqrt{\frac{h \lambda}{2}} \quad (2.7)$$

Across-track resolution

Across track resolution ρ_y depends on the antenna beam pattern only. The Doppler analysis is not possible since in this direction there is not relative movement respect the ground point. In this direction, the dipole radiates in an isotropic way, and consequently, echoes are collected from the backscattering in all directions. Off-nadir surface reflection is sufficiently weak not to mask the desired signal, but surface's not-ideal roughness degrades

the across-track resolution. In the case of a smooth surface, the resolution of the radar is equal to the diameter of the first Fresnel zone D_F :

$$\rho_y^{flat} = D_F = 2 \sqrt{(h + \lambda/4)^2 - h^2} \approx \sqrt{2h\lambda} \quad (2.8)$$

In case of rough surface, the echos come within the entire antenna aperture. The across-track resolution is higher than in the previous case as it depends on the projection of antenna aperture on the ground. The across-track resolution can be approximated as:

$$\rho_y^{rough} = D_F = 2 \sqrt{\frac{hc}{BW}} \approx 0.88 \frac{h\lambda}{L_a} \quad (2.9)$$

where h indicates the moving platform height, λ is the wavelength of the transmitted signal, and L_a the maximum length of the antenna dipole.

Range resolution

Range resolution ρ_z is associated with the depth direction and is defined in (2.10). ρ_z depends on the bandwidth of the transmitted signal. As the bandwidth increases, the resolution decreases and improves. The resolution is proportional to the medium velocity, which depends on the dielectric properties of the medium.

$$\rho_z = \frac{v_{medium}}{2BW} \quad (2.10)$$

where v_{medium} is the propagation velocity in the medium defined in (2.3), and BW is the bandwidth of the transmitted signal. In non-ideal materials, dielectric response strongly varies with the frequency so that increasing the frequency increases the attenuation losses.

2.2.3 Interaction with subsurface targets

The nature of the interaction between the wave and the interface depends on its dielectric and geometric nature. In radar sounding, subsurface scatterers can be broadly represented by one or more combinations of the following types [53]:

1. *Smooth and horizontal interfaces of significant dielectric contrast.* They are characterized by a strong, horizontal, and specular reflection, e.g., the interface between ice and an underlying subglacial lake (see Fig. 2.3.a).
2. *Compositional interfaces representing a change in the material dielectric properties.* They are characterized by a change in the signal strength, e.g., the interface between porous regolith overlying a solid bedrock (see Fig. 2.3.e).
3. *Structural interface represented by changes in the crystal properties.* They are also characterized by a change in the signal strength, e.g., the interface between brittle and ductile ice and ice layers (see Fig. 2.3.a).

4. *Geological offset.* It is characterized by a vertical offset in the received echo, i.e., a vertical discontinuity in otherwise horizontally continuous distinct layers (e.g., a normal fault as shown in Fig. 2.3.d).
5. *Distributed subsurface scatterers.* They are small-sized reflectors of significant dielectric contrast, which are randomly distributed within an otherwise homogeneous background (e.g., pockets of water within ice and mines, as shown in Fig. 2.3.c). They are characterized by a loss of coherence in the signal and appear like diffused reflections of relatively low strength spread over many ranges and along-track samples in the radargram.
6. *Absorbing interfaces caused by a highly conductive dielectric medium.* These interfaces result in the total loss of signal strength, and no echoes are obtained from depths below them (e.g., air - seawater interface, see Fig 2.3.b).

Note that the transmitted signal properties are crucial for determining what is visible in the radar image. The bandwidth and the frequency are related to the penetration capabilities and the range resolution. The target detectability depends on the platform altitude, two-way antenna gain, the working frequency, and transmitted signal power. These factors are related to the signal-to-noise ratio (SNR) and thus the reflection power in radargrams. The higher is the SNR the higher is the probability of detecting the targets in radargrams. The design of the radar parameters should consider both the mission requirements and the target detectability. The target detectability can be assessed using data analysis algorithms on radargrams simulated by varying the RS design (see Chapter 3).

2.3 Radar sounder instruments

The scientific return of radar sounding in providing critical information on the subsurface geological processes and structure has been well-recognized by the scientific community. Ground-penetrating radars (GPRs) are commonly exploited for field surveys in several applications for detecting buried objects, including ice-sheet imaging and urban environment monitoring, e.g., [62]. In remote sensing, GPRs are flanked by airborne-mounted RS instruments that provide a regional mapping of the subsurface. In the last decades, airborne RSs have been commonly used to map Greenland and Antarctica at a regional scale (e.g., Polaris [28], MCORDS [29], and P-Band [30] radar sounders). A global coverage can be achieved with an RS mounted on a satellite, mainly used in the past for planetary exploration. Several RSs have been acquiring information on the other planets of the Solar System, and many others are under development for near-future radar-sounding missions. Fig. 2.4 lists past satellite RS missions in black (MASRIS,

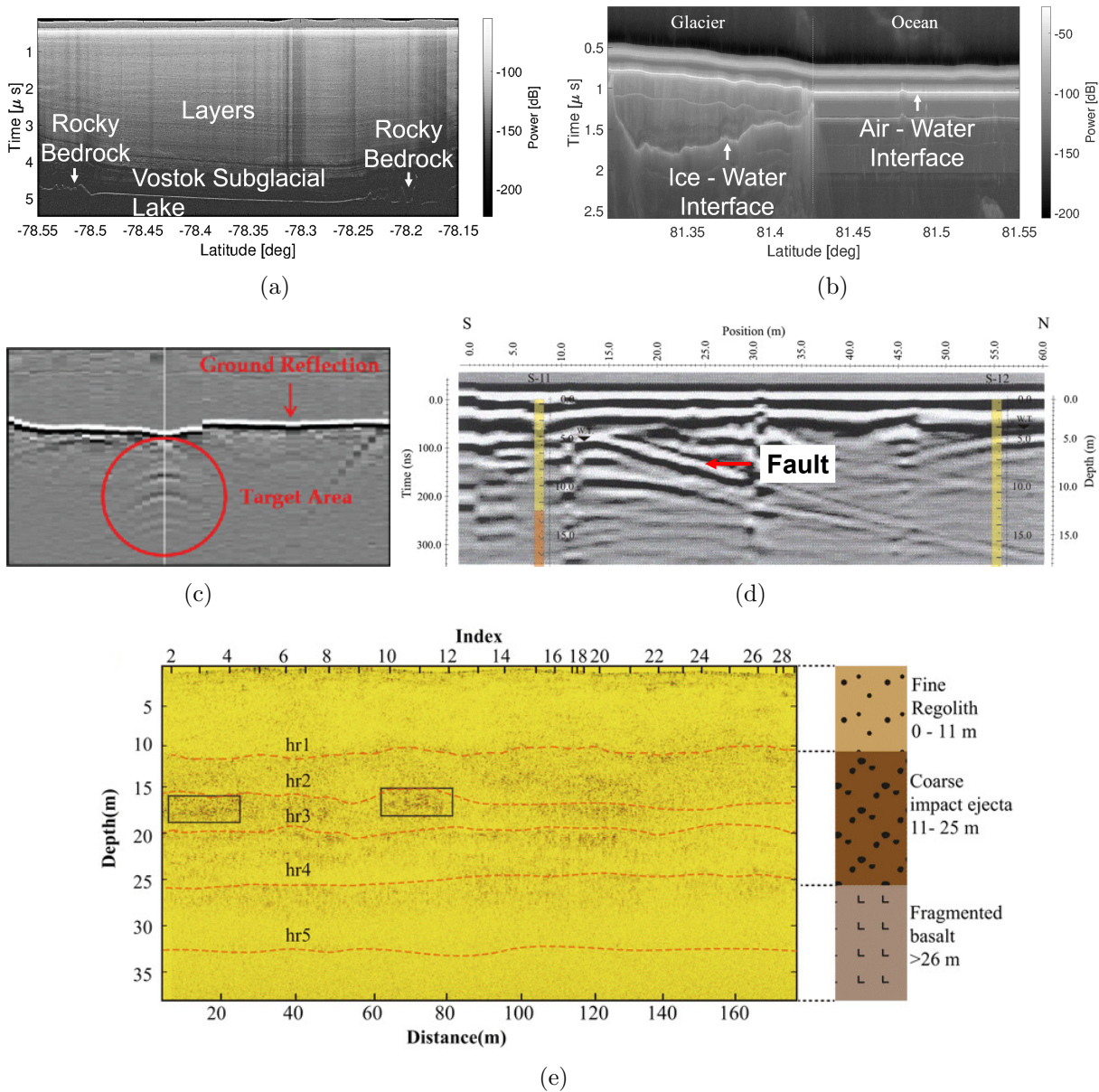


Figure 2.3: Examples of radargrams explaining the different interaction between the wave and the subsurface targets. Figure (a) is a radargram acquired over the Lake Vostok in Antarctica showing interaction 1 (smooth and horizontal interfaces of significant dielectric contrast between the ice and the water) and 3 (structural interface represented by changes in the crystal properties, i.e., the ice strata). Figure (b) is a radargram acquired in the coastal areas of Greenland showing interaction 6 (absorbing interfaces caused by a highly conductive dielectric medium) at the air - seawater interface. Figure (c) is a Ground Penetrating Radar (GPR) radargram over a mine from [59] showing interaction 5 (distributed subsurface scatterers). Figure (d) is a GPR radargram of subsurface faults from [60] showing interaction 4 (geological offset). Finally, Figure (e) is a lunar radargram of a GPR in CE-4 site from [61] showing interaction 2 (compositional interfaces representing a change in the material dielectric properties).

SHARAD, CONSERT), the approved missions for which RSs are under development in green (RIME, REASON), and those under study (not yet approved) in blue (Envision SRS). Recently, a new idea is emerging for profiling the Earth subsurface of arid areas and the cryosphere with radar sounding to studying the subsurface of critical regions to monitor climate change. To this end, two new RS are under study, i.e., STRATUS and OASIS. Particularly, STRATUS has as a primary objective the study of the cryosphere, and as a secondary objective the study of the subsurface of arid and desert areas. The RS design leverages the heritage of the past and currently operating RSs and already available radargrams for designing and predicting the performance.

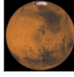

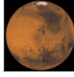







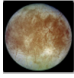



	Radar Sounder	Mission	Target	Developed by
2003	MARSIS	Mars Express	Mars 	
2006	SHARAD	MRO	Mars 	
2007	LRS	SELENE – Kaguya	Moon 	
2014	CONSERT	ROSETTA	Comet 67P 	
2022	RIME	JUICE	Jupiter Moons 	
2024	REASON	Europa Clipper	Jupiter Moons 	
2032	SRS	Envision	Venus 	

Figure 2.4: Past and future satellite missions carrying on-board RS instruments. Among these instruments, past missions are in black, approved missions under development are in green, and SRS (highlighted in blue) is currently in the Phase A study.

2.3.1 Exploration of Mars subsurface

Mars was probed by two radar sounder: the Mars Advanced Radar for Subsurface and Ionosphere Sounding (MARSIS) and The Mars SHallow RADar sounder (SHARAD). The Mars Advanced Radar for Subsurface and Ionosphere Sounding (MARSIS) [63] radar

Table 2.1: Parameters of the main past and present radar sounder missions for planetary exploration and Earth observation.

Target	Instrument	Central Frequency	Bandwidth	Maximum Penetration	Range Resolution	Azimuth Resolution
Planetary Exploration	SHARAD [2]	20 Mhz	10 Mhz	1 km	15 m	400 m
	MARSIS [63]	5.5 Mhz	1 Mhz	5 km	150 m	5.5 km
	LRS [3]	5.0 Mhz	2 Mhz	5 km	100 m	60m
Earth Observation	MCoRDS [29]	195 Mhz	30 Mhz	5 km	4.3 m	25 m

sounder is from the Italian Space Agency (ASI) and was on board the ESA’s Mars Express orbiter launched in 2003. Starting from 2005, MARSIS probed the subsurface of Mars for several kilometers. MARSIS was also designed for ionosphere sounding and large-scale surface altimetry. The transmitted wave has a central frequency in the range of 1.8, 3, 4, and 5 MHz and a bandwidth of 1 MHz. For minimizing the ionosphere distortion, two central frequencies of 1.8 and 3 MHz are used for night-side operation and 4 and 5 MHz for day-side operation. The Doppler filtering (SAR processing) is performed onboard to reduce the volume of the downlinked signal. Further processing is associated with the signal transformation in the time domain and correction of the ionosphere phase distortions. The primary radar antenna to transmit and receive is a dipole of 40 m long oriented orthogonal to the moving direction to illuminate the subsurface. The radar is equipped with another monopole antenna vertically oriented that captures off-nadir echoes.

MARSIS revealed the first-ever images of the Martian subsurface. In the literature, several important discoveries about the martian geology and past evolution history have been possible because of the MARSIS data, e.g., [25, 64, 26]. The study in [25] showed that the polar caps of Mars are rich in ice, i.e., the North and South Polar Layered Deposits, respectively NPLD and SPLD. A 250 km wide buried impact basin was discovered hidden by a low-loss icy material in the Chryse Planitia [64]. Recently, MARSIS data provided evidence of subglacial liquid water (20 km wide subglacial lake) near the SPLD 1.5 km in the subsurface.

The Mars SHallow RADar sounder (SHARAD) [2] was launched by ASI onboard the Mars Reconnaissance Orbit (MRO) probe. SHARAD operated with a central frequency of 20 Mhz and a bandwidth of 10MHz. Such wave characteristics highly increase the sounding resolution of MARSIS to 15 m in the vacuum and the penetration to several hundreds of kilometers. Contrary to MARSIS, SHARAD strongly reduces the onboard

processing and analog electronics, such as the baseband conversation. This allows the achievement of high fidelity of the signal by decreasing the distortions and side lobes. The raw data downlink has a large volume due to the low onboard processing, and it is possible for the MRO high data rate. On-ground processing, further analyses improve the quality of the data [65].

SHARAD data, similarly to MARSIS, contributed to the better understanding of scientific questions on the geology, such as the dielectric composition of the surface and subsurface, formation, and evolution of Martian features. The study in [66] provided evidence of the ice composition of the lobate debris aprons in the Martian mid-latitudes. SHARAD resolved polar layered deposit details, giving insights into the stratigraphy and paleoclimatic records [67]. Another example is the detection of horizontal layering, which is the interface between the newer Vestitas Borealis and the beneath Hesperian plains [68]. SHARAD acquisitions complemented MARSIS ones providing global mapping of the Martian subsurface and shallow crust.

2.3.2 Exploration of the Moon subsurface

Kaguya (SELENE) spacecraft was launched in 2007 onboard the Lunar Radar Sounder (LRS) [3]. The LRS aimed to i) detect buried regolith layers, ii) map the subsurface structures, and iii) perform passive observation of radio and plasma waves of the lunar orbit. Table 2.1 lists the parameter of the LRS. The LRS central frequency is at 5 MHz with a frequency sweep from 4 to 6 MHz, at a $2\pi \times 10^{10} rad/s^2$ sweep rate of angular frequency. Assuming a loss tangent of 0.006 for the lunar regolith, the LRS can achieve a penetration up to 5 km. Due to the absence of the Moon ionosphere, the received signal is not affected by phase dispersion. The radar sounder was equipped with two dipoles working at a frequency of 5 Mhz and having a length of 30m. The characteristics allow the penetration in the subsurface of some kilometers with a resolution of 100m.

The LRS has a global coverage of the Moon. In the nearside (Maria), sounder data reveals several volcanic interfaces, such as layered deposits, with a depth of several meters generating strong reflection [27]. The farside (Highlands) has a high surficial roughness and the presence of large and thick craters. Hence, Highlands radargram is strongly affected by clutter.

2.3.3 Exploration of comet 67P subsurface

The COmet Nucleus Sounding Experiment by Radiowave Transmission (CONSERT) [69] is a bi-static radar sounder onboard the ROSETTA probe. ROSETTA, an ESA mission, after a cruise of about ten years, entered into the orbit of the 67P/Churyumov-Gerasimenko comet. ROSETTA lander, called Philae, investigated the nucleus internal

structure to extract information on the comet evolution and early Solar System formation. The comet has a small body of a few km, making the CONSERT design specific for the acquisition scenario. To this end, ROSETTA orbiter and Philae were equipped with a bistatic configuration operating at a central frequency of 90 MHz with a bandwidth of 10 MHz. The bulk dielectric permittivity is estimated considering the time delay and the amplitude of the signal transmitted between the orbiter and the lander that passes through the comet. An accurate estimation strongly depends on the accuracy of the relative position between the orbiter and lander. Analyzing prior hypotheses on the dielectric properties supported the spatial resolution required for dealing with this problem [70]. Dielectric assumptions are based on 3D simulations, considering a wide range of values of porosity, temperature, composition, and the comet inner structure. The parameter values are from laboratory measurements of the comet-analog dust-ice-void composition. The dust/ice ratio was in the range of 0.4-2.6, and porosity around 58%-75%.

2.3.4 Exploration of the Jovian Moon subsurface

RSs showed to address meaningful scientific challenges on the geologic evolution of the Solar System planets. For this reason, there is a growing scientific interest in the exploration of the outer Solar System, such as the Jovian system, addressed with a radar sounder. Giant gas planets are composed of volatile that suggest the possibility of past or present life or habitability. The largest Jovian Moons are Ganymede, Callisto, and Europa, which are composed of water-ice. Images of these Moon surfaces show interesting geomorphological features, such as multi-ringed basins, palimpsests, and paterae [71]. Investigating the formation and composition of these features would explain the evolution of the Jovian and Solar Systems. Leveraging on the heritage of past radar-sounding missions, two missions have been proposed to investigate the subsurface of the Jovian Moons motivated by the need for direct measurements of subsurface liquid water.

The JUpiter ICy moons Explorer (JUICE) [71] has been chosen in the ESA's Cosmic Vision 2015-2025 program. JUICE aims at studying the Jovian system and investigating potentially habitable zones in the Jovian Moons. The Radar for Icy Moon Exploration (RIME) [53] is the RS onboard JUICE and will be the first instrument to probe the Jovian moon subsurface. RIME operates at a central frequency of 9 MHz with a bandwidth of 1 MHz or 2.8 MHz, resulting in penetration in the ice up to 9 km. Radargrams will be acquired in multiple flybys, followed by a circular orbit at an altitude of 500 km (nominal phase) around Ganymede, providing global coverage of the Ganymede subsurface. RIME [53] scientific objectives are i) characterizing the structure of the ice shell and the distribution of subsurface water; ii) understanding the formation of surface features; iii) searching for past and present life-related activities; and iv) determining the global composition,

distribution, and evolution of surface materials. RIME addresses these objectives with subsurface that stores information on the subsurface geological targets with significant contrast in dielectric permittivity [53]. Onboard processing is enough to guarantee a factor of 8 in the digital sampling, and robust data processing will be done in the ground segment.

The other radar sounder under development for investigating the subsurface of the Jovian Moon is REASON [72], onboard the Europa Clipper mission by NASA. REASON aims to study the subsurface of Europa, the smallest and most active Jupiter icy moon. There is evidence that, in the shallowest subsurface, there are interesting geodynamic processes, including plumes and ice diapirs. Although the low depth favors their detection, REASON will be strongly affected by the Jovian emission intensity. To overcome this limitation, Europa Clipper will operate with a fly-by-centric mission. REASON aims at investigating the habitability of Europe and the inner geological structure. REASON works with a dual-frequency of 9MHz and 60MHz, resulting in both deep and shallow penetration.

2.3.5 Exploration of the Venus subsurface

The exploration of the Venus subsurface is essential to understand the evolution of the Solar system. Envision mission was shortlisted and now in phase A of study by the ESA fifth medium-class mission (M5) in its Cosmic Vision science programme. Envision aims to be equipped with a Subsurface Radar Sounder (SRS) for investigating the present-day geological activity on Venus. Previous missions with SAI instruments (Magellan and Venus Express) [73, 74] provided images of the complexity of Venus topography, possible active volcanism, and the presence of long lava channels. Now, the SRS is designed to operate in the frequency range of 9 - 30 MHz with about 60% of fractional bandwidth. SRS is in the preliminary design phase (phase A), and the RS parameters (including the frequency) are still under design, considering the mission requirements and the expected target properties. The SRS will investigate i) layering in modified craters, ii) buried craters, iii) the constraints in the three-dimensional structure of complex targets, such as the tesserae, and iv) it will estimate the flow unit volume.

2.3.6 Exploration of the Earth subsurface

Radar sounders mounted on airborne platforms effectively profiled the subsurface of ice and arid areas of the Earth. In the cryosphere, radar sounder revealed buried geologic targets and processes that help in better understanding ice-sheets dynamics [29, 75, 28]. For example, analyzing targets like ice stratigraphy allowed the study of the terrestrial past climate history. Radar sounding also gives insights on basal boundary conditions,

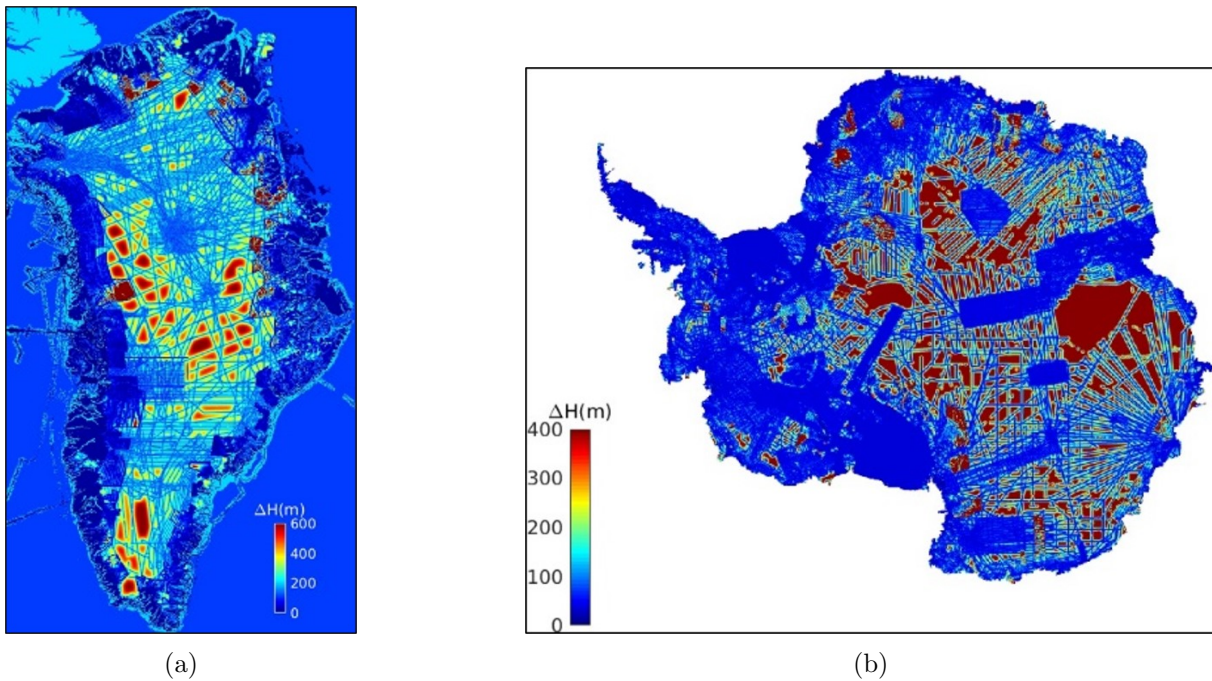


Figure 2.5: Uncertainty in the current estimates of (a) the Greenland ice-sheet thickness from BEDMACHINE v3 [32] dataset, (b) the Antarctic ice-sheet thickness from BEDMACHINE v1 [33].

ice-sheets dynamics [76, 77], including the melting processing related to the ice-sheet forward sliding toward the sea. In arid areas, several buried targets can be unveiled by radar sounding. These include buried craters, faults that act as water conduits, and sand stratigraphy. Another crucial target is shallow water tables that are critical in arid areas. RSs have already proved to be able to map shallow aquifers (e.g., [78, 30]), considering the high electric conductivity of the water.

There is no RS mounted on a satellite that probes the Earth subsurface because of: i) the difficulties in allocating the EM spectrum needed for an Earth-observation RS, and ii) the challenges of the signal propagation in the ionosphere. Areas of interest for Earth radar sounding are arid and desert region and the cryosphere. These regions are characterized by a low water presence in the shallow subsurface, as water has a high electrical conductivity that prevents the EM wave penetration. Currently, the cryosphere and arid areas are imaged with regional campaigns by RSs mounted on airborne. ARS provides local measurements of the subsurface, and large and inaccessible areas of Antarctica and Greenland and the arid areas are still not explored (see Fig. 2.5). Recently, a need emerged for complete coverage of the cryosphere subsurface to map ice-sheet processes related to climate change. Hence, this motivated the proposal for an Earth-orbiting radar sounder (EORS) mission that provides full coverage and time-series data. Recently, two EORS

proposals are under study: STRATUS [20] and OASIS [79]. One of the main challenges is the propagation of the wave through the terrestrial ionosphere. The RS central frequency should be greater than the ionospheric cut-off, varying with the geographical location and the solar zenith angle. An RS operating at 45 MHz will propagate through the ionosphere with minimum distortions [15]. At this frequency, the EORS wave can propagate through the ionosphere and penetrate through 4-5 km of ice and a few hundred meters of desert sand. The selection of the other RS parameters and the acquisition geometry parameters are based on the target detection requirements. Nevertheless, an EORS is feasible and can strongly support the scientific community in studying the effects of climate change and water resources management.

2.4 Conclusion

The design of the radar parameters depends on the mission technical and scientific requirements. RS scientific requirements are mainly based on the detectability of several important subsurface targets. Target detectability can be assessed using data analysis algorithms on radargrams simulated by varying the RS design (see Chapter 3). The main parameters affecting target detectability are the frequency, bandwidth, transmitted power, platform altitude, and two-way antenna gain. These factors are related to the signal-to-noise ratio (SNR) and thus to the power of the target reflections with respect to the noise in the radargram. The higher is the SNR the higher is the probability of detecting the targets in radargrams. Past and currently operating RS are designed with different parameters, which match the mission science and technical requirements. This is reflected in the characteristics of radargrams, including the range resolution and penetration capability. Finally, in the literature, few algorithms exist for automatically analyzing radargrams. Moreover, existing techniques are designed for specific targets and specific radargram characteristics. Hence, they can extract information on the target and the radargrams for which they are designed. Thus, a need emerge for an approach for designing radar sounders that consider the subsurface target detectability.

Part II: Performance assessment of future radar sounder missions

Chapter 3

An approach to the assessment of detectability of subsurface targets in polar ice from satellite radar sounders

A satellite mission with onboard a radar sounder for the observation of the Earth polar regions can greatly support the monitoring of the cryosphere and climate change analyses. Several studies are in progress proposing the design and demonstrating the performance of such an Earth-orbiting radar sounder (EORS). However, one critical aspect of the cryospheric targets that are often ignored and simplified in these studies is the complex geo-electrical nature of the polar ice. This chapter ¹ presents a performance assessment of the polar ice target detectability by focusing on their realistic representation. This is obtained by simulating the EORS radargrams corresponding to different regions of the polar cryosphere, by leveraging the data available from airborne campaigns in Antarctica and Greenland. We propose novel performance metrics to analyze the detectability of the internal reflecting horizons (IRH), the basal interface, and to analyze the nature of the basal interface. This performance assessment strategy can be applied to guide the design of the SNR budget at the surface, which can further support the selection of the main EORS instrument parameters such as the transmitted power, the two-way antenna gain, and the processing gains.

¹Part of this chapter appears in

Donini, E., Thakur, S., Bovolo, F. and Bruzzone, L., 2019, July. Assessing the Detection Performance on Icy Targets Acquired by an Orbiting Radar Sounder. In IGARSS 2019-2019 IEEE International Geoscience and Remote Sensing Symposium (pp. 997-1000). IEEE.

3.1 Introduction

The Earth polar ice sheets are crucial components of the cryosphere that affect global climate change and sea-level rise. Several cryo-hydrodynamic processes occurring at the base of the ice sheets affect the stability and seaward flow of the ice. Direct measurement and imaging of the ice-sheet down to the base are essential for studying these processes and modeling the stability of the ice sheets. This can be appropriately achieved by profiling the ice using radar sounders (RS), also referred to as ice-penetrating radar. Considering the need for RS data for imaging the polar ice caps, several airborne RS (ARS) campaigns have been conducted in Antarctica and Greenland [29, 47]. Relevant scientific returns have been obtained from data acquired by these campaigns, such as (1) estimation of the thickness of the ice sheets, (2) analysis of the internal reflecting horizons (IRH), (3) detection of subglacial lakes [80], (4) analysis of basal flow regime [81], and (5) identification of basal refreezing [38]. However, these acquisition campaigns are expensive and time-consuming, and despite a large number of campaigns, radar profiles are absent over very large portions of the polar areas (e.g. 500,000 sq. km of Antarctica), resulting in incomplete information on the polar ice characteristics [18]. Moreover, since the data are collected in one-time campaigns with local coverage to study specific phenomena, repeat-pass acquisitions are also not available. Furthermore, due to the use of different instruments and airborne platforms, the data quality strongly varies between the different campaigns.

An Earth-orbiting radar sounder (EORS) operating from a satellite platform can address the limitations posed by the airborne campaigns by providing homogeneous data quality with uniform and multi-temporal coverage of the Earth. However, at orbiting altitudes, RSs are subjected to many performance limiting factors. These mainly include: (1) the propagation losses due to the large distance to the target, (2) the distortions caused by the ionosphere, (3) the surface clutter due to a relatively large antenna footprint, (4) the presence of galactic noise, and (5) frequency band allocation required for Earth observation. Many of these factors can be mitigated at the system design level or in post-processing to ensure the extraction of valuable scientific information, as successfully demonstrated by the current heritage of planetary RSs (SHARAD [82] and MARSIS [63] on Mars, LRS [83] on the Moon, RIME [84] and REASON [85] scheduled for the Jovian icy moons).

Leveraging the heritage of terrestrial airborne and planetary RSs, currently, studies are in progress for the proposal of an orbital RS, operating in the HF-VHF bands [20, 16, 15, 19]. These studies are based on assessing the performance of a given orbital design in detecting the critical targets and achieving the scientific goals of the mission. These assessments are used to guide the selection of the instrument parameters by deter-

mining the appropriate trade-off between the achievable performance and the technical and physical limitations [4]. Many of these studies focus on understanding the impact of the Earth's ionosphere [15, 16, 17], the surface clutter [18, 19], and the capability to penetrate up to the base of the ice-sheet (assuming homogeneous dielectric properties of the ice) [20].

However, only a few of these studies (e.g. [18, 19]) assess the performance considering the structural details of the targets (such as the IRHs), which are both (1) a performance-limiting factor (e.g., in terms of subsurface scattering and attenuation losses) and (2) a detection objective of the instrument. Given the need to analyze the detectability of the cryospheric targets, it is imperative to model and simulate their radar response. The complex dielectric permittivity profile of the ice depends on several factors, such as the presence of impurities (e.g., dust, ash, rocks, salts, acids), the crystal orientation fabric, the thermal profile, and the distribution of melt-zones. The high variability of these factors over unknown spatial scales and the lack of geophysical models to translate them to the corresponding electrical properties make it difficult to subjectively define the dielectric profile of the ice. This inhibits their assessment using conventional 3D electromagnetic RS simulators [86, 21, 23]. Recently a novel simulation approach has been proposed, which is based on reprocessing the radargrams acquired over geological analogs of the target [24]. A specific case of application of this approach has been adapted for reprocessing the airborne data to simulate the orbital radargrams over the regions acquired by previous airborne campaigns [87].

In this work, we adopt this simulation approach based on reprocessing the airborne data to predict orbital performance. The airborne data are a rich source of information of the targets due to (1) the availability of large archives of data from multiple campaigns [29, 47], (2) the widespread and full-depth coverage of the Antarctic and Arctic ice-sheets, and (3) the similarity with the actual radar signatures of complex cryospheric targets (principles of operation of the airborne and the orbital RS are similar). The input airborne data are selected to represent different regimes on Antarctica and Greenland, i.e., grounded ice, floating ice, and subglacial lakes. The performance assessment analyzes the achievability of the main objectives of an orbital RS mission: (1) detectability of IRHs, (2) detectability of the basal interface, and (3) characterization of the nature of the basal interface.

Assuming the feasible range of central frequency and bandwidth provided by the previous studies, the proposed detailed assessment of detectability of the targets is aimed at revealing the required signal-to-noise (SNR) budget at the surface that maximizes the detectability of these three target categories. The required SNR budget can guide the selection of main instrument parameters, such as the two-way antenna gain and the

transmitted power. These parameters can support the optimization of the orbital sensor configuration, such as in the case of a recently proposed distributed orbital RS architecture [48].

The chapter is structured as follows. Section 3.2 illustrates the previous studies on the challenges of the EORS design, i.e., ionospheric distortion, surface and firn scattering, volume scattering losses, and the target structure. Section 3.3 describes the proposed approach to the design and performance analysis of EORS, focusing on (1) the limitation of state-of-the-art studies, (2) the EORS simulation approach, (3) the extraction of the ice targets from the simulated EORS radargrams, and (4) the evaluation of target detection performances. Section 3.4 focuses on the description of the datasets used in the study and the experimental results. Finally, Section 3.5 concludes the work and discusses future works.

3.2 Challenges of orbital sounding of the Earth

Airborne RSs have successfully demonstrated that subsurface targets of scientific interest in the ice (IRHs, basal interface, basal flow regimes, etc.) can be detected and interpreted (e.g. [76, 38, 46, 41]). However, extending this capability of sounding the Earth's cryosphere to orbital platforms requires addressing some challenges related to the detectability of the targets. The Earth's ionosphere has the peak electron density at an altitude of 200 - 400 km that can distort the received signal during propagation. Orbital altitudes are typically larger than 500 km, which implies that the signal transmitted from satellite platforms has to propagate through the Earth's ionosphere twice before the reception. At orbital altitudes at relatively low frequencies, the antenna footprint is larger and incidence angles are smaller, resulting in a critical signal to clutter ratio (SCR). The large distance between the RS and the target results in higher propagation losses and beyond the Earth's atmosphere, radar sounding is impacted by the high levels of galactic noise, which is absent in airborne sounding. These factors contribute also to degrade the range resolution and the subsurface SNR and must be considered while designing the orbital RS. Another component that further complicates the design of the orbital RS is the highly complex nature of the target.

The design of the existing and scheduled RSs for planetary bodies are based on a trade-off analysis between the achievable performance given a set of design constraints (instrument and orbit characteristics) and the limitations imposed by the physical scenario (target and environment) [82, 63, 84, 4].

For an orbital RS, previous feasibility studies considered two end-member design concepts: (a) an RS in VHF band operating at the central frequency of 45 MHz [16, 20, 17, 15] and (b) an RS system in P-band operating at a central frequency of 435 MHz [19, 18].

The choice of these two bands is justified by the trade-off between penetration and range resolution, constrained by the ionospheric cut-off frequency and clutter mitigation. A proper frequency choice can significantly improve clutter mitigation [88, 89, 18, 19, 90]; about 40 dB improvement in firm clutter suppression can be obtained with the 45 MHz sounder compared to a P-band one [18]. As for the 45 MHz system, clutter only limits the detection of IRHs deeper than 3000 m [18]. On the one hand, the VHF band can reasonably mitigate the effects of propagation through the Earth's ionosphere while providing high penetration capability. On the other hand, P-band is the lowest possible frequency currently allocated by the International Telecommunication Union (ITU) for Earth observation. With this view, the allocation of the VHF band for Earth observation is included in the preliminary agenda of the 2023 World Radio-communication Conference. In this context, this section will analyze and discuss some of the critical design challenges for an orbital RS, reviewing the previous studies and design concepts.

3.2.1 Propagation through Ionosphere

The ionosphere interacts with the signal by introducing distortions in the radargrams that critically affect the phase and the range resolution. These effects are more pronounced at low frequencies, and sounding is impossible at frequencies lower than the plasma frequency of the ionosphere. For the Earth's ionosphere, Freeman et. al. showed that the cutoff frequency is less than 4 MHz at all latitudes at the solar minimum at 4 AM local time [15]. Even while operating at frequencies much higher than the cut-off (e.g., 40-50 MHz), the received signal can still be distorted in terms of loss of signal power, Faraday rotation of linearly polarized waves, propagation delays leading to uncertainties in the range and phase of the signal, phase dispersion, loss of coherence time, and phase and amplitude variations caused by scintillation (changes in the electron density). Nevertheless, the authors in [15] show that for a signal with a central frequency of 45 MHz and bandwidth of 10 MHz, most of these effects can be tolerable and mitigated with an appropriate design and with data correction. E.g., the Faraday rotation effects can be mitigated by using a circularly polarized signal instead of linear polarization, and the irregularities in the ionosphere occur less than 10% of the time. Moreover, statistical analyses of observations in polar regions show that scintillations causing high power fading have a very low probability of occurrence around the solar minimum; their RMS phase error is lower than 30° more than 50% of the times (depending on the solar zenith angle), which implies a loss of less than 0.2 dB in the gain obtained by coherent integration.

These qualitative assessments of the ionospheric effects were quantitatively analyzed considering the 45 MHz central frequency [17]. The authors demonstrated the feasibility of mitigating these effects with a compensation technique based on Legendre polynomials.

The study considered the range of expected ionospheric parameters, namely the total electron count (TEC) and the magnetic field intensity. It estimated the impact of the ionosphere on the: (1) peak to sidelobe ratio, (2) loss of peak power, and (3) loss of range resolution by the main lobe widening. The compensation approach was based on estimating the TEC values. The authors concluded that the distortion effects can be effectively compensated depending on the accuracy of the parameter estimation; at less than 5% error on the TEC values, the resolution loss factor is nearly 0, and the power loss is less than 1 dB during most of the solar cycle.

The analysis of the ionospheric effects and the satisfactory performance obtained at 45 MHz central frequency with a bandwidth of 10 MHz, especially when operating close to the solar minimum, are the basis of the Orbiting Arid Subsurface and Ice Sheet Sounder (OASIS) [16] and the SaTellite Radar sounder for eArTh sUbsurface Sensing (STRATUS) [20] mission concepts.

3.2.2 Surface and firn scattering

The reflections from off-nadir surface structures can potentially mask the nadir subsurface target reflections in radargrams. The impact of surface clutter in polar ice sounding and its increase with the increase in platform elevation and the radar frequency was studied by airborne sounding over an ice-stream in Greenland at two altitudes (500 m and 4400 m), and operating at two central frequencies (150 MHz and 450 MHz) [90]. The study found that surface clutter is the primary scattering mechanism that can obscure the basal interface, and limits the choice of higher frequencies. To evaluate the impact of clutter at orbital altitudes, and therefore the feasibility of a P-band orbital sounder for Earth, Dall et. al. acquired data using the POLarimetric Airborne Radar Ice Sounder (POLARIS) campaign in Antarctica [19, 28]. Electromagnetic models of the ice targets were extracted from the POLARIS radargrams and integrated with ancillary information on the attenuation properties. These models were used to evaluate the SNR and SCR of the IRHs and the basal interface, using the radar equation. The authors concluded that surface and within-ice volume clutter (from the firn layer) are the primary factors limiting the detectability of the basal interface (in two-third of the considered scenarios in Antarctica, the bed was not detectable).

In a recent study, the contribution of firn clutter has been analyzed in detail by first determining the most appropriate physical model defining the firn layer, followed by simulating and comparing the SCR and SNR achievable at central frequencies of 45 MHz and 435 MHz, with variable bandwidths [18]. The performance simulations at different frequencies show that very high fractional bandwidths are needed at UHF frequencies to maintain the firn clutter at a 25 dB level below the surface power. They recommend

orbital sounding at frequencies below 80 MHz to suppress the impact of near-surface firn clutter. Moreover, it is found that the SCR of the 45 MHz radar is significantly better, the basal interface detection is not affected by clutter, and only the IRHs deeper than 3000 m may have critically low SCR to be detected [18].

Nevertheless, several techniques can mitigate the issues with clutter at design and processing levels. Fully focused SAR processing reduces along-track clutter. Novel RS architectures such as the distributed RS can drastically reduce cross-track clutter [48]. There are also several clutter discrimination approaches based on co-registering the radar-grams with the simulated cluttergrams [54, 91, 92], using single-pass interferometry [93] or exploiting the polarization signatures [94]. Another interesting approach draws inspiration from the clutter discrimination capabilities of big brown bats [55] and exploits the split spectrum and frequency differences for distinguishing between surface and subsurface reflections.

3.2.3 Volume scattering losses

Volume scattering was considered to be the main contributor to firn clutter in POLARIS data, and therefore a critical performance-limiting factor in orbital sounding at UHF frequencies [28]. This interpretation was based on the assumption that firn can be modeled as composed of distributed pores, that result in incoherent backscattering of the signal power. Culberg et. al. analyzed the validity of this assumption by comparing the electromagnetic models of dry firn obtained from ice-core data with airborne radar profiles acquired by MCoRDS (central frequency of 195 MHz) [29] and Accumulation Radar (central frequency of 725 MHz) [95]. They concluded that the firn is best modeled as composed of quasi-specular layers with small-scale roughness (thus contributing to firn clutter, as described in Sec. 3.2.2) rather than a contributor to volume scattering.

The study presented in [18] further evaluated the backscattered power in the 40-50 MHz band by assuming air-filled spherical pores with radii ranging from 1 mm to 1 cm, with realistic porosity derived from ice-cores, and found the volume scattering contribution to be at least 40 dB below the surface power. The authors also studied the two-way attenuation losses due to volume scattering assuming density inhomogeneities and found the losses to be even lower (less than a few dB at HF frequencies). Therefore, these experiments concluded that for the VHF radar, volume scattering is not a major impeding factor in the detection performance.

3.2.4 Ability to resolve the target signal from noise

The galactic noise temperatures at the VHF band and P-band are 6320 K and 19.6 K, respectively [96]. The corresponding noise power levels are -120 dBW and -135 dBW,

respectively, which indicates that at the VHF frequencies, the galactic noise levels are 15 dB higher than at P-band. Thus, previous studies [18, 19, 20] have identified that for orbital ice sounding radar operating at a central frequency of 45 MHz, SNR is a more critical factor than SCR in the detectability of the targets. Accordingly, the galactic noise levels have been considered while projecting the penetration performance of OASIS [16] and STRATUS [20]. At the design level, mitigating these noise levels needs increasing the transmitted power and antenna gain, and improving the effectiveness of along-track processing by increasing the integration length and by choosing appropriate PRF and pulse width.

Many of these technical requirements can be fulfilled by using a distributed architecture based on a flying formation, as elucidated in [48]. With regards to the effectiveness of the along-track processing, the impact of RS acquisitions from orbital altitudes on the SNR was studied in [97]. The authors modeled a point target located 2 km below the ice surface and simulated its radar response to a P-band RS flying at two different altitudes: (1) an airborne altitude of 1 km, and (2) an orbital altitude of 500 km. The study showed that the SNR improvement obtained after focusing on the case of orbital sounding is not as significant as the airborne one. Nonetheless, the improvement in the along-track resolution is achievable with an orbital RS.

3.2.5 Complex structure of the target

The polar ice strata have very complex structural and compositional properties, as revealed by several ice-core data, observations of outcrops, GPR, and airborne campaigns (e.g., [76, 38]). The ice subsurface is characterized by a finely layered structure representing paleoclimatic records of seasonal accumulation and deposition of snow, interbedded by various impurities. The thickness, topography, and composition of these internal reflecting horizons (IRHs) are highly variable, thus inhibiting the precise and uniform modeling of the ice targets across the entire polar ice.

The target geo-electrical models (representing structure, composition, and dielectric properties) play a crucial role in predicting radar detection performance. The previous studies proposing the orbital mission concept were based on evaluating the radar equation, assuming a specular ice surface and basal interface, and a homogeneous dielectric medium [20, 16]. Dall et. al. show that this assumption is not valid for terrestrial ice, which is certainly highly heterogeneous in the top few hundred meters [19].

Ice-core dielectric and density profiles, as well as airborne radar profiles, have been used in some studies to derive realistic physical models of the targets [18, 98, 19], for understanding their detectability. Other studies went a step further and used the ice-core data to generate models for 3D electromagnetic simulations of the radar response of GPR

instruments [99, 100]. While these studies pave the way to the accurate modeling and simulation of RS response of the ice targets, the sparse sampling and shallow depth of ice cores limits their use in continent-wide estimation of detection performance. To the best of our knowledge, there is no study on the detection performance of IRHs with an orbital RS over large areas of the polar ice caps, especially at 40-50 MHz frequencies.

Based on the studies summarized in this section, an orbital RS operating at a central frequency of 45 MHz with a bandwidth of 10 MHz will be able to minimize the distortions caused by the ionosphere and surface clutter, while maintaining the range resolution required to discriminate the IRHs. The studies also indicate that the SNR degradation caused by galactic noise levels may be a limiting factor for the 40-50 MHz orbital RS and may affect the detectability of the IRHs and the basal interface, which has not been studied so far.

3.3 Methodology

3.3.1 Limitations in the previous studies

Although several performances limiting factors, such as the ionosphere and firn clutter have been deeply analyzed in the previous works, there is a lack of studies considering the targets in detail. Regarding the targets, the existing literature on orbital RS design has several limitations:

1. Polar ice is strongly non-homogeneous and has high spatial variability in the structure up to the centimeter scale. The resulting variability in the subsurface scattering losses and dielectric attenuation profiles [101, 102] translates to significant spatial variability in the radar penetration capability. Thus, it is necessary to study the impact of this variability on the retrieval of the ice-thickness across different regions.
2. Detectability of the IRHs is critical for the science goals of an orbital mission to model historical records of processes occurring within the ice. While ice-core data provides detailed information on the IRHs with a resolution of a few centimeters, achieving such levels of detail from an orbiting platform is technically insurmountable. However, the goal of orbital RS profiling is to image the prominent IRHs detectable at the feasible bandwidth with sufficient SNR. The existing orbital studies usually assume a homogeneous target and ignore the IRHs.
3. To support the scientific goals of an orbital mission, it is not only required to detect the basal interface (i.e., to penetrate the full thickness of the ice), but also to characterize its geophysical properties. This includes detecting geological targets within the ice column and extracting information on the glacier processes, which includes

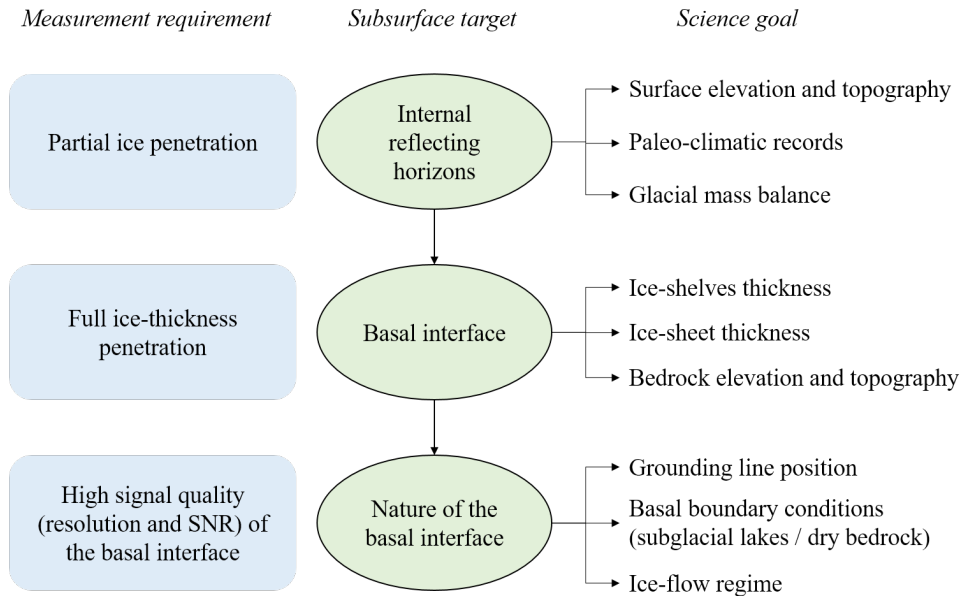


Figure 3.1: Hierarchical performance analysis of the targets based on progressively increasing measurement requirements and achievability of the science goals of subsurface sounding of the polar ice.

the mapping of the water distribution at the basal interface (e.g., basal flow regime and subglacial lakes). This is of critical importance for predicting the stability of the ice sheets and the rate of seaward flow of the ice. Such analyses require detailed geo-electrical modeling of the targets, rather than considering a homogeneous structure.

This work aims to address these limitations by proposing an approach to the assessment of the detection performance of an orbital RS considering a realistic representation of the polar ice targets. The target modeling is handled in a non-subjective and automatic way by leveraging the airborne data and using them as inputs to an airborne-to-satellite radargram simulation technique [87]. This allows us to account for the IRHs and the spatial variability in the dielectric properties. The simulation of the orbital radargrams also enables an assessment of the automatic interpretability of the detected targets and thus, demonstrates the scientific feasibility of the mission.

3.3.2 Science goals of orbital sounding: a hierarchical approach to the performance analysis

From the perspective of the scientific objectives of subsurface sounding of the polar ice and the nature of the related targets, a hierarchical relationship between the radar performance and the target detectability can be observed (Figure 3.1). At a preliminary level of performance, an important scientific requirement of polar ice sounding is that

the prominent near-surface IRHs should be mapped. This requires penetration through the top part of the ice and with sufficient power, so that signal received from the IRHs is above the noise and the off-nadir clutter levels. The detectability of the IRHs is significant for inferring the paleoclimatic models and the ice mass balance.

In the next higher level of performance, the orbital RS should be able to delineate the basal interface, representing the interface between ice-bedrock (for grounded ice) or ice-water (subglacial lakes, i.e., grounded ice having a large pool of melt-water at the base, or floating ice). This requires a penetration capability higher than the full ice thickness, overcoming the scattering and power attenuation losses caused by the ice. The detected basal interface can be used to estimate the thickness of ice sheets and ice shelves, and generate the 3D topography of the bedrock (which can also support other relevant scientific studies such as detection of buried craters [103, 104]).

Finally, for extracting scientifically valuable information from the data acquired by the mission, it is not only necessary to detect the prominent dielectric interfaces, but also to accurately interpret the geophysical properties characterized by these interfaces (e.g., composition, structure, dielectric properties). Such studies have been widely applied to the airborne radargrams, such as to the automatic detection of subglacial lakes [46] and mapping of basal units [41]. In this context, if the requirement on the penetration through the full ice thickness is satisfied, a higher level of performance requires the interpretation of the basal conditions (e.g., presence or absence of subglacial lakes, subglacial channel-flow, accreted ice). This is possible only if the SNR of the signal received from the base is sufficiently high and there are adequate range and along-track resolutions. Identifying the nature of the basal interface (such as ice-freshwater, ice-sea water, ice-bedrock) can support the inference of the grounding line position, basal boundary conditions, and the ice-flow regime.

3.3.3 Proposed approach

Fig. 3.2 shows the schematic representation of the proposed methodology. In the first step, orbital radargrams are simulated for different values of a variable design parameter, starting from a large database of airborne radargrams acquired over different geographical zones in Antarctica and Greenland. The radargrams are two-dimensional matrices in which the rows represent time samples of the received signal, the columns represent the frames acquired while the RS moves in the along-track direction and the values in the matrix represent the received signal (which is a complex number, but in this case, we convert it into the received power expressed in Watt or dB as required). The input airborne radargram is denoted as $P_{r,A}(r_A, a_A)$, where the subscript A refers to airborne, a_A is the frame index, and r_A is the sample index of the airborne radargram. The simulated

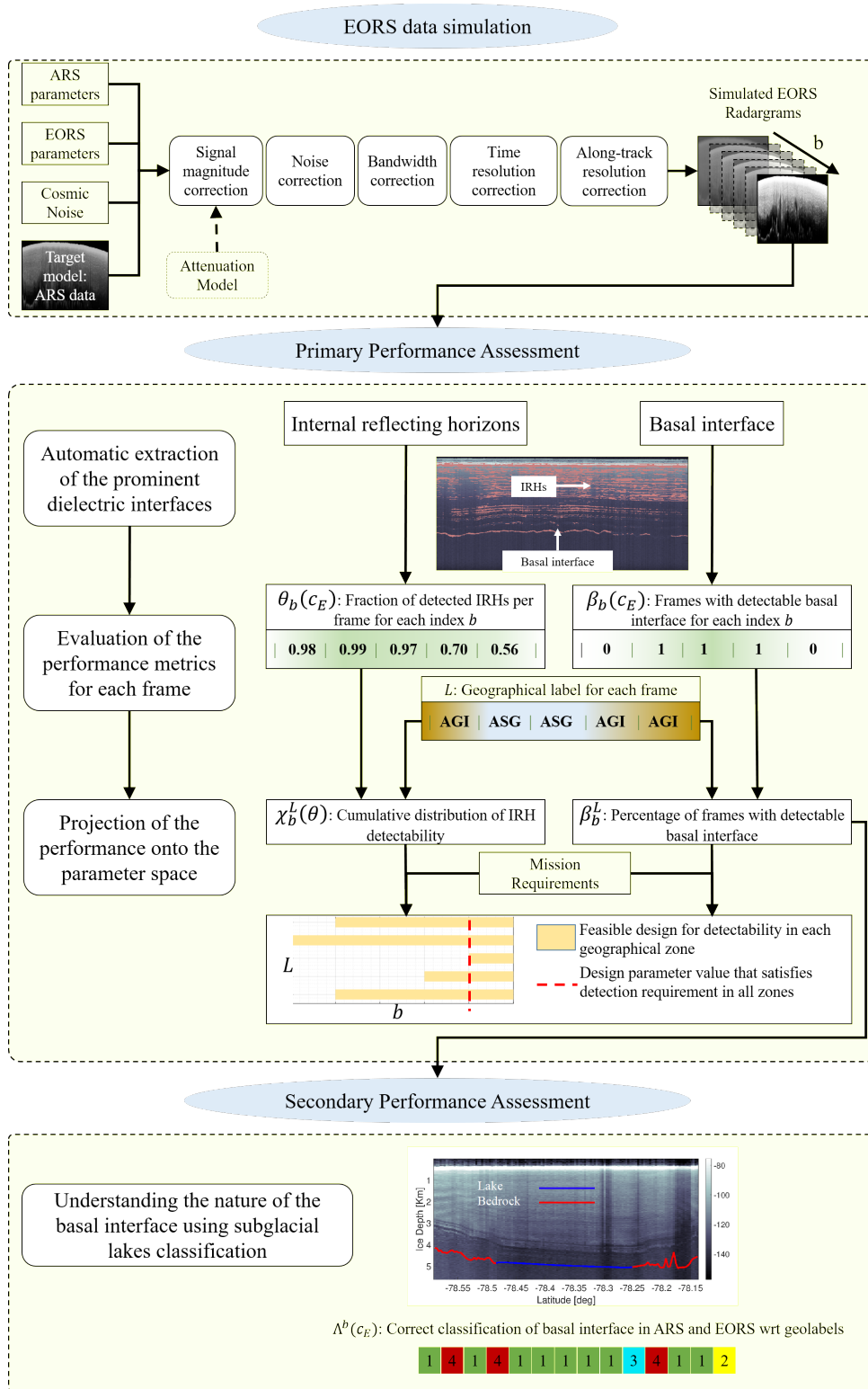


Figure 3.2: Flowchart of the proposed methodology.

orbital radargram is denoted as $P_{r,E}(r_E, a_E)$, where the subscript E refers to EORS, a_E is the frame index, and r_E is the sample index of the orbital radargram.

A useful approach to the design of RSs is based on evaluating the maximum achievable SNR at the surface (referred here as SNR budget and represented by the notation SNR) that depends mainly on the instrument parameters and the orbit configuration. From the budget, the losses due to the target and the environment (subsurface reflectivity, attenuation rate, scattering losses, ionospheric distortions, and coherence losses) are excluded to determine the SNR margin available at the expected depth of the subsurface interface. This is justified on the basis of previous studies (see Section 3.2.3). The SNR margin should be positive and higher than the sensitivity of the RS to detect the subsurface interface. To represent the range of possible values of the budget, N_b different hypotheses of the SNR parameter are considered, referred by the simulation index $b = 1, 2, \dots, N_b$. The corresponding values of the budget parameter are denoted with the simulation index as the subscript, i.e. SNR_b .

Each of the N_b simulated radargrams is analyzed for evaluating the orbital performance using metrics defined in the proposed approach. To adopt a hierarchical approach (see Section 3.3.2), we have defined performance assessment at two levels representing the primary and the secondary objectives of an orbital mission. The primary assessment pertains to the detectability of the prominent dielectric interfaces, while the secondary assessment analyzes the ability to characterize these interfaces. First, the IRHs and the basal interface are extracted from the simulated radargrams with the help of the ground truth available in the input airborne data. From these dielectric interfaces, we evaluate the primary performance metrics for each frame a_E of the simulated radargrams.

Since the structural and geophysical properties of the ice targets vary with their location, we have selected the input ARS radargrams widely distributed in different geographical conditions. To separately analyze the radar performance in each of the geographical settings, we have defined five principal geographical zones based on the known differences in the dielectric and radar characteristics of the basal interfaces [46, 105, 102] and properties of the IRHs. These zones include grounded ice (interior of the ice-sheets having an ice-bedrock interface), floating ice (coastal ice-shelves and floating ice-tongues having ice-seawater interface), and subglacial lakes (ice-freshwater interface). These are further segregated by their location in Antarctica and Greenland, due to the different thickness and age of the ice in the two continents. The zones are designated by a geographical label L (henceforth referred to as geolabel). The geolabels are Greenland grounded ice (GGI), Greenland floating ice (GFI), Antarctica grounded ice (AGI), Antarctica floating ice (AFI), and Antarctica subglacial lakes (ASG).

The geolabels L are defined at each geographical coordinate (latitude, longitude) of the

airborne and orbital ground tracks, and then assigned to the corresponding frames. The frame indices with the label L are denoted as $c_E^L = 1, 2, \dots, N_E^L$ (N_E^L is the total number of frames corresponding to the label L). The labeled frames are used to estimate the cumulative performance for each simulation index b grouped by the geographical zone L . The cumulative performance is matched with an appropriate mission requirement (typically flowing down from the science goals of polar subsurface sounding) to identify the feasible range of the design parameter. For visualization and comparison, the performance is projected onto a parameter space defined by the design parameter SNR_b and the geolabel L . Based on this performance mapping, guidelines are presented for the selection of the design parameter that represents a trade-off between the feasible design and the achievable performance.

Finally, we define and evaluate a secondary performance metric that quantifies the interpretability of the detectable basal interface. This is achieved by applying an automatic subglacial lakes detection algorithm [46] to the simulated radargrams. The lake detection performance is assessed by comparing the accuracy of basal interface classification using the airborne and the simulated orbital data for the frames having a detectable basal interface.

3.3.4 Assumptions

In this work, we consider a VHF band orbital RS, with a central frequency of 45 MHz and a bandwidth of 10 MHz. The selected airborne operates at UHF frequencies with a central frequency of 195 MHz and bandwidth of 30 MHz (Table 3.1). Note that the use of a UHF airborne RS (which depends on data availability) is detrimental for the estimation of performances of the considered orbital RS, as we can simulate the degradation of performance due to the minor bandwidth but we cannot recover the advantages in terms of clutter and volume scattering at a lower frequency (see Appendices 3.6 and 3.4 for more details).

The proposed simulation approach used in the first step of the methodology is based on the following assumptions:

1. The real part of the permittivity of ice has negligible variability with frequency, as reported in previous studies [106, 107]. For pure ice, the imaginary part is higher by a factor of 4 at 45 MHz compared to UHF frequencies, while the conductivity is nearly constant [108]. However, for polar ice, the imaginary permittivity and conductivity are affected by structural imperfections, presence of impurities, and freezing/melting processes [108]. The ice-sheet conductivity values are reported to have a spatially variable frequency-dependence in Antarctica and Greenland [107, 101]. Given such ambiguities and the absence of empirical models for polar ice

electromagnetic properties, we have assumed the dielectric profile (i.e. position of the dielectric interfaces and the complex permittivity values) to be the same at the frequency of the airborne and the orbital sounders.

2. The change in the complex permittivity with depth is not substantial over small distances. Due to the heterogeneous nature of cryosphere targets, the dielectric profile changes with depth in a way that cannot be estimated easily. However, we assume that for a small thickness (the order of a few resolution cells), the dielectric profile is locally constant along the range direction. This is generally true at RS wavelengths since the sensitivity of the RS to small changes in the dielectric profile depends on the bandwidth, which is relatively lower for long-wavelength RSs [106].
3. Volume scattering caused by distributed targets is considered independent of the frequency (i.e., the volume scattering observed by the airborne is retained in the orbital radargrams). Thus, the volume scattering losses between 40-50 MHz are overestimated in the current approach (see Appendix 3.6), and the real orbital RS will be subjected to much lower levels of these losses.
4. The effects of clutter at the orbital footprint and the ionospheric distortions are not addressed by the simulations. These can be addressed in separate studies using well-established techniques [54, 18], and their effects can be mitigated. Nonetheless, we have considered the power loss due to the ionosphere in the definition of the SNR margin (see Appendix 3.6) for the assessment of target detectability.
5. The radar echo processing techniques applied to the airborne and possibly applicable to the orbital RS are likely to be different due to the differences in the acquisition scenarios. The simulations do not account for the differences in the echo processing techniques, except the contribution of the range and along-track processing gains to the signal power.
6. The difference in the antenna pattern between the airborne and orbital systems is not corrected using this approach.
7. In low altitude airborne RS operating at UHF frequencies, the geometry (high dipping angles) of IRHs causes energy dispersion via several mechanisms such as destructive stacking, SAR processing, and off-nadir ray path extension [109]. These losses are ignored in the proposed approach, which is constrained by the information available in the airborne data (i.e. the observed IRH reflectivity). This assumption can result in an underestimation of the IRH and basal interface detection performance of the orbital RS, which does not suffer from these losses.

3.3.5 Orbital data simulation approach

For the simulations, we use an approach based on reprocessing available radargrams acquired over geological analogs of the investigated target [24]. This is done by identifying the differences in the analog and investigated acquisition scenarios (in terms of the instrument parameters, acquisition geometry, and target geo-electrical properties) and understanding the impact of these differences on the characteristics of the analog and investigated radargrams. In this work, the orbital radargrams are simulated using a special case of the analog-based simulation approach, in which the analog and the investigated RSs acquire the data over the same target (in this case the polar ice regions). The advantage is that it is not necessary to model the differences in the target geo-electrical properties, and this also gives high structural fidelity between the analog and investigated target representation. However, the target attenuation factor depends on the central frequency of the RSs, which should be accounted for by processing the profile of the target radar response. The adaptation of the analog-based simulation approach to the case of orbital simulations by minimizing the assumptions on the target geo-electrical modeling is described in detail in [87].

The simulation steps are briefly outlined as follows, where subscript A refers to the ARS, subscript E refers to the EORS scenarios, r and a are row and column indices of the radargram, respectively, z refers to the depth computed at each row index r_A assuming a constant ice permittivity of 3.15:

1. *Target geo-electrical modeling*: Besides the instrument parameters and the range to the target, the received power depends on the target propagation factor $\hat{\gamma}_A(z, a_A)$. It can be estimated from the airborne received power $P_{r,A}(r_A, a_A)$, depth z , and the known instrument parameters (platform altitude H_A , two-way antenna gain G_A^2 , signal wavelength λ_A , transmitted signal power $P_{t,A}$) and is given by:

$$\hat{\gamma}_A(z, a_A) = 10 \log \left[P_{r,A}(r_A, a_A) \frac{64\pi^2(H_A(a_A) + z)^2}{P_{t,A}G_A^2G_{r,A}G_{az,A}\lambda_A^2} \right] \quad (3.1)$$

Equation (3.1) is based on the specular version of the radar equation, which assumes that (i) the targets are flat and specular, (ii) the properties of the target are constant over an area larger than the first Fresnel zone [110, 58] and (iii) refraction gain is equal to 1. The actual target propagation factor $\gamma_A(z, a_A)$ depends on the target reflectivity profile $\rho(z, a_A)$, the attenuation profile $\alpha(z)$ and the central frequency of the airborne $f_{c,A}$, given by:

$$\gamma_A(z, a_A) = 10 \log\{\rho(z, a_A)\} - \int_0^z f_{c,A}\alpha(z, a_A)dz \quad (3.2)$$

where \log is the logarithm to base 10. The reflectivity depends on the presence of discontinuities in the ice-sheet (e.g., IRHs) at the scale of the RS wavelength. Assuming that the medium between successive IRHs is homogeneous at the airborne frequency (and therefore is homogeneous at the orbital frequency, which is even lower), the attenuation factor $\hat{\alpha}(z, a_A)$ is estimated as the local gradient of the $\hat{\gamma}_A(z, a_A)$ profile. The corresponding EORS target propagation factor $\hat{\gamma}_E(z, a_A)$ is given by:

$$\hat{\gamma}_E(z, a_A) = \hat{\gamma}_A(z, a_A) + (f_{c,E} - f_{c,A})\hat{\alpha}(z, a_A) \quad (3.3)$$

where $f_{c,E}$ is the central frequency of the orbital RS.

2. *Signal magnitude correction:* Using the radar equation (3.1), the orbital received power $P_{r,E}(r_A, a_A)$ is given by:

$$\frac{P_{r,E}(r_A, a_A)}{P_{r,A}(r_A, a_A)} = \frac{P_{t,E} G_E^2 G_{r,E} G_{az,E} \lambda_E^2 (H_A(a_A) + z)^2 \Gamma_E(r_A, a_A)}{P_{t,A} G_A^2 G_{r,A} G_{az,A} \lambda_A^2 H_E(a_A)^2 \Gamma_A(r_A, a_A)} \quad (3.4)$$

where $\Gamma_A(r_A, a_A)$ and $\Gamma_E(r_A, a_A)$ represent $10^{\hat{\gamma}_A(r_A, a_A)/10}$ and $10^{\hat{\gamma}_E(r_A, a_A)/10}$, respectively for each frame a_A .

3. *Noise correction:* This step considers the differences in the noise power level of the two scenarios due to the presence of different sources of noise. Note at airborne flying altitudes, the data are not affected by the galactic noise. On the contrary, sounding from a satellite platform is subjected to the isotropic cosmic microwave background (CMB). In this step, Rayleigh distributed galactic noise power [96] corresponding to an equivalent noise temperature at the orbital frequency, and bandwidth is stochastically added to the processed airborne radargrams.
4. *Bandwidth correction:* The orbital bandwidth is typically lower than that of the airborne (as considered in this study). This difference is corrected by applying a low-pass filter to the processed airborne radargrams after the signal magnitude correction. The bandwidth correction ensures that the target reflectivity profile corresponds to the dielectric interfaces detectable with the bandwidth of the orbital.
5. *Range and along-track sampling correction:* The spacing between the samples in the range direction depends on the sampling frequency of the RSs. Similarly, the distance between successive pulses (frames of the radargrams) depends on the PRF of the RSs. These differences are addressed by appropriately resampling the radargram in range and along-track direction, using the nearest neighbor resampling technique. The details of the filtering and resampling process can be found in [24].

Thus, we obtain the simulated radargram represented in terms of received power $P_{r,E}(r_E, a_E)$.

3.3.6 Primary performance assessment

Automatic extraction of the prominent dielectric interfaces from radargrams

The dielectric interfaces representing the IRHs are known to have high reflectivity and a horizontal aspect. This information is well-known and used in the literature for automatic detection of the IRHs [40, 111, 42]. These techniques identify the IRHs based on their connectivity in the along-track direction and high contrast with respect to their neighboring range samples. We have adapted the state-of-the-art approaches [40] to formulate a computationally simple IRH detection algorithm applied to the large database of radargrams under consideration. The algorithm extracts horizontally connected linear features from the denoised radargram by wavelet decomposition. The extracted edges are refined by a morphological closing operation to eliminate isolated speckle reflections. The result is a binary IRH position mask, which is extracted from the input airborne and the simulated orbital radargrams for computing the IRH detection performance metric.

The basal interface is the deepest reflecting horizon in the radargram having a significantly high intensity (due to high dielectric contrast) and a horizontal continuity with its along-track neighboring samples. This knowledge has been used for the automatic detection of the basal interface from the radargrams following the techniques described in [44, 45].

Definition of the primary performance metrics

In the next step, we define metrics to quantify the detection performance corresponding to the b^{th} simulated radargram. For verifying whether a prominent interface is detected or not in the simulated orbital radargrams, the input airborne data is used as reference ground truth (this is valid since the data quality, and therefore the detection performance of the airborne, is higher than the orbital) and has been validated in the literature. Thus, for a given interface, we check its presence in the airborne data by creating an interface position mask and cross-checking the signal power at the corresponding positions in the orbital radargrams. The subsurface targets, at the positions defined by the reference interface position mask, are considered detected if their SNR is above a given SNR margin.

The evaluation of the IRH detection metrics consists of two main steps: (1) defining the IRH position mask from the airborne data, and (2) comparing the orbital IRH detection with the airborne mask to estimate the two-dimensional detected-IRH matrix. The IRH position mask is derived by extracting the IRHs from the airborne (as described in Section 3.3.6) and resampling it to the resolution of the simulated orbital radargrams (in terms of range resolution, sampling frequency, and along-track sampling to achieve a pixel-to-pixel correspondence). The mask has a value of 1 at positions where the IRHs are present in the airborne radargram and 0 elsewhere. Next, the IRH position mask is compared pixel-by-pixel to the simulated radargram to create a binary detected-IRH matrix. This

matrix has a value of 1 at positions for which the IRH position mask is 1 as well as the IRH SNR is above the SNR margin and has 0 elsewhere. For the b^{th} simulated radargram, the IRH detection performance metric $\theta_b(a_E)$ is the probability of IRH detection in the frame a_E , which is estimated as the ratio between the total number of detected IRHs and their total number in the IRH position mask in each frame.

Similarly, the basal interface detection metric is evaluated by comparing the 2D basal interface position mask with the simulated radargrams. The mask is created by resampling the basal interface extracted from the airborne radargram to match the resolutions of the orbital radargram. It has a value of 1 at positions where a detectable basal interface is present in the airborne radargram and 0 elsewhere. The basal interface position mask is compared pixel-by-pixel with the simulated radargram to create the basal interface detection metric $\beta_b(a_E)$, defined for each frame a_E and the b^{th} simulated radargram. The metric $\beta_b(a_E) = NULL$ for the frames for which the mask is 0 in every row of the simulated radargram, representing the case where the basal interface is not detectable in the airborne data, and hence definitely not present in the simulated data (due to the simulation process adopted). The metric $\beta_b(a_E) = 1$ if the SNR at the pixel positions where mask = 1 is above the SNR margin, representing the cases of the detectable basal interface in the simulated orbital data. Finally, the metric $\beta_b(a_E) = 0$ if the SNR at the pixel positions where mask = 1 is below the SNR margin, representing the cases of non-detectability of the basal interface in the simulated orbital data.

Projection of the performance onto the parameter space

Next, the performance metrics are grouped by the geolabels. The values of the IRH detection metric $\theta_b(a_E)$ are grouped for the frames c_E^L having the same geolabel L and defined as the cumulative fraction of frames $\chi_b^L(\theta)$ for which the per-frame probability of IRH detection is greater than a probability threshold $\theta \in [0, 1]$.

$$\chi_b^L(\theta) = \frac{\text{count}[\theta_b(c_E^L) \geq \theta]}{N_E^L} \quad (3.5)$$

The plot of χ_b^L vs θ can be understood as a cumulative distribution of IRH detection performance for each geolabel and each simulated radargram. For interpreting the performance and supporting the design, the information from the cumulative plots is projected onto the parameter-space defined by the geographical zone vs the design parameter. This can be done by knowing the requirement on the probability threshold θ and the cumulative performance $\chi_b^L(\theta)$ which should be satisfied by the design. These are defined in terms of the minimum required per-frame probability of IRH detection θ_{min}^L and the minimum required cumulative fraction of frames χ_{min}^L . The superscript L denotes that these requirements may be different for different geographical zones.

The minimum required SNR for the detectability of the IRHs in the zone L is given by the smallest value of SNR_b such that at least χ_{min}^L frames have more than θ_{min}^L IRHs detectable per frame:

$$SNR_{min}(\theta_{min}^L, \chi_{min}^L, L) = \min_{\forall b} \{SNR_b : \chi_b^L(\theta_{min}^L) \geq \chi_{min}^L\} \quad (3.6)$$

However, the orbital instrument should be designed for a single value of SNR that should satisfy the detection requirements across all the geographical zones. For a set of requirements $(\theta_{min}^L, \chi_{min}^L)$, the best design parameter SNR_{design} is given by:

$$SNR_{design} = \max_{\forall L} \{SNR_{min}(\theta_{min}^L, \chi_{min}^L, L)\} \quad (3.7)$$

In a more straightforward approach, the values of the basal interface detection $\beta_b(a_E)$ are grouped for the frames c_E^L having the same geolabels. The grouped performance is estimated as the fraction of frames β_b^L for which the basal interface detection metric is equal to 1, and is given by:

$$\beta_b^L = \frac{\text{count}[\beta_b(c_E^L) = 1]}{\text{count}[\{\beta_b(c_E^L) = 1\} \vee \{\beta_b(c_E^L) = 0\}]} \quad (3.8)$$

For a mission requirement of β_{min}^L on the basal interface detectability for the geographical zone L , the minimum required SNR is given by the smallest value of SNR_b such that at least β_{min}^L frames have a detectable basal interface:

$$SNR_{min}(\beta_{min}^L, L) = \min_{\forall b} \{SNR_b : \beta_b^L \geq \beta_{min}^L\} \quad (3.9)$$

The design SNR is obtained similar to (3.7), as the maximum value of SNR_{min} that satisfies the requirement in all the zones.

3.3.7 Secondary performance assessment

Characterization of the nature of the basal interface

For the secondary performance assessment, we focus on the ability to characterize a crucial basal boundary condition, i.e. the presence of subglacial lakes. The secondary performance is analyzed only for frames for which the primary performance is satisfied, i.e. basal interface is detectable in the orbital data. To detect subglacial lakes, the automatic algorithm proposed in [46] for analyzing airborne radargrams is considered and adapted to the case of orbital data. The algorithm exploits the extreme differences in the properties of the basal interface depending on its constituent materials, namely ice-bedrock or ice-water (i.e. subglacial lake). The ice-water interfaces have much higher reflectivity since the dielectric permittivity of water $\varepsilon_r^{water} \approx 80$ is much higher than other subglacial materials at the interface, such as sediments and bedrock for which $\varepsilon_r \approx 6$. Moreover, the basal

interface appears flat and smooth when a subglacial lake is present, while it has a high degree of roughness at the ice-bedrock interface. As a result, the leading and the trailing edges of the basal waveforms (the frames around the basal interface peak) related to ice-water interfaces are steeper and have a higher correlation between consecutive waveforms than those of the ice-bedrock interface.

For each pixel of the basal interface, considering these properties, a set of features are extracted that model the topography, the shape of the waveforms, and the power statistical properties. Regarding the topography features, we consider the root mean square height (the standard deviation) of the basal topography and the local waveform correlation. For the shape of the waveform, the method estimates the leading and the trailing edge steepness. Finally, for the statistical features, we consider the first four statistical moments of the basal interface, namely the mean adjusted basal peak power, the coefficient of variation, the skewness, and the kurtosis. For each frame of the interface detected, we extract the features according to [46]. These features are then normalized and analyzed by a Support Vector Machine (SVM) classifier with a Radial basis function (RBF) kernel to discriminate between samples related to a subglacial lake n_+ or not n_- .

The subglacial lake detection algorithm [46] is applied to the airborne and the simulated orbital radargrams acquired in the Lake District of East Antarctica and Siple Coast. As ground truth, as in [46], we consider the radar-detected lakes [112] present along the East Antarctica radar track. We performed the experiments using 50% randomly picked training samples from the labeled lake n_+ and not-lake n_- samples, respectively, and the remaining 50% of the samples for the test phase. The training samples are chosen in a way that half are labeled as lake n_+ and the remaining half as not-lake n_- . The classification performance is expressed in terms of overall accuracy, precision, specificity, and recall (also called hit rate) for the orbital data and the airborne data [46]. The specificity is computed as $= 100 - \text{false alarm rate}$, while the recall $= 100 - \text{miss rate}$. The overall accuracy is defined as the number of correctly classified pixels over the number of processed pixels. The specificity indicates the probability that a pixel is not labeled as belonging to a class, given that it does not belong to that class. The precision is the number of true positives (i.e., the number of samples correctly labeled) over the total number of samples correctly and wrongly labeled as belonging to that class. The recall indicates the number of samples correctly labeled for a class over the total number of elements that belong to that class.

Subglacial lakes detection metric

Next, we define the lake detection performance metric as a vector $\Lambda_b(a_E)$ defined for each frame of the b^{th} simulated radargram. The metric is evaluated as follows: (i) The trained SVM classifier is separately applied to the airborne and simulated orbital

radargrams to obtain two vectors ℓ_{ARS} and ℓ_{EORS} of the predicted labels of the basal interface (i.e., n_+ lake and n_- non-lake). (ii) The vector of the ARS predicted labels ℓ_{ARS} is resampled to match the along-track resolution of the orbital, to have a one-to-one correspondence between the two vectors. (iii) For both the ARS and the EORS predicted labels, we compute the vectors representing correct prediction, i.e., ξ_{ARS} and ξ_{EORS} as follows:

$$\xi_i = \begin{cases} 1, & \text{if } \ell_i = GT_i; \\ 0, & \text{otherwise} \end{cases} \quad (3.10)$$

where GT_i indicates the ground truth and the index i indicates $i = EORS, ARS$. Hence, vectors ξ_{ARS} and ξ_{EORS} are equal to 0 when the label is correctly predicted whereas it is equal to 1 if the prediction is incorrect. (4) Finally, we define $\Lambda(a_E)$ by comparing the vectors ξ_{ARS} and ξ_{EORS} as follows:

$$\Lambda(a_E) = \begin{cases} 0, & \text{if } \beta_b(a_E) = 0; \\ 1, & \text{if } \xi_{ARS} = 0 \wedge \xi_{EORS} = 0 \\ 2, & \text{if } \xi_{ARS} = 0 \wedge \xi_{EORS} = 1 \\ 3, & \text{if } \xi_{ARS} = 1 \wedge \xi_{EORS} = 0 \\ 4, & \text{if } \xi_{ARS} = 1 \wedge \xi_{EORS} = 1 \end{cases} \quad (3.11)$$

3.4 Experimental Results

3.4.1 Definition of the data set

Based on the significant advantages of a 45 MHz sounder (see Section 3.2) with respect to the other cases presented in the literature, we consider an orbital RS with parameters similar to the one proposed in [20] and [15]. The airborne radargrams are taken from the database provided by the Centre for Remote Sensing of the Ice-Sheets (CReSIS), acquired by the airborne multi-channel coherent radar sounder (MCoRDS) [29]. The details of the selected campaigns and flight lines are: 2017_Greenland_P3 (0328_01, 0410_03, 0413_01, 0502_01, 0505_01, 0412_01, 0511_01); 2017_Antarctica_P3 (1125_03, 1116_03, 1112_03, 1124_03, 1103_05); 2013_Antarctica_P3 (1120_01, 1119_01, 1126_01, 1127_01); 2016_Antarctica_DC8 (1115_03, 1115_04, 1103_06).

Table 3.1 lists the parameters of the airborne and the proposed orbital systems. The input radargrams are processed with the range and azimuth compression, and minimum variance distortionless response (MVDR) algorithm [88, 113]. The MVDR algorithm mitigates clutter and noise in the data with better performance than other techniques, which helps in the primary performance assessment by reducing misclassification of clutter as

Table 3.1: Proposed orbital [20] and airborne MCoRDS [29] parameters

Parameter	MCoRDS (ARS)	EORS
Central frequency (MHz)	195*	45*
Wavelength λ (m)	1.54	6.66
Galactic noise temperature T_{cmb} (K) [96]	-	6320
Bandwidth B (MHz)	30	10
Altitude H (km)	2 - 4	500
Along-track resolution (m)	300	30
Sampling frequency (MHz)	45	12
Transmitted power P_t (W)	1050	200 - 800
Pulse length τ (μs)	10	100
Range processing gain $G_r = \tau B$ (dB)	24.77	30
Pulse-repetition frequency PRF (Hz)	343	1200
Platform velocity vel (m/s)	144	7616
Along-track processing gain $G_{az} = \sqrt{\frac{\lambda H}{2}} \frac{PRF}{vel}$ (dB)	16	23
Two-way antenna gain G^2 (dB)	6	4 - 20
Surface reflectivity Γ_S (dB)	-10**	
SNR budget at surface SNR_b (dB)	107.6	65 - 90

* These are the parameters for the MCoRDS-3 instrument in the following of the considered campaigns: 2017_Greenland_P3, 2017_Antarctica_P3, 2013_Antarctica_P3. For the flight lines from the 2016_Antarctica_DC8 campaign, the central frequency is 190 MHz with a bandwidth of 50 MHz.

** This value of surface reflectivity is considered in the definition of the design parameter assuming a constant surface real permittivity of 3.5 (ice). It has no bearing on the simulation technique, which is based on the surface power derived from the input airborne radargram.

subsurface reflectors. Moreover, the algorithm in [46] used for the secondary performance assessment is also based on MVDR-processed data. However, the MVDR processing suffers from a self-nulling problem that is related to the suppression of very strong signals relative to the noise [88, 113].

The SNR budget at the surface (which is considered as the main variable for the design of the system) is given by:

$$SNR_b = \frac{P_t G^2 \lambda^2 \Gamma_S G_r G_{az}}{64\pi^2 H^2 k B T_{cmb}} \quad (3.12)$$

where k is the Boltzmann constant and the other symbols are described in Table 3.1. In this experiment, we consider six different values of the SNR budget at the surface $SNR_b = \{65, 70, 75, 80, 85, 90\}$ dB. Thus, the simulation index $b = 1, 2, \dots, 6$ represents each case of the design parameter SNR_b . Note that these values have been obtained by considering a constant -10 dB surface reflectivity corresponding to ice real permittivity of 3.5, to be consistent with the conventional definition of SNR budget. In reality, the surface reflectivity varies with the location and is a property of the target. However, in the simulation step, this has been taken into account as implicitly modeled from the airborne radargram (see Section 3.3.5). For considering the subsurface reflector to be detectable, the SNR margin at the subsurface is taken to be 5 dB, accounting for ionospheric and coherence losses. Justification of the value of the SNR margin is provided in Appendix 3.6.

The five geolabels L are determined with the help of several ancillary datasets available for Earth's polar regions. For Greenland, the MEASURE's Greenland Ice Mapping Project (GIMP) ice, ocean, and grounded-ice masks [114] are used to obtain the geolabels grounded ice $L = \text{GGI}$ and floating ice $L = \text{GFI}$ in Greenland. For Antarctica, the Norwegian Polar Institute's Quantarctica package [115] is used to identify the grounded ice $L = \text{AGI}$ and the floating ice $L = \text{AFI}$ from the boundaries dataset [116, 117]. The subglacial lakes $L = \text{ASG}$ are labeled using the radar-detected lakes [112] in the subglacial lakes inventory [118, 119] and the demarcated boundary of the Vostok lake [120]. Fig. 3.3 shows the locations of the airborne tracks of the input radargrams used in this analysis along with their geolabels. The selected airborne dataset covers a track of 108,000 km, of which about 99,000 km are expected to have a detectable basal interface in the airborne data.

In the following, we present the experimental results obtained by applying the proposed approach to the selected set of airborne radargrams. First, we show some examples of simulated orbital radargrams. Next, we present the results of the primary performance assessment for the detection of the IRHs and the basal interface. Finally, we report the secondary performance analysis related to the characterization of the basal interface, in terms of classification accuracy of subglacial lakes.

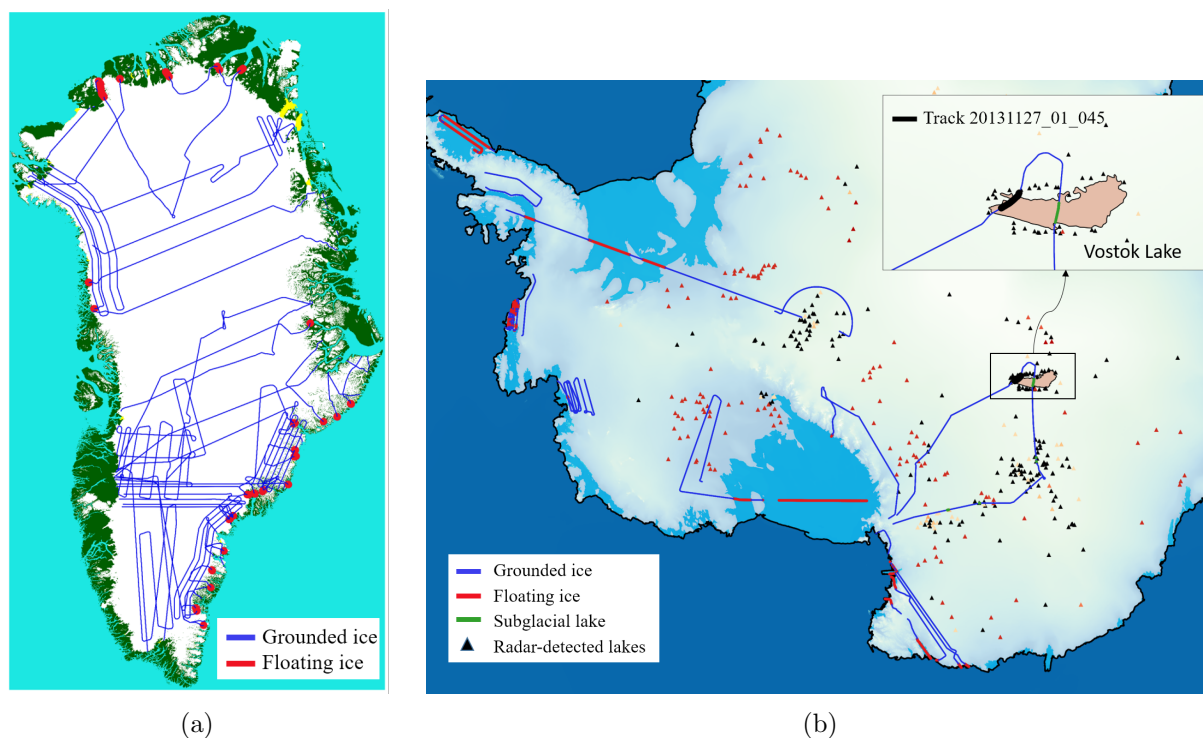


Figure 3.3: Selected airborne radargram tracks and related geolabels: (a) in Greenland, (b) in Antarctica. The black triangles in (b) indicate radar-detected lakes [118, 112], which were used to generate the geolabels for the subglacial lakes. The inset map shows the location of the track corresponding to Fig. 3.4.

3.4.2 Simulated orbital radargrams

Fig. 3.4(a) shows an example of the average received power profile of the simulated orbital and the airborne frames for a radargram acquired over the Vostok lake in East Antarctica. The effect of the power correction step in modifying the slope of the power profile, as a function of the orbital frequency is visible. Furthermore, the effect of noise correction resulting in the noise floor nearly matching the galactic noise level can also be observed. Figures 3.4(b-d) show examples of the input airborne radargram and the simulated radargrams for two extreme values of the SNR budget. Visually we can see that increasing the SNR budget increases the detectability of the IRH and the basal interface. Another observation is the reduction in the range resolution due to a lower bandwidth of the orbital. This results in a reduced spatial sampling of the detectable IRHs in the simulated radargrams.

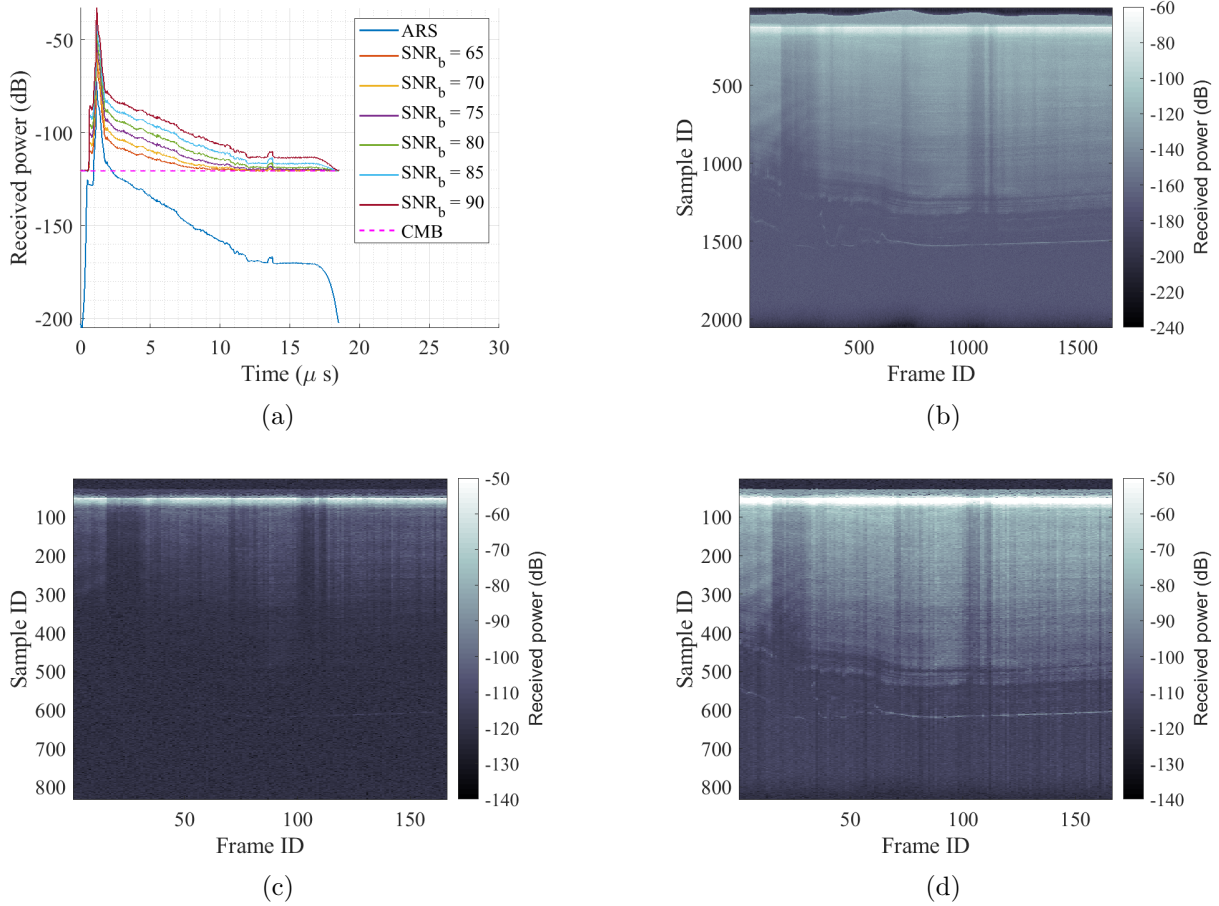


Figure 3.4: Examples of simulated radargrams and average received power profile corresponding to the airborne radargram 20131127.01.045 in East Antarctica. (a) Average frame power of the airborne and the simulated orbital radargrams for different SNR_b values, (b) airborne radargram, (c) simulated orbital radargram for $SNR_b = 65$ dB, (d) simulated orbital radargram for $SNR_b = 90$ dB. The location of the track is shown in the inset map in Fig. 3.3

3.4.3 IRH detection performance

Figures 3.5(a-e) show the cumulative distribution of the IRH detection performance for each geolabel L . The horizontal axis shows the probability threshold θ , while the vertical axis shows the cumulative fraction of frames $\chi_b^L(\theta)$ having IRH detection greater than θ . We see that the distribution shifts towards the top right corner by increasing the SNR budget, indicating an improvement in the grouped IRH detection performance (i.e., a higher number of frames has a higher IRH detection metric). Furthermore, the plots reveal that the targets in Greenland have higher detection performance compared to those in Antarctica, and the poorest performance occurs for the subglacial lakes zone

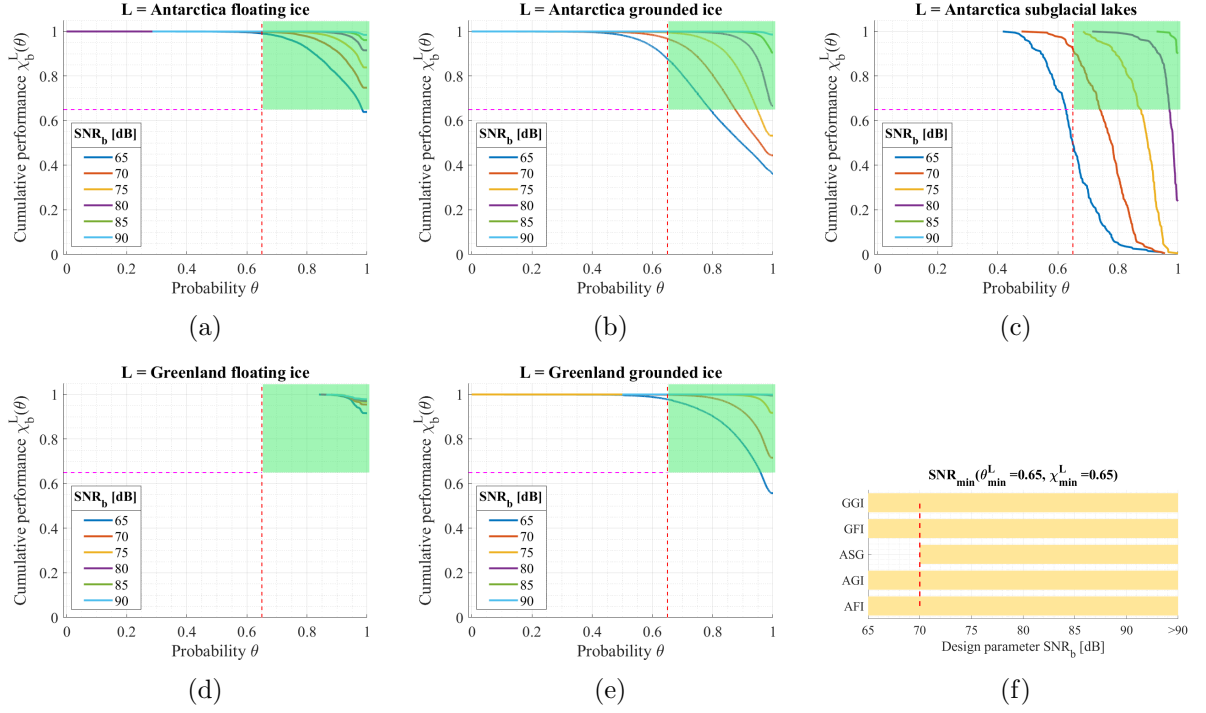


Figure 3.5: Results of the IRH detection performance for different geolabels and SNR_b . Cumulative distribution of the IRH detection performance for: (a) Antarctica floating ice, (b) Antarctica grounded ice, (c) Antarctica subglacial lakes, (d) Greenland floating ice, and (e) Greenland grounded ice. An example of the SNR budget selection based on a possible set of mission requirements is presented in (f). It shows the value of SNR_b that gives the per-frame IRH detection probability θ greater than 0.65 (red dashed vertical line), which is satisfied by at least 65% of all the frames (magenta dashed horizontal line). The region of the cumulative distribution plots that satisfy these requirements is highlighted in the green box. The corresponding minimum required SNR_b values for detectability in each zone are indicated by the yellow bars in (f). The red dashed vertical line in (f) corresponding to $SNR_b = 70$ dB indicates the design SNR budget necessary for satisfying the IRH detection requirements for all the five geolabels.

in Antarctica. An example of projecting the performance onto the parameter-space is demonstrated here, considering the requirements $\theta_{min}^L = 0.65$ and $\chi_{min}^L = 0.65$ for all L . These requirements are indicated by the red vertical lines and the magenta dashed horizontal lines, respectively in Figures 3.5(a-e). For ease of understanding, the region of the cumulative distribution satisfying these two conditions is marked by a green box. For each geolabel, the plots occurring within the green box represent the required SNR_b values. For example, for the Antarctica subglacial lakes, the green box contains the plots corresponding to $SNR_b \geq 70$ dB. Therefore, for this zone, the minimum required SNR budget is $SNR_{min}(0.65, 0.65, L = ASG) = 70$ dB. Similarly analyzing for each of the zones, we obtain the projection of the geolabels vs the required SNR budget shown by the yellow bars in Fig. 3.5(f). From this graph, we can see that the design SNR budget

		Requirement on Probability of IRH detection per frame																					
		0.00	0.05	0.10	0.15	0.20	0.25	0.30	0.35	0.40	0.45	0.50	0.55	0.60	0.65	0.70	0.75	0.80	0.85	0.90	0.95	1.00	
Requirement on Cumulative fraction of frames	1.00	65	>90	>90	>90	>90	>90	>90	>90	>90	>90	>90	>90	>90	>90	>90	>90	>90	>90	>90	>90	>90	
	0.95	65	65	65	65	65	65	65	65	65	65	65	70	70	75	75	80	80	80	80	85	90	
	0.90	65	65	65	65	65	65	65	65	65	65	65	70	70	70	75	75	80	80	80	85	85	
	0.85	65	65	65	65	65	65	65	65	65	65	65	65	70	70	75	75	75	80	80	80	85	
	0.80	65	65	65	65	65	65	65	65	65	65	65	65	70	70	75	75	75	80	80	80	85	
	0.75	65	65	65	65	65	65	65	65	65	65	65	65	70	70	70	75	75	75	80	80	85	
	0.70	65	65	65	65	65	65	65	65	65	65	65	65	65	70	70	75	75	75	80	80	85	
	0.65	65	65	65	65	65	65	65	65	65	65	65	65	65	70	70	75	75	75	80	80	85	
	0.60	65	65	65	65	65	65	65	65	65	65	65	65	65	70	70	70	75	75	80	80	85	
	0.55	65	65	65	65	65	65	65	65	65	65	65	65	65	70	70	70	75	75	80	80	85	
	0.50	65	65	65	65	65	65	65	65	65	65	65	65	65	70	70	70	75	75	80	80	85	
	0.45	65	65	65	65	65	65	65	65	65	65	65	65	65	65	70	70	75	75	75	80	85	
	0.40	65	65	65	65	65	65	65	65	65	65	65	65	65	65	70	70	75	75	75	80	85	
	0.35	65	65	65	65	65	65	65	65	65	65	65	65	65	65	65	70	70	70	75	75	80	85
	0.30	65	65	65	65	65	65	65	65	65	65	65	65	65	65	65	70	70	70	75	75	80	85
	0.25	65	65	65	65	65	65	65	65	65	65	65	65	65	65	65	65	70	70	75	75	80	85
	0.20	65	65	65	65	65	65	65	65	65	65	65	65	65	65	65	65	70	70	75	75	80	80
	0.15	65	65	65	65	65	65	65	65	65	65	65	65	65	65	65	65	70	70	75	75	80	80
	0.10	65	65	65	65	65	65	65	65	65	65	65	65	65	65	65	65	70	70	75	75	80	80
	0.05	65	65	65	65	65	65	65	65	65	65	65	65	65	65	65	65	65	70	75	75	80	80
0.00	65	65	65	65	65	65	65	65	65	65	65	65	65	65	65	65	65	65	65	65	65	65	

Figure 3.6: The design SNR values for detectability in all the five zones for different sets of mission requirements on the probability of IRH detection and the cumulative fraction of frames. The red box identifies the scenario shown in Fig. 3.5. The values in the matrix indicate the minimal value of SNR_b that satisfies the requirements in the corresponding row and column headings.

that satisfies the detectability of IRHs in all the five geographical zones for the given set of requirements is $SNR_{design} = 70$ dB (indicated by the red dashed vertical line).

The mission requirements typically flow down from the scientific goals of the mission and may be different for different geographical zones. However, due to the absence of a well-defined orbital mission, and to avoid introducing any bias due to subjective assumptions, we evaluate the design SNR for the full range of the mission requirements and also consider them to be independent of the geolabels. Fig. 3.6 tabulates the design SNR budget that satisfies the detectability in all zones computed for the full range of possible θ_{min} and χ_{min} .

Depending on the scientific objectives of the mission and the feasibility of obtaining the desired SNR , a trade-off between the requirements and the instrument design should be identified. Let us illustrate how the performance projection supports this trade-off analysis. From the cumulative distribution plots (Figure 3.5), we see that for the floating ice in Greenland, even with $SNR_b = 65$ dB, very high IRH detection performance is

obtained (more than 95% of the IRHs are detectable in more than 95% of the frames). For the floating ice in Antarctica and the grounded ice in both regions, more than 90% of the IRHs can be detected in more than 90% of the frames with an SNR of 70 dB, and the performance improves further up to almost all the IRHs with $SNR_b \geq 85$ dB. For the Antarctica subglacial lakes, it requires an $SNR_b \geq 85$ dB to achieve a detectability of more than 90% of the IRHs in more than 90% of the frames; however, in all the frames, at least 40% of the IRHs are detectable even with $SNR_b = 65$ dB (likely to be the shallow high reflectivity layers). These results reveal that the subglacial lake zone (dominated by Lake Vostok in this study) are critical targets for the detectability of IRHs, which may not be a challenge to an orbital RS design if the science goal of subsurface profiling over subglacial lakes does not require the deeper IRHs to be detected.

Thus, considering the same requirements for all geolabels, the values of the design SNR shown in Fig. 3.6 are predominantly affected by the subglacial lakes (as shown by its resemblance to Fig. 3.5(c) and illustrated by the example in Fig. 3.5(f)). Besides design and performance assessment, such trade-off analysis combined with the study on the scientific interests in each zone can also be used to define the feasible IRH detection requirements for each geographical zone.

3.4.4 Basal interface detection performance

Table 3.2 shows the performance projection of the basal interface detection for each geographical zone and SNR budget. The reported values are the grouped performance metric (β_b^L), which denotes the percentage of frames having a detectable basal interface in the simulated radargrams. As an example of the selection of the design SNR, let us consider a basal interface detection requirement of $\beta_{min}^L = 0.95$ for all zones. With a design SNR budget of 75 dB, this requirement is satisfied in all five zones.

The table can be used for a trade-off analysis similar to that described for IRH detection performance. Like IRH detection, even in terms of the basal interface, the Antarctica subglacial lakes, particularly in the region around Lake Vostok, are critical targets and result in the lowest performance for $SNR_b \leq 70$ dB among the five groups. The detection performance is relatively lower for the subglacial lakes since these zones represent the deepest basal interfaces in the polar ice radargrams (up to 4.5 km in some cases) and thus require higher radar penetration capability. In contrast, the floating ice of Antarctica and Greenland, being shallow targets with high interface reflectivity (ice-water dielectric discontinuity), have a very high basal interface detection performance, even with low SNR values.

Note that with $SNR_b \geq 80$ dB, nearly 100% of the basal interfaces in all five zones are detectable indicating that, with this value of the design parameter, the thickness of the

Table 3.2: Basal interface detection performance for different geographical zones

L	Design parameter SNR_b [dB]					
	65	70	75	80	85	90
AFI	99.7	99.8	99.9	99.9	99.9	99.9
AGI	84.4	90.8	95.2	98.0	99.5	99.9
ASG	66.7	88.0	97.4	100	100	100
GFI	100	100	100	100	100	100
GGI	80.0	90.8	99.0	100	100	100

ice-shelves and ice-sheets in Antarctica and Greenland can be surely estimated in nearly all the frames where they are detectable in the airborne data.

3.4.5 Subglacial lakes detection performance

We illustrate the subglacial lakes performance considering two cases: case (i) $SNR_b = 85$ dB and case (ii) $SNR_b = 90$ dB, where the basal interface detection metric is 100%. To determine the kernel parameters of the SVM classifier, we apply a 10-fold cross-validation considering the range of the parameters $c_{RBF} \in [10^{-3}, 10^8]$ and $\gamma_{RBF} \in [10^{-2}, 10^4]$. In the cross-validation, for each value of c_{RBF} and γ_{RBF} , the training samples are divided in $k = 10$ folds, and an SVM model is trained with c_{RBF} and $k - 1$ folds. Each SVM model is then validated on the remaining sample fold, considering the accuracy as a metric. The validation accuracy is averaged over the k experiments. Finally, the best value of c_{RBF} and γ_{RBF} are defined as those maximizing the average accuracy. The optimal kernel parameters are $c_{RBF} = 8$ and $\gamma_{RBF} = 16$ for both $SNR_b = 85$ and $SNR_b = 90$ experiments. Table 3.3 shows the classification performance for the airborne [46] data, and for the orbital data for $SNR_b = 85$ and $SNR_b = 90$ experiments. For both cases, the accuracy is higher than 97%. Also, the other classification performances (specificity, precision, and recall) have high values, confirming the possibility of detecting subglacial lakes from the orbital data with high performance. The difference in the classification performance of experiments with $SNR_b = 85$ and $SNR_b = 90$ is extremely small indicating that, if the basal interface is detectable, it is possible to analyze the nature of the interface and detect the presence of subglacial lakes.

Fig. 3.7 shows a simulated orbital radargram corresponding to $SNR_b = 90$ dB and the predicted labels of the basal interface. In this radargram, the Vostok lake, which appears as a continuous flat reflector (indicated in blue), is detected by the algorithm

Table 3.3: Classification performance of the subglacial lake detection algorithm applied to the airborne data and the orbital data for $SNR_b = 85$ and $SNR_b = 90$.

	ARS [46]	$SNR_b = 85$	$SNR_b = 90$
Recall	99.08	99.81	99.8
Specificity	99.08	97.12	96.87
Precision	99.28	97.61	97.56
Overall Accuracy	98.22	97.46	97.39

and well discriminated from the surrounding bedrock samples (indicated in magenta). Fig. 3.8 shows the lake detection metric for $SNR_b = 90$ dB, plotted along the radar tracks in the Lake District of Antarctica. From the map, it is evident that the algorithm effectively classifies the basal interface into lakes and non-lakes for a major part of the track (marked in green) for both the airborne and the orbital. The basal interface around the margins of Vostok lake is misclassified (marked in red) in both the airborne and the orbital radargrams. A noteworthy observation relevant for this study is that there are very few locations where the classification is accurate for the airborne and not for the orbital (yellow) and vice versa (blue).

3.5 Discussions and Conclusions

In this work, we have presented a methodology for a detailed and realistic assessment of the performance of an orbital RS in detecting important scientific targets in the polar ice subsurface. The performance assessment methodology is based on simulating the orbital radargrams, starting from the available databases of airborne radargrams, and evaluating a set of performance metrics defined in this work. The orbital radargrams are simulated corresponding to different values of the SNR budget at the surface, and the performance analysis of the simulated radargrams is used to reveal the SNR budget that maximizes detectability of the targets across different geographical regions of the polar cryosphere. A hierarchical approach is used to evaluate the detection performance of (1) internal reflecting horizons, (2) basal interface, and (3) subglacial lakes.

The methodology, which in general, has been demonstrated on an orbital RS with a carrier of 45 MHz and bandwidth 10 MHz, by simulating the radargrams starting from data acquired by MCoRDS (operating in the UHF band). The results indicate that an SNR budget of 80 dB is required for the detection of 90% of the IRHs (in each frame) in more than 90% of the frames in different geographical zones. In particular, nearly all

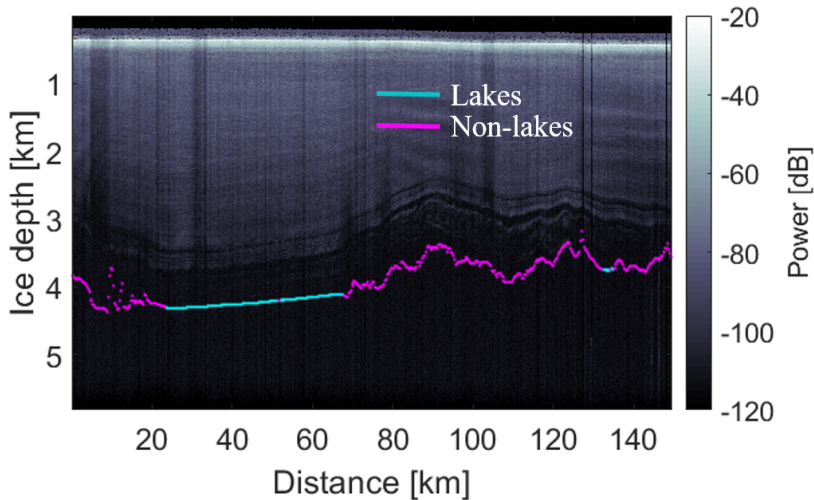


Figure 3.7: Results of the automatic lakes detection algorithm applied to simulated orbital radargram corresponding to $SNR_b = 90$ dB and for the radar track 20131127.01.045-047 in East Antarctica containing the Vostok lake. The blue region of the basal interface is detected as lake while the magenta region is detected as non-lake.

IRHs in Greenland and the floating ice regions can be detected in up to 95% of the frames with an SNR budget of 80 dB. Moreover, in all the zones, more than 95% of the basal interface detectable in airborne radargrams can be detected with an SNR budget of 75 dB, which approaches 100% with further increase in the SNR budget.

The detectable basal interfaces are also identified as subglacial lakes and bedrock with very high accuracy using an automatic classification algorithm [46] applied to the orbital simulated radargrams. The accuracy is comparable to that of the airborne data, which has been demonstrated for the SNR budget of 85 dB and 90 dB for illustration purposes. Of course, as in all automatic techniques, there is an intrinsic error rate of the classifier, irrespectively of whether the airborne or orbital data are used. This also shows that existing automatic algorithms for airborne radargrams can be successfully adapted for the extraction of similar information also from future orbital data.

As an additional experiment, we have verified the proposed approach by comparing the simulated orbital RS performance obtained from MCoRDS with that obtained from another airborne system [39] having parameters close to the 45 MHz orbital RS. The results of this experiment are presented in Appendix 3.7 and show a good agreement between the performance obtained from different airborne radargrams.

Recently, a distributed radar sounder [48] architecture has been proposed, which is based on the deployment of an array of small satellite sensors in a suitable orbital flying configuration. Such an architecture allows the synthesis of very large antenna apertures,

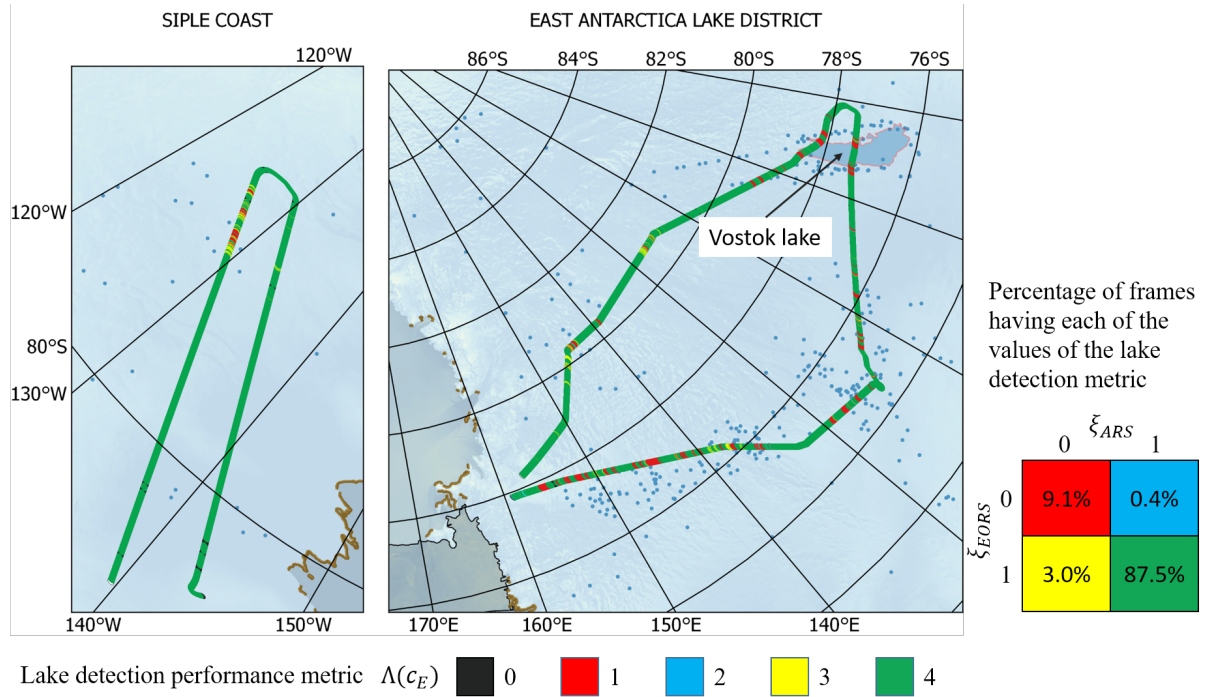


Figure 3.8: Lakes detection performance metric $\Lambda(a_E)$ plotted along the radar track in Antarctica Lake district and Siple Coast. The metric values indicate locations for which the basal interface is: not detectable (0); not correctly classified in both the airborne and the simulated orbital radargrams (1); correctly classified in the airborne but not in the orbital (2); correctly classified in the orbital but not in the airborne (3); and correctly classified in both the airborne and the simulated orbital radargrams (4). The matrix on the right shows the percentage of frames for each of the metric values.

thereby significantly improving the along-track resolution, the clutter performance, and the SNR. In particular, the SNR of such a system depends on the antenna gain and transmitted power of individual sensors, and the total number of sensors. Therefore, the performance analysis presented in this work can support and simplify the design of the distributed architecture for an orbital RS. The results presented here can also support a risk assessment of the distributed architecture, such as evaluation of the loss in detection performance due to damage of some of the individual sensors (the resulting loss in SNR budget can be computed and the corresponding detection performances can be extracted).

For simplicity, the simulation approach proposed here is not integrated with the ionospheric effects and the off-nadir clutter response. However, the losses due to propagation through the ionosphere, roughness of the surface, and volume scattering have been included in the SNR margin. Another performance-limiting factor that has not been considered in this study is the effect of seasonal changes in englacial water storage, which can cause a seasonal increase in the attenuation factor that should be considered in the mission design phase [121, 122]. On the contrary, certain factors degrade the quality of

the input airborne radargrams and may lead to underestimation of the orbital RS performance. For example, in the radar equations (3.1) and (3.4) we do not consider refraction effects in estimating the subsurface path lengths [58]. These effects are negligible for the orbital RS, while they increase the losses in the case of the airborne systems. Including the refraction effects can improve the orbital RS detection performance, especially over deeper targets such as the Vostok lake. Moreover, the ARS frames for which the roll angle of the aircraft is significantly high may also be degraded resulting in an underestimation of the orbital RS performance. These frames could be removed or corrected in future simulations to further improve the accuracy of the performance assessment.

Clutter is an important factor in the selection of the orbital RS frequency as shown in previous studies [18]. The clutter performance can be integrated into the proposed analysis, by complementing it with the simulation of the cluttergram (using several well-established approaches [92, 54]) over the selected airborne tracks using available digital elevation models. The masking of the IRHs by the off-nadir clutter should be considered for evaluating the actual IRH detection performance in terms of SCR. However, in the context of this work, clutter does not significantly influence the SNR budget parameter. Regarding the ionosphere performance, the loss of signal strength and coherence (due to phase errors) may reduce the estimated detection performance in case of extreme values of TEC. The ionospheric effects can also be easily integrated into the proposed simulation approach using the phase information of the input airborne data and applying the estimated phase distortions as a function of the Earth's ionospheric parameters. The integration of ionospheric distortions and clutter simulations into the proposed methodology presents scope for future research. Moreover, there are several theories for modeling the radar attenuation at the airborne and orbital RS frequencies (such as frequency-dependent or independent), which also depend on the fraction and type of impurities present in the ice. The implications of these assumptions and the accurate modeling of the attenuation factor will also be explored in future extensions of this work.

The simulated radargrams generated by the proposed method can also be used to test the adaptability of automatic target detection algorithms developed for the airborne data to the orbital case. This has been demonstrated in this work using a subglacial lakes detection algorithm. In preparation for the scientific interpretation of the data in the advanced phases of development of the mission, the proposed simulation approach can be used to adapt the existing algorithms for applications to the orbital radargrams. As a final remark, it is worth noting that the scientific objectives of an orbiting RS are not restricted to the detection of bedrock, subglacial lakes, and ice shelves. In future activities, we plan to analyze the required conditions for interpreting the basal state, such as frozen or thawed bedrock [105], subglacial water flow channels [81], and the presence of marine

ice and cavities at the base of ice-shelves [123].

3.6 Appendix A: SNR margin calculations

The proposed simulation approach does not include some of the losses that can be critical for the detection of the ice targets. To include their effects in the detectability analysis, we consider an SNR margin of 5 dB, i.e. a subsurface interface is considered to be detected if its SNR is at least 5 dB. In this section, we justify how 5 dB is a conservative SNR margin and is sufficiently higher than the total expected losses.

Let $\mathcal{L}(f_c)$ denote the total loss in power in dB caused by phenomena that are not accurately modeled in the simulation approach and depend on the central frequency f_c of the orbital RS. These include two-way volume scattering attenuation $\nu(f_c)$, ionospheric effects $\Omega(f_c)$, and coherence loss due to surface roughness $\psi(f_c)$. Out of these, the simulations do not include ionospheric effects, while overestimating the volume scattering and coherence losses (the simulation represents these losses around 190-195 MHz, i.e. the central frequency of the ARS, which are expected to be much higher than the losses at 45 MHz, i.e. the orbital RS central frequency). Let us quantitatively examine the overestimation and the missing loss terms one by one.

At $f_c = 45$ MHz, the volume scattering loss is nearly 0, whereas at $f_c = 195$ MHz, it is about 8 dB (obtained from Fig. 16 in [18], averaged over a radius of 0 to 0.5 m of the volume scatterers). The ionospheric peak loss at 45 MHz after ionospheric compensation is reported in Figure 4 of [17] and ranges between 0.1 dB to 2 dB during the solar minimum and rises to 6 dB during extreme events and high errors in TEC estimations, during the 11-year solar cycle. For this calculation, we will consider the worst-case peak loss of 6 dB to be conservative.

The coherence loss due to roughness depends on the surface elevation and slopes of Greenland and Antarctica. We have used 90 m resolution digital elevation model (DEM) of Greenland [114] and 400 m resolution DEM of Antarctica [124] to first evaluate the slopes at the DEM resolution and estimate the Hurst exponent, which was then used to scale the slopes to a horizontal lag distance of 6.6 m (wavelength at 45 MHz) and 1.5 m (wavelength at 195 MHz) [125]. The coherence loss is related to the slope and is obtained from back-scattering models based on Kirchhoff's approximation [126]. Fig. 3.9 shows the spatial distribution of the estimated coherence losses over Antarctica and Greenland at 45 MHz. Note that the interior of the ice sheets in most of the areas is relatively flat, and has a minor contribution to the low coherence loss. The literature values of the slopes obtained with other datasets, including higher resolution DEMs are consistent or even lower than what we report here [127, 128, 129, 130]. In any case, we found that the difference between the coherence loss at 45 MHz and 195 MHz is not significant and it is

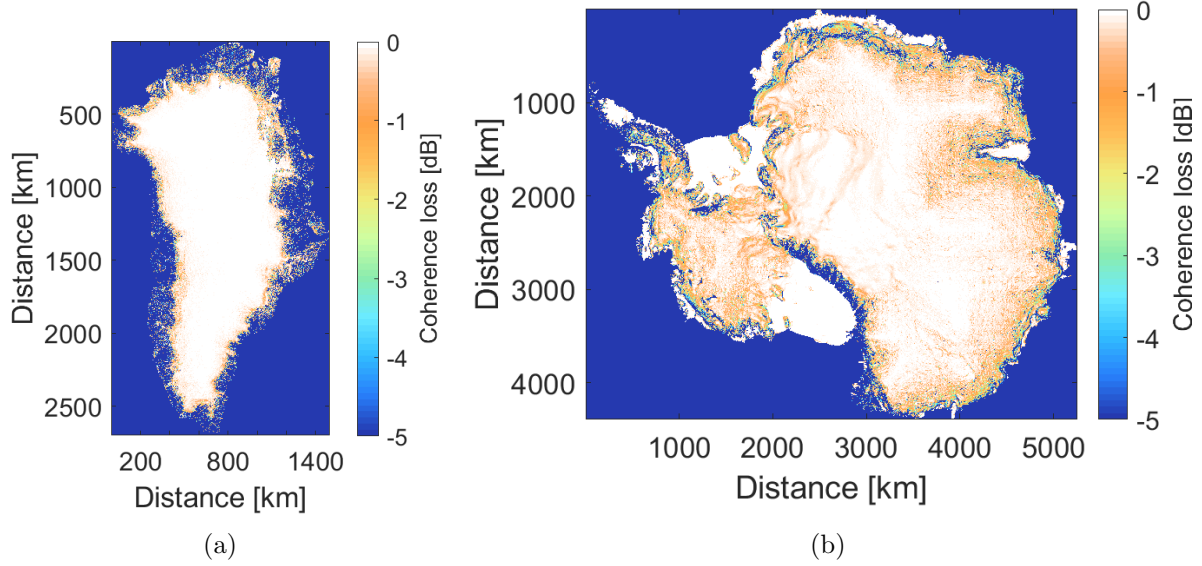


Figure 3.9: Coherence loss estimated over (a) Greenland and (b) Antarctica at 45 MHz central frequency.

not changing the SNR margin. We have estimated the average coherence loss at 45 MHz and 195 MHz as 1.56 dB and 2.22 dB, respectively.

Thus, the total loss at 45 MHz is:

$$\mathcal{L}(45) = \nu(45) + \Omega(45) + \psi(45) = 0 + 6 + 1.56 \approx 8 \text{ dB} \quad (3.13)$$

However, the losses already included in the simulation are:

$$\nu(195) + \psi(195) = 8 + 2.22 \approx 10 \text{ dB} \quad (3.14)$$

Therefore, from (3.13) and (3.14), we see that there is a net overestimation of 2 dB of losses in the simulated radargrams. To further allow for uncertainties in the ionospheric and volume scattering losses, we have considered an additional SNR margin of 3 dB for assessing the detectability, thus resulting in a total margin of 5 dB over the expected SNR of the targets.

3.7 Appendix B: Comparison of simulated orbital RS performance obtained from different airborne radargrams

The simulation technique based on reprocessing available RS data on a geologically similar terrain, which is the basis for the EORS simulations in this work, has been already validated in [24]. In this section, we present an experiment to compare the performance assessment of an orbital RS for a specific case starting from different airborne data, to show the reliability and robustness of the proposed approach. The experimental results

presented in Section 3.4 have been obtained using as input the data acquired by the airborne MCoRDS-3 instrument, which operates in the UHF band (with central frequency around 195 MHz). However, there exist other airborne instruments, such as the high-capability radar sounder (HiCARS) system [39] operating at a central frequency of 60 MHz with a bandwidth of 15 MHz, and thus very close to the parameters of the proposed orbital RS (Table 3.1). While this is favorable for obtaining more reliable and realistic simulations, the coverage of HiCARS is limited to Antarctica only (this is the reason for which they were not used in this work).

Nevertheless, we have exploited the opportunity presented by the availability of HiCARS data to further validate the proposed methodology. To this purpose, we have selected the following pair of nearly overlapping MCoRDS and HiCARS radargrams: (1) the HiCARS-2 Level 1B time-lagged echo strength profiles data IR2HI1B_2011349_VCD_JKB2g_DVD01a_000 [39, 131] (only the high gain acquisition was used) and (2) the MCoRDS-3 MVDR processed echoes 20131127_01_032-033 from the 2013_Antarctica_P3 campaign [29] provided by CReSIS (see Table 3.1). These cover a track length of about 80 km in the grounded ice of East Antarctica.

Next, starting from the MCoRDS and the HiCARS data, we simulated the radargrams of an orbital RS having the same parameters as reported in Table 3.1 and using the technique described in Section 3.3.5. The two sets of simulated radargrams obtained are referred by the subscript $H - E$, i.e. HiCARS to EORS, and $M - E$, i.e. MCoRDS to EORS. Finally, we compared the primary detection performances in terms of (i) the received power from the basal interface and (ii) the IRH detection performance metric. Note that the secondary performance analysis (i.e. detection of subglacial lakes) is implicitly validated because (i) it depends on the detectability of the basal interface and (ii) the underlying classification algorithm has been already validated in [46] using ground truth data.

Fig. 3.10 shows comparison of the two performance metrics for three values of the design parameter $SNR_b = 70, 75, 80$ dB. The plots in the first column show the histograms of the basal interface power for each frame of the $M - E$ and $H - E$ simulated radargrams. The histograms show a close matching in both cases for all the values of the design parameter. Recall that the basal interface power defines the SNR of the basal interface, which is compared with the SNR margin to obtain the basal interface detection metric $\beta_b(a_E)$. Thus, from the histograms, we can infer that irrespective of the galactic noise level or the SNR margin, the estimated $\beta_b(c_{M-E})$ and $\beta_b(c_{H-E})$ are matching.

The plots in the second column show the histograms of the IRH detection metrics $\theta_b(c_{M-E})$ and $\theta_b(c_{H-E})$, which represent the probability of IRH detection in each frame of the simulated radargrams (obtained with SNR margin of 10 dB for ease of compar-

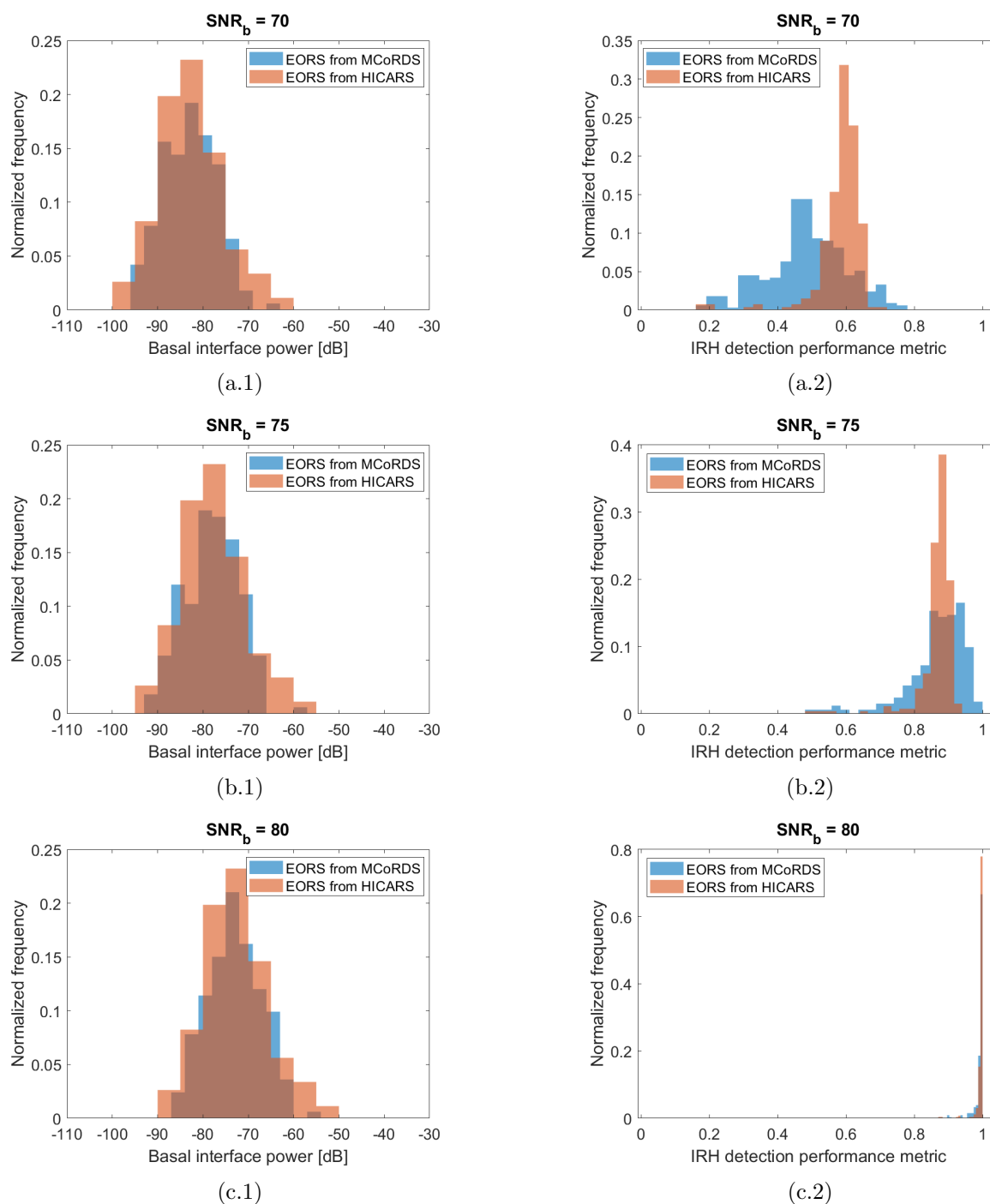


Figure 3.10: Comparison of performance metrics for the EORS simulations obtained from MCoRDS and HiCARS instruments. The simulations correspond to design parameter values of (a) $SNR_b = 70$ dB, (b) $SNR_b = 75$ dB, and (c) $SNR_b = 80$ dB. The performance metrics are: (1) basal interface power in dB and (2) IRH detection performance metric for each frame of the simulated radargrams.

ison, otherwise with 5 dB SNR margin the IRH performance metric is saturated close to 100% for the considered track). In this case, the $H - E$ radargram shows slightly higher performance in detecting the IRHs compared to the $M - E$ radargram, which is an obvious effect of the different original penetration capabilities of MCoRDS and HiCARS. This especially impacts the detection of the weak IRHs that have low reflectivity in general. These IRHs are strongly detectable in the HiCARS data [131], and thus also detectable in the simulated $H - E$ radargrams. Whereas, these IRHs have low SNR in the MCoRDS data, and therefore are masked by the galactic noise in the simulated $M - E$ radargrams. Note that, the unavoidable effect of the difference in penetration capabilities is more prominent at lower values of SNR_b (e.g., see Fig 3.10(a.2)), while converging to similar performance as the SNR budget increases, (e.g., see Fig 3.10(c.2)).

In conclusion, these experiments demonstrate the validity of the proposed performance assessment methodology, and further show that the proposed approach is not biased by the choice of the input airborne data (although, when possible ARS as much similar as possible to the orbital RS should be considered). To show the effectiveness of the methodology, we have presented the comparison for lower-level metrics, which are more closely related to the simulated radargrams. However, the final performance assessment of an EORS, made on a larger database covering several thousand kilometers of track length and grouped by the geolabels, is expected to be less sensitive to relatively small differences in the simulated radargrams.

**Part III: Automatic analysis of radar
sounder data with fuzzy logic and
deep learning**

Chapter 4

An unsupervised fuzzy system for the automatic detection of candidate lava tubes in radar sounder data

Lava tubes are buried channels that transport thermally insulated lava. Nowadays, lava tubes on the Moon are believed to be empty and thus indicated as potential habitats for humans. In recent years, several studies investigated possible lava tube locations, considering the gravity anomaly distribution and surficial volcanic features. This Chapter proposes a novel and unsupervised method to map candidate buried empty lava tubes in radar sounder data and extract their physical properties.¹ The approach relies on a model that describes the geometrical and electromagnetic (EM) properties of lava tubes in radargrams. According to this model, reflections in radargrams are automatically detected and analyzed with a fuzzy system to identify those associated with lava tube boundaries and reject the others. The fuzzy rules consider the EM and geometrical properties of lava tubes, thus their appearance in radargrams. The proposed method can address the complex task of identifying candidate lava tubes on a large number of radargrams in an automatic, fast, and objective way. The final decision on candidate lava tubes should be taken in post-processed by expert planetologists. The proposed method is tested on both a real and a simulated dataset of radargrams acquired on the Moon by the Lunar Radar Sounder (LRS). Identified candidate lava tubes are processed to extract geometrical parameters, such as the depth and the thickness of the crust (roof).

¹Part of this chapter appears in

Donini, E., Bovolo, F., Gerekos, C., Carrer, L., and Bruzzone, L. (2018, July). An Approach to Lava Tube Detection in Radar Sounder Data of the Moon. In IGARSS 2018-2018 IEEE International Geoscience and Remote Sensing Symposium (pp. 8424-8427). IEEE.

4.1 Introduction

A lava tube is a natural conduit formed beneath the surface that contained thermally insulate lava and transported it over long distances during the active volcanic period [132]. Initially, the basaltic lava streams down from a volcanic vent and streams on the surface similar to a river. While flowing, the lava develops a continuous thick crust because of the extreme difference of temperature between the hot lava and the outer colder environment [133]. While moving forward, the hard film above the lava continuously congeals, becoming thicker. In this way, a tunnel forms in the subsurface that transports the lava with almost no heat loss [134]. When the lava flows away, the tunnel empties, generating an elongated cavity with a hardened and thick roof. The size and the shape of the tubes strongly depend on the characteristics of lava streams [132]. This phenomenon appears in many bodies of the Solar System, such as the Earth, Moon, Mars, and Venus. On the Moon and Mars, the volcanic period finished about 50 million years ago [135] and 100-150 million years ago [136], respectively. Hence, lunar and martian tubes are inactive and expected to be entirely or almost empty, e.g., containing solidified lava or regolith [137]. On the Moon and Mars, hollow and stable tube can persist for significantly more time than on the Earth because of the colder and drier climate and weakness of the tectonic activity and weathering rates [138]. Moreover, for the same reasons, martian and lunar lava tubes have larger dimensions than those on the Earth, which typical width is between 10 and 30 meters [49]. Hence, terrestrial tubes can be considered as analogs to understanding their formation mechanism and geometrical structure. A lava tunnel network generally consists of the main tube and several smaller ones. It is reasonable to suppose that such networks exist on the Moon and Mars, but there is no specific knowledge on it. It is unknown where the locations, extension of lava tube networks [132]. Also, the characteristics of the single conduit are obscure, such as the inner aspect (collapsed, fully or partially filled, hollow), the depth, and the rooftop thickness [139]. However, there are some studies on the possible range of the size of stable lava tubes on the Moon. In [140, 141], the authors simulated tunnels of different dimensions and roof thickness subjected to the lithostatic and the Poisson stress, and the tectonic strain in the subsurface. The results show that stability is correlated with the height of the rooftop and the initial stress state. Lava tubes with a relatively thin roof of 50m are stable with a width of up to 3.5km. With a roof thickness up to 200m, lava tubes are stable with a maximum width of 5.25km. Deeper tunnels with a roof thickness of 500m do not collapse with a width up to 5km [140, 141]. Note that the roof thickness is of critical importance for the stability of the tube.

Lava tubes, and more in general subsurface void spaces on the Moon and Mars, have gained an increasing interest in the literature in the past years. First, from a geological

point of view, lava tubes are of critical importance as the study of their properties (e.g., the type of minerals and rocks and the elongation) can help in understanding the geological evolution of a planet. Secondly, lava tubes are the perfect place where humankind can build structures for living and storing food and electronics [142, 143, 51]. Thirdly, several works identify subsurface cavities as the perfect place where humankind can safely settle sheltered from the threats on the surface [144] [145]. The roof of the tube acts as a shelter against the threats on the surface, such as the cosmic and solar radiations and Gamma rays [133, 142, 146], the extreme temperature variation [142], the little and toxic dust of the regolith, and the frequent meteoritic impacts. Finally, when the surface is a hostile environment, buried cavities may store water and be a stable physic-chemical environment that can preserve microbial biosignature, as an analogy to those on the Earth [147, 148].

Lava tubes can hardly be mapped with direct measurements, especially on the Moon, Mars, and in isolated places on the Earth. On Earth, lava tubes are mapped and studied on-site, which is not possible in space. There exist four main strategies for mapping lava tubes i) scanning optical and Synthetic Aperture Radar (SAR) images identifying surface volcanic features linked to subsurface cavities [149, 150, 151, 133, 152, 153]; ii) studying skylights from oblique views in images acquired at different wavelengths [154, 51], iii) detecting distribution anomalies in the gravity data that may correspond to subsurface mass deficits [155], and iv) analysing radar sounder data [139, 156, 132]. The first approach investigates geological volcanic structures on the surface that are correlated with buried lava tubes, i.e., rilles [149, 150, 151, 133] and huge pits [152]. These structures can be interpreted as locally collapsed lava tubes because of preexisting fractures in the roof, meteoric impacts, or a thin roof unable to sustain the tube weight. Note that the subsurface void should be large enough to contain the crust material, especially for pits in a chain formation. The second approach analyzes the differences between impact crater holes and skylights at visible and thermal wavelengths with several angles of incidence [154, 51]. At visible wavelength, skylights lack any impact crater properties (e.g., raised rims and ejected patterns). At infrared wavelength, during the day inside the skylights, the temperature fluctuates less widely than in the nearby surface and adjacent bowl-shaped pit craters. At nighttime, the pit floor shows a higher temperature than in the surrounding pits, which suggests the presence of an extended subsurface cavity mitigating the fluctuation [51]. The third strategy analyzes anomalies in the gravity distribution to identify mass deficits that can be compatible with the presence of hollow lava tubes. [155] estimates the subsurface density and detected buried cavities by exploiting negative anomalies, i.e., lower density values. The fourth strategy analyzes radar sounder and ground-penetrating radar (GPR) data as they provide a direct measure of the subsurface. Investigating GPR data, [139, 132] mapped and characterized complex networks of lava

tubes. Authors in [139] proposed a method to detect the pattern of lava tubes that exploits prior knowledge of the tunnel connections and geometries, e.g., the tube dimensions and roof thickness. However, this knowledge is not always available neither for terrestrial nor planetary cases. Authors in [132] proposed an approach to detect lava tubes by analyzing the vertical profiles of radargrams (A-scan). A-scans were compared with a specific pattern characterized by two high peaks, compatible with the expected lava tube behavior. The same approach was applied to radargrams of the Moon, with the aim of mapping the network of empty tunnels [156]. However, in both studies, each a-scan is separately analyzed without checking the spatial correlation of the peaks or extracting information on the tube dimension. Note that peaks do not uniquely represent lava tubes but any strong reflections in the subsurface, such as clutter. Recently, a new strategy was proposed to analyze possible detected lava tubes [156] for discriminating between clutter and subsurface reflections [157]. The strategy is based on three criteria: i) analysis of multiple orbit data (if available), ii) evaluation of the correlation between radargrams and surface scattering simulations, and iii) analysis of the surface slope echo. However, radar sounder data store more information that can be used to identify buried geological structures and understand the processes in the subsurface. By analyzing radargrams, it is possible to extract information on the subsurface structures and processes, which is not possible with the other aforementioned approaches.

This Chapter proposes a novel automatic method to detect reflections from candidate cavities, such as empty and buried lava tubes, in radar sounder data. The method, which extends and develops the initial idea in [158], is unsupervised (does not require a training phase), considers the intrinsic nature of the lava tubes in the subsurface, and is flexible. It consists of three main concepts: i) the EM modeling of the lava tube signature in the radargrams, ii) extracting reflections in the radargram, and iii) analyzing the reflections to identify those related to candidate lava tubes. The EM modeling describes how lava tubes appear in radargrams by analyzing the interaction between the propagating EM wave and the buried cavities, seen as the transition rock-void-rock in the subsurface. Considering the lava tube model, the method extracts reflections in radargrams and then analyzes them to identify those related to buried cavities and reject the others. The analysis consists of a fuzzy detection system based on the lava tube EM model that evaluates the properties of the reflections and the relation among them. The proposed method identifies candidate lava tubes in an automatic, fast, and objective way. Given the complexity of the task, this is not feasible with visual analysis on a large number of radargrams. The final decision on the identified candidate lava tubes should be taken in the post-processing by expert planetologists. The effectiveness of the proposed method is demonstrated with experiments on two datasets: a dataset of simulated radargrams and

a dataset of radargrams acquired on the Moon by the LRS.

The Chapter is organized as follows. Section 4.2 presents the geological and electromagnetic models for lava tubes. Section 4.3 focuses on the method proposed to detect lava tubes by describing the algorithm to extract the reflection from the radargram and the fuzzy system that analyzes the reflections to identify lava tubes. Section 4.4 is devoted to the description of the two datasets and the experimental results. Section 4.5 discusses the limitations and the assumption of the proposed method. Finally, Section 4.6 presents the conclusions and future work.

4.2 Lava Tube Model

Lava tubes are tunnel-like structures that drain over time, generating elongated buried cavities. The void and the rock have highly different dielectric properties, which make the interfaces between the two materials detectable by radar sounders. In radargrams, interfaces appear as strong reflections with specific qualities in amplitude and phase. This Section describes the electromagnetic (EM) model of lava tubes in terms of reflections generated by the surface and the lava tube boundaries. To investigate the properties of these reflections, we simulated the amplitude and phase radargrams with a coherent multilayer simulator [21]. The simulator takes into input the parameters of the radar EM wave (e.g., the central frequency, the bandwidth, and the modulation of the carrier signal). Moreover, the simulator allows choosing the crossing angle α between the moving direction of the radar and the lava tube longitudinal axis. Finally, the simulator requires the geometrical and dielectric models of the surface and the subsurface. It considers the surface topography (e.g., roughness and craters), the geometry of the buried geologic structures, and the dielectric properties of the materials. Here, we first simulate an ideal scenario where above the surface is void, and the rocky subsurface contains an empty lava tube. We simulate lava tubes considering the geometric model in [140, 159] for planetary lava tubes. The lava tube geometrical model considers stable structures with the tunnel sizes and the roof thicknesses indicated in Table 4.1 that follow the analyses in [140, 159]. The tunnels are approximated as half-cylinders with a height-to-width ratio of 1:3, i.e., the tube height is one-third of the tube width, as in [140]. For the dielectric model, we consider the ideal case with the void in the tube, which is characterized by a unitary relative dielectric constant $\varepsilon_r^{void} = 1$. Note that in real scenarios, the lava tube inside can be partially filled by regolith or other materials having a lower dielectric constant than that of the rock. The basaltic rock around the conduit is approximated by a relative dielectric constant of $\varepsilon_r^{rock} = 4$ and a loss tangent of $\delta_{rock} = 0.01$. Considering the lunar scenario, at the central frequency f_c of the simulations, the analysis of the dielectric constant and tangent loss values of the surface shows that ε_r varies from 4 up to 8 and the upper limit

Table 4.1: Parameters of the geometrical model of the simulated lava tube, considering the stable scenario [140, 159]. Note that the tube height is assumed to be one third of the tube width.

Frequency	Bandwidth	Tube Width	Roof Thickness	Tube Size
10 MHz	5 MHz	250 m	5 m	small
10 MHz	5 MHz	625 m	50 m	
60 MHz	30 MHz	1000 m	75 m	average
10 MHz	5 MHz	1000 m	130 m	
10 MHz	5 MHz	1250 m	20 m	
10 MHz	5 MHz	1500 m	20 m	
10 MHz	5 MHz	2000 m	200 m	large
10 MHz	5 MHz	4000 m	200 m	
10 MHz	5 MHz	3000 m	200 m	

of δ is in the range of (0.1-0.3) [160]. Hence, simulations refer to the worst-case scenario in terms of surface dielectric properties. Recently, a study [161] showed that in the range of frequency 10-100 MHz the regolith absorption and volume scattering are negligible. Thus, the surface is affected only by losses due to the roughness, i.e., the topography. The attenuation depends on the loss tangent and mainly affects the reflections from the lava tube rather than from the surface. Considering a loss tangent and a dielectric constant at the ceiling and floor of the tube equal to that of the surface, the maximum detectable depth of lava tubes is strongly depending on f_c [161]. At frequencies in the range of 60-100 MHz, it is in the range of some hundred meters and it increases as f_c decreases [161]. For the signal modulation, the EM wave has a chirp waveform that is smoothed by a Hann window [162]. We simulated signals with different central frequencies, transmitted power, and height of the radar from the surface, as shown in Table 4.2. For the crossing angle α , we simulated the cases in the range of $\alpha \in (0, \pi/2)$. The two extreme cases are i) $\alpha = 0$, which represents the tube axis being parallel to the moving direction of the radar, and $\alpha = \pi/2$, which models the tube axis being perpendicular to the moving direction of the radar. Figures 4.1a and 4.1d show the tube in yellow and the moving direction of the radar in red for $\alpha = 0$ and $\alpha = \pi/2$, respectively. Regarding the topography of the surface, we first considered an ideal and flat surface to focus on the reflections due to the lava tubes. Then, we simulated a more complex and realistic topography to analyze how the superficial clutter interacts with the pattern of lava tubes. Considering such a scenario, here we describe the EM model of lava tubes from the amplitude and phase point of view.

Lava tube amplitude model. The amplitude radargram shows three strong and linear

Table 4.2: Radar parameters of the simulations and the LRS [3], and resolution parameters of the radargrams.

Parameter	Simulations	LRS [3]
Orbit Altitude	100 Km	100 Km
Central Frequency	10-60 MHz	5 MHz
Bandwidth	5-30 MHz	2 MHz
Sampling Time	0.17 μ s	0.16 μ s
Maximum Penetration Depth	7.5 Km	5 Km
Azimuth Resolution	5 m	60 m
Range Resolution in free space (pulse compressed)	15 m	75 m

reflections that represent the surface, the ceiling, and the floor of the tube (see Figures 4.1). The surface reflection (S) ideally appears as a bright line as long as the radargram with the greatest amplitude. This reflection is the first interface that the radar wave encounters. The tube generates a pattern made of a couple of reflections that represent the two interfaces between the void and the basaltic rock. The upper reflection (C) is generated by the ceiling of the tube, while the lower one (F) by the floor. The amplitudes a_C and a_F are smaller than that of the surface but similar to each other. The distance between the reflections in the range direction is proportional to the depth of the interfaces. The reflection lengths (l_C, l_F) along the azimuth depend on the size of the tube and the crossing angle α . Concerning the angle α of intersection between the tube axis and the flight track of the sounder, there are two limit cases: $\alpha = 0$ and $\alpha = \pi/2$. In the parallel case $\alpha = 0$ (see Figure 4.1d), the couple of reflections is ideally as long as the radargram in azimuth (see Fig. 4.1b). Note that the reflection couple length depends on the acquisition— a radargram may image part of the lava tube or cover a wider area than that of the tube. In the perpendicular case $\alpha = \pi/2$ (see Figure 4.1a), the reflection lengths (l_C, l_F) are similar and shorter than the radargram in azimuth (see Fig. 4.1e). Smoothly moving from the latter to the former case, the reflections preserve the (almost) linear shape stretching until the the parallel case.

Lava tube phase model. In the phase domain, the lava tube model has three reflections with the same length and depth (i.e., range position) as in the amplitude domain. The main property of the phase model is the phase inversion [161] of the reflections originating from the lava tube ceiling when compared to the surface reflection. This effect on the radar signal is expected from a dielectric discontinuity where the first medium has a higher permittivity than the second one. In our case, the first medium is basalt, while the latter is the vacuum, modeling the lava tube’s inner free space. The lava tube floor is expected

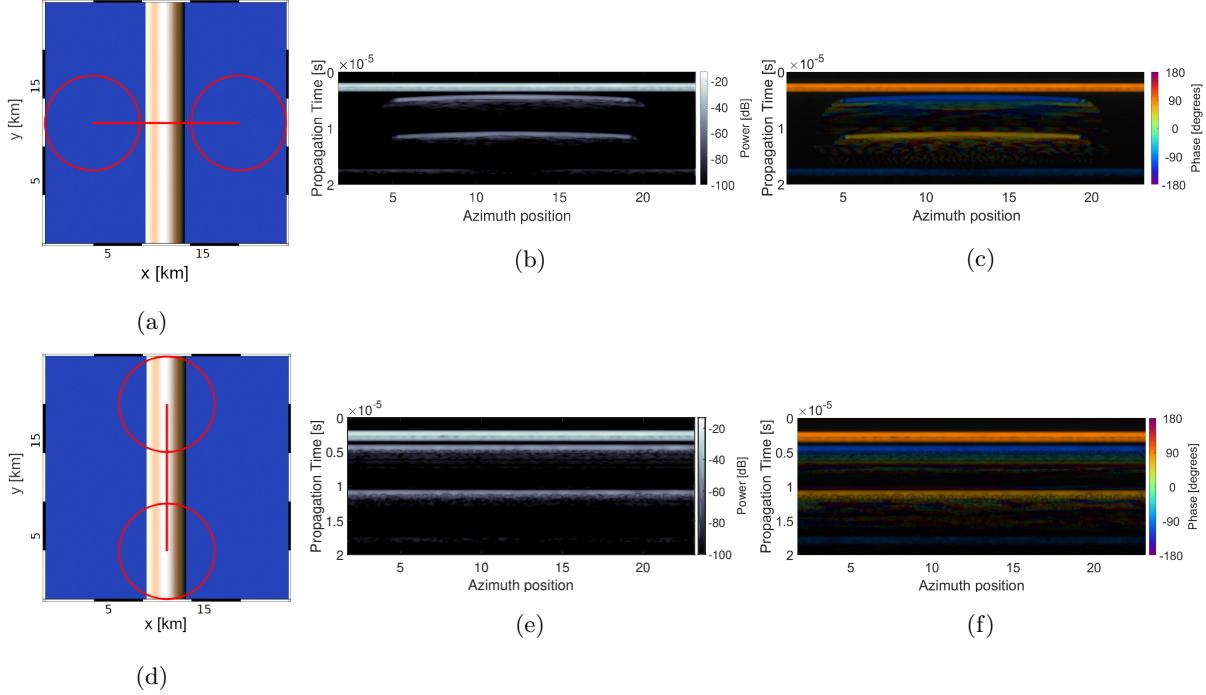


Figure 4.1: Simulated amplitude and phase radargrams of a lava tube with deep $d_{LT} = 200$ m and diameter $2r = 4$ km for the cases $\alpha = \pi/2$ and $\alpha = 0$. Figures (a) and (d) show the track of the direction of the radar and the tube axis (both in red) with an angle $\alpha = \pi/2$ and $\alpha = 0$, respectively. Figures (b) and (c) are the simulated amplitude and phase radargrams for the perpendicular case, while Figures (e) and (f) show the simulated amplitude and phase radargrams for the parallel case.

to have the same phase sign as the surface reflection. The property of the phase model is the inversion of phase occurring at each interface since the wave propagates in between materials with highly different dielectric properties, such as the void and the rock. Here, we have three inversions generated by the three interfaces between the inner free space and rock represented by the surface, the ceiling, and the floor of the tube.

The above-mentioned amplitude and phase models assume an ideal scenario with flat topography, i.e., a plane and roughness-free surface. In this scenario, we identify the reflection pattern of empty tubes without the presence of clutter. We further investigate more realistic scenarios with complex surface topography. To this end, we introduce sharp roughness and deep craters to verify the impact of the surface clutter on the reflection pattern of the tubes (see Fig. 4.2). The simulations indicate that craters generate clutter reflections with a pattern similar to that of the lava tubes in amplitude but not in phase. The lava tube models are not affected by significant changes, i.e., the three reflections maintain the main properties described above. The model preserves the inversion of the phase at interfaces of materials with considerably different dielectric constants. The surface reflection S is affected by the volume scattering due to the roughness and clutter

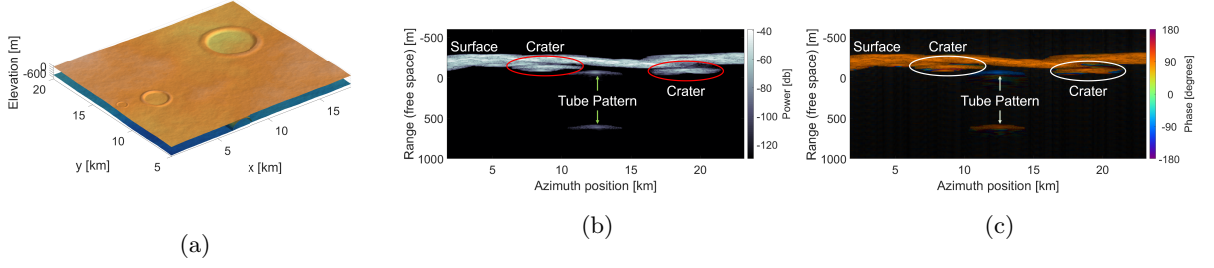


Figure 4.2: Simulated amplitude (b) and phase (c) radargrams of a lava tube with deep $d_{LT} = 200$ m and diameter $2r = 4$ km for the case $\alpha = \pi/2$. The surface terrain (a) is characterized by a high rough surface and thick craters. Reflections generated by the surface, the craters, and the lava tube ceiling and floor are highlighted in radargrams (b) and (c).

signals. The rim and the ground of the craters create several clutter signals above and below the surface. However, the crater reflections do not have phase inversion, and thus, are distinguishable from those of the tube boundaries (see Fig. 4.2). Regarding the pattern of lava tubes, C and F maintain the properties of the phase model. In amplitude, the ceiling and the floor reflections show a loss of about 5 dB, which is confirmed in [156]. In a more realistic scenario, lava tubes are not perfect cylindrical bodies but have a more complex geometrical shape [163]. The profile of lava tubes is typically characterized by a flat and extended floor and shorter and sharper ceiling. Moreover, lava tubes are not straight and parallel to the surface, but they have a sinuous track and may have an inclination toward the surface. This geometry is reflected in the shape and position of C and F : i) C and F are not expected to be perfectly parallel between them and with the surface; ii) C and F may not share the same length and may not fully overlap in the azimuth direction. However, the lava tube pattern is still distinguishable because of the phase inversion between C and F . Finally, recent studies show that the tube may be filled with regolith [132] or other media having dielectric properties similar to that of the void. Thus, the EM model for the lava tube is still valid as the large difference in the dielectric properties of the media produces a phase inversion.

4.3 Proposed Approach to Detect Candidate Lava tubes

Let us consider a radargram as a 2D matrix of N_T traces and N_S samples

$$\mathbf{R}_C = \{R_C(a, r) | a \in [1, \dots, N_T], r \in [1, \dots, N_S]\} \quad (4.1)$$

where R is the coherent sum of the echoes stored in the radargrams, r and a indicate the range and the azimuth coordinates, respectively. The radargrams contain the complex signal reflected from the interfaces between different media in the subsurface, such that $R_C(a, r) = R(a, r) + jR_I(a, r)$, where $R(a, r)$ is the real part of the signal and $R_I(a, r)$

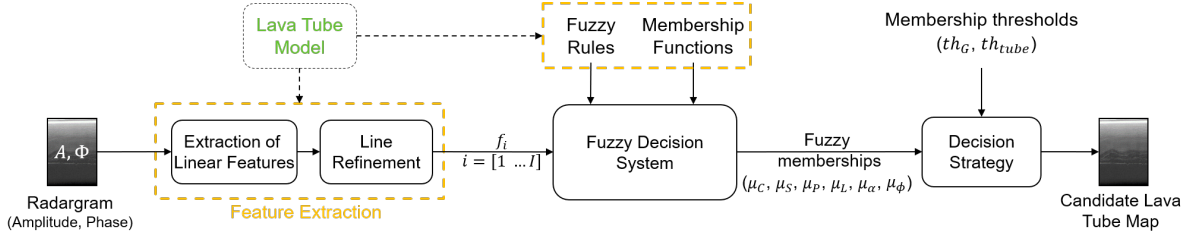


Figure 4.3: Flow chart of the proposed approach to detect candidate lava tubes.

the imaginary part. The amplitude $A(a, r)$ and phase $\Phi(a, r)$ radargrams are defined as follows

$$\begin{aligned}
 A(a, r) &= \sqrt{R^2(a, r) + R_I^2(a, r)} \\
 \Phi(a, r) &= \arctan \frac{R_I(a, r)}{R(a, r)}
 \end{aligned} \tag{4.2}$$

Let $\mathcal{F} = \{\mathbf{F}_i, i \in [1, \dots, \mathbf{N}_F]\}$ be the set of features extracted from the radargram, where F_i indicates the i -th feature, i.e., the coordinates of the pixels of the reflection in the radargram and the related properties. The proposed approach assigns to each feature a class in $\Omega_c = \{\omega_g, \omega_{LT}^c, \omega_{LT}^f, \omega_n\}$. ω_g indicates the best candidate to represent the surface, ω_{LT}^c and ω_{LT}^f indicate features that can be generated by the candidate tube boundaries (the ceiling and the floor, respectively). ω_n labels features that are related neither to buried cavities nor to the surface but probably generated by the surface topography and other volcanic structures, e.g., impact craters, tesserae, and off-nadir clutter.

A novel automatic technique is proposed with three steps (Fig. 4.3):

1. Extraction of the coordinate of the reflections in the radargram.
2. Extraction of the properties of each reflection to define the feature set.
3. Analysis of the features to detect those generated by the surface and candidate lava tube boundaries, exploiting the model in Section 4.2.

According to the analysis in Section 4.2, the properties of the lava tube EM model are the following. i) There should be at least one candidate to be the surface reflection having the shallowest depth in the range and with the stronger power. ii) There should be at least two other deeper reflections, i.e., the candidates for the boundaries of the lava tube C and F . iii) The reflection length depends on the tube width and the crossing angle α between the tube axis and the moving direction of the radar. iv) Candidate features for the same tube should have as similar as possible length, independently on the crossing angle α . v) There should be alignment between the candidate features C and F , i.e., the barycenters of the candidate C and F should lie on the same line. vi) Phase inversion

should occur at each candidate feature. Note that candidate features in the radargrams will have different characteristics, including thickness, shape, and orientation, according to the acquisition geometry, the resolution in the range direction (which also depends on the specific dielectric properties of the medium), and the physical properties of the geological structures. Further, real radargrams usually present other reflections related to undesired signals, such as clutter from off-nadir and surface topography variations. Hence, the automatic system to detect lava tube reflections must be robust to noise and uncertainties in radargrams, given by the impossibility of precisely modeling the structures in the subsurface.

4.3.1 Detection of the Reflections

Considering the EM model presented in Section 4.2, the signature of both the lava tube boundaries and the surface consists of reflections with a linear shape. Hence, the first step of the proposed approach extracts the candidate features with a line detection algorithm. In the literature, there exist several methods to detect lines in radargrams, such as [40], [42]. Here, we used the unsupervised method in [40] that can extract lines with different properties, e.g., orientation, shape, and length. Further, the method is robust to both the thermal and background noise of radargrams. The algorithm [40] automatically detects lines in radargrams by applying a local scale Hidden Markov Model (HMM) and the Viterbi Algorithm (VA). The overall approach consists of the following steps: i) layers enhancement, ii) segment detection using a combination of the VA and HM model in small regions of the radargram, and iii) combination of adjacent segments. The HMM detects the most probable location of the lines and transforms the pixels in these regions into a graph. The VA analyzes the graphs to identify the pixels belonging to the lines. The approach divides radargrams into small portions processed separately. Then, a detection strategy links inferred local segments.

The initial step enhances the signal while reducing the noise in the radargram with an incoherent averaging filter that magnifies locally flat lines with a size of N_{AV} (reflections that are flat at least at the scale of the averaging length). Then, the algorithm adaptively estimates the conditional density function (CDF) of the noise and the signal. Knowing these CDFs and fixing the probability of false alarm, the algorithm computes the probability of detection and the peak threshold. The peak threshold is applied to each rangeline (a column of the radargram) to detect the local peaks, potentially associated with lines. Since reflections are spread in range, i.e., they are some pixels thick, the algorithm considers only peaks separated by at least a unit of range resolution (skeleton thickness) to avoid multiple detections of the same reflection.

The second step applies the HMM and the VA to detect the lines. HMM transforms

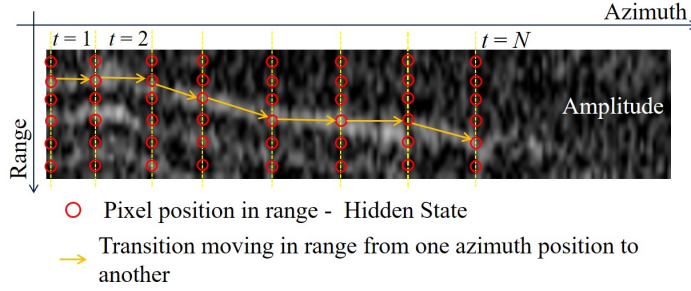


Figure 4.4: Illustration of the tracking procedure of a single layer edge. The pixels with the red circle connected by the yellow arrow identifies a retrieved best path.

the radargram into a graph where the VA searches for the optimal state sequence, see Fig. 4.4 for a schematic representation. For each azimuth position, the VA considers as initial seeds the previously detected peaks. Then, it iteratively identifies the optimal state sequence in the radargram portion surrounding the seeding points. The amplitude of the pixels in the best path is thresholded th_{line} to check if the path is related to a reflection. Then, the algorithm connects the line of adjacent radargram portions in a way that the initial seeds of the next portion are the last pixels of the best paths of the previous block. The algorithm stops when it reaches the end of the radargram, or when the thresholding condition is no longer verified. When a line is detected, the corresponding pixels are removed from the radargram to avoid multiple detections.

The algorithm extracts a set of lines $\mathcal{L} = \{\mathbf{L}_k, k \in [1, \dots, N_L]\}$ corresponding to high reflection values in the radargram. For each line, the algorithm provides the azimuth a and range r coordinates for each pixel. The algorithm extracts many segments for each reflection as it is sensitive to the amplitude variations. Hence, a step of post-processing combines segments related to the same reflection. Segments shorter than L_{min} are removed as they are expected to represent noise or unwanted reflections. Segments are grouped by considering the relative distances in the azimuth and range. Two segments are grouped if i) they overlap in the azimuth or the range directions of O_a and O_r pixels, and ii) the amplitude of the edge connecting the two lines is constant and higher than the threshold th_{line} . The first condition identifies the candidate segments to combine. The second one combines only the segments that are likely to represent the same reflection, see Fig. 4.5 for the schematic representation. The output of this step is a set of reflections $\mathcal{R} = \{\mathbf{R}_i, i \in [1, \dots, N_R]\}$, where the i -th reflection groups several segments \mathbf{L}_k^i . For each reflection, a geometrical region is built by considering as starting and ending point the coordinates of the most left and most right pixel of each line group.

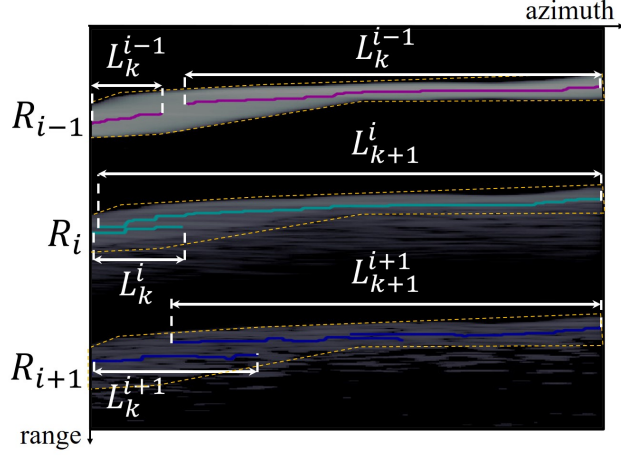


Figure 4.5: Examples of the refinement step: several segments \mathbf{L}_k^i are extracted for each reflection \mathbf{R}_i .

4.3.2 Characterization of the Reflections

The second step of the proposed approach characterizes the i -th reflection by extracting the length l_i , the average depth ρ_i , the barycenter coordinates b_i , the average amplitude a_i , and the average phase ϕ_i (see Fig. 4.6). These parameters compose a feature vector $\mathbf{F}_i = \{l_i, \rho_i, b_i, a_i, \phi_i\}$ for each reflection \mathbf{R}_i .

Length. For each reflection \mathbf{R}_i , the length l_i considers the extension in the azimuth direction of the reflection with

$$l_i = \max\{l_a^k\} - \min\{l_a^k\}, k \in [1 \dots N_L^i] \quad (4.3)$$

where l_a^k is an array indicating the azimuth coordinates of the k -th line, and N_L^i is the number of segments of the i -th reflection. The reflection length is equal to the distance between the point with the lowest and the highest azimuth coordinate. This considers the distance between the two extreme points, without considering the overlapping of the lines in the azimuth.

Depth. The average depth ρ_i considers the average range coordinate of each reflection according to

$$\rho_i = \frac{\max\{l_r^k\} + \min\{l_r^k\}}{2}, k \in [1 \dots N_L^i] \quad (4.4)$$

where l_r^k is the array of the range coordinates of the k -th line of the i -th reflection. The average depth of the reflection is equal to the midpoint between the lowest and the highest range coordinate. This takes into account the reflection thickness but not the overlapping of the lines in the range direction.

Barycenter. The barycenter b_i is calculated considering the centroid of the geometrical region of each reflection. Hence, the azimuth b_a^i coordinate of the centroid is calculated

as follows

$$b_a^i = \frac{\max\{l_a^k\} + \min\{l_a^k\}}{2}, k \in [1 \dots N_L^i] \quad (4.5)$$

While the range coordinate is equal to the average depth of the feature $b_r^i = \rho_i$.

Amplitude. The average amplitude a_i of each reflection is considered as the average amplitude of the pixels belonging to the N_L^i lines of the i -th reflection. Hence, the average amplitude is computed as follows

$$a_i = \text{mean}\{A(l_a^k, l_r^k)\}, k \in [1 \dots N_L^i] \quad (4.6)$$

where $A(l_a^i, l_r^i)$ is the amplitude radargram at the azimuth and range coordinates of the lines in the i -th reflection.

Phase. The last parameter is the average phase ϕ_i related to the change of media in the propagation path of the EM wave. The phase radargrams store the phase signal that depends on i) the interactions between the EM wave and the medium where it propagates, and ii) the length of the path traveled by the EM wave. Here, the aim is to identify the phase shift due to the interaction between the EM wave and the subsurface structures and media. The phase shift can be estimated as the difference in the length of the traveled path and the total phase value. To this end, for each reflection, the phase value of each pixel is computed by analyzing the signal properties in the frequency domain. Let us consider the i -th reflection to define the strategy to extract the average phase value from the phase radargram. In the amplitude domain, the range coordinate of the signal peak r_p^i is identified for each column of the geometrical region. In the phase domain, the p -th column of the geometrical region is convolved with a Hann window $W_{hann}(r)$ centered in the peak, see (4.7).

$$W_{hann}(r) = \begin{cases} \frac{1}{2} \left(1 + \cos \left(\frac{2\pi r_p^i}{T} \right) \right), & |r_p^i| \leq T/2 \\ 0, & |r_p^i| > T/2. \end{cases} \quad (4.7)$$

where r_p^i is the range coordinate of the peak in the p -th column of the geometrical region of the i -th reflection, and T is the length of the considered surrounding window. In the frequency domain, the Hann window has low aliasing, low sidelobes, and a narrow main lobe. These properties limit the impact of the filtering on the phase signal while having an accurate selection of the frequency and a low level of signal distortions. Then, the output of the convolution is transformed into the frequency domain by applying the Fourier Transformation (FT). In the frequency domain, the signal is complex and the phase can be estimated by calculating the angle of the signal. Hence, the average phase value θ_i for the i -th reflection is the average of the phase computed for each range line. Note that θ_i is the phase value having the contributions from the length of the EM wave

propagation path θ_i^{path} and the interaction of the wave with the material ϕ_i . ϕ_i can be estimated with $\phi_i = \theta_i - \theta_i^{path}$, where θ_i^{path} is defined by setting $r = \rho_i$ in (4.8).

$$\theta^{path}(r) = \frac{4\pi}{\lambda} [\rho(r) + h] \sqrt{\varepsilon_r(r)} \quad (4.8)$$

where λ is the wavelength of the signal, h is the elevation of the radar, and $\varepsilon_r(r)$ is the relative permittivity of the propagation medium, which depends on the range. Note that $\rho_i + h$ is the length of the propagation path of the EM wave from the radar to the interface in the subsurface. $\varepsilon_r(r)$ indicates the propagation medium: here, the dielectric profile considers basaltic rock ε_r^{rock} in the subsurface, and vacuum in the buried cavities and above the surface. Once the phase contribution given by the propagation path is calculated, the phase shift from the change of dielectric properties in the medium can be estimated. Note that the lava tube model considers the phase inversion between a couple of reflections, such as the reflection from the cavity boundaries. Once the candidate features to be the surface and the tube boundaries are identified, the relative phase between the reflections can be computed. The phase signal of the candidate to be the surface, and the tube ceiling and floor are estimated in (4.9), as the difference between the phase contribution from the propagation path of the EM wave and that of the dielectric properties.

$$\begin{aligned} \Phi_G &= \frac{4\pi h}{\lambda} \sqrt{\varepsilon_r(\rho_S)} \\ \Phi_C &= \frac{4\pi h}{\lambda} \sqrt{\varepsilon_r(\rho_S)} + \frac{4\pi(\rho_C - \rho_S)}{\lambda} \sqrt{\varepsilon_r(\rho_C)} + \phi_C \\ \Phi_F &= \frac{4\pi h}{\lambda} \sqrt{\varepsilon_r(\rho_S)} + \frac{4\pi(\rho_F - \rho_S)}{\lambda} \sqrt{\varepsilon_r(\rho_F)} + \phi_F \end{aligned} \quad (4.9)$$

where ρ_S , ρ_C , and ρ_F are the average depth of the ground reflection S , ceiling reflection C , and floor reflection F , respectively. $\rho_C - \rho_S$ is the roof thickness (the propagation path of the EM wave from the surface to cavity ceiling), while ϕ_C is the phase contribution given by the change of dielectric properties of the material at the tube ceiling. $\rho_F - \rho_S$ is the propagation path from the surface to the floor of the cavity (sum of the roof thickness and the tube height), while ϕ_F is the phase contribution given by the change in the dielectric properties of the material at the tube floor. Finally, the dielectric properties $\varepsilon_r(r)$ depends on the dielectric profile, and thus, the depth. Comparing the phase of two reflections, we can check the phase inversion as the difference between the phases of the two candidate features:

$$\begin{aligned} \Phi_C - \Phi_G &= \frac{4\pi(\rho_C - \rho_S)}{\lambda} \sqrt{\varepsilon_r(\rho_C)} + \phi_C \\ \Phi_F - \Phi_C &= \frac{4\pi(\rho_F - \rho_C)}{\lambda} \sqrt{\varepsilon_r^{tube}} + \phi_F - \phi_C \end{aligned} \quad (4.10)$$

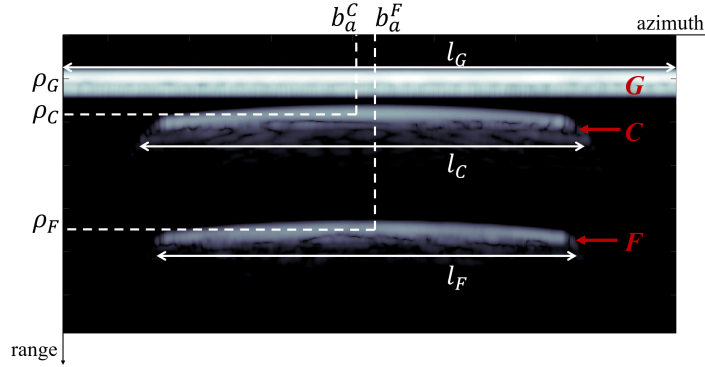


Figure 4.6: Simulated radargram imaging the surface reflection S , the tube ceiling C and floor F with the main geometrical parameters for each i -th reflection (length l_i , average depth ρ_i , azimuth barycenter coordinate b_a^i).

The first part of both equations is related to the phase signal due to the propagation path, while the latter is from the dielectric properties of the medium. In the first Equation of (4.10), the wave propagates into the lava tube roof, which consists of basaltic rock. In the second Equation of (4.10), the wave propagates in the tube that generally is void and has a relative permittivity $\varepsilon_r^{tube} = \varepsilon_0 = 1$. The phase contribution from the materials ϕ_C and ϕ_F is the unknown of the equation that can be estimated by inverting (4.10). Note that according to the lava tube EM model, $|\phi_C|$ is ideally equal to π since a phase inversion occurs when moving from the rock to the void of the tube. Hence, the phase difference depends on the unknowns (ε_r^{tube} , ϕ_C , and ϕ_F) and allows us to derive the phase shift.

4.3.3 Fuzzy Detection Approach

This section focuses on the proposed strategy to analyze the set of features $F = \{\mathbf{F}_i, i \in [1 \dots N_F]\}$ extracted from the radargram with a fuzzy logic-based system. The system examines the properties of the features ($\mathbf{F}_i = \{l_i, \rho_i, b_i, a_i, \phi_i\}$) and assigns to each of them a label in $\Omega_c = \{\omega_g, \omega_{LT}^c, \omega_{LT}^f, w_n\}$. The fuzzy logic models the uncertainty of the lava tube EM model in the realistic scenario and accounts for the characteristics of the data, such as their low resolution. The fuzzy system consists of two steps: i) the best candidate feature to be the surface reflection is identified and removed from the feature set; ii) the remaining features are analyzed two by two to detect the couples of features that can be candidates to be the lava tube ceiling and floor. When two features are identified as possible reflection generated by the lava tube boundaries, these are removed from F to avoid multiple detections of the same cavity. The analysis of the features is done with a set of rules (see Table 4.3) based on the EM model presented in Section 4.2. Each rule evaluates the features by providing a membership value in the range of $[0, 1]$. This value indicates how much that rule is fulfilled, i.e., a high membership value indicates that the

Table 4.3: Summary of the fuzzy rules used to classify each feature as possible surface reflection ω_g , lava tube ceiling reflection ω_{LT}^c , lava tube floor reflection ω_{LT}^f , and none of them ω_n .

Rule	Attribute	Membership Function
1. Presence of at least 3 candidate features F_c , F_f , and F_g (completeness)	p	$\mu_p(p) = \{0, 1\}$
2. Surface length of the candidate feature F_g	$r_G = \frac{l_g}{l_R}$	$\mu_G(r_G) = \frac{1}{1 + \exp(-a_G(r_G - c_G))}$
3. Equivalence of length of the candidate features F_c and F_f	$r_L = \min\{\frac{l_c}{l_f}, \frac{l_f}{l_c}\}$	$\mu_L(r_L) = \frac{1}{1 + \exp(-a_L(r_L - c_L))}$
4. Proportionality of the candidate features F_c and F_f	$r_P = \min\{\frac{L}{l_c}, \frac{L}{l_f}\}$	$\mu_P(r_P) = \frac{1}{1 + \exp(-a_P(r_P - c_P))}$
5. Alignment of the barycenters of the candidate features F_c and F_f	$r_{al} = m - m_{al} $	$\mu_{al}(r_{al}) = \frac{1}{1 + \exp(-a_{al}(r_{al} - c_{al}))}$
6. Comparison of the amplitude values of the candidate features F_c and F_f	$r_A = \min\{\frac{a_c}{a_f}, \frac{a_f}{a_c}\}$	$\mu_A(r_A) = \frac{1}{1 + \exp(-a_A(r_A - c_A))}$
7. Phase inversion between the candidate features F_c and F_f	$r_\phi^1 = \min\left\{\left \frac{\phi_c}{\pi}\right ; \left \frac{\pi}{\phi_c}\right \right\}$ $r_\phi^2 = \min\left\{\left \frac{\phi_c}{\phi_f}\right ; \left \frac{\phi_f}{\phi_c}\right \right\}$	$\mu_\phi^1(r_\phi^1) = \frac{1}{1 + \exp(-a_\phi^1(r_\phi^1 - c_\phi^1))}$ $\mu_\phi^2(r_\phi^2) = \frac{1}{1 + \exp(-a_\phi^2(r_\phi^2 - c_\phi^2))}$

rule is verified for that feature, while a low value indicates the contrary.

The first step aims at detecting the best candidate feature to represent the reflection generated by the ground surface among the candidate features $\mathbf{F}_i, i \in [1 \dots N_F]$. Ideally, the surface reflection has a length comparable to that of the radargram in azimuth. Furthermore, it has the smallest average range coordinate since it is the first interface encountered by the wave. To identify the surface reflection, two fuzzy rules described below evaluate the candidate features and associate a grade of membership to all of them. According to the overall membership value, the best candidate to represent the surface reflection is detected.

Completeness. Three reflections generated from the surface and the tube ceiling and floor must be detected in the radargram to identify a possible candidate. This rule evaluates the presence of at least three features, such that $\mathbf{F}_i, i \in [1 \dots N_F], N_F \geq 3$. Fixing the parameter $p = N_F$, p is evaluated with a crisp membership function $\mu_C(p)$, defined as $\mu_C(p) = [0, 1]$. The function analyzes the number of features N_i and is $\mu_C(p) = 1$ when three or more reflections are detected, otherwise is $\mu_C(p) = 0$.

Surface Length. This rule aims at detecting the best candidate to represent the surface reflection by evaluating the length l_i of each candidate feature. Ideally, the length of the surface reflection is the same as the radargram in the azimuth direction. This can be evaluated with a sigmoid membership function (4.11) evaluating the attribute r_G . The

attribute $r_G = l_i/l_R$ is defined as the ratio between the length l_i of each candidate feature and the radargram length l_R . In general, a sigmoid function is defined as follows:

$$\mu_j(r_j) = \frac{1}{1 + \exp(-a_j(r_j - c_j))} \quad (4.11)$$

where $\mu_j = \mu_G$ and $a_j = a_G$, $a_G > 0$ indicates the center of the function, and $c_j = c_G$, $c_G > 0$ is a parameter modeling the slope curvature. $\mu_G(r_G)$ returns a value in the range of $[0, 1]$; the higher the value of r_G , the higher the membership value and the possibility for that feature to be the candidate for the surface reflection. A low value of r_G indicates that the feature length is small compared to that of the radargram one. The best candidate to be the ground surface feature is identified with the aggregated membership value M_G , calculated by combining the Completeness and Surface Length rules as in (4.12):

$$M_G = \mu_C \mu_G \quad (4.12)$$

Among the fuzzy aggregation method, the Larsen product implication [164] is chosen since it is conservative. A small membership value forces a small final aggregation, regardless of the other membership values. The candidates are sorted considering their average depth. The feature with the lowest range coordinate, having an overall membership value M_G higher than a threshold Th_G , is classified as ω_g . The value M_G indicates the grade of reliability for that feature to be the best candidate to represent the surface reflection. Finally, the feature classified as ω_g is removed from \mathcal{F} to avoid the multiple labeling of the same feature.

The second step of the proposed method analyzes the remaining features $\mathcal{F} \setminus \{\mathbf{F}_i = \omega_g\}$ to detect possible candidates to represent the lava tube ceiling and floor. Ideally, the tube boundaries generate two reflections having a linear shape and comparable length. These reflections correspond to the tube ceiling and floor, where the former is expected to have a lower range coordinate than the latter. Furthermore, the amplitude values of the two reflections are comparable since the void in the cavity only slightly attenuates the signal. Finally, the reflections are characterized by phase inversion due to the extreme difference between the dielectric materials at the interface. Hence, the related features need to match those in the EM model presented in Section 4.2. The matching is evaluated by applying five fuzzy rules that analyze all the pairs of candidates. For each pair, the system provides a grade of membership that can be used to detect those representing tube boundaries. Couples of features are defined by choosing two features \mathbf{F}_c and \mathbf{F}_f in $\mathcal{F} = \{\mathbf{F}_i, i \in [1, \dots, N_F - 1]\}$ to be the candidate for the ceiling and the floor reflection, respectively. To identify the candidates, the features are sorted according the increasing value of their average depth. Then, the candidates \mathbf{F}_c and \mathbf{F}_f are iteratively selected in a way that the average depth of \mathbf{F}_c is shallower than that of \mathbf{F}_f . At the i -th iteration,

the candidate are $\mathbf{F}_c = \mathbf{F}_i$ and $\mathbf{F}_f = \mathbf{F}_{i+1}$. If the candidates are evaluated by the fuzzy system to represent a possible lava tube, they are labeled as $\mathbf{F}_c = \omega_{LT}^c$ and $\mathbf{F}_f = \omega_{LT}^f$, respectively, and both removed from \mathcal{F} . If this is not valid, the candidate feature for the floor is changed, such that $\mathbf{F}_f = \mathbf{F}_{i+t}$, $t \in [1, \dots, N_F^i - 1]$, where N_F^i is the size of the feature set at the i -th iteration. When $t = N_F^i$ and the candidate couple \mathbf{F}_c and \mathbf{F}_f are evaluated as not related lava tube boundaries, the candidate ceiling feature is set to $\mathbf{F}_c = \mathbf{F}_i = \omega_n$ and removed from \mathcal{F} . Then, at the next iteration $i + 1$, the candidate feature for the ceiling is changed and the above-mentioned procedure repeated. This approach stops when all the features in \mathcal{F} are labeled with one of the labels in $\Omega_c = \{\omega_g, \omega_{LT}^c, \omega_{LT}^f, \omega_n\}$. Each couple of candidate feature $\mathbf{F}_c = \{l_c, \rho_c, b_c, a_c, \phi_c\}$ and $\mathbf{F}_f = \{l_f, \rho_f, b_f, a_f, \phi_f\}$ is examined with the following rules, that are summarized in Table 4.3.

Equivalence of Lengths. This rule checks that the lengths of the candidate ceiling l_c and floor l_f features are similar. Ideally, when considering tubes with a cylindrical shape, the reflections generated by the boundaries of the tube have similar lengths. More realistically, reflections have a similar length rather than the same one. However, this is mitigated by the fuzziness of the approach, and if needed, it can be considered explicitly in the definition of the rule by adding a margin on the similarity. This rule can be implemented with a sigmoid membership function (4.11) with $a_i = a_L$, $a_L > 0$ and $c_i = c_L$, $c_L > 0$ (see 4.11) that evaluates the attribute $r_L = \min\{l_c/l_f, l_c/l_f\}$. The function computes the membership value μ_L in the range of $[0, 1]$, which indicates the confidence to have similar lengths. μ_L is maximum when the candidates have a similar length. Decreasing the length of one feature decreases the value of μ_L .

Proportionality. This rule verifies that the candidate features overlap in the azimuth direction and thus eliminates a pair of features not sharing enough azimuth coordinates. Ideally, to represent a lava tube, the reflections should be completely overlapping in the azimuth direction. More realistically, reflections may not fully overlap. However, this is mitigated by the fuzziness of the approach. Also for this rule, it can be included in the definition by including a margin. The proportionality membership μ_P is obtained by evaluating the attribute r_P with a sigmoid membership function (4.11) with $a_i = a_P$, $a_P > 0$ and $c_i = c_P$, $c_P > 0$. The attribute is $r_P = \min\{L_a/l_c, L_a/l_f\}$, where L_a is the number of pixels with the same azimuth coordinate in the candidate features. The higher the number of overlapping pixels, the higher is the membership value μ_P . μ_P goes to 0 when there are not overlapping pixels.

Alignment of Barycenters. This rule verifies that the candidate features are parallel. Ideally, approximating lava tubes as cylinders, the two reflections should be parallel to the azimuth direction. More realistically, the tube has a more complex shape, which, in radargrams, translates into reflections neither perfectly parallel to each other nor perfectly

perpendicular to the range direction. Note that tubes can show a steepness coefficient higher than zero, i.e., the tube is inclined. Fixing $\alpha = 0$, the reflections in the radar-gram from the tube ceiling and floor may be neither parallel to the surface. Possible non-idealities of reflection barycenters not laying on the same line are mitigated by the fuzziness of the approach as the membership function gives a value indicating the goodness of the matching between the candidate features and the rule. To evaluate the alignment of the candidate features, the barycenter coordinates of the candidate features b_a^i and b_r^i in the azimuth and range directions, respectively, are considered as defined in Section 4.3.2. According to the lava tube EM model, the barycenters of the two reflections lay on the same line, which is perpendicular to the azimuth direction. The slope m_{al} of the line connecting the barycenter of the two features is defined as

$$m_{al} = -\frac{b_r^c - b_r^f}{b_a^c - b_a^f} \quad (4.13)$$

Finally, the slope of the line is compared with that of the azimuth direction. The attribute r_{al} considers the orientation of the range direction and the line passing in the barycenters of the tube reflections. Hence, the attribute is calculated as the angle between the two lines, i.e., $r_{al} = |m - m_{al}|$, where m is the orientation of the range direction. The membership function is a sigmoid membership function (4.11) with parameters $a_i = a_{al}$, $a_{al} < 0$ and $c_i = c_{al}$, $c_{al} < 0$ since r_{al} is an angle in the range of $[-\pi/2, \pi/2]$. The value of r_{al} is 1 in the ideal case when the ceiling and floor features are parallel between them but perpendicular with the azimuth direction. r_{al} decreases to zero when the ceiling and floor features are not parallel between them nor perpendicular to the azimuth direction m .

Amplitude Comparison. This rule compares the amplitude signal of the candidate features among them and with that of the surface reflections. Ideally, the surface reflection has the highest amplitude in the radargram, thus, the tube candidate features have a lower amplitude. The EM model indicates that the tube boundary reflections have a comparable amplitude signal since losses inside the tube are almost null. The difference in the amplitude signal is mitigated by the fuzziness of the approach. Attribute r_A is defined as $r_A = \min\{a_c/a_f, a_c/a_c\}$, where a_c and a_f are the mean amplitude of the candidate ceiling and floor candidate features, respectively. To compute μ_A , the attribute is evaluated with a sigmoid membership function (4.11) with $a_i = a_A$, $a_A > 0$ and $c_i = c_A$, $c_A > 0$. The membership value μ_A is maximum when the amplitude of the two reflections is similar, and it tends to zero when the difference is high.

Phase Inversion. This rule analyzes the phase of the candidate features. Ideally, a phase inversion occurs at each interface between materials with considerably different dielectric properties (see Section 4.3.2). Here, two interfaces, i.e., the tube ceiling and bottom, generate the inversion of the phase signal. This rule is of critical importance to

discriminate subsurface reflections of the tube boundaries from clutter. Clutter indicates the undesired reflections from the topography variations and the off-nadir surface due to the large antenna footprint. The surface clutter appears in the subsurface of the radargram when considering the acquisition time. The power of the clutter signal is higher than that of subsurface reflections. Since it may mask subsurface reflections, clutter can cause serious issues. However, the phase inversion is a property of subsurface echoes and helps in identifying clutter [161]. Here, the phase inversion is checked between i) the surface reflection and the candidate feature for the ceiling, and between ii) the candidate features for the tube ceiling and floor. The difference of the phase signals is calculated for the two cases according to (4.10). The phase difference considers the path traveled by the wave from one reflection to the other and the contribution from the dielectric interfaces. Here, the interest is in the contribution from the dielectric interfaces. Thus, the contribution given by the wave propagation is computed by considering the average depth of the reflection. The contribution given by the dielectric interfaces is computed by inverting (4.10). Ideally, the phase difference is equal to π ; but more realistically, the phase difference may be slightly higher or lower. However, this is mitigated by the fuzziness of the proposed approach. The attributes for this rule r_ϕ^1 and r_ϕ^2 are computed considering the phase contributions from the dielectric interfaces, as follows

$$r_\phi^1 = \min\{|\phi_c/\pi|; |\pi/\phi_c|\} \quad (4.14)$$

$$r_\phi^2 = \min\{|\phi_c/\phi_f|; |\phi_f/\phi_c|\} \quad (4.15)$$

where ϕ_c is the average relative phase of the candidate feature for the ceiling, and ϕ_f is the average relative phase of the candidate feature for the floor. The attributes are evaluated with a sigmoid membership function (4.11) with $a_i = a_\phi$, $a_\phi > 0$ and $c_i = c_\phi$, $c_\phi > 0$ to have the membership values μ_ϕ^1 and μ_ϕ^2 . The memberships tend to 1 when the phase inversions occur for μ_ϕ^1 between the surface reflection and the candidate feature for the tube ceiling, while for μ_ϕ^2 between the candidate features for the tube ceiling and floor.

For each couple of candidate features \mathbf{F}_c and \mathbf{F}_f the membership values are aggregated with the Larsen product implication [164] as follows

$$M_{cf} = \mu_C \mu_L \mu_P \mu_a l \mu_A \mu_\phi^1 \mu_\phi^2 \quad (4.16)$$

The value of the overall membership M_{cf} indicates the reliability for the candidate features \mathbf{F}_c and \mathbf{F}_f to represent the boundaries of a lava tube. The higher is M_{cf} , the higher is the probability that the candidate features are associated with lava tubes. The decision strategy consists of thresholding M_{cf} . When M_{cf} is larger than the empirically defined threshold t_{tube} , the candidate reflections are associated with a candidate lava tube, such that $F_c = \omega_{LT}^c$ and $F_f = \omega_{LT}^f$. On the contrary, when $M_{cf} < t_{tube}$, the candidate reflection are not associated with lava tubes reflection.

The parameters of the fuzzy memberships a_i and c_i in (4.11) indicate the grade of tolerance of the system. The sigmoid center c_i represents the case when the candidate features satisfy the rule with a membership of 0.5. The slope a_i indicates the flexibility of the system, i.e., the robustness of the rules to clutter, noise, and irregularity of the geometrical structures. Hence, c_i is fixed by considering the EM model for lava tubes. The slope a_i is empirically selected according to the data characteristics, e.g., the expected size of the cavities and the average interface depth in that area. The choice of c_i and a_i is related to the degree of fuzziness of the approach and thus, to the grade of tolerance of the proposed method to the possible non-idealities of the candidate reflections. Considering the experimental results (see the next Section), one can conclude that the selection and tuning of the parameters are not critical and do not require complex prior knowledge.

4.4 Description of the Datasets and Experimental Results

To assess the effectiveness of the proposed method, we carried out several experiments on two datasets. The first dataset consists of data simulated with the approach proposed in [21] by (i) varying the dimensions and depth of the tube according to [140, 159], and (ii) varying the characteristics of the terrain. The experiments on the simulated dataset aim at proving the effectiveness and the validity of the proposed method in a controlled scenario. The second dataset consists of radargrams acquired on the Moon by the Lunar Radar Sounder (LRS) [3] onboard of the SELENE (SELEnological and ENgineering Explorer) spacecraft. The results are validated considering the state-of-the-art methods for detecting lava tubes, such as the superficial volcanic structures, the gravity and the thermal data, and eventual radar sounder measurements.

4.4.1 Simulated Dataset

The simulated dataset consists of radargrams simulated with the setup described in Section 4.2 with the radar parameters in Table 4.2. We performed two types of analyses: i) by varying the geometry of the tubes and a smooth surface, and ii) by varying the surface topography and fixing the tube geometry. The first analysis aims to validate the proposed method in detecting lava tubes having different geometries, i.e., tube width and height, and roof thickness. The second analysis aims at understanding the impact of the topography of the surface, which generates clutter that masks the reflections of the subsurface on the performance of the proposed method.

Description of the Dataset

For the first analysis (geometry analysis), the geometries of the lava tube varies as in Table 4.1, considering stable lava tube on the Moon according to [140, 141]. The height of the tube is varied from 250 m up to 2 Km, considering small, medium, and large lava tubes.

The roof thickness varies accordingly, increasing up to 200 m, with the dimension of the tube. For all the geometries, we simulated different angles of intersection between the tube longitudinal axis and the moving direction of the radar (α): $\alpha = 0$ (parallel case) centered and off-centered, $\alpha = \pi/2$ (perpendicular case), and $\alpha \in (0, \pi/2)$ (diagonal cases). The difference between centered and off-centered simulations is in the axis where the lava tube is in the radargram, i.e., in the center of the tube or not. In the radargrams, this is reflected in the distance between the tube ceiling and floor reflections. The difference in the radargrams between the $\alpha = \pi/2$ and $\alpha \in (0, \pi/2)$ cases is in the length of the tube ceiling and floor (see Section 4.2).

For the analysis of the impact of the topography surface (terrain analysis), we fixed the tube dimension to 1000 m and the roof thickness to 75 m. We simulated three different surface topographies: smooth topography as a reference, surface with deep and large craters, and surface with deep and large craters and large roughness. Craters generate clutter reflections below the surface (see Fig. 4.2) that are not affected by the phase inversion. The surface roughness generates diffuse scattering around the reflection of the surface and the craters (see Fig. 4.2). For the terrain analysis, we performed simulation with $\alpha = 0$ (parallel case) and $\alpha = \pi/2$ (perpendicular case).

Experimental Setup

The first step is the extraction of the lines in the radargrams with the technique in [40]. The input parameters are estimated as in [40] and are reported in Table 4.4. The value of N_{AV} is set to 20 to guarantee an average probability of detection larger than 0.95 and a probability of false alarm of 10^{-3} . The value of Th_{line} is set to 60 by fixing the probability of false alarm to 10^{-3} after computing the conditional empirical noise distribution. The Viterbi length and excursion are experimentally set to 20 and 4, respectively. The Viterbi length indicates the maximum allowed range of the ‘jump’ of the layer tracking from one azimuth position to another. Finally, the skeleton thickness is set to 10 pixels.

It is worth noting that a relevant number of lines are extracted. Some are irrelevant from the application viewpoint as they are generated by the topography of the surface (clutter) or other subsurface structures. The topography increases the complexity of the problem of automatically detecting lava tube reflections. The second step of the proposed approach includes line refinement. The overlapping in azimuth and range are empirically set to $O_a = 7$ pixels and $O_r = 5$ pixels, respectively. Considering the azimuth resolution, the minimum feature length L_{min} is fixed to 50 pixels. The algorithm groups together segments that represent the same reflection as for the surface. Fig. 4.7 shows the outcome of the line detection algorithm for the simulations of a lava tube having an height of 1000 m and 75 m roof thickness with a surface characterized by a large roughness and thick craters with crossing angles $\alpha = 0$ (see Fig. 4.7.a) and $\alpha = \pi/2$ (see Fig. 4.7.b). Fig.

Table 4.4: Values of the parameters of the proposed method.

Parameter	Simulated Dataset	LRS Dataset
N_{AV}	20	16
Viterbi Length	20	20
Viterbi Excursion	4	4
Th_{line}	40	40
Skeleton Thickness	10 pixels	3 pixels
L_{min}	50 pixels	10 pixels
O_a	7 pixels	2 pixel
O_r	5 pixels	2 pixel
a_P, c_P	10, 0.3	10, 0.3
a_L, c_L	10, 0.5	10, 0.5
a_{al}, c_{al}	-10, $\frac{\pi}{3}$	-10, $\frac{\pi}{3}$
a_A, c_A	10, 0.5	10, 0.5
a_ϕ^1, c_ϕ^1	-10, 0.5	-10, 0.5
a_ϕ^2, c_ϕ^2	10, 0.5	10, 0.5
Th_G	0.50	0.50
Th_{tube}	0.1160	0.1160

4.8.a and 4.9.a show the outcome of the line refinement step with the extracted features in different colors. All the reflections are characterized by computing the length in pixels, the average depth and the barycenter coordinates in range and azimuth, and the average amplitude and phase values. For the phase evaluation, the Hanning window length T is estimated by considering the thickness of each reflection in the range direction. The relative dielectric properties of the rock is set to $\epsilon_r^{rock} = 4$ [165], while that of the air to $\epsilon_r^{air} = 1$. The height of the radar above the surface is set to $h = 100$ Km (Table 4.2). The third step analyzes the features with the fuzzy detection system to identify the best candidates to be the surface reflection and the lava tube ceiling and floor. For the detection of the surface reflection, the rule in (4.12) is evaluated with the parameters in Table 4.4. It is worth noting that the threshold Th_G was selected to minimize the missed alarms, considering the definition of the membership functions and the algebraic product as aggregation strategy (Larsen implication [164]). In this experiment, $\mu_G = 0.5$ and $\mu_p = 1$ were selected as a limit case, which results in an aggregate membership function for the surface of $M_G = \mu_G \mu_p = 0.5$, considering (4.12). Hence, $Th_G = 0.5$, as it is the value of M_G at the limit case. The aggregate membership value for the surface reflection was $M_G \geq 0.95$. The last step labels the reflection with ω_{LT}^c and ω_{LT}^f , and ω_n . The parameters

for the fuzzy rules memberships are in Table 4.4. $\mu_P = \mu_L = \mu_{al} = \mu\phi = \mu_A = 0.7$ were selected as a limit cases, which result in an aggregate membership function for the tube detection of $M_{cf} = 0.1160$, considering (4.16). Hence, the lava tube threshold is set to $Th_{tube} = 0.1160$.

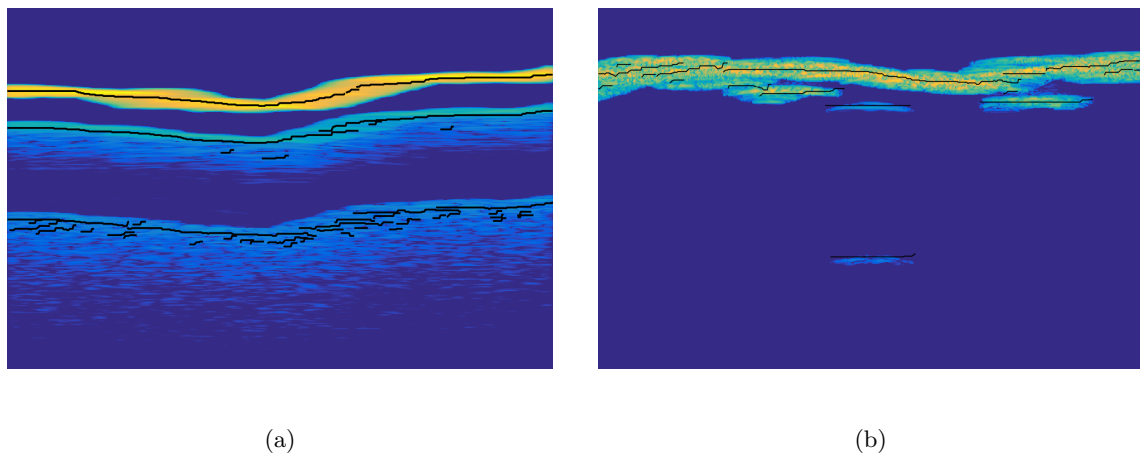


Figure 4.7: Line detected (in black) with the technique in [40] for crossing angle values (a) $\alpha = 0$ and (b) $\alpha = \pi/2$. The case of a simulated radargram with a tube height of 1000 m and a roof thickness of 75 m and surface topography with a large roughness and thick craters is considered.

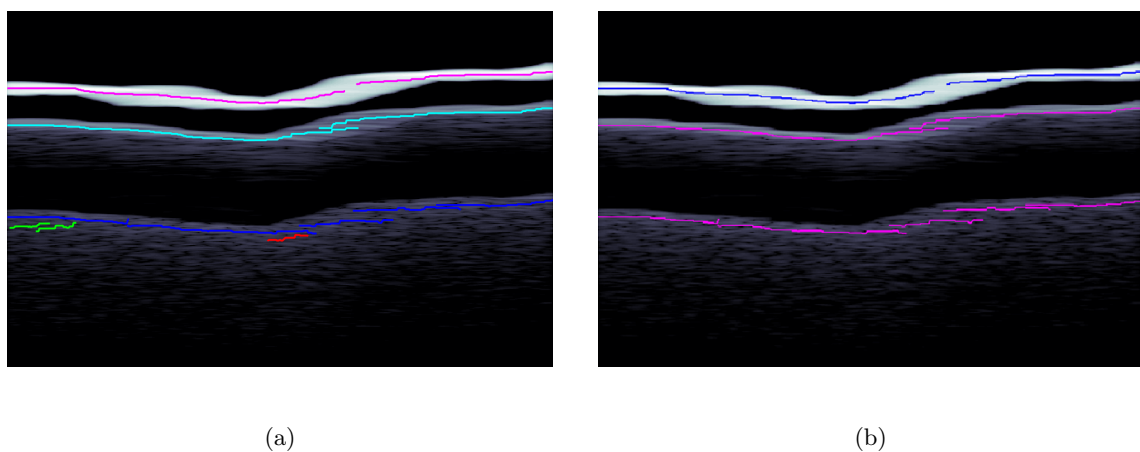


Figure 4.8: Processing of the simulated radargram for $\alpha = 0$ (parallel case). (a) Extracted features in different colors, (b) reflections recognized by the proposed approach as the surface in blue and the lava tube boundaries in magenta. The case of a tube having a height of 1000 m and a roof thickness of 75 m and surface topography with a large roughness and thick craters is considered.

Experimental Results

The proposed method detected in all the radargrams the lava tubes with a high value of overall membership, i.e., higher than 0.98 in all the cases. It showed to detect lava

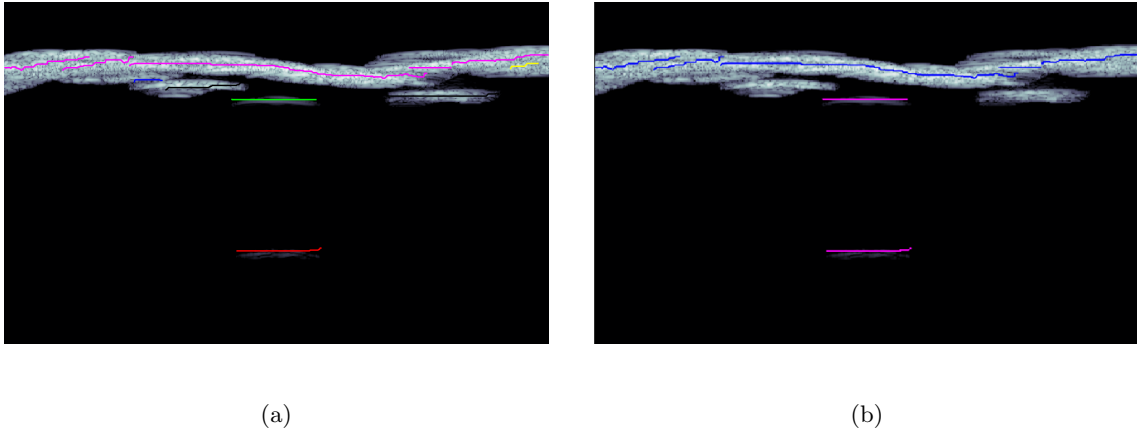


Figure 4.9: Processing of the simulated radargram for $\alpha = \pi/2$. (a) Extracted features in different colors, (b) reflections recognized by the proposed approach as the surface in blue and the lava tube boundaries in magenta. The case of a tube having a height of 1000 m and a roof thickness of 75 m and a surface topography with large roughness and thick craters is considered.

tubes with different sizes, roof thickness, and crossing angle α , showing high robustness to the surface topography and the clutter in the simulated radargrams. For the sake of space, we report here only the analysis for two radargrams simulated with tube height of 1000 m and roof thickness of 75 m, and surface topography characterized by large and deep craters and high roughness. Fig. 4.8 shows the processing for $\alpha = 0$ (parallel case): Fig. 4.8.a depicts the features extracted, while 4.8.a presents the outcome of the detection algorithm (in blue the surface reflection and magenta the detected lava tube ceiling and floor). Fig. 4.9 shows the processing for $\alpha = \pi$ (perpendicular case). Note that the rule of the phase inversion is of major importance to discriminate between the clutter in the subsurface (generated by craters in the simulations), and the reflections from subsurface targets.

4.4.2 LRS Dataset

The second dataset consists of radargrams acquired by the LRS onboard the SELENE spacecraft [3]. LRS had two dipoles of 30 m working at a frequency of 5 MHz. The characteristics allow penetration into the subsurface for some kilometers with a range resolution of 100 m in the vacuum. Table 4.2 summarizes the parameters of the LRS and the characteristics of the related radargrams. The Section is structured as follows— first, we describe the dataset in Section 4.4.2, then, we analyze the radargram preprocessing and the experimental setup, and finally, we describe the experimental results in Section 4.4.2.

Description of the LRS Dataset

The LRS dataset considers radargrams acquired in i) the Marius Hills region (MH), where lava tubes are expected in the subsurface due to the strong presence of superficial volcanic features and gravity evidence, and ii) in the highlands, where buried lava tubes are not expected, and the surface topography is affected by a large roughness and many impact craters [166, 167, 49]. In the MH region, the proposed method detects in an automatic and fast way candidate lava tubes in locations that are in line with the literature [156, 168, 166, 169, 49]. The reflections should be then further analyzed with a clutter simulator, but we believe this is out of the scope of the work. In the highlands, where lava tubes are not expected, we analyzed the rate of the false alarms, considering any reflection identified by the proposed method as a candidate lava tube as a false alarm. Hence, the number of false alarms N_{FA} is equal to the number of couples of reflections classified as candidate lava tubes.

Marius Hills. MH (14°N, 56°W) is in the western equatorial region of Oceanus Procellarum. The region is a young pyroclastic deposit with a high concentration of volcanic features related to buried lava tubes, such as volcanic domes around 200-500 m high, rilles, pits, and depression lacking ejected rima. The characteristics of these geological formations are strongly different from others on the Moon [166, 167, 49, 170]. Hence, MH was an active volcanic region in recent years and with a high probability of having buried lava tubes. This is confirmed by the presence of C-shaped domes having a lower height and smaller diameter than others on the Moon. Another confirmation comes from the block abundance on the surface that makes the surface rougher than in the surrounding. The blocks have uniform size and are smaller than others in the surrounding, and thus they are strongly different from the others on the Moon (such as those related to impact craters) [166]. The analysis of the pits in the MH region showed the presence of possible skylights, locally collapsed lava tube roof [169, 49]. Authors in [169] focused on the MH hole (see the green placemark in Fig. 4.10) that was imaged with oblique views by the LROC camera under different illumination. The analysis of the images showed an extended subsurface void that can extend laterally in cavernous spaces. Hence, this hole is a candidate to be a skylight of a buried lava tube [169]. Further, GRAIL data of the region show mass anomalies that can be explained with void volumes [171]. The size of the voids is comparable to that of empty and stable lava tubes, as defined in [140]. Finally, [172, 156] identified a possible location of lava tubes by analyzing rangelines of radargrams. Hence, the LRS dataset for the MH region consists of six radargrams: LRS_SAR05KM_C_xxN_yyE with xxN_yyE in { 10N_303594E, 10N_303632E, 10N_303067E, 10N_303734E, 10N_303249E, 10N_303801E }. Fig. 4.10 shows the radargram tracks in magenta superimposed on an optical image of the surface acquired by the Lunar Reconnaissance Orbiter Camera

(LROC). The tracks are parallel to each other. Thus, it is reasonable to assume that a candidate lava tube in a radargram also appears in the other radargrams at a similar latitude.

Highlands. Highlands cover around 83% of the lunar surface and are characterized by impact craters. The surface topography is not flat, and thus radargrams show a large number of clutter reflections in the subsurface. Lava tubes are not expected in these regions [166, 167, 49]. Hence, the LRS dataset for the highlands region consists of hundred radargrams acquired in the rectangular area with latitude in the range of $[45^\circ\text{N}, 45^\circ\text{S}]$ and longitude in the range of $[90^\circ\text{E}, 90^\circ\text{W}]$.

Experimental Setup

Radargrams have N_T 1000 samples (rows), of which 500 are removed— 200 from the radargram top as they represent the free space above the surface, and 300 from the bottom as the signal-to-clutter ratio is low below ~ 3 Km of penetration [156]. All radargrams have 8011 traces (columns). Radargrams of the MH are cut 807 traces to image the latitude coordinates in the range of 13°N to 15°N , like in [156] to focus on the MH region. All the radargrams are pre-processed with range compression to enhance the range resolution and SAR focusing [173] to enhance the azimuth resolution with a synthetic antenna length of 5 Km.

As described in the methodological Section, the first step of the proposed approach is the extraction of the lines in the radargrams with [40]. The input parameters are estimated as in [40] and are reported in Table 4.4. For the LRS dataset, the value of N_{AV} is set to 16 to guarantee an average probability of detection larger than 0.95 and a probability of false alarm of 10^{-3} for all the radargrams. The value of Th_{line} is set to 60 by fixing the probability of false alarm to 10^{-3} after computing the conditional empirical noise distribution. The Viterbi length and excursion are set to 20 and 4, respectively, for both the radargrams of the LRS Dataset. Finally, the skeleton thickness is set to 3 pixels. The second step of the proposed approach includes line refinement. The overlapping in azimuth and range are empirically set to $O_a = 2$ pixels and $O_r = 2$ pixels, respectively. Considering the LRS azimuth resolution, the minimum feature length L_{min} is fixed to 10 pixels. Hence, the smallest width of a possible lava tube is about 600 m, which should have a roof thickness of 50 m to be stable [140, 141]. In free space, the LRS range resolution is about 75 meters, which is in the range of 100 - 150 m in the basaltic rock, which roughly corresponds to 1 pixel. The algorithm groups together segments that represent the same reflection, as for the surface. All the reflections are characterized by computing the length in pixels, the average depth and the barycenter coordinates in range and azimuth, and the average amplitude and phase values. For the phase evaluation, the length of the

Hanning window T is estimated by considering the thickness of each reflection in the range direction. The relative dielectric properties of the rock is set to $\epsilon_r^{rock} = 4$ [165], while that of the air to $\epsilon_r^{air} = 1$. The height of the radar above the surface is set to $h = 100$ Km (Table 4.2). The third step analyzes the features with the fuzzy detection system to identify the best candidate to be the surface reflection and the best candidates to be reflections generated by the lava tube ceiling and floor. For the detection of the surface reflection, rule in (4.12) is evaluated with the parameters in Table 4.4. It is worth noting that the threshold T_G was selected to minimize the missed alarms, considering the definition of the membership functions and the algebraic product as aggregation strategy (Larsen implication [164]). In this experiment, $\mu_G = 0.5$ and $\mu_p = 1$ were selected as a limit case, which results in an aggregate membership function for the surface of $M_G = \mu_G \mu_p = 0.5$, considering (4.12). Hence, $Th_G = 0.5$, as the value of M_G at the limit case. The aggregate membership value for the surface reflection was $M_G \geq 0.71$. The last step labels the reflection with ω_{LT}^c and ω_{LT}^f , and w_n . The parameters for the fuzzy rules memberships are in Table 4.4. $\mu_P = \mu_L = \mu_{al}, = \mu\phi = \mu_A = 0.7$ were selected as a limit cases, which result in an aggregate membership function for the tube detection of $M_{cf} = 0.1160$, considering (4.16). Hence, the lava tube threshold is set to $Th_{tube} = 0.1160$.

Experimental Results

This Section describes the experimental results for radargrams acquired in the MH and Highlands.

Marius Hills. The method identified 20 candidate lava tubes in the LRS dataset– in Fig. 4.10 the detected tubes are in red. Table 4.5 lists the fuzzy rule membership values and the tunnels estimated parameters. Note that the aggregate membership values are all above 0.65. M_G and M_{cf} can be considered as a grade of reliability that the couples of reflections are related to a buried candidate lava tube. For the sake of space, Fig. 4.11 shows the steps of the proposed method for the candidate tube C. Identified candidate lava tubes correspond with those in [156]. Reflections of the identified candidate lava tubes should be further analyzed with a clutter simulator to discriminate subsurface reflections from clutter (this is outside this research scope).

Assuming that the reflections are generated by lava tubes, we can estimate the roof thickness and the tube dimension. The roof thickness is estimated by considering the depth of the ceiling reflection to the surface and $\epsilon_r^{rock} = 4$ as the rock relative dielectric constant [165]. The tube height is estimated by considering i) the difference between the depth of the tube ceiling and the floor, and ii) a void tube $\epsilon_r^{void} = 1$. The tube width cannot be correctly estimated as it depends on the length of the reflection and the crossing angle between the moving direction of the radar and the longitudinal axis of the tube, which is unknown. The estimations in Table 4.5 are computed by considering that i) the

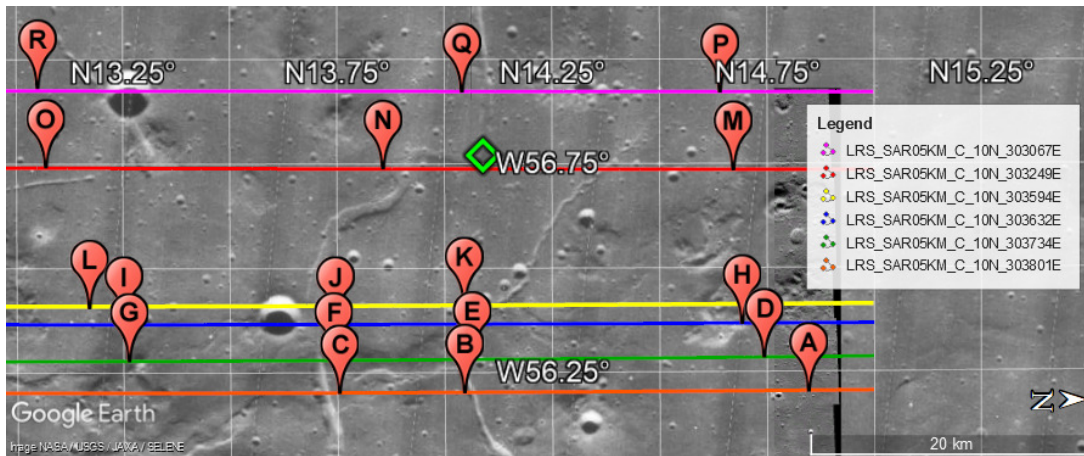


Figure 4.10: MH region: lines are the tracks of the radargrams (see the legend for their ID). Candidate lava tube locations identified with the proposed method are indicated with the red pointers. (Optical image credits: NASA/GSFC/Arizona State University and NASA/USGS/JAXA/SELENE).

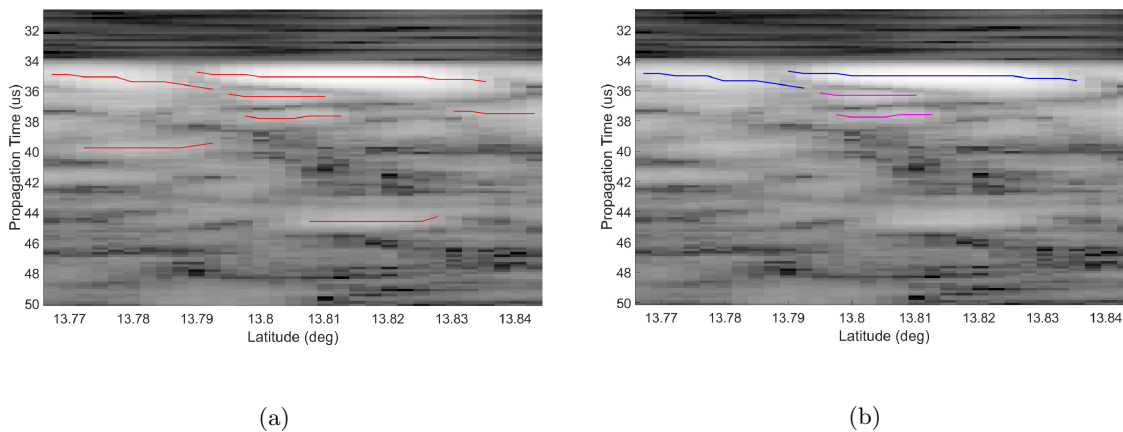


Figure 4.11: Analysis of the part of the radargram LRS_SAR05KM.C_10N_303801E between 13.75°N and 13.85°N : (a) the extracted features, (b) the reflections indicated by the proposed approach as the surface in blue and the candidate lava tube boundaries in magenta. The placemark of this tube is B in Fig. 4.10.

Table 4.5: Output values of the proposed method for the LRS dataset in the MH region: membership values for pairs of reflections identified candidate lava tubes, central latitude and longitude coordinates of the locations (lat and $long$), and tube height (h_{lt}) and roof thickness (h_{roof}) estimated in the mid of the reflections. The width (w_{lt}) of the lava tubes is estimated. IDs correspond to the labels in Fig. 4.10.

ID	μ_L	μ_s	μ_α	μ_P	μ_ϕ	M	lat (°N)	$long$ (°E)	h_{roof}	h_{lt}	w_{lt}
A	0.908	0.973	0.973	0.943	0.899	0.730	14.84	303.79	900 m	900 m	2.7 Km
B	0.986	0.927	0.996	0.998	0.897	0.816	14.44	303.79	600 m	525 m	1575 m
C	0.944	0.848	0.971	0.962	0.963	0.721	13.72	303.79	700 m	600 m	1800 m
D	0.976	0.957	0.953	0.975	0.943	0.820	14.74	303.73	500 m	600 m	1.8 Km
E	0.928	0.934	0.998	0.905	0.916	0.719	14.08	303.73	700 m	900 m	2.7 Km
F	0.977	0.916	0.896	0.937	0.950	0.715	13.74	303.73	1 Km	750 m	2250 m
G	0.999	0.964	0.979	0.917	0.903	0.782	13.25	303.73	800 m	675	2025 m
H	0.982	0.973	0.990	0.926	0.899	0.790	14.69	303.63	900 m	825 m	2475 m
I	0.928	0.934	0.998	0.905	0.836	0.656	14.25	303.63	800 m	1125 m	3375 m
J	0.983	0.975	0.980	0.953	0.941	0.844	13.82	303.63	700 m	525 m	1575 m
K	0.970	0.933	0.908	0.927	0.895	0.683	14.01	303.59	1.3 Km	1050 m	3150 m
L	0.992	0.935	0.954	0.970	0.936	0.805	13.17	303.59	1.2 km	975 m	2925 m
M	0.995	0.988	0.936	0.934	0.880	0.758	14.67	303.59	1.1 Km	600 m	1.8 Km
N	0.936	0.962	0.988	0.970	0.933	0.807	13.86	303.26	500 m	675 m	2025 m
O	0.981	0.967	0.941	0.972	0.868	0.755	13.05	303.59	1 Km	750 m	2250 m
P	0.958	0.996	0.967	0.886	0.892	0.730	14.64	303.26	1.4 Km	1050 m	3150 m
Q	0.928	0.934	0.998	0.954	0.908	0.751	13.86	303.26	1.3 Km	975 m	2925 m
R	0.995	0.892	0.952	0.937	0.879	0.697	13.05	303.26	1.1 Km	450 m	1350 m

moving direction of the radar is perpendicular to the longitudinal axis of the tube, and ii) the ratio between the tube height and width is 1:3 as in [140]. Hence, the tube width is calculated by multiplying the tube height by 3 to understand if it may exist such a stable tube on the Moon according to [140]. Considering their height and roof thickness, tunnels identified by the proposed method can exist and be stable on the Moon (i.e., not collapsed) under the Lithostatic and the Poisson stress states.

Highlands. The method identifies $N_{LT} = 12$ couple of reflections of candidate lava tubes. The average overall membership value is equal to 0.3205, which is much lower than the minimum overall membership value of the candidate lava tubes detected in the MH region. Since in the highlands lava tubes are not expected, the number of false alarms

is set equal to $N_{FA} = 12$. The false alarm rate ξ_{FA} is defined as

$$\xi_{FA} = \frac{N_{FA}^a}{N_{TOT}^a} \quad (4.17)$$

where N_{FA}^a indicates the number of rangelines (traces) covered by the candidate lava tubes (false alarms), and N_{TOT}^a the total number of traces being processed. The total number of traces is equal to $N_{TOT}^a = 801100$ since each radargram has 8011 traces and we analyzed 100 radargrams. The number of false alarm rangelines N_{FA}^a is defined as the sum of the length in the azimuth of candidate lava tubes. For each detected lava tube candidate i , we considered the length of the longer features, i.e., $l^i = \max\{l_c^i, l_f^i\}$. Hence, the number of false alarm rangelines is defined as $N_{FA}^a = \sum l_i, i = [1, \dots, N_{LT}]$. For the LRS radargrams in the highlands, $N_{FA}^a = 127$, and thus, the false alarm rate is $\xi_{FA} = 1.5853 \cdot 10^{-04}$. Note that the false alarm rate is estimated for the LRS radargrams considered in the Highland area, and it may vary by region and datasets.

4.5 Discussion

The core assumption of the proposed method is the detection of the reflections from the tube ceiling and floor and the surface. This assumption is not always valid as it depends on the acquisition system and the dimension of the target. The proposed EM model of lava tubes assumes that the range resolution of the radargram is high enough to image the surface and the tube ceiling and floor. Under this assumption, the proposed method is demonstrated to be effective. However, stable and empty lava tubes exist on the Moon and Mars with a thin roof [140] [159] smaller than the range resolution of the radar sounder. Therefore, in radar sounder data, the lava tube ceiling may be masked and incorporated in the surface reflection, and thus, not detectable.

Another assumption of the proposed method is that the signal-to-noise ratio (SNR) is high enough to detect the reflections of the tube ceiling and floor. Relevant factors in the SNR are the attenuation of the subsurface, the depth of the floor reflection, and the two-way rough surface transmission loss (depending on the frequency). The SNR also impacts the error of the phase signal. Considering the properties of the Maria on the Moon, the study in [161] showed that an SNR > 10dB is enough to detect lava tubes and to guarantee a negligible absolute phase error. Further information about the SNR analysis can be found in [161], where the SNR estimation and impact on the absolute error phase are described in details. Radargrams with low SNR values show dense and fragmented reflections, i.e., subsurface targets are imaged with discontinuous reflections. The considered line detection algorithm is suitable to process radargrams with low SNR as the HMM and the VA are applied with a divide and conquer strategy [40]. The line refinement step groups together lines belonging to the same reflection.

The proposed method analyses radargrams reflections as candidates to be the lava tube ceiling or floor. Identified candidate lava tubes should be then studied in post-processing by expert planetologists to detect possible unidentified clutter reflections and take the final decision. However, it is worth noting that surface clutter does not generate any phase inversion [161], and thus, Rule 7 (phase inversion rule) is likely to assume a small value, bringing to a small overall membership. An example of a geological structure that generates reflections with a geometry similar to that of lava tubes are craters (see Fig. 4.2). Crater reflections do not generate phase inversion – Rule 7 has a small membership value, which leads to an overall small membership value.

4.6 Conclusions

This Chapter proposed a novel method to detect candidate buried cavities, such as empty lava tubes, in radar sounder data. The approach consists of three main steps: i) EM modeling of the lava tube defined by considering the propagation of the EM wave in the subsurface, ii) extraction and characterization of relevant reflections in a radargram, and iii) analysis of the reflections to identify those related to the surface and lava tube ceiling and floor and associate them with a grade of reliability.

The method takes advantage of the theoretical modeling of how cavities and lava tubes appear in radargrams. The model describes the physical properties of the reflection generated by the surface and subsurface cavities. From this model, the surface and lava tube boundaries can be identified by a pattern of linear reflections with specific alignment, geometrical, and signal properties. The candidate linear reflections are analyzed with a fuzzy system based on the lava tube model. The fuzzy rules consider the backscattering mechanisms of buried and empty lava tubes imaged by radar sounders and provide a membership value that indicates the reliability of each detected tunnel. The proposed approach requires the tuning of some parameters that depend on the approximated size of the expected lava tubes in the investigated area and the radar range and azimuth resolutions. This information is usually available and easy to include in the processing. After tuning, the method is automatic and unsupervised.

The effectiveness of the proposed method has been demonstrated with experiments on two datasets: a simulated and real LRS datasets. The accurate detection of the lava tubes in the simulated dataset demonstrated that the method is effective and accurate in detecting lava tubes in radargrams with i) different dimension and depth values, ii) different crossing angles between the tube axis and moving direction of the spacecraft, and iii) varying surface topography. The results showed the high robustness of the proposed method to deviations from the ideal lava tube model due to the definition of adequate fuzzy rules. For the LRS dataset, the proposed method analyzed radargrams in the Maria

region (Marius Hills) where lava tubes are expected to be present and in the highlands area where lava tubes are not expected. In the MH region, the proposed method identified several candidate lava tubes that were already documented in the literature in a completely automatic way. This resulted in a fast detection that would be not possible in a large number of radargrams with state-of-the-art methods based on the visual inspection of surficial volcanic features. Identified candidate lava tubes should be further analyzed with a clutter simulator to take a reliable final decision on them. It is worth noticing that the comparison of the identified reflections with the clutter simulations requires a dedicated analysis that goes beyond the scope of this work. In the highlands regions, we analyzed 100 radargrams characterized by the presence of a large amount of surface clutter due to the irregularities of the surface topography. The proposed method resulted in a false alarm rate of $\xi_{FA} = 1.5853 \cdot 10^{-04}$. Note that the false alarm rate is an estimate for the dataset considered in the Highlands areas, and it may vary by region and datasets. The low false alarm rate is mainly due to the phase inversion rule, in which the membership assumes small values with clutter (as there is no phase inversion), bringing to a small overall membership. Hence, the phase inversion rule showed to increase the robustness of the proposed method against the clutter.

As future development, we plan to improve the EM model of lava tube to consider cavities totally or half-filled with other materials, such as sand and rock. We also intend to further analyze the detected candidate lava tube reflections on the MH and the Moon by comparing them to clutter simulations. Finally, we plan to model other targets of planetary arid areas, such as craters and tesserae, and design rules to include them in the system.

Chapter 5

A method based on deep learning for the automatic semantic segmentation of radar sounder data

During the last decades, radar sounders provided direct measurements (radargrams) of the Earth's polar caps subsurface. Radargrams are of critical importance for a better understanding of glaciological structures and processes in the ice sheet in the framework of climate change. This Chapter aims at automatically extracting information on basal boundary conditions given their substantial relevance for modeling the ice-sheet processes, such as the ice-sheet sliding. This Chapter introduces ¹ a novel automatic method based on deep learning to detect the basal layer and basal units in radargrams acquired in the inland of icy areas. Radargrams are segmented into traditional classes, including englacial layers, bedrock, echo-free zone (EFZ) and thermal noise, as well as new classes of basal ice and signal perturbation. The network is a U-Net with attention gates and the Atrous Spatial Pyramid Pooling (ASPP) module that automatically extracts semantically meaningful features. Experimental results on two datasets acquired in north Greenland and west Antarctica by the Multichannel Coherent Radar Depth Sounder (MCoRDS3) indicate high overall segmentation accuracy. The accuracy of basal ice and signal perturbation detection is high, which that of the other classes is comparable with literature techniques based on handcrafted features. The results show the effectiveness of the proposed method in mapping the basal layer and basal units.

¹Part of this chapter appears in

Donini, E., Thakur, S., Bovolo, F., and Bruzzone, L. (2019, October). An automatic approach to map refreezing ice in radar sounder data. In *Image and Signal Processing for Remote Sensing XXV* (Vol. 11155, p. 111551B). International Society for Optics and Photonics.

5.1 Introduction

feed ice-shelves that calve and melt into the sea, representing one of the main causes of the global sea-level rise. The ice-sheet sea-ward flow depends on the basal boundary conditions, related to several thermal and mechanical factors at the basal interface [174, 175, 81]. The basal layer, i.e., the last part of the ice column, is critical for understanding the ice-sheet processes, including the sliding. Accurate modeling of the basal conditions requires the direct measurements of the ice sheet up to the bedrock. Traditionally, information on the ice sheet is extracted by analyzing either ice core samples obtained by drilling or radar sounder data. Ice core samples have been providing a large amount of information [176, 177], but extracting them is intrusive and expensive. To deal with these issues, Radar Sounders (RSs) have been widely used during the last decades to image the inside of the ice sheets in Greenland and Antarctica [29]. A large amount of data is available from airborne radar sounders acquisitions, and the data volume is expected to grow further in the future. Recently, the basal layers have been visually analyzed to identify geological structures, such as basal units [37, 38] and Units of Disrupted Radiostratigraphy (UDR) [178, 179]. They elongate for several kilometers and extend up to half of the ice sheet thickness, causing the ice layering to fold toward the surface. Although visual inspection has been supporting the characterization of several targets, it is subjected to several limitations. Visual inspection is time-demanding and not suitable for analyzing a large number of radargrams. Moreover, it is subjective and can lead to inconsistencies and misinterpretations. Hence, automatic methods are now emerging to address these limitations and automatically extract information on the subsurface [158, 41, 45, 180].

In the literature, the methods for the automatic analysis of the basal boundary conditions in RS data fall into three strategies. The first one uses numerical modeling for ice-sheet geological processes and locally infers the basal boundary condition type. Numerical models [181, 105] consider data from different sensors (e.g., altimeter and optical images) and analyses (e.g., subsurface temperature profile) as input, extracting only the ice-sheet thickness and the topography of the basal interface from RS data. However, other studies [38, 182, 80] indicate that RS data contain more information, including basal units and water at the interfaces that can further enhance the modeling of the basal conditions. The second strategy automatically analyzes the layer stratigraphy of radargrams to identify disruptions in the basal layer without considering the basal interface. The englacial stratigraphy is extracted with a line detection algorithm, and the line (i.e., the layer) slopes are used to model the disruption [183, 178, 184]. However, these techniques focus on analyzing the ice stratigraphy disruption without mapping the basal layer, e.g., basal ice and basal units. The third strategy extracts the main geological targets by semantically segmenting radargrams. The study in [45] segmented radargrams into three

targets: the stratigraphy of the ice layering, the bedrock, and the echo-free zone (EFZ) and thermal noise. The authors in [41] expanded the work in [45] by considering also basal ice. Both methods extract hand-crafted features based on apriori information on the target class spatial and statistical properties to perform a pixel-based classification with Support Vector Machines (SVM). Hand-crafted features strongly depend on human design and model-specific classes. However, increasing the number of classes, this approach is subjected to degradation of performance in tackling the problem complexity. Thus, there is a need to develop methods capable of extracting robust features automatically. Recently, deep learning has provided powerful means for image segmentation in various applications [185, 186, 187, 188, 189, 190]. Deep learning-based methods handle the feature extraction automatically and provided robust results in other applications. In this study, we leverage deep learning to analyze inland radargrams acquired in the cryosphere.

In the semantic deep learning literature, several works exist to perform a supervised pixel-based learning task, given reliable training samples [185, 186, 187, 188, 189, 190]. The common approach is based on fully convolutional deep neural networks (FCNNs) [185] made of fully connected layers, where each neuron in one layer is connected to each neuron in the previous and next layers. In the last years, many variants of FCNNs have been proposed [186, 187, 188, 189, 190] mostly to analyze passive data (e.g., optical data). For instance, a U-Net architecture with a contracting path to capture context and a symmetric expanding path enabling segmentation was proposed in [189]. Attention U-Net is enriched with attention gate modules that force the network to focus on relevant regions of the input data in [191]. The model was further improved in [192] by adding the Atrous Spatial Pyramid Pooling (ASPP) module in the bottleneck to control the feature resolution. The ASPP module robustly segments images at multiple scales by enlarging the receptive field to incorporate a greater context while saving on the number of the network parameters compared to the regular convolution [190]. Recently, deep learning has been applied to radargrams obtaining good performance for i) detecting the ice layers [193, 194], ii) simulating RS images with Generative Adversarial Network (GAN) [195], and iii) segmentation [196]. The study in [196] applied a ResNet with an ASPP module to segment radargrams in ice layers, thermal noise and Echo-Free Zone (EFZ), and bedrock with an overall accuracy slightly lower than other literature methods based on the SVM [45, 41]. The study did not consider the basal layer and the targets related to basal boundary conditions.

This work proposes a novel automatic method based on deep learning to segment icy inland radargrams and locate meaningful geological targets for better understanding the ice-sheet and the basal boundary conditions processes. Radargrams are segmented

into classes, including englacial layers, bedrock, echo-free zone (EFZ) and thermal noise already considered in the literature, as well as new classes of basal ice and signal perturbation. The classes are characterized by a specific spatial distribution in the range and azimuth directions. Moreover, the dimension and scale of the targets significantly vary between them. Inland radargrams are processed with an Attention U-Net with the Atrous Spatial Pyramid Pooling (ASPP) module that automatically extracts relevant features for the semantic segmentation problem. The encoder blocks are connected to the decoder block at the same level with skip connections. Attention gates filter skip connection signals to remove the irrelevant information. At the bottleneck of the network, the ASPP module extracts features at multiscale levels to improve the identification of targets having different sizes. An argmax operation analyzes the output features to predict labels. The segmentation map is refined using morphological filters. The method effectiveness was tested on two datasets of radargrams by the MCoRDS3 radar sounder in the inland of Greenland and Antarctica with basal units in the basal layers.

The work is structured in five Sections. Section 5.2 defines the segmentation problem. Section 5.3 proposes the deep learning method to segment radargrams and describes the related architecture. Section 5.4 illustrates the datasets, the network setup, the evaluation criteria, and the experimented results to prove the effectiveness of the proposed method. Finally, Section 5.5 provides concluding remarks and insights for future works.

5.2 Formulation of the problem

Let us consider radargrams acquired in the inland of icy areas, including information on the basal boundary conditions, specifically on the ice refreezing and melting processes. We aim at locating meaningful geological targets for the analysis of the ice-sheet and basal boundary conditions, such as the basal unit. Let \mathbf{R} be the a 2D radargram of N_T traces and N_S samples:

$$\mathbf{R} = \{P(a, r) | a \in [1, \dots, N_T], r \in [1, \dots, N_S]\} \quad (5.1)$$

where P is the power of the reflections stored in the radargrams, and (a, r) the azimuth and the range coordinates, respectively. We aim at segmenting inland icy radargrams into N_C classes representing meaningful geological targets related to the basal boundary conditions. The classes are defined as $\{\omega_c, c \in [1, \dots, N_C = 4]\}$, moving down from the surface along the range (see Fig. 5.1), where ω_1 is englacial layers, ω_2 basal ice, ω_3 bedrock, and ω_4 thermal noise and echo-free zone and signal perturbations. The EFZ and the thermal noise represent the regions that reflect waves having a lower power than the antenna sensitivity.

Basal ice occurs at the base of the ice sheet in the presence of melt-water at the basal interface, i.e., the ice-bedrock interface [182, 197] (see Fig 5.1). Close to the core of the

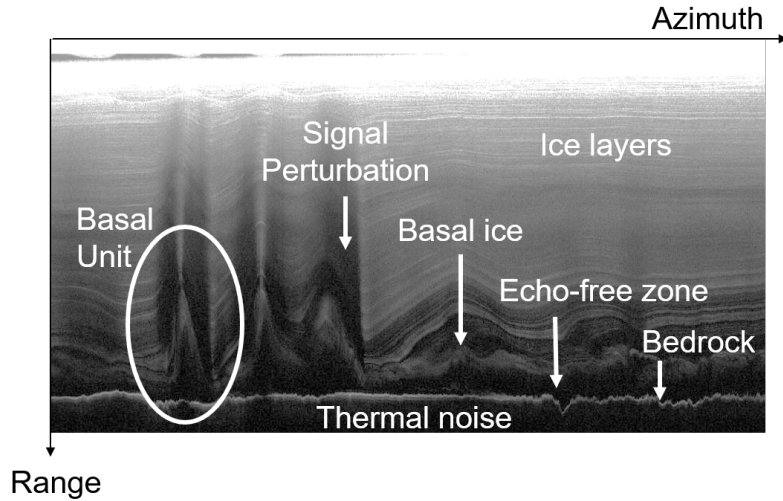


Figure 5.1: Part of a radargram from MCoRDS [29] campaign 20170413 in Greenland imaging an ice-sheet with three basal units. The labels indicate the geological targets in the basal layer and the classes for the proposed method.

basal ice, the layers fold toward the surface, generating large structures with steep edges, called disrupted layers that can extend up to half of the layer pack [178, 38]. The upper parts of the layers, close to the surface, are usually not affected by the folding, and thus, remain flat. Increasing the steepness of the disrupted layer, also the intensity of the signal perturbation (or shadow) increases, and thus masking part of the ice strata, see Fig. 5.1. It is worth noting that the target dimension largely varies between them. Ice layers cover a larger area than the other classes. The bedrock is typically thinner than the ice pack, the thermal noise, EFZ, and also shadows. The basal layer and the signal perturbation dimensions depend on the deformation of the ice-sheet bottom. Thus classes are modeled best at different scales.

Basal ice is characterized by a strong reflection, having four main radiometric properties. Firstly, the signal of the folded layers above the basal units shows fading due to the redistribution of the energy in the spectrum [197]. Secondly, the basal ice is characterized by diffuse scattering that can be modeled with the specularity in the along-track direction, i.e., the amplitude of the echo strength for the surrounding. The specularity inside the basal ice core is higher than in the upper layers and the EFZ/thermal noise [182, 80]. Thirdly, the basal layer temperature is higher than the rest of the ice sheet, as it is subjected to the higher pressure by the ice sheet. Studies [182, 80] have analyzed the absolute reflection power estimated from the radar equation by considering the ice attenuation coefficient at the radar frequency and the ice temperature. A loss in the reflection power can be due to deformation of the layers, impurities (e.g., soil or stones),

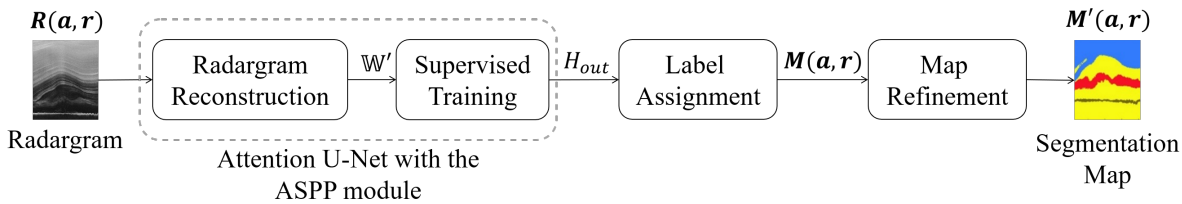


Figure 5.2: Flowchart of the proposed deep method for the supervised segmentation of radargrams.

and a higher ice temperature [80]. Finally, the last radiometric characteristic regards the bedrock. With the basal unit, water is generally present at the interface between the ice and the bedrock as a thin film or even a lake [38, 37, 182, 80]. Hence, the bedrock under freeze-on ice should appear as an anisotropic specular reflector, i.e., a smooth and bright reflection. The EM interacting with one target also affects the representation of the other targets in the radargrams. This property should be considered in the data analysis.

5.3 Proposed deep learning-based method

This Section presents the proposed method for the segmentation of the inland radargrams. Its overall flow is based on a supervised CNN that segments the radargram into four classes (see Fig. 5.2). Here, we consider a U-Net enriched with the Atrous Spatial Pyramid Pooling (ASPP) module and Attention Gates (AG) as it previously showed good performance for semantic segmentation [192, 189, 191]. The network learns the characteristic of the classes and automatically extracts relevant features at different levels for the radargram segmentation. Extracted features are semantically meaningful given the generalization capability of the network [198]. The AG helps to focus on the relevant regions of the radargram by filtering the features in input at the decoder from the skip connections [191]. The AG suppresses irrelevant low-level features to better focus on the radargram salient regions in contrast with the background, i.e., to distinguish between the noise and EFZ (background classes) and the signal classes, including the basal ice, the ice layers, and the bedrock [199]. The ASPP module extracts multiscale features to better segment objects and classes at different scales [190], such as the ice layers, basal ice, and bedrock that are characterized by a different scale in radargrams. The multiscale features avoid the loss of information in the network compression that generates poor-resolution segmentation maps, i.e., fuzzy boundaries. ASPP helps the processing of inland radargram to detect classes with different dimensions and scales, such as the thin bedrock and thick layers. The training of the network consists of two stages. In the first step, unsupervised training minimizes the reconstruction loss between the input and the output to initialize the network parameters and extract multiple scales features. In the second step, the network is tuned in a supervised fashion for the segmentation of

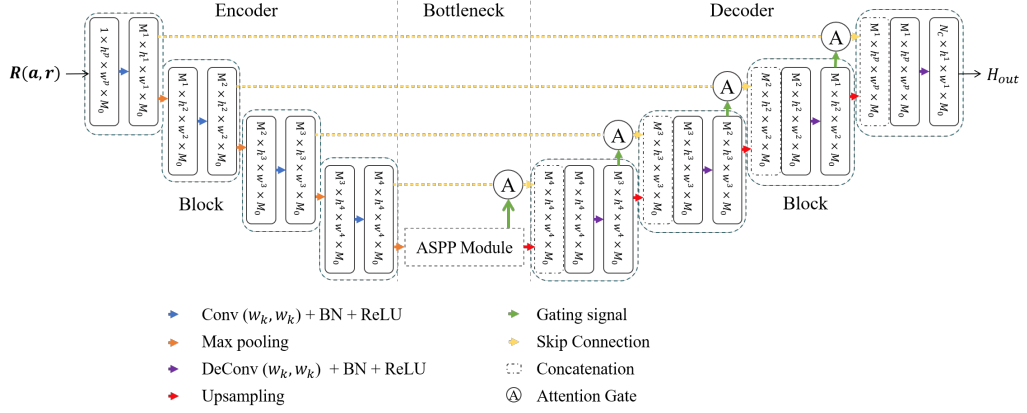


Figure 5.3: Architecture of the attention U-Net embedded with the ASPP module.

radargrams into the classes of interest. Segmentation labels are obtained by the argmax classification of the features of the last layer of the network. Then the map is refined in the spatial domain using morphological filters.

5.3.1 Deep network architecture

The proposed network has an autoencoder shape, providing an output of the same size as the input data. The encoder compresses the input into a lower dimension. The decoder decompresses it to obtain an output with the same input dimension. Here, we use a U-Net architecture [189] that showed very good performance in the segmentation task coupled with efficient use of the GPU memory [199]. U-Net has skip connections linking the encoder and the decoder (see Fig. 5.3). Input radargrams are split into N_p patches $P_t, t \in [0, \dots, N_p]$ of size (x_p, y_p) , and each patch is separately processed. In the range direction, the patches have the same size as the radargram depth, i.e., $x_p = N_S$. This leads to samples that capture the global context and are fully representative of the class characteristics (see Section 5.2) in terms of the variability, pattern, and vertical spatial distribution. In the azimuth direction, the patch size y_p is proportional to the average dimension of basal units. After the processing, the output patches are concatenated to have the same shape as the original radargram. In the following, the structure of the network is described in detail.

Let us define the input of each layer as H_i^l , where l indicates the block number, and i indicates the type of layer or activation function: c stands for convolutional layer, b for batch normalization layer, r ReLU activation function, m for max-pooling, and d for deconvolutional layer.

Encoder. The encoder is made of N_L downsampling blocks which consist of two sets each made of a convolution layer, followed by a batch normalization layer, and a rectified

linear unit (ReLU). Each convolutional layer l learns high-level semantic features from the spatial and semantic information in the data [198]. The first block ($l = 1$) inputs are the radargram patches $P_t, t \in [0, \dots, N_t]$. Each block l gives in output a set of M_l features, downsampled by the max-pooling operation.

To extract the features, the convolutional layer applies a kernel of size (k_x, k_y) , such that the learnable weight set W^l has size $k_x \times k_y \times M_0 \times M_l$, where M_0 is the channel size and is fixed to $M_0 = 1$. The output of the convolutional layer H_c^l is normalized with a batch normalization layer according to the batch normalization parameters (μ_t, σ_t) to obtain H_b^l . A ReLU activation function introduces nonlinearity to obtain H_r^l . Each block is followed by a max-pooling operation of size (m_x^l, m_y^l) to reduce the dimension of the features, and thus the number of parameters to learn and the computational cost. For each patch t , the encoder gives in output a set of M_l features H_m^l of shape $(M^l \times h^l \times w^l \times M_0)$.

Atrous Spatial Pyramid Pooling (ASPP). In the bottleneck of the network, an ASPP module, based on the Atrous (also called dilated) convolution [200, 190], applies parallel Atrous convolution to increase the receptive field of the network filters (see Fig. 5.3). This helps the network to integrate the global view and the focus on the details. Atrous convolution is an operation that contracts or expands the receptive field of the convolutional filters by varying the dilation rate parameter d . Considering signal $a[i]$, the output $b[i]$ of the dilated convolution $(*_d)$ with the filter/kernel window $w[k]$ of length K is defined as

$$b[i] = (a *_d w)[j] = \sum_{i+dk=j} a[i]w[k] \quad (5.2)$$

The dilation rate parameter d corresponds to the input signal sampling stride, and standard convolution is a particular case with $d = 1$. A dilated rate d indicates that the convolutional filter are enlarged by adding $d - 1$ spaces between the filter coefficients (see Fig.5.4). The kernel dimension is enlarged from $(k_x \times k_y)$ to $(k'_x \times k'_y)$, where

$$\begin{aligned} k'_x &= k_x + (k_x - 1)(d - 1) \\ k'_y &= k_y + (k_y - 1)(d - 1) \end{aligned} \quad (5.3)$$

The output of the ASPP module is H_{ASPP} of shape $(M^{ASPP} \times 1 \times M_0)$, where M^{ASPP} indicates the feature number. The ASPP module applies a set of parallel Atrous convolutions with varying dilation rates $d_i, i \in [1, \dots, N_{ASPP}]$ (see Fig.5.4) and a global average pooling (GAP). Different dilation rates filters extract features at different scales, concatenated with the GAP to include the global context information. The ASPP module consists of N_{ASPP} parallel Atrous convolution blocks with different dilatation rates $d_i, i \in [1, \dots, N_{ASPP}]$ and a GAP (see Fig.5.5). Each Atrous block contains a dilated convolution layer of rate d_i , a batch normalization layer, and a ReLU. The outputs of

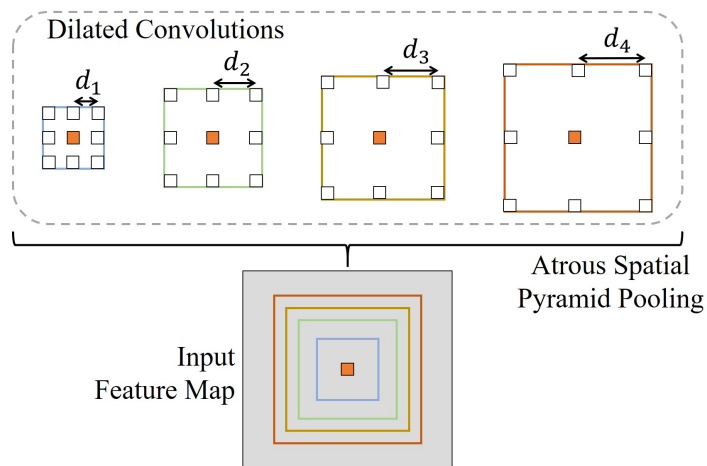


Figure 5.4: Representation of the dilated convolution filters with different dilation rate coefficients $[d_1, \dots, d_4]$ applied to the orange pixel. Atrous Spatial Pyramid Pooling module applies parallel dilated convolutions to the input map to extract multi-scale features. The different reception fields of the filters are shown in different color.

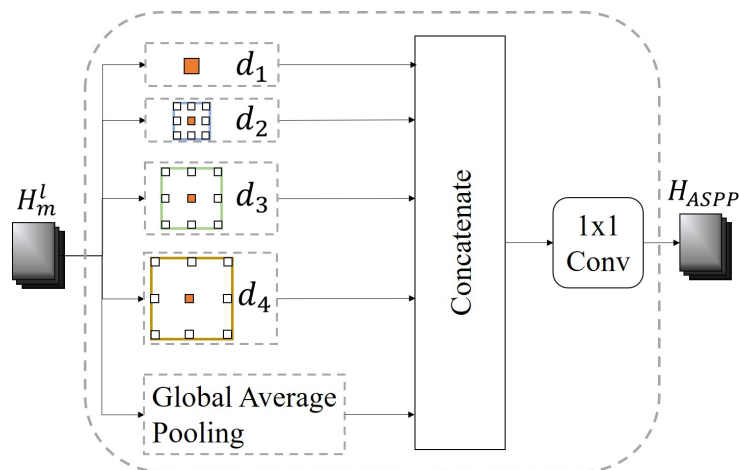


Figure 5.5: Structure of the ASPP module. The output of the encoder H_m^l is processed by parallel dilated convolutions with different dilation rate coefficients $[d_1, \dots, d_4]$ and a global average pooling. All the convolutions are followed by a batch normalization layer and a ReLU. The outputs of the branches are concatenated and processed by a (1×1) convolution to obtain the output of the ASPP module H_{ASPP} .

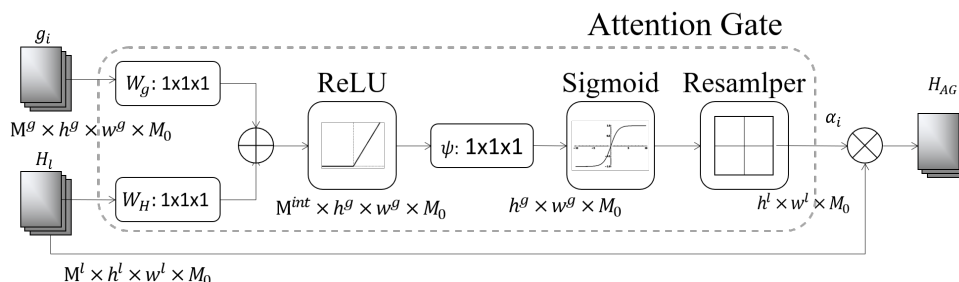


Figure 5.6: Structure of the Attention Gate module to filter the signal from the skip connection H_l . The gate signal g_i highlights the salient spatial regions of the feature set H_l and determines the attention coefficients α_i . The attention coefficients are then element-wise multiplied with the low-level feature set to obtain the output of the AG module H_{AG} .

the Atrous blocks and the GAP are concatenated together and followed by a (1×1) convolution operation.

Decoder and the Attention Gates (AG). The decoder consists of L upsampling blocks having embedded the attention mechanism based on [191] to suppress the activation of irrelevant radargram regions by filtering the features from the skip connections. The attention gate takes in input the features H_l from the skip connections and the features $g_i, i = l - 1$ from the next lowest layer ($l - 1$). The assumption is that low-level features from the encoder are redundant and poorly represent the data. Features g_i from the decoder better represent the data as they are at a higher level extracted in the decoder. Hence, features g_i can be used to filter the features H_l from the skip connections and activate the most informative ones [191]. To highlight radargram salient regions, the AG computes the attention coefficients $\alpha_t \in [0, 1]$ [191]. For each pixel, the AG module extracts a scalar attention value considering the feature vectors g_i . In multi-class semantic segmentation tasks, the AG extracts multi-dimensional attention coefficients [201].

As Fig.5.6 shows, an AG takes as input the set of lower-level feature H_r^l from the skip connections and the gating vector $g_i \in \mathbb{R}^{M_g}$, where M_g is the number of features of each pixel i . For each level l , the gating vector is composed of the features extracted from the next lowest layer (i.e., $l - 1$). High-level features better represent the input data than features from the encoder, and thus, they contain the spatial information that indicates focus regions. After the gating signal is upsampled at the same dimension of the lower-level feature map, these are summed to obtain the gating coefficients (additive attention) (see Fig.5.6). The gating coefficients are processed by a ReLU followed by a sigmoid activation function. The sigmoid output signal is resampled using the trilinear interpolation, generating a grid signal conditioned to the data spatial information. Each pixel i of the grid is the attention coefficient α_i^l of the attention gate module l . Finally,

the output of the l -th attention gate H_{AG}^l is the element-wise multiplication between the features map H_r^l and the attention coefficient, i.e., $H_{AG}^l = H_r^l \alpha_i^l$. For the first AG, the gating signal consists of the output features of the ASPP module H_{ASPP} (see Fig.5.3). For the other l AGs, the gating signal is the output of the next lowest layer (i.e., $l - 1$). The output of the l -th AG H_{AG}^l is concatenated with the upsampled output version of $g_i, i = l - 1$. For the first decoder block, the AG output is concatenated with the upsampled output of the ASPP H_{ASPP} .

Decoder blocks $l \in [1, \dots, L]$ consist of a (k_x, k_y) deconvolutional layer, a batch normalization layer, followed by a ReLU, all applied twice (see Fig.5.3). Each block takes as input the skip connection signal filtered by the attention gate and the output upsampled features from the next lowest block. Each block l gives in output a set of M^l features H_d^l of shape $(M^l \times x_p \times y_p \times M_0)$. In the case of the last block, the output H_d^L is further processed twice with a (k_x, k_y) deconvolutional layer, a batch normalization layer, followed by a ReLU. This generates the output of the network H_{out} that has a shape $(M^{out} \times x_p \times y_p \times M_0)$. The value of M^{out} depends on the task of interest, as described in the following paragraphs.

5.3.2 Unsupervised pre-training of the network

All the weights W of the network can be learned by training the network according to the optimization of a loss function. Using randomized parameters is less efficient than using an unsupervised pre-training phase [202]. Hence, this step aims at initializing the network parameters and train the network to learn the feature response to radar data. To this end, we aim at training the network to learn how to reconstruct a given input radargram. This is a regression task as the network should reconstruct the values of each pixel of the input radargram at the output. Therefore, the number of features expected in the network output is fixed to $M^{out} = 1$. For training, we use a regression loss. Here, we used the Mean Square Error (MSE), defined in (5.4), but any regression loss from the literature can be used.

$$MSE = \frac{1}{N_S N_T} \sum_{a=1}^{N_T} \sum_{r=1}^{N_S} \left[\mathbf{R}_{\text{pred}}(\mathbf{a}, \mathbf{r}) - \mathbf{R}(\mathbf{a}, \mathbf{r}) \right]^2 \quad (5.4)$$

The MSE estimates the average squared difference between the predicted values $\mathbf{R}_{\text{pred}}(\mathbf{a}, \mathbf{r})$ and the actual value $\mathbf{R}(\mathbf{a}, \mathbf{r})$ of the radargram. This metric gives an estimation of the goodness of the reconstruction.

5.3.3 Generation of the segmentation map

After initializing the network parameters, we train in a supervised manner the network to segment the radargram into ω_1 englacial layers, ω_2 basal ice, ω_3 bedrock, and ω_4 thermal

noise, EFZ, and signal perturbations (shadows). The last deconvolutional layer of the network extracts $M^{out} = N_c$ features, where N_c is equal to the number of classes of the segmentation task. This work considers four classes as we investigate inland icy radargram and characterize the basal layer. However, the network is flexible enough to analyze more classes [198] after the fine-tuning.

Loss Function. For the supervised segmentation, we use the cross-entropy loss function between the radargram and reference labels. The cross-entropy loss helps the network during the training phase to have a features response so that the network assigns the labels in a semantic meaningful way. For each pixel (a, r) , the cross entropy loss function is applied to predicted label $\omega_c^{a,r}$ and the reference label $\omega_{rl}^{a,r}$ for each pixel (a, r) as follows:

$$\ell_t(a, r) = - \sum_{c=1}^{N_c} \omega_{rl}^{a,r} \log(\omega_c^{a,r}) \quad (5.5)$$

where N_c is number of classes of the segmentation task. The loss term \mathcal{L}_t for all the pixels of the radargram is computed as follows

$$\mathcal{L}_t = \frac{1}{N_S N_T} \sum_{a=1}^{N_T} \sum_{r=1}^{N_S} \ell_t(a, r). \quad (5.6)$$

After processing the radargram \mathbf{R} , we obtain a matrix of M^{out} deep features $H_{out}(a, r, k)$, where $k \in [1, \dots, M_{out}]$.

Label Assignment. Analyzing a radargram \mathbf{R} with such a network, semantically similar pixels produce high values in the same deep features. Hence, for each pixel (a, r) , the label ω_c is defined by choosing the output feature with the maximum value [203]:

$$\omega_c^{a,r} = \operatorname{argmax}_{k \in [1, \dots, M_{out}]} \{H_{out}(a, r, k)\}. \quad (5.7)$$

The segmentation map \mathbf{M} is defined as:

$$\mathbf{M} = \{m(a, r) | a \in [1, \dots, N_T], r \in [1, \dots, N_S]\}. \quad (5.8)$$

where the labels are assigned according to (5.7).

Label Refinement. In semantic segmentation, pixels are expected to be spatially correlated. Even if this property is partially ensured by the network convolutional nature, we refine the segmentation map with a morphological filter [204]. We performed a morphological opening (erosion followed by dilation) and a closing (a dilation followed by erosion) of the segmentation map. The structuring element defines the neighborhood used to process each pixel. Opening removes small groups of isolated pixels labeled differently than the surrounding, while closing removes small holes. This helps in preserving spatial consistency.

Table 5.1: Parameter of the radar sounder instrument MCoRDS3 [29] and the geometrical resolutions of the radargrams.

Parameters	Value
Central frequency f_c	195 MHz
Wavelength λ	1.54 m
Bandwidth BW	30 Mhz
Sampling Frequency	45 MHz
Transmitted Power P_{tr}	1050 W
Aircraft Amplitude h	2-4 km
Range Resolution in Ice	4.3 m
Azimuth Resolution	25 m

Table 5.2: List of the campaigns and the radargram IDs for each dataset, and the number of traces N_T for each campaign.

	Campaign	Radargram ID	N_T
Dataset 1	2017.0403.01	6–16	35551
North Greenland	2017.0413.01	36–56	70026
Dataset 2	2014.0403.01	12–13, 21–24	19992
West Antarctica	2018.1104.01	4–5	6668
	2018.1020.01	4, 8–10, 15–18, 21–22	30009

5.4 Description of the dataset and experimental results

This Section describes the datasets used to assess the effectiveness of the proposed method and presents the experimental results. We consider two datasets acquired on the polar areas of the Earth by the MCoRDS3 radar sounder [29] mounted on an aircraft. The first dataset consists of radargrams acquired in the North of Greenland. The second dataset consists of radargrams acquired in Antarctica. Figure 5.7 shows the ground track of the radargrams selected for each dataset. The results are compared with state-of-the-art methods for the segmentation of inland icy radargrams, i.e., [45, 41, 196]. As reference data, samples representing the four classes were manually picked from the radargrams. These regions are selected in a way that there is no ambiguity regarding the target class. To this end, we perform the selection based on examples of radargrams visually inspected and available in the literature [37, 38].

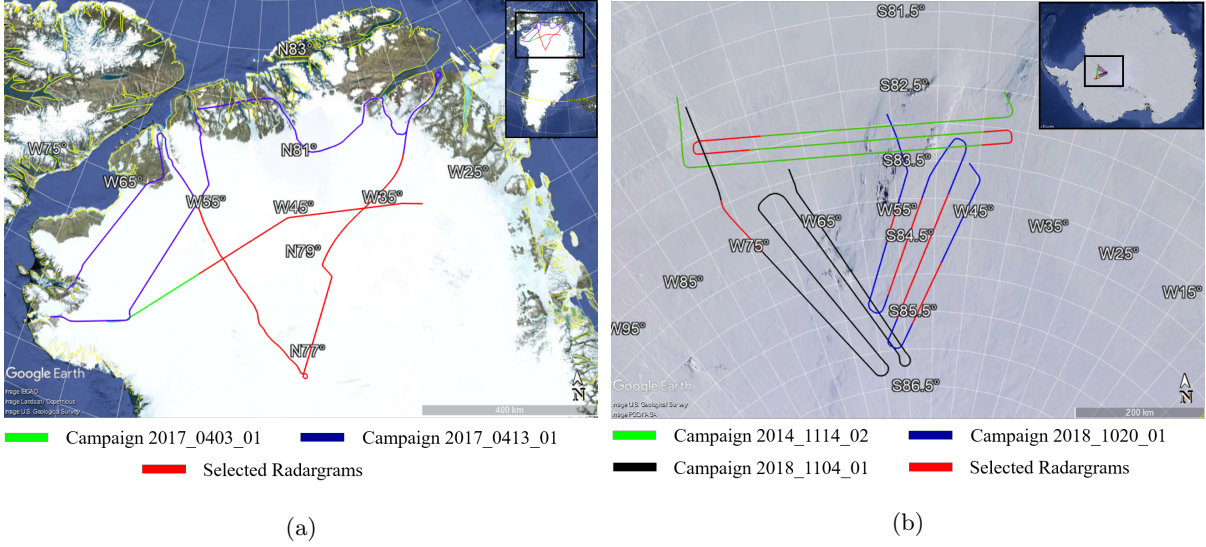


Figure 5.7: Ground tracks of the campaigns used for (a) dataset 1 and (b) dataset 2. Dataset 1 consists of radargrams from campaign 20170403_01 (in blue in (a)) and campaign 20170413_01 (in green in (a)) in North Greenland. Dataset 2 consists of radargrams from campaign 20141114_02 (in green in (b)), campaign 20181020_01 (in blue in (b)), and campaign 20181104_01 (in black in (b)) in West Antarctica. The transect of the radargrams used in our experiments of each dataset is highlighted in red.

Table 5.3: Parameters of the proposed method and the neural network.

Parameter	Description	Value
(x_p, y_p)	Patch size in the range and the azimuth	(32, 1280)
M_0	Number of channels of the input data	1
K	Number of patches before the data augmentation	
N_L	Number of downsampling and upsampling blocks	4
$M_l, l = [1, \dots, 4]$	Features extracted by the l -th block of the encoder and the decoder	[64, 128, 256, 512]
(k_x, k_y)	Convolutional kernel size in the range and azimuth	(3, 3)
(m_x^l, m_y^l)	Maxpooling and upsampling size in range and azimuth	(2, 2)
$d_i, i = [1, \dots, 4]$	Dilate rate parameters of the ASPP	[1, 6, 12, 18]
ℓ_r	Learning rate	0.0001
\mathcal{E}	Number of epochs for the training	200

5.4.1 Pre-processing of the datasets

The radar sounder data [29] are distributed by the Center for Remote Sensing of Ice Sheets (CReSIS) for NASA Operation IceBridge. The radar data are already range compressed, azimuth focused via synthetic aperture radar (SAR) techniques, and the clutter is partially compensated. To prepare the radar data, we concatenated adjacent acquired radargrams with attention to remove overlapping regions. Moreover, we corrected the data for the fluctuations due to the movements of the platform. While acquiring the data, an aircraft has three undesired movements, i.e., pitch, roll, and yaw, which influence and degrade the quality of the radargram signal. To mitigate the signal degradation, we normalized the power of the radargram concerning the surface power for each column. This helps in mitigating the fading of the power due to the rolling movement of the aircraft on the curves. Considering the preprocessing, the vector of the range coordinate of the surface $s(a)$ was identified as the maximum power for each azimuth column a . Hence, the power of the surface $P_s(a)$ of each azimuth trace was defined as $P_s(a) = \mathbf{R}(\mathbf{a}, s(a))$. The region above the surface is the free space and was removed from the study of the subsurface by masking it. Radar data are affected by speckle, which can be approximated as multiplicative noise. Hence, by applying a log-transformation to the power radargram, the noise can be approximated as additive, reducing the complexity of handling the data and enhancing the spatial information:

$$\mathbf{R}_{\text{dB}}(\mathbf{a}, \mathbf{r}) = 10 \log_{10}(\mathbf{R}(\mathbf{a}, \mathbf{r})). \quad (5.9)$$

5.4.2 Setup of the neural network

Adjacent radargrams are concatenated and pre-processed with the steps described above. Each radargram is divided into patches normalized by removing the mean of the dataset and dividing by the standard deviation. Such a dataset \mathcal{J} is divided into training \mathcal{J}_{tr} and test \mathcal{J}_{te} patches so that 90% of the patches are used for the training and the remaining 10% for the test phase. Table 5.3 shows the parameters of the network. We used 4 downsampling blocks in the encoder and four upsampling blocks in the decoder. The convolutional kernels are of size $(k_x = 3, k_y = 3)$ and the upsampling and downsampling are with $m_x^l = 2, m_y^l = 2$. The ASPP consists of four dilated convolutions with the dilated rate parameters equal to $[d_1 = 1, d_2 = 6, d_3 = 12, d_4 = 18]$. We set the number of epochs equal to $\mathcal{E} = 200$ and the batch size equal to 16. For the optimization, we used Adam optimizer as it showed to have good results in the literature [205]. The learning rate is set to $\ell_r = 0.0001$ after running several experiments varying its values in $\ell_r = [0.1, \dots, 10^{-6}]$. We train the network using standard data augmentation techniques, i.e., affine transformations, horizontal flips, and random crops. The affine transformations, including rotation, shear, scale, and translation, are designed to preserve the geometrical

and structural properties of the subsurface geological structures. For example, rotation and shear are constrained so that the steepness of the transformed englacial layer and the basal interface are realistic.

5.4.3 Evaluation criteria

To evaluate the performance of the proposed method, we considered two sets of metrics: one for the unsupervised reconstruction of the radargrams and the other for the supervised segmentation task. For the unsupervised reconstruction task, we consider the mean square error between the input and the output radargrams, as defined in (5.4). For the semantic segmentation task, we consider how well the pixels of each class are detected. In the inference phase, N_{tot} pixels are analyzed with the proposed semantic segmentation method. For each pixel, the technique predicts a label that can be compared with the reference data. TP^c is defined as the number of true-positive pixels, i.e., the pixels correctly classified for the c -th class, and TN^c the true negative, i.e., the pixels correctly classified for the other $N_C - 1$ classes. FN^c is defined as the false negative, i.e., the number of pixels belonging to the class c but wrongly labeled and FP^c as the false positive, i.e., the number of pixels not belonging to the class c labeled with ω_c . The sensitivity indicates the probability that the pixels is classified as the c -th class given that it actually belongs to that class:

$$\text{Sensitivity} = \frac{TP^c}{TP^c + FN^c}, c \in [1, \dots, N_C]. \quad (5.10)$$

The specificity indicates the probability that a pixels is not labeled as ω_c , given that it does not belong to that class:

$$\text{Specificity} = \frac{TN^c}{TN^c + FP^c}, c \in [1, \dots, N_C]. \quad (5.11)$$

Finally, the overall accuracy (OA) is defined as the number of correctly classified pixels TP over the number of processed pixels, i.e., $OA = TP/N_{tot}$.

5.4.4 Dataset 1: North Greenland

Dataset 1 consists of 30 radargrams acquired by airborne campaigns with MCoRDS [29] radar sounder (for the radar parameters see Table 5.1) in the north of Greenland in 2017. We consider two campaigns imaging a region with the basal ice layer and basal units [178]. Figure 5.7.a shows the ground track of the campaigns 20170403_01 and 20170413_01 in blue and green, respectively. The radargrams selected for dataset 1 are highlighted in red, and their IDs are listed in Table 5.2. We choose radargrams 6 to 16 from campaign 20170403_01 and radargrams 36 to 56 from campaign 20170413_01. Table 5.1 shows the parameters of the radar MCoRDS3 [29] and also the radargram characteristics, e.g., resolution in the range and azimuth directions.

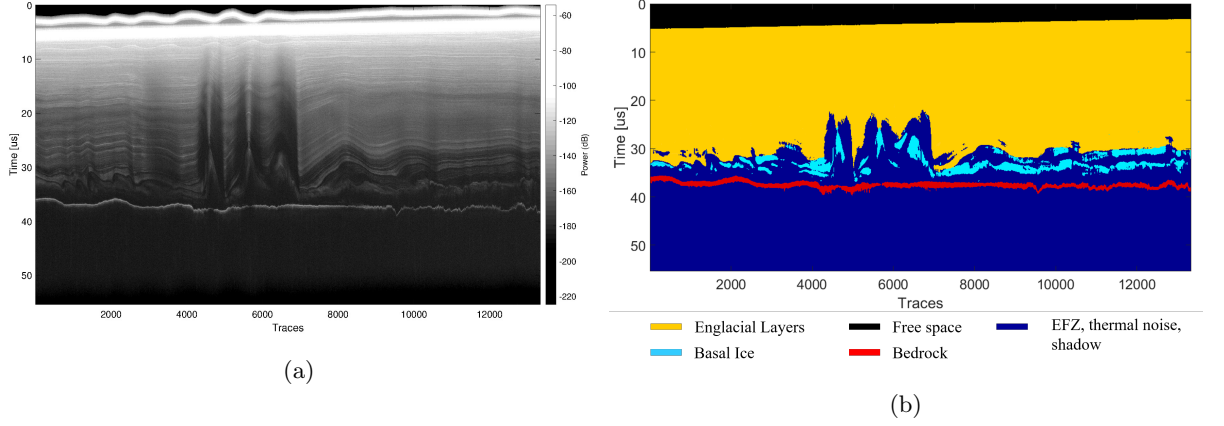


Figure 5.8: Example of the method applied to part of dataset 1 (radargrams 43 to 49) of the campaign 20170413_01: (a) input radargram, (b) segmented radargram. Englacial layers are in yellow, the basal ice is in light blue, the bedrock is in red, and the shadow, EFZ, and thermal noise in dark blue.

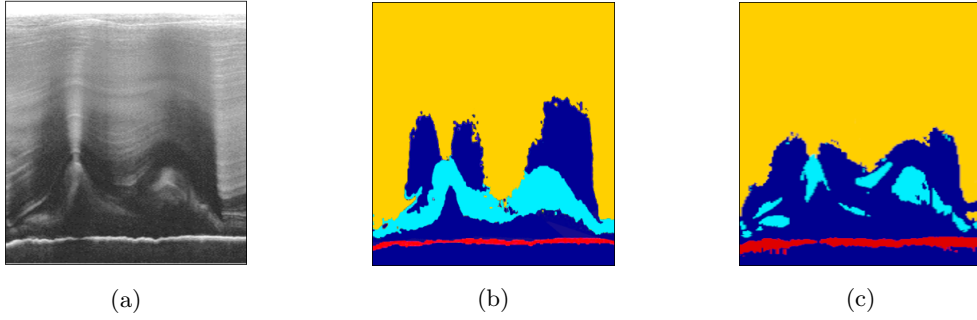


Figure 5.9: Part of radargram 45 of the campaign 20170413_01: (a) input radargram, (b) segmented radargram with [41] considering the shadow class, and (c) segmented radargram with the proposed method. Englacial layers are in yellow, the basal ice is in light blue, the bedrock is in red, and the shadow, EFZ, and thermal noise in dark blue.

The radargrams are preprocessed to generate two radargrams with traces $N_T^1 = 35551$ and $N_T^2 = 70026$, respectively. The radargrams are divided into patches of size $x_p = 32$ and $y_p = 1280$ in the range and azimuth direction, respectively. y_p is set so that the neural network has a complete view of the vertical distribution of the classes. Dataset 1 consists of $K = 3299$ patches before data augmentation. The patches are divided so that $K_{tr} = 2969$ patches for the training and $K_{test} = 330$ for the inference. The unsupervised training to extract relevant features is conducted with 200 epochs. At the end of unsupervised training, the reconstruction error is equal to $MSE = 0.0134$. The supervised training takes 200 epochs. The labels are assigned according to (5.7) and refined by applying a morphological disk-shaped filter of radius 3, see Section 5.3.3.

Considering the large size of the dataset, we show radargrams 43 to 46 of campaign

Table 5.4: Segmentation performance of the proposed method and state-of-the-art methods applied to the dataset 1, where ω_1 is englacial layers, ω_2 basal ice, ω_3 bedrock, ω_4 thermal noise and echo-free zone and signal perturbations, and ω_4^R that is the reduced version of ω_4 as it consider the thermal noise and the EFZ as in [45, 41].

	Metric	Overall	ω_1	ω_2	ω_3	ω_4	ω_4^R
Proposed Method	Accuracy	0.9824	0.9865	0.9804	0.9796	0.9832	0.9871
	Sensitivity	0.9857	0.9934	0.9807	0.9801	0.9887	0.9856
	Specificity	0.9852	0.9950	0.9763	0.9793	0.9902	0.9899
SoA Method	Accuracy [45]	0.9821	0.9868	–	0.9751	–	0.9845
	Accuracy [41]	0.9817	0.9898	0.9723	0.9832	–	0.9815
Extended SoA	Accuracy [41]	0.9524	0.9942	0.9821	0.9986	0.8347	0.9872

20170413_01 of dataset 1 in Fig. 5.8.a and the related segmentation map in Fig. 5.8.b. Figure 5.9 shows a detail of dataset 1 (part of radargram 20170413_01-45) that contains two basal units. From qualitative analysis, basal ice and shadow classes are finer segmented with the proposed method than with that in [41], which is based on handcrafted features processed by the SVM classifier. This result is expected as the handcrafted features are not designed for detecting shadows. Table 5.4 shows the performance of the proposed method for dataset 1. The accuracy for the basal ice is 98.04 %, while that for the signal perturbation is 98.32 %. The accuracy of the other classes (i.e., bedrock and ice layers) are comparable or slightly lower than those of the state-of-the-art methods in [45, 41] (see Table 5.4). The proposed method achieves an average sensitivity of 0.9857 and an average specificity of 0.9852. The sensitivity of the basal ice is equal to 0.9807, and the sensitivity of the EFZ, thermal noise, and shadow is equal to 0.9887. The specificity of the basal ice is equal to 0.9763, and the specificity of the EFZ, thermal noise, and shadow is equal to 0.9902. The last row of Table 5.4 reports the results of the analysis of dataset 1 with the method in [41] based on handcrafted features and the SVM classifier for segmenting basal ice and shadows. The accuracy is high for the classes for which the features are designed, i.e., basal ice, ice layer, bedrock. However, as expected, it is low for the class not considered in the design, i.e., shadow (see the accuracy for ω_4).

5.4.5 Dataset 2: West Antarctica

Dataset 2 consists of 18 radargrams acquired in several campaigns by the MCoRDS radar sounder in the west of Antarctica in 2014 and 2017. We consider three campaigns imaging a region where the basal ice layer is visible [184, 37]. Figure 5.7.b shows the ground track of the campaigns 20141114_02, 20181020_01, and 20181101_01 in green, blue, and

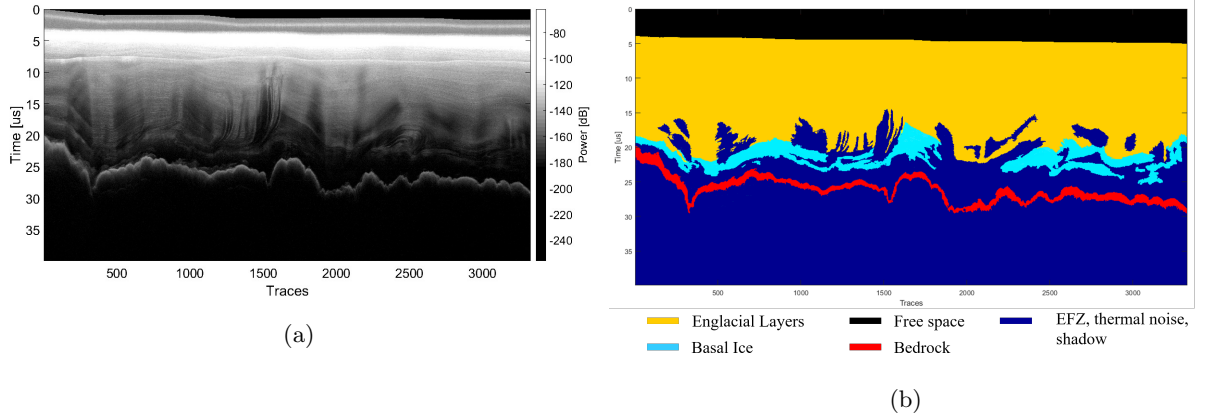


Figure 5.10: Example of the method applied to part of dataset 2 (radargram 23) of the campaign 20141114.02: (a) input radargram, (b) segmented radargram. Englacial layers are in yellow, the basal ice is in light blue, the bedrock is in red, and the shadow, EFZ, and thermal noise in dark blue.

black, respectively. The tracks of selected radargrams are in red, and their IDs are listed in Table 5.2. We choose radargrams 12, 13, and 21 to 24 from campaign 20141114.02, radargrams 4 and 5 from campaign 20181104.01, and radargrams 4, 8 to 10, 15 to 18, and 21 to 22 from campaign 20181020.01. Table 5.1 shows the parameters of the radar MCoRDS3 [29] and the radargram characteristics.

The radargrams are preprocessed to generate three radargrams with traces $N_T^1 = 19992$, $N_T^2 = 30009$, and $N_T^3 = 6668$, respectively. The radargrams are divided into patches of size $x_p = 32$ and $y_p = 1280$ to have a dataset of $K = 1770$ patches. The patches are divided into $K_{tr} = 1593$ patches for the training and $K_{test} = 177$ for the inference. The unsupervised training to extract relevant features is conducted with 200 epochs. At the end of unsupervised training after 200 epochs, the reconstruction error is equal to $MSE = 0.00125$. The supervised training is performed with 200 epochs. The labels are assigned according to (5.7) and then refined by applying disk-shaped morphological filtering of radius 3.

Considering the large size of the dataset, we show radargram 23 of campaign 20141114.02 in Fig. 5.10.a and the related segmentation map in Fig. 5.10.b. Table 5.5 report the performance of the proposed method for dataset 2. The accuracy for the basal ice is 0.9832, while that for the signal perturbation is 0.9877. The accuracy of the other classes (i.e., bedrock and ice layers) are comparable with the state of the art in [45, 41] (see Table 5.5). The proposed method achieves an average sensitivity of 0.9795 and an average specificity equal to 0.9796. The sensitivity of the basal ice is equal to 0.9797, and the sensitivity of the EFZ, thermal noise, and shadow is equal to 0.9845. The specificity of the basal ice is equal to 0.9754, and the specificity of the EFZ, thermal noise, and shadow is equal to

Table 5.5: Segmentation performance of the proposed method and state-of-the-art methods applied to the dataset 2, where ω_1 is englacial layers, ω_2 basal ice, ω_3 bedrock, ω_4 thermal noise and echo-free zone and signal perturbations, and ω_4^R that is the reduced version of ω_4 as it consider the thermal noise and the EFZ as in [45, 41].

	Metric	Overall	ω_1	ω_2	ω_3	ω_4	ω_4^R
Proposed Method	Accuracy	0.9848	0.9890	0.9832	0.9791	0.9877	0.9833
	Sensitivity	0.9795	0.9762	0.9797	0.9774	0.9845	0.9802
	Specificity	0.9796	0.9814	0.9754	0.9793	0.9821	0.9812
SoA Methods	Accuracy [45]	0.9837	0.9966	–	0.9751	–	0.9793
	Accuracy [41]	0.9846	0.9858	0.9891	0.9774	–	0.9859
Extended SoA	Accuracy [41]	0.9566	0.9868	0.9771	0.9885	0.8739	0.9846

0.9821. The accuracy of the handcrafted features and the SVM classifier is comparable with the proposed method for the classes for which the features are designed, including the layers (ω_1) and the EFZ and thermal noise (ω_4^R) (see Table 5.5). As for dataset 1, class ω_3 has a slightly lower accuracy for the proposed method than for the literature method in [41] as it is the one with the lowest number of samples in the radargram. For the classes not considered in the feature extraction design step (such as the shadow), the proposed method is performing better: the accuracy of class ω_4 (signal perturbation, thermal noise, and EFZ) for the proposed method is equal to 98.77 % and that for the SVM method in [41] is 87.39 %. Considering that the accuracy for the thermal noise and EFZ (class ω_4^R) is 98.46 % with the SVM method in [41], the handcrafted features show their limit in modeling target not considered in the design step. On the contrary, the neural network can automatically extract semantically meaningful features in the learning phase.

5.5 Conclusions and future works

We proposed a fully automatic method for detecting the basal layer and the basal units in airborne radargrams acquired inland. To this end, the technique aims at segmenting the radargrams into four classes: englacial layering, basal ice, bedrock and EFZ, and thermal noise and shadows (i.e., signal perturbation). We proposed to use a U-Net with embedded attention gates and the ASPP module to extract relevant features for segmenting radargrams. The attention gates filter irrelevant features to focus the network on critical areas of the radargrams. The ASPP module extracts features with different receptive fields, improving the identification of targets of several dimensions and scales, such as the basal ice, the ice layers, and the bedrock. The network weights are initialized with unsupervised training for better handling the properties of the radar signal. The

attention U-Net is trained to extract features for labeling. Finally, morphological filters refined the predicted labels.

The method is tested on two datasets of radargrams acquired in Greenland and Antarctica, where the basal layer and basal units are visible. We applied the method to vertical strides of the radargram (patches) to capture the global context and the vertical spatial distribution of the classes. The results prove that the method can assign semantically accurate labels. The proposed method showed to identify the radargram areas basal ice and signal perturbations with high accuracy. The other classes, i.e., the englacial layers, the bedrock, and the EFZ and the thermal noise, are segmented with high accuracy that is comparable to the literature methods but without requiring the feature extraction design procedure. As the technique does not use handcrafted features, it is adaptable to analyze data acquired in different scenarios, such as coastal areas characterized by floating ice, marine and meteoric ice, and the grounding areas.

In future works, we plan to test the proposed method on other icy areas to detect different targets, such as ice shelves and crevasses in coastal regions, which have completely different geometric and radiometric properties than those in the inland regions. Moreover, we plan to investigate other approaches for semi-supervised training to improve the network performance while reducing the number of labeled samples required for supervised fine-tuning.

Chapter 6

An unsupervised deep learning method for subsurface target detection in radar sounder data

Radar sounder data are widely used for investigating geological structures and processes in the subsurface. Automatic techniques for processing radargrams are mostly based on handcrafted features analyzed by a supervised classifier requiring labeled data to provide reliable results. Labeled datasets are hard to extract from radargrams, considering the difficulties in modeling the subsurface composition. Thereby, unsupervised methods are needed for extracting information from radargrams. The literature methods for detecting subsurface targets are based on statistical analyses and handcrafted features related to the target-specific characteristics. However, recent techniques based on deep learning showed high generalization capability in other applications, as the feature extraction is automatic. Hence, there is a need for developing novel methods to extract information from radargrams in an unsupervised manner employing deep learning. Here, we propose an automatic and unsupervised technique based on deep learning for extracting information on the subsurface geological targets. The proposed method aims at segmenting the radargram to detect targets of interest. The technique is built upon three steps: i) generating a coarse segmentation map based on the radargram statistical properties, ii) refining the coarse map with deep learning to detect target reflections, and iii) analyzing the deep features to identify buried targets. We tested the proposed method on MARSIS radar data acquired near the South Pole of Mars. The experimental results prove the effectiveness of the proposed unsupervised method in detecting subsurface features.

6.1 Introduction

In the literature, few automatic methods have been proposed for the automatic extraction of information from radargrams. They are mostly based on a supervised approach, considering handcrafted features designed for specific classes and a classifier, such as Support Vector Machines (SVM), [41, 45, 46]. Despite the promising results on the investigated classes, these methods are hardly adaptable to analyze other targets. This is because the features are designed by considering the geometric statistical radiometric properties of the targets. Thereby, new classes require the design of novel features to allow for capturing the target characteristics. Moreover, supervised approaches require reliably labeled datasets, which can hardly be available in radar sounder. Hence, unsupervised algorithms are needed, considering the difficulties in retrieving reliable RS-labeled datasets. In the literature, few automatic methods analyze radargrams in an unsupervised way for different applications, such as extracting linear reflections [42, 40] and subsurface target reflections based on the analysis of the statistical properties of the radargrams [44, 206], and detecting specific targets as lava tubes [158]. However, more automatic methods are needed for further exploiting radar sounders. Recently, deep learning has shown to have high performance in several applications. Also, for radar sounder data, few methods based on deep learning have been proposed considering a supervised approach for segmenting inland radargrams [196], detecting internal layers [207], and resolving the bed topography of Antarctica [208]. Despite their intrinsic effectiveness, deep learning-based approaches require a large amount of labeled data for the network training, which is hard to find for the RS data. Therefore, novel and unsupervised methods are required for analyzing radargrams and extracting information on the subsurface.

This Chapter proposes a novel and unsupervised method based on deep learning for extracting information from RS data. The technique is fully unsupervised and does not require any initial labeled data. The proposed approach aims at detecting subsurface reflections in radargrams by analyzing the related deep features to identify buried targets. The proposed method consists of three main steps: i) generation of a coarse segmentation map based on the statistical properties of the targets, ii) refinement of the coarse map with deep learning to detect target reflections, and iii) analysis of the deep features of the target reflections to identify buried targets. We tested the proposed method on a dataset of MARSIS radargrams acquired near the South Pole of Mars to identify anomalies in the basal return that astrophysicists identified as subglacial lakes [26].

The Chapter is structured as follows: Section 6.2 proposes the deep learning method to segment radargrams and describes the neural network. Section 6.3 describes the datasets, the network setup, and the experiment to prove the proposed method's effectiveness. Finally, Section 6.4 provides concluding remarks and insights for future works.

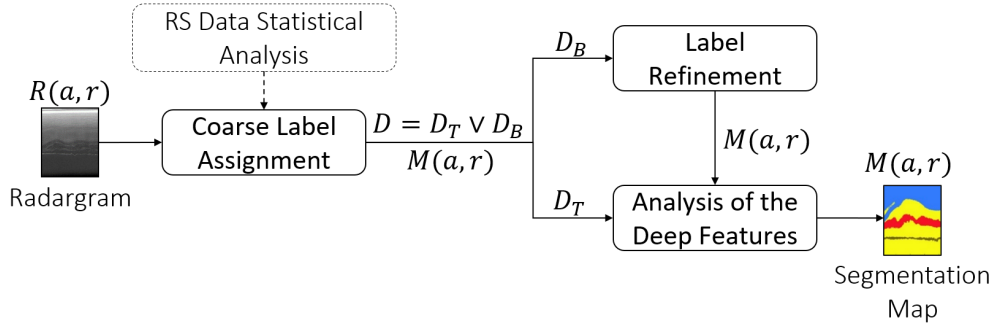


Figure 6.1: Block scheme of the proposed deep approach for the unsupervised segmentation of radargrams

6.2 Proposed deep learning method

Let us consider a radargram as a 2D matrix of N_T traces and N_S samples defined as $\mathbf{R} = \{R(a, r) | a \in [1, \dots, N_T], r \in [1, \dots, N_S]\}$, where R is the power of the reflections in the radargrams, and (a, r) the azimuth and the range coordinates, respectively. Each radar acquisition corresponds to a trace of the radargram. Thus, adjacent pixels capture the same geologic targets in a given area of the subsurface. This Chapter proposes a novel unsupervised method for detecting subsurface targets in radargrams. The technique is fully unsupervised and does not require any initial labeled data.

We model radargrams with two main semantic classes: the background and the target. The background includes the no-signal areas and the thermal noise above the surface and below the basal return. The targets include the reflections from different dielectric interfaces in the subsurface, such as ice layers and basal return. Thus, the target class can be further divided into other subclasses. This hierarchical division is exploited by the proposed method to segments the radargram. At first, we discriminate between the background and target to extract reflections in the radargrams. Then, analyzing the deep features, the target (i.e., radargram reflections) is segmented into subclasses $\omega_c, c \in [1, \dots, N_C]$. The method consists of three main steps (see the flow chart in Fig. 6.1):

1. Generation of a coarse segmentation map $M(a, r)$ by exploiting the statistical properties of RS data;
2. Refinement of the coarse segmentation map $M(a, r)$ to detect target reflections with deep learning;
3. Hierarchical updating of $M(a, r)$ by analyzing deep features of the target reflections.

The rest of the Section describes in detail the steps of the proposed method.

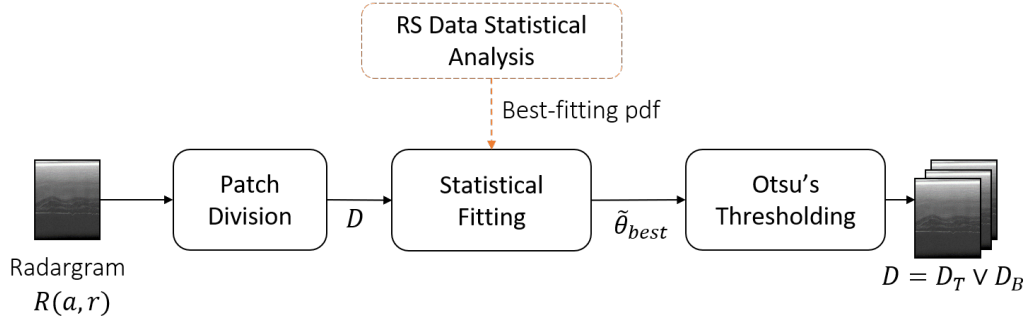


Figure 6.2: Block scheme for the initial candidate label assignment.

6.2.1 Candidate label assignment

Considering the radargram statistical properties, the first step generates a candidate label for all the pixels that will be refined using a deep network. Fig. 6.2 shows the block diagram for this step of the proposed method. Here, we plan to use a convolutional neural network (CNN) architecture, as this model showed good performance in several applications [189, 209]. As CNNs require patches in the input, we divide the input radargrams into patches of dimensions (w_p, h_p) to compose the dataset \mathcal{D} . The patch dimensions (w_p, h_p) are defined so that the patch is large enough to be representative of the data and small enough not to include multiple classes. \mathcal{D} is further divided into two subsets: \mathcal{D}_B and \mathcal{D}_T so that $\mathcal{D} = \mathcal{D}_B \vee \mathcal{D}_T$. \mathcal{D}_B contains the patches only imaging the background, and thus, the candidate label of the pixels in these patches is that of the background ω_B . \mathcal{D}_T contains patches mostly capturing targets, and thus, the candidate label of the pixels in these patches is that of the target ω_T . Note that patches in \mathcal{D}_B contain only background pixels, while patches in \mathcal{D}_T image background and target pixels generated by different geological interfaces. The background patches are statistically more homogeneous than the target patches as they capture just one class. The target patches are less homogeneous as they image the background and reflections from different targets.

To separate target and background patches, we exploited the statistical properties of the two classes. Considering the method in [44], we fitted several distributions to the amplitude radargram of the targets to find the best fitting pdf. Considering [44, 45], here we fitted the Rayleigh probability density function (pdf) $p_R(A)$, the Nakagami pdf $p_N(A)$, Gamma pdf $p_\Gamma(A)$, K pdf $p_K(A)$, and the Weibull pdf $p_W(A)$. For a detailed analysis of the fitting procedure, we refer to Appendix 6.5. The evaluation of the distribution is done considering the Means Square Error (MSE) and the Kullback-Leibler divergence (KL) between the normalized histogram of the data and that obtained by fitting the

distribution. The KL divergence between two distributions p_1 and p_2 is defined as [210]

$$KL(p_1, p_2) = \sum_{A_i} p_1(A_i) \frac{p_1(A_i)}{p_2(A_i)}. \quad (6.1)$$

The best-fitting distribution p_{best} is the one minimizing the MSE and the KL divergence in (6.1). The parameter defining p_{best} depends on the best fitting distribution. Thus, if the best distribution is the K pdf, $p_{best} = p_K$ and the parameters are $\theta_{best} = (\mu_z, \beta_K)$. If the best distribution is the Gamma pdf, $p_{best} = p_\Gamma$ and the best parameters are $\theta_{best} = (\alpha_\Gamma, \beta_\Gamma)$, and so on for the other distributions. The patches in \mathcal{D} are fitted with the p_{best} distribution to estimate the parameter $\tilde{\theta}_{best}$. Hence, a vector $\tilde{\Theta}$ is generated that contains for each patch P_p the estimated parameters $\tilde{\theta}_p$. The parameter $\tilde{\theta}_p$ is representative of the class imaged by the p -th patch. The histogram of $\tilde{\Theta}$ shows a bimodal distribution: one for the target patches and the other for the background patches. The two modes can be separated with a threshold T_θ . Here, we used Otsu's method [211] as it has good performance with histograms with a bimodal distribution, but any other reliable approach in the literature can be used. For each patch P_p , $\tilde{\theta}_p$ is thresholded:

$$P_p \in \begin{cases} D_B & \text{if } \tilde{\theta}_p \leq T_\theta \\ D_T & \text{if } \tilde{\theta}_p > T_\theta \end{cases} \quad (6.2)$$

Finally, we define the segmentation map $M(a, r)$, where pixels in the patches in \mathcal{D}_B are labeled with ω_B , and pixels in the patches in \mathcal{D}_T are labeled with ω_T .

6.2.2 Label refinement for target reflection detection

This step updates the labels in $M(a, r)$ to extract reflections generated by dielectric interfaces in the subsurface, see Fig. 6.3 for the block scheme. To this end, we updated $M(a, r)$ to generate a binary map for each pixel (a, r) to distinguish background and target pixels. We train a neural network in an unsupervised manner with the task of reconstructing patches in \mathcal{D}_B (background patches). The training aims at minimizing the reconstruction loss between the input $P(r, a)$ and output $P_{out}(r, a)$ patches so that $P_{out}(r, a)$ should be the most similar to $P(r, a)$. To this end, the network architecture should be a fully convolutional autoencoder. The network parameters, i.e., weights and bias, are tuned during the training phase so that the network extracts relevant features from the radargrams at multiple scales.

Here, we use a W-Net [209] as it showed good performances in many applications. Each convolutional layer learns semantic features from the spatial and semantic view-point related to the background and not the target [198]. The W-Net [209] has two fully convolutional networks (FCNNs) with a modified U-Net architecture [189]. The W-Net

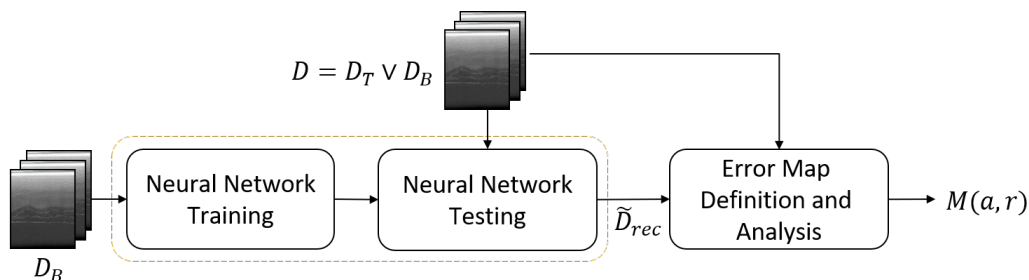


Figure 6.3: Block scheme for the label refinement step to detect target reflections.

has an autoencoder architecture, where the first FCNN acts as an encoder that extracts compact features representation map from the input patch $P(r, a)$. The encoder converts $P(r, a)$ to a pixel-wise segmentation map (i.e., a soft-segmentation map) with the same size of $P(r, a)$. The decoder consists of the second FCN, which processes the compact features representation map to reconstruct $P(r, a)$. The W-Net architecture has 46 convolutional layers structured in 18 modules: 9 for the contraction at the encoder and 9 for the reconstruction at the decoder). Each module consists of two 3×3 convolutional layers, each followed by a ReLU non-linearity and a batch normalization layer. Each U-Net consists of a contracting part (encoder) that captures the general spatial context, followed by an expansive path (decoder) that analyzes the details. Each module in the encoders is connected to the following module with a max-pooling operation. The modules in the decoders are linked to a transposed 2D convolution layer. The number of features is doubled at each module in the encoders, and it is halved in the decoders. As in the U-Net [189], the decoder modules are linked with skip connections to the corresponding module of the encoder to recover the spatial information lost in the downsampling. The final layer of both the FCNs is a 1×1 convolution processing the n_f -component feature vector. In the first FNC, the 1×1 convolutional layer is followed by a softmax that maps the features vector into a soft segmentation map of N_C classes. In the second FNC, the 1×1 convolutional layers maps the feature vector in the reconstructed patch $P_{out}(a, r)$. The more significant modification with respect to the U-Net in [189] is the use of depthwise separable convolution layers [212] expect for the modules in the edges on the encoder and decoder, i.e., modules 1, 9, 10, 18. The depthwise separable convolution examines the spatial correlation and cross-channel correlation independently to achieve higher performance with the same number of parameters. A depthwise convolution performs a spatial convolution independently over each channel, followed by a pointwise convolution of the features channels to generate the new feature space.

The training is done in an unsupervised fashion with the joint minimization of two losses– i) a soft normalized cut loss function for the encoder, and ii) a reconstruction loss

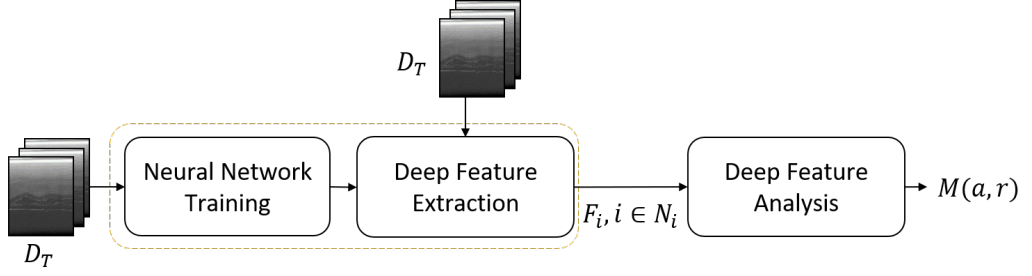


Figure 6.4: Block scheme for the extraction and the analysis of the deep features.

between the input and the output of the W-Net. The soft normalized cut loss is a modified version of the cut loss [213] as the cut loss is non-differentiable. The soft normalized loss is differentiable and allows calculating and updating the gradient during the backpropagation. Minimizing the soft normalized cut loss means reducing the total normalized dissociation between pixels of the same class while increasing the normalized association within the pixels of the same class. For training the W-Net, any regression loss can be considered as a reconstruction loss. The training aims at estimating the network parameters so that the features extracted by the network are semantically meaningful. Here, the reconstruction loss L_{rec} as defined between the input $P(a, r)$ and output $P_{out}(a, r)$ patches as follows

$$L_{rec} = \| P(a, r) - P_{out}(a, r) \|_2^2 \quad (6.3)$$

The W-Net is trained to reconstruct the noisy patches \mathcal{D}_B . Hence, testing such a network with \mathcal{D} , we expect to have an excellent reconstruction of background patches and a poor reconstruction of target patches. Similar to [62], we can exploit the normalized reconstruction error map $\mathcal{E}(a, r)$ defined for all the pixels (a, r) to identify pixels representing the background and the targets. Background pixels have a small reconstruction error, while target pixels have a larger reconstruction error. We update the pixels labeled as ω_T in $M(a, r)$ so that pixels with small error belong to the background (ω_B), and pixels with large error belong to the target class (ω_T). Reflections can be identified as groups of pixels similarly labeled that are not separated by background pixels.

6.2.3 Extraction and analysis of deep features

The third step aims at analyzing the pixels labeled as $\omega_c, c \in [1, \dots, N_C]$ in $M(a, r)$, i.e., discriminate between different geological targets, by constructing a decision tree considering feature representative of each class. To this end, we analyze the deep features of the pixels labeled as ω_T in $M(a, r)$ to identify subclasses by constructing a decision tree with an approach similar to [214]. Fig. 6.4 shows the block diagram for this step of the proposed method.

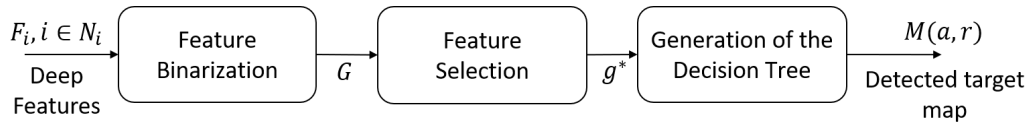


Figure 6.5: Block scheme for the analysis of the deep features.

As the network is trained only with background patches and the aim is to analyze subclasses of the target, we train the network with $\mathcal{D}_{\mathcal{T}}$ and the task of reconstructing the related patches. Then, we extract deep features for the patches in $\mathcal{D}_{\mathcal{T}}$ from N_{FL} convolutional layers. The features can be extracted from any of the convolutional layers in the network. Ancillary layers (batch normalization, activation, and pooling) are deterministic functions applied to convolutional layer outputs to regularize the network, incorporate non-linearity, and improve the generalization capability. The characteristics extracted by the features depend on the layer from which they are extracted. Initial layers of an autoencoder extract low-level features coding visual concepts, such as edges and curves. Higher-level features capture more complex characteristics that combine the lower-level features from the previous levels. Higher-level features lack spatial finesses and generalization capabilities. Hence, when analyzing deep features, a balance is needed between low and high-level features. [214] proposed to concatenate features extracted from convolutional layers at a different level to guarantee a multi-scale abstraction of the data. Fig. 6.5 shows the detailed block scheme for analyzing the deep features. Such a feature map considers low-level features capturing the spatial features and higher-level features capturing more complex characteristics without the spatial finesse. The number of features extracted from the deep network is large, which increases the complexity of the problem. In the W-Net, the maximum feature number per layer is 512 and the minimum 64. Hence, we extracted semantically meaningful features from N_{FL} convolutional layers of the network for each patch p . The number of features extracted at each convolutional layer can vary significantly—since we are training a W-Net but, the maximum number is 512 for each patch. The features extracted from the N_{FL} layers are upsampled to the original patch size (h_p, w_p) with bilinear interpolation. The deep features are masked by $M(a, r)$ to keep only those for the target pixels labeled with ω_T , obtaining $\mathcal{F}(a, r, k), k \in [1, \dots, N_G]$, where N_G is the total number of extracted features. $\mathcal{F}(a, r, k)$ is min-max normalized and then concatenated together to obtain $\mathcal{G} = g^k(a, r), k \in [1, \dots, N_G]$.

We discretize the features to reduce the problem complexity and the feature sparsity while preserving the information. We binarize \mathcal{G} so that features with g^k greater than 0.5 are set to 1 and those with g^k smaller than 0.5 to 0. Each class is expected to correspond to a specific binary signature. To select the most informative feature k^* to build the decision tree, we followed the approach in [214]. Hence, features are analyzed by considering the

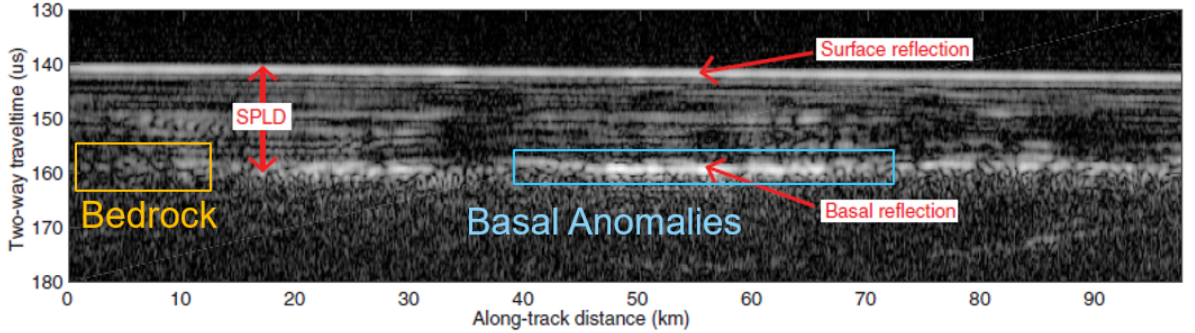


Figure 6.6: Example of MARSIS radargram with the labels of the subsurface targets.

index R_k based on the Hamming distance (number of different pixels). k^* is defined as to maximize R_k and is used to divide the pixels into two subclasses to build the decision tree and update $M(a, r)$. Features similar to k^* , i.e., those having a small Hamming distance from k^* , are discarded. This approach is iterated to divide target pixels and update $M(a, r)$.

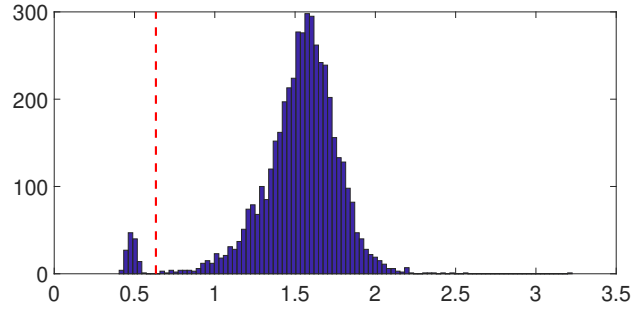
6.3 Description of the dataset and experimental results

To prove the effectiveness of the proposed method, we analyzed a dataset of radargrams acquired by the MARSIS radar sounder near the South Pole of Mars. MARSIS transmits chirp pulses with 1 MHz bandwidth and centered at 1.8, 3, 4, or 5 MHz, alternating two frequencies. The dataset consists of 37 radargrams with High and Medium SNR in [26]. Each radargram has $N_T = 3200$ traces and $N_S = 980$ samples and covers a track of 100 km long. We aim at discriminating the characteristics of the basal return between non-anomalies or anomalies (see Fig. 6.6), which can be interpreted as a rocky interface and subglacial lakes, respectively [26]. Hence, the method has to detect reflections in the radargram (i.e., the ice layers and the basal return) and then discriminate the basal return pixels between non-anomalies (ω_1) and anomalies (ω_2). The results in [26] are considered as a reference to qualitatively and quantitatively evaluate the proposed method. The radargrams are preprocessed with range compression and geometric calibration to compensate for altitude variations (geometric power fall-off). Since the surface of the investigated area is flat, and the roughness is low at the MARSIS wavelength, the scattering is mostly coherent. SAR focusing is not required since it would reduce to a moving average filtering [26].

For generating the dataset, we consider patches of dimensions $w_p = 48$ and $h_p = 32$ as each patch is small enough to capture one class and large enough to be processed by the network. The number of patches is 75500. The two datasets are independent as the patches for the training and test are extracted from different radargrams. The best-fitting

Table 6.1: Evaluation of the goodness of the statistical distribution estimation for subsurface targets.

Pdf	Noise above the surface		Noise below the bedrock		Ice Layers		Bedrock		Bedrock Anomalies	
	KL	MSE	KL	MSE	KL	MSE	KL	MSE	KL	MSE
Rayleigh	0.0003	0.0109	0.0013	0.0172	0.0273	0.0306	0.0966	0.0171	0.1266	0.0178
Nakagami	0.0002	0.011	0.0008	0.0138	0.0134	0.0234	0.0493	0.0152	0.0583	0.0132
Gamma	0.024	0.1032	0.0178	0.0738	0.005	0.0145	0.0601	0.0142	0.0612	0.0159
K	0.0002	0.0108	0.0013	0.0172	0.0273	0.0306	0.906	0.0365	0.806	0.0165
Weibull	0.002	0.0109	0.0006	0.012	0.0089	0.0194	0.0661	0.0145	0.0688	0.0155

Figure 6.7: Histogram of $\tilde{\Theta}$ in blue and the threshold T_θ in red.

distribution is the Nakagami pdf (see Table 6.1).

For dividing target and background patches, the threshold is $T_\theta = 0.6$. Fig. 6.7 shows the histogram of $\tilde{\Theta}$ and the threshold. The W-Net is trained with a learning rate of 10^{-4} and 100 epochs. Fig. 6.8 shows two examples of pairs of input and reconstructed patches of the background (Fig. 6.8.a and b) and target (Fig. 6.8.c and d). Fig.6.9 shows the input radargram and the binary map $\mathcal{M}(a, r)$ at the end of the label refinement step for the basal return for the orbit 10737 acquired at 4MHz. The performance of the label refinement step over the dataset of 37 radargrams is good. The overall accuracy is equal to 88.87%, and the sensitivity to 0.889, and the specificity to 0.8681 (see Table 6.2).

Table 6.2: Performance of the classes of the basal return segmentation over the whole dataset.

Class	Accuracy	Sensitivity	Specificity
Background	88.87%	0.8890	0.8681
Non-Anomalies	80.45%	0.9025	0.8937
Anomalies	85.54%	0.8956	0.8715

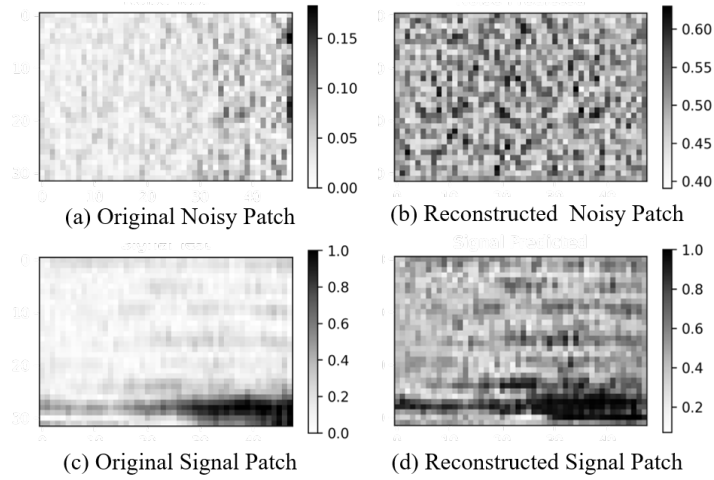


Figure 6.8: Two examples of pairs of input and reconstructed patches: (a) and (b) background, and (c) and (d) target.

Fig.6.10 shows a zoom over the basal return of (a) the input radargram, (b) the binary map $M(a, r)$ at the end of the label refinement step, and (c) the segmented map. The background is in blue, the non-anomaly of the basal return is in green, and the anomalies are in yellow. Table 6.2 shows the proposed method performance for the segmentation map for the basal return averaged for the 37 radargrams. The background class accuracy is 88.87%, that of the non-anomaly is equal to 78.45%, and that of the anomalies is 76.54%. The performance proves the effectiveness of the method in detecting the reflections and identifying targets of interest.

6.4 Conclusions and future works

This Chapter has proposed a deep learning-based method for analyzing radargrams in an unsupervised and automatic way. The proposed method generates a binary map of the radargram from which it is possible to detect the reflections from subsurface interfaces. Then it extracts and analyzes a set of deep features extracted by a W-Net to identify subsurface targets of interest in an unsupervised way. The proposed method was validated with the tasks of detecting the layers reflections in planetary radargrams and then detecting the basal return and its characteristics, i.e., rocky interface or anomalies. The radargrams analyzed were acquired by the MARSIS radar sounder in the South Pole of Mars. For the experimental analysis, we used an NVIDIATM Tesla T4 GPU with 15 GB of RAM. Both training phases took about 7.5 hours, and the testing, feature extraction, and analysis took about one hour. The results show the effectiveness of the proposed method. As future work, we plan to perform an extensive analysis with data from other radar sounders and considering other target classes.

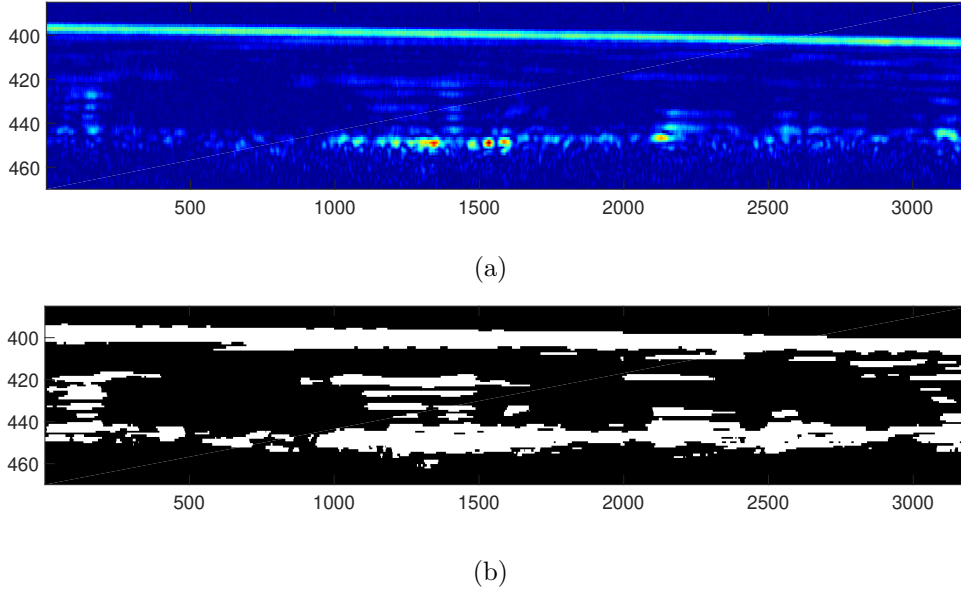


Figure 6.9: (a) Input radargram 10737 acquired at 4MHz, (b) $M(a, r)$ at the end of the label refinement step (binary map).

6.5 Appendix: Statistical analysis

The Rayleigh pdf of the amplitude $A > 0$ for a large number of scatters is defined as

$$p_R(x) = \frac{2x}{\mu_z} \exp\left(-\frac{x^2}{\mu_z}\right) \quad (6.4)$$

where z indicates the power of the amplitude signal defined as $z \propto A^2$. μ_z is the mean of the power signal, and the mean of the amplitude signal is $\mu_A = \sqrt{\pi\mu_z}/2$. The Rayleigh distribution is the theoretical model for a radar signal of the areas of no-subsurface scattering affected in amplitude and in phase by the zero-mean additive white Gaussian noise (AWGN) [44]. The Nakagami distribution is defined as

$$p_N(A) = 2 \left(\frac{\beta_N}{\mu_z}\right)^{\beta_N} \frac{A^{2\beta_N-1}}{\Gamma(\beta_N)} \exp\left(-\frac{\beta_N A^2}{\mu_z}\right) \quad (6.5)$$

where $\beta_N \geq 0$ the shape or order parameter, and $\Gamma(\cdot)$ indicates the Gamma function. the Nakagami distribution showed good performance in modelling radar data subjected to multilooking processing for speckle reduction [45]. The Nakagami pdf for the amplitude correspond in the intensity domain to a Gamma pdf with parameters $\beta_\gamma = \beta_N$ and μ_z . The Gamma pdf is defined as follow

$$p_G(A) = \left(\frac{A}{\alpha_\Gamma}\right)^{\beta_\Gamma-1} \frac{\exp^{-\frac{A}{\alpha_\Gamma}}}{\alpha_\Gamma \Gamma(\beta_\Gamma)} \quad (6.6)$$

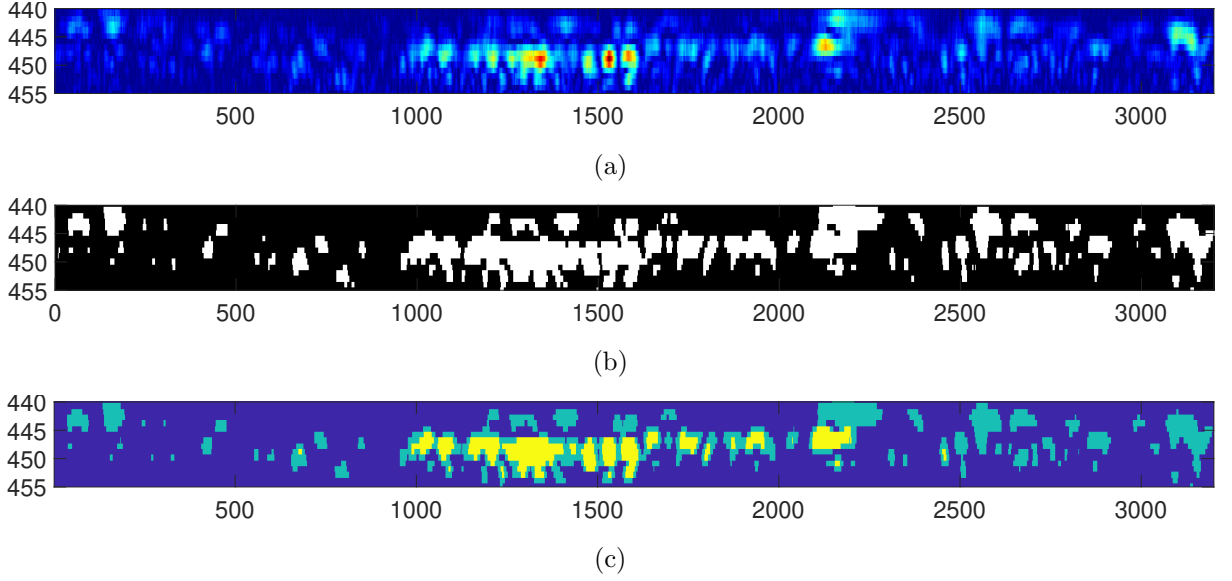


Figure 6.10: Zoom of the basal return of (a) radargram 10737 acquired at 4MHz, (b) $M(a, r)$ at the end of the label refinement step, and (c) segmented map (blue indicate the background, green indicates non-anomaly and yellow the anomalies).

where α_Γ is the scale parameter. The Gamma distribution is used to the model data which original distribution has been altered by the processing [45]. The K distribution is defined by

$$p_K(A) = \frac{4}{\Gamma(\beta_K)} \left(\frac{\beta_K}{\mu_z} \right)^{\frac{\beta_K+1}{2}} A^{\beta_K} K_{\beta_K-1} \left[2A \sqrt{\frac{\beta_K}{\mu_z}} \right] \quad (6.7)$$

where K_{β_K-1} is the Bessel function of the second order of $\beta_K - 1$. β_K is the shape parameter and is defined for $\beta_K \geq 0$. The K distribution is suitable to model spatially non-homogeneous targets [44]. The Weibull distribution is defined for $A \geq 0$ as

$$p_W(A) = \frac{\beta_W}{\alpha_W} \left(\frac{A}{\alpha_W} \right)^{\beta_W-1} \exp - \left(\frac{A}{\alpha_W} \right)^{\beta_W} \quad (6.8)$$

where β_K is the shape parameter and α_K is the scale parameter, and both are non-negative. The Weibull distribution has been used in SAR radar data to model clutter signal [215]. Other distributions can fit the data, such as Rice or exponential pdf. However, we considered Rayleigh, Nakagami, K, and Weibull as they describe physical phenomena and are successfully used in the radar sounder literature [44, 45].

The estimation of the parameters for the distribution is done with the Maximum Likelihood Estimation (MLE) approach. For the Rayleigh distribution, the parameter to estimate is $\tilde{\mu}_z$ for μ_z , which is defined as [216]

$$\tilde{\mu}_z = E\{A^2\} \quad (6.9)$$

where $E\{\cdot\}$ is the expectation operation. For the Nakagami distribution, the parameters to estimate are $\tilde{\mu}_z$ and $\tilde{\beta}_N$, where $\tilde{\mu}_z$ is given by (6.9), and the shape parameter $\tilde{\beta}_N$ by [217]

$$\tilde{\beta}_N = \begin{cases} \frac{0.5000876+0.1648852y-0.0544274y^2}{y} & 0 > y \geq 0.5772 \\ \frac{8.98919+9.05995y+0.9775373y^2}{y(17.79728+11.968477y+y^2)} & 0.5772 > y > 17 \end{cases} \quad (6.10)$$

where $y = \ln(\tilde{\mu}_z F^{-1})$, and $F = (\prod_{i=1}^n A^2)^{\frac{1}{n}}$ where n is the number of samples considered for the estimation. For the Gamma distribution, the parameters to estimate are the scale $\tilde{\alpha}_\Gamma$ and the shape $\tilde{\beta}_\Gamma$ parameters as solution of [218]

$$\begin{cases} \hat{\alpha}_\Gamma = \frac{\bar{A}}{\hat{\beta}_\Gamma} \\ \log(\hat{\beta}_\Gamma) - \psi(\hat{\beta}_\Gamma) = \log[\bar{A}F^{-1}] \end{cases} \quad (6.11)$$

where $\psi(\cdot)$ is the di-gamma function and $\bar{A} = E\{A\}$. For the K distribution, the $\tilde{\mu}_z$ and the shape $\tilde{\beta}_K$ parameters are estimated by maximizing the likelihood function $f_{ML}(\beta_K, \mu_z; \forall A_i, i \in [1, \dots, n])$ [210] so that

$$(\tilde{\mu}_z, \tilde{\beta}_K) = \underset{(\mu_z, \beta_K)}{\operatorname{argmax}} \{\ln(f_{ML})\}. \quad (6.12)$$

Finally, for the Weibull distribution, the $\tilde{\alpha}_W$ and the shape $\tilde{\beta}_W$ parameters are estimated by maximizing the likelihood function $f_{ML}(\beta_W, \alpha_W; \forall A_i, i \in [1, \dots, n])$ [219].

Chapter 7

Conclusions

This Chapter concludes the thesis by presenting an overall discussion, a recap of the novel contributions, and the related critical analysis. Moreover, we propose possible future developments.

7.1 Summary and discussion of the novel contributions

The proposed work enriched the RS data processing chain with two main contributions: i) the performance assessment of target detection in simulated radargrams for guiding RS design, and ii) novel automatic data processing algorithms focusing on extracting information on different subsurface targets. The first contribution highlights the importance of assessing the performance of an RS design with simulated radargrams considering realistic modeling of the subsurface profile and structure. Realistic target modeling can narrow the error margin in the estimated performance, thus supporting a more effective design of the instruments. The second contribution highlights the importance of data analysis algorithms to automatically extract information on the subsurface structures and processes for scientific studies and practical applications. Automatic data analysis is extremely important for effectively exploiting the large number of available radargrams and those planned to be acquired (e.g., RIME and REASON). The proposed automatic methods for analyzing the subsurface are based on fuzzy logic and deep learning, having powerful generalization capabilities. Fuzzy logic handles the discrepancy between the theoretical EM model of targets and how they appear in radargrams. Deep networks automatically extract meaningful features from the data, which avoids handcrafted features. This strategy increases the adaptability of the proposed methods to deal with problems showing a wider number of classes. Note that data analysis is essential for target detection to assess simulated radargram performance with given RS parameters. Evaluation of the target detectability provides feedback on the simulating RS parameters, which can effectively support the radar design. Remarkably, the proposed approaches for data analysis and

performance assessment are versatile and can be easily adapted to any RS instrument developed for past, present, or future missions, targeting subsurface observations of any planetary body. The approach characteristics can be adjusted to the diverse mission scientific requirements for detecting the target subsurface interfaces.

In Chapter 3 we presented an approach for a detailed and realistic assessment of the performance of an EORS in detecting important scientific targets in polar ice subsurface. The performance assessment methodology evaluates simulated EORS radargrams from the available ARS with a set of performance metrics. The EORS radargrams are simulated by varying the SNR budget at the surface. Performance analysis is used to reveal the SNR budget that maximizes the target detectability across different geographical regions of the polar cryosphere. The methodology has been demonstrated by simulating an EORS with a carrier of 45 MHz and a bandwidth of 10 MHz. The results assess the target detectability, such as ice layers and basal interface, by varying the SNR budget. Furthermore, ARS automatic algorithms have been successfully applied to the EORS simulated radargrams, resulting in a high accuracy comparable to that of ARS data. The results highlight that existing methods to analyze ARS data can be successfully adapted for extracting information from satellite RS data and thus future EORS data. It is noteworthy that simulated radargrams enable the test the adaptability of automatic target detection algorithms developed for the ARS data to the EORS case. This has been demonstrated using a subglacial lakes detection algorithm. In preparation for the scientific interpretation of the acquired EORS in its advanced phases of development, the proposed simulation approach can adapt the existing algorithms for applications to the EORS radargrams. Note that simulated radargrams do not consider the ionospheric effects and the off-nadir clutter response. However, losses due to propagation through the ionosphere, roughness of the surface, and volume scattering have been included in the SNR margin. Clutter and volume scattering can be a critical performance-limiting factor in extreme polar regions such as high ice-flow regimes, ice-tongues, unstable ice-shelves, high surface roughness, and the presence of wet firn in the shallow surface. Regarding the ionosphere performance, the loss of signal strength and coherence (due to phase errors) may reduce the estimated detection performance for extreme TEC values.

Chapter 4 presents an unsupervised method for detecting candidate lava tubes in radar sounder data. We model the surface and lava tube boundaries as linear reflections with specific properties. The candidate linear reflections are extracted from radargrams and analyzed with a fuzzy system to identify the surface and candidate lava tube reflections. The fuzzy system provides an overall membership value for each detected candidate tube, indicating the reliability degree. The experimental results on the simulated dataset show that the proposed method can detect lava tubes with different geometries (tube width and

height and roof thickness) and crossing angles between the tube axis and the spacecraft moving direction. The method is robust against clutter due to the surface topography. For the LRS dataset, the proposed method recognized several candidate lava tubes in the MH region documented in the literature. Planetologists should analyze identified candidate tubes for a reliable final decision. In Highlands radargrams, characterized by large surface clutter, the proposed method shows a low false alarm rate. This is mainly because the phase inversion rule membership assumes small values for clutter reflections (showing no phase inversion), bringing to a small overall membership. Hence, the phase inversion rule showed to increase in the robustness of the proposed method against the clutter. The proposed method has some limitations related to clutter and range resolution. Clutter reflections with high power may mask subsurface reflections, e.g., the tube ceiling and floor, hiding the tube. The method robustness against clutter is guaranteed by the phase inversion rule and is tested with an ad-hoc experiment. Another limitation is the range resolution of the sensor. If the tube depth (roof thickness) is lower than the range resolution, the ceiling reflection is incorporated in the surface reflection, resulting in undetectable tubes.

Chapter 5 and 6 propose two deep learning-based methods for automatically analyzing radar sounder data. We proposed a method for detecting the basal layer and the basal unit in continental radargram (Chapter 5) with a deep learning network. The network is trained in a supervised manner and tested on previously unseen radargrams. The results on two datasets of radargrams acquired in Greenland and Antarctica illustrate the proposed method ability to accurately segmenting inland radargrams and detecting basal units. The results prove that the method can assign semantically significant labels. The proposed method showed to identify the radargram areas imaging basal ice and signal perturbations with high accuracy. The other classes, i.e., the englacial layers, the bedrock, and the EFZ and the thermal noise, are segmented with high performance, comparable to the literature methods but without needing the feature design procedure. The results highlight the importance of using vertical radargram strides (patches) for the network input as it captures the global context and the vertical spatial distribution of the classes. Furthermore, the meaningful features extracted by the network are improved by the ASPP module features extracted at multiple scales and the AGs. As the network can automatically extract semantically meaningful features, it is not required to design handcrafted features to model the desired classes. Hence, the proposed method is adaptable to process data acquired in multiple scenarios, such as coastal areas characterized by floating ice, marine and meteoric ice, and the grounded ice. These targets have different geometric and dielectric properties from those of the classes analyzed here, but the proposed method can be easily adapted for performing the segmentation. Note that supervised training of

a deep learning network requires several labeled data samples. Here, it means that an expert, i.e., radio-glaciologists, should generate a reference segmentation map for each patch in the dataset. This is a subjective and expensive task in terms of time. However, in the literature, there are techniques to diminish the amount of labeled data required for the supervised training, including data augmentation and unsupervised pre-training as in Chapter 5. Data augmentation applies realistic transformations to the input patches and the related reference map to generate realistic patches. The unsupervised pre-training initializes the network parameters and reduces the number of labeled patches required for the training. Chapter 6 proposed a novel method for the unsupervised and automatic segmentation of radargrams with deep learning. The technique is unsupervised and does not require any labeled data. The proposed method has two main outputs: the signal vs background binary map and the segmentation map. From the binary map, it is possible to extract the reflections of the subsurface interfaces. The results on a dataset of MAR-SIS radargrams acquired in the Mars SPLD show that in low SNR radargrams (such as those from an ORS) of icy areas, the proposed method can effectively identify reflections representing the ice layers and the basal return. Compared to literature methods, the proposed method is not affected by the reflection shape and can detect reflections regardless of the curvature. The segmentation map is generated by analyzing the set of deep features extracted by the deep learning network. The proposed method was validated with the tasks of detecting the reflections in radargrams and then identifying the layers and the basal return characteristics, i.e., rocky interface or anomalies. The results show the effectiveness of the proposed method in detecting with high accuracy the ice layers, the basal return, and the type of interface of the basal return. This highlights the goodness of the features extracted by the deep network. Remarkably, the proposed approach can perform the segmentation in an unsupervised manner with a limited number of input radargrams. A critical issue of deep learning is the high computational and time cost required for the network training, affecting both methods proposed in Chapter 5 and 6. The computational cost depends on the size of the training dataset and the network depth and complexity (i.e., the number of network parameters). The cost can be reduced using pre-trained neural networks. It is noteworthy that the network trained for analyzing basal units in Chapter 5 and that for the unsupervised segmentation of radargrams in Chapter 6 can be further re-trained to process different scenarios.

7.2 Future works

Regarding the approach for performance assessment, we plan to extend the simulation approach, considering the ionosphere effects and clutter as they may further degrade simulated radargrams. Clutter performance can be integrated into the proposed analysis,

by complementing it with the simulation of the cluttergram (using several well-established approaches [92, 54]) over the selected ARS tracks using available digital elevation models for evaluating the actual performance in terms of SCR. Ionospheric effects can also be easily integrated into the proposed simulation approach using the phase information of the ARS data and applying the estimated phase distortions as a function of the Earth ionospheric parameters. Moreover, the simulation approach can be modified by combining the realistic target modeling from analog radargrams and the accurate representation of the signal response from electromagnetic simulators. The proposed techniques can be applied to the development of future RS missions (e.g., Envision SRS), to the proposal of new RS instruments (e.g., EORS), and to the design of novel RS systems (e.g., the distributed RS [48]). The simulated radargrams generated by the proposed method can also be used to test the adaptability of automatic target detection algorithms developed for the ARS data to the EORS case. The scientific goal of an orbiting RS is not restricted to the detection of bedrock, subglacial lakes, and ice shelves. As a future extension of the work, we plan to analyze the feasibility of interpreting the basal conditions, such as frozen or thawed bedrock [105], subglacial water flow channels [81], and the presence of marine ice and cavities at the base of ice-shelves [123]. In preparation for the scientific interpretation of the acquired EORS in its advanced phases of development, the proposed simulation approach can be used to adapt the existing algorithms for applications to the EORS radargrams.

Automatic data processing is critical to analyze a large number of radargrams available and planned to be acquired. For the fuzzy approach in Chapter 4, we plan to expand the system to model and recognize other targets, including craters. This can be done by modeling the EM and geometric behavior of different targets and then exploit this model to define a set of novel fuzzy logic for detecting the target. For the proposed method in Chapters 5 and 6, we plan to investigate another way for the unsupervised training of the network. Recently, several losses have been proposed for the unsupervised training of deep networks, such as momentum contrast [220]. Momentum contrast showed good performance in a large variety of applications, including semantic segmentation. However, more methods are needed for extending the processing chain and extract information on other scenarios. For instance, no approaches exist to automatically analyze coastal areas, despite the high importance of monitoring the evolution of floating ice and ice calving. Detection of the floating ice, marine, meteoric ice may be done with the segmentation of radargrams acquired in the coastal areas. To this end, coastal radargrams can be segmented using the method proposed in Chapter 5. The neural network for inland segmentation can be further trained with a dataset of labeled coastal patches. The processing chain can also be extended with algorithms analyzing data from different sensors, such as

altimeter, optical, and SAR data. In the literature, several works (e.g., [221]) show the combination of RS data and those from different sensors extracts information and generates crucial products on the subsurface structure. Another interesting possible extension of the processing data chain is the multitemporal analysis of radargrams. Although the multitemporal analysis is hardly possible with available radargrams on the Earth, it may become reality with the future orbiting RS missions, such as the STRATUS that, if selected, will have a seasonal revisit time. This would enable the multitemporal analysis of radargrams for extracting information for a better assessment of the impact of climate change on the Earth.

Regarding the proposed methods, we plan to test their effectiveness on other datasets and automatizing the parameter selection. Further tests and full automatizing can also help to adapt the proposed techniques to process data acquired in different scenarios. This is critical to effectively incorporate the proposed methods in the data processing chain and make the techniques available to process a large amount of RS data.

Bibliography

- [1] G. Picardi, D. Biccari, M. Cartacci, A. Cicchetti, O. Fuga, S. Giuppi, A. Masdea, R. Noschese, R. Seu, C. Federico, A. Frigeri, T. Melacci, R. Orosei, O. Bombaci, D. Calabrese, E. Zampolini, L. Marinangeli, E. Pettinelli, E. Flamini, and G. Vanaroni, “MARSIS, a radar for the study of the Martian subsurface in the Mars Express mission,” *Memorie della Societa Astronomica Italiana Supplement*, vol. 11, pp. 15–25, 01 2007.
- [2] R. Seu, R. Phillips, D. Biccari, R. Orosei, A. Masdea, G. Picardi, A. Safaeinili, B. Campbell, J. Plaut, L. Marinangeli, *et al.*, “SHARAD sounding radar on the Mars Reconnaissance Orbiter,” *Journal of Geophysical Research: Planets*, vol. 112, no. E5, 2007.
- [3] T. Ono, A. Kumamoto, Y. Kasahara, Y. Yamaguchi, A. Yamaji, T. Kobayashi, S. Oshigami, H. Nakagawa, Y. Goto, K. Hashimoto, Y. Omura, T. Imachi, H. Matsumoto, and H. Oya, “The Lunar Radar Sounder (LRS) Onboard the KAGUYA (SELENE) Spacecraft,” *Space Science Reviews*, vol. 154, pp. 145–192, July 2010.
- [4] L. Bruzzone, G. Alberti, C. Catallo, A. Ferro, W. Kofman, and R. Orosei, “Sub-surface radar sounding of the Jovian moon Ganymede,” *Proceedings of the IEEE*, vol. 99, no. 5, pp. 837–857, 2011.
- [5] M. C. Peel, B. L. Finlayson, and T. A. McMahon, “Updated world map of the köppen-geiger climate classification,” *Hydrology and earth system sciences*, vol. 11, no. 5, pp. 1633–1644, 2007.
- [6] J. G. Fyke, M. Vizcaíno, W. Lipscomb, and S. Price, “Future climate warming increases greenland ice sheet surface mass balance variability,” *Geophysical Research Letters*, vol. 41, no. 2, pp. 470–475, 2014.
- [7] A. Neumann, E. Bayler, R. Christian, A. Dahl, D. DeLisle, P. DiGiacomo, M. Hales, J. Hall, V. Camacho-Ibarra, S.-I. Iwasaki, *et al.*, “For the monitorin of our environment from space and from earth-2006 an international partnership for cooperation in earth observations,” *IGoS Coastal Theme Report*, pp. 1–48, 2006.

-
- [8] A. O’Neill, D. Barber, P. Bauer, H. Dahlin, M. Diament, D. Hauglustaine, P. Le Traon, F. Mattia, W. Mauser, C. Merchant, *et al.*, “Esa’s living planet programme: Scientific achievements and future challenges—scientific context of earth observation science strategy for esa,” *Earth Observation Science Strategy*, 2015.
- [9] D. Dahl-Jensen, K. Mosegaard, N. Gundestrup, G. D. Clow, S. J. Johnsen, A. W. Hansen, and N. Balling, “Past temperatures directly from the greenland ice sheet,” *Science*, vol. 282, no. 5387, pp. 268–271, 1998.
- [10] R. G. Bingham and M. J. Siegert, “Radio-echo sounding over polar ice masses,” *Journal of Environmental and Engineering Geophysics*, vol. 12, no. 1, pp. 47–62, 2007.
- [11] V. Bogorodsky, C. Bentley, and P. Gudmandsen, “Radioglaciology: Glaciology and quaternary geology,” 1985.
- [12] R. B. Alley and I. Joughin, “Modeling ice-sheet flow,” *Science*, vol. 336, no. 6081, pp. 551–552, 2012.
- [13] D. G. Vaughan and R. Arthern, “Why is it hard to predict the future of ice sheets?,” *Science*, vol. 315, no. 5818, pp. 1503–1504, 2007.
- [14] R. K. Pachauri, M. R. Allen, V. R. Barros, J. Broome, W. Cramer, R. Christ, J. A. Church, L. Clarke, Q. Dahe, P. Dasgupta, *et al.*, *Climate change 2014: synthesis report. Contribution of Working Groups I, II and III to the fifth assessment report of the Intergovernmental Panel on Climate Change*. Ipcc, 2014.
- [15] A. Freeman, X. Pi, and E. Heggy, “Radar sounding through the earth’s ionosphere at 45 mhz,” *IEEE Transactions on Geoscience and Remote Sensing*, vol. 55, no. 10, pp. 5833–5842, 2017.
- [16] E. Heggy, P. A. Rosen, R. Beatty, T. Freeman, and Y. Gim, “Exploring Desert Aquifers and Polar Ice Sheets and Their Responses to Climate Evolution: OASIS Mission Concept,” in *Advances in Remote Sensing and Geo Informatics Applications*, (Cham), pp. 7–10, Springer International Publishing, 2019.
- [17] T. Scuccato, L. Carrer, F. Bovolo, and L. Bruzzone, “Compensating earth ionosphere phase distortion in spaceborne vhf radar sounders for subsurface investigations,” *IEEE Geoscience and Remote Sensing Letters*, vol. 15, pp. 1672–1676, Nov 2018.
- [18] R. Culberg and D. M. Schroeder, “Firn Clutter Constraints on the Design and Performance of Orbital Radar Ice Sounders,” *IEEE Transactions on Geoscience and Remote Sensing*, 2020.

-
- [19] J. Dall, H. F. Corr, N. Walker, B. Rommen, and C.-C. Lin, “Sounding the antarctic ice sheet from space: a feasibility study based on airborne p-band radar data,” in *IGARSS 2018-2018 IEEE International Geoscience and Remote Sensing Symposium*, pp. 4142–4145, IEEE, 2018.
- [20] L. Bruzzone *et al.*, “STRATUS-SaTellite Radar sounder for eArth sUb-surface Sensing,” *Final Report to STRATUS Project, Italian Space Agency*, 2018.
- [21] C. Gerekos, A. Tamponi, L. Carrer, D. Castelletti, M. Santoni, and L. Bruzzone, “A coherent multilayer simulator of radargrams acquired by radar sounder instruments,” *IEEE Transactions on Geoscience and Remote Sensing*, vol. 56, no. 12, pp. 7388–7404, 2018.
- [22] C. Gerekos, L. Bruzzone, and M. Imai, “A coherent method for simulating active and passive radar sounding of the jovian icy moons,” *IEEE Transactions on Geoscience and Remote Sensing*, 2019.
- [23] E. Sbalchiero, S. Thakur, and L. Bruzzone, “3D radar sounder simulations of geological targets on Ganymede Jovian Moon,” in *Image and Signal Processing for Remote Sensing XXV* (L. Bruzzone and F. Bovolo, eds.), vol. 11155, pp. 442 – 454, International Society for Optics and Photonics, SPIE, 2019.
- [24] S. Thakur and L. Bruzzone, “An Approach to the Simulation of Radar Sounder Radargrams Based on Geological Analogs,” *IEEE Transactions on Geoscience and Remote Sensing*, 2019.
- [25] G. Picardi, J. Plaut, D. Biccari, O. Bombaci, D. Calabrese, M. Cartacci, A. Cicchetti, S. Clifford, P. Edenhofer, W. Farrell, *et al.*, “Radar soundings of the subsurface of Mars,” *Science*, vol. 310, no. 5756, pp. 1925–1928, 2005.
- [26] S. Orosei, Rand Lauro, E. Pettinelli, A. Cicchetti, M. Coradini, B. Cosciotti, F. Di Paolo, E. Flamini, E. Mattei, M. Pajola, *et al.*, “Radar evidence of subglacial liquid water on Mars,” *Science*, vol. 361, no. 6401, pp. 490–493, 2018.
- [27] T. Ono, A. Kumamoto, H. Nakagawa, Y. Yamaguchi, S. Oshigami, A. Yamaji, T. Kobayashi, Y. Kasahara, and H. Oya, “Lunar Radar Sounder observations of subsurface layers under the nearside Maria of the Moon,” *Science*, vol. 323, no. 5916, pp. 909–912, 2009.
- [28] J. Dall *et al.*, “ESA’s polarimetric airborne radar ice sounder (POLARIS): Design and first results,” *IET Radar, Sonar & Navigation*, vol. 4, no. 3, pp. 488–496, 2010.

-
- [29] L. Shi, C. Allen, J. Ledford, F. Rodriguez-Morales, W. Blake, B. Panzer, S. Prokopiack, C. Leuschen, and S. Gogineni, “Multichannel coherent radar depth sounder for NASA operation ice bridge,” in *2010 IEEE International Geoscience and Remote Sensing Symposium*, pp. 1729–1732, IEEE, 2010.
- [30] S. Perna, G. Alberti, P. Berardino, L. Bruzzone, D. Califano, I. Catapano, L. Ciofaniello, E. Donini, C. Esposito, C. Facchinetti, *et al.*, “The ASI Integrated Sounder-SAR System Operating in the UHF-VHF Bands: First Results of the 2018 Helicopter-Borne Morocco Desert Campaign,” *Remote Sensing*, vol. 11, no. 16, p. 1845, 2019.
- [31] M. Lythe and D. Vaughan, “BEDMAP: A new ice thickness and subglacial topographic model of Antarctica,” *Journal of Geophysical Research: Solid Earth*, vol. 106, no. B6, pp. 11335–11351, 2001.
- [32] M. Morlighem, C. N. Williams, E. Rignot, L. An, J. E. Arndt, J. L. Bamber, G. Catania, N. Chauché, J. A. Dowdeswell, B. Dorschel, *et al.*, “Bedmachine v3: Complete bed topography and ocean bathymetry mapping of greenland from multi-beam echo sounding combined with mass conservation,” *Geophysical research letters*, vol. 44, no. 21, pp. 11–051, 2017.
- [33] M. Morlighem, E. Rignot, T. Binder, D. Blankenship, R. Drews, G. Eagles, O. Eisen, F. Ferraccioli, R. Forsberg, P. Fretwell, *et al.*, “Deep glacial troughs and stabilizing ridges unveiled beneath the margins of the antarctic ice sheet,” *Nature Geoscience*, vol. 13, no. 2, pp. 132–137, 2020.
- [34] S. Palmer, J. Dowdeswell, P. Christoffersen, D. Young, D. Blankenship, J. Greenbaum, T. Benham, J. Bamber, and M. Siegert, “Greenland subglacial lakes detected by radar,” *Geophysical Research Letters*, vol. 40, no. 23, pp. 6154–6159, 2013.
- [35] C. Lewis, S. Gogineni, F. Rodriguez-Morales, B. Panzer, T. Stumpf, J. Paden, and C. Leuschen, “Airborne fine-resolution UHF radar: an approach to the study of englacial reflections, firn compaction and ice attenuation rates,” *Journal of Glaciology*, vol. 61, no. 225, pp. 89–100, 2015.
- [36] M. G. Cavitte, D. A. Young, R. Mulvaney, C. Ritz, J. S. Greenbaum, G. Ng, S. D. Kempf, E. Quartini, G. R. Muldoon, J. Paden, *et al.*, “A detailed radiostratigraphic data set for the central east antarctic plateau spanning the last half million years,” *Earth System Science Data Discussions*, pp. 1–27, 2020.
- [37] R. E. Bell, F. Ferraccioli, T. T. Creyts, D. Braaten, H. Corr, I. Das, D. Damaske, N. Frearson, T. Jordan, K. Rose, *et al.*, “Widespread persistent thickening of the

-
- east antarctic ice sheet by freezing from the base,” *Science*, vol. 331, no. 6024, pp. 1592–1595, 2011.
- [38] R. Bell, K. Tinto, I. Das, M. Wolovick, W. Chu, T. Creyts, N. Frearson, A. Abdi, and J. Paden, “Deformation, warming and softening of Greenland’s ice by refreezing meltwater,” *Nature Geoscience*, vol. 7, no. 7, p. 497, 2014.
- [39] D. D. Blankenship, S. D. Kempf, D. A. Young, T. G. Richter, D. M. Schroeder, G. Ng, J. S. Greenbaum, T. van Ommen, R. C. Warner, J. L. Roberts, N. W. Young, E. Lemeur, and M. J. Siegert., “IceBridge HiCARS 2 L1B Time-Tagged Echo Strength Profiles, Version 1. Subset: IR2HI1B_2011349_VCD_JKB2g_DVD01a_000,” 2017. Accessed:2021-02-12.
- [40] L. Carrer and L. Bruzzone, “Automatic enhancement and detection of layering in radar sounder data based on a local scale hidden Markov model and the Viterbi algorithm,” *IEEE Transactions on Geoscience and Remote Sensing*, vol. 55, no. 2, pp. 962–977, 2017.
- [41] E. Donini, S. Thakur, F. Bovolo, and L. Bruzzone, “An automatic approach to map refreezing ice in radar sounder data,” in *Image and Signal Processing for Remote Sensing XXV*, vol. 11155, p. 111551B, International Society for Optics and Photonics, 2019.
- [42] A. Ferro and L. Bruzzone, “Automatic extraction and analysis of ice layering in radar sounder data,” *IEEE Transactions on Geoscience and Remote Sensing*, vol. 51, no. 3, pp. 1622–1634, 2013.
- [43] G. Freeman, A. Bovik, and J. Holt, “Automated detection of near surface Martian ice layers in orbital radar data,” in *Image Analysis & Interpretation (SSIAI), 2010 IEEE Southwest Symposium on*, pp. 117–120, IEEE, 2010.
- [44] A. Ferro and L. Bruzzone, “Analysis of radar sounder signals for the automatic detection and characterization of subsurface features,” *IEEE Transactions on Geoscience and Remote Sensing*, vol. 50, no. 11, pp. 4333–4348, 2012.
- [45] A.-M. Ilisei and L. Bruzzone, “A system for the automatic classification of ice sheet subsurface targets in radar sounder data,” *IEEE Transactions on Geoscience and Remote Sensing*, vol. 53, no. 6, pp. 3260–3277, 2015.
- [46] A.-M. Ilisei, M. Khodadadzadeh, A. Ferro, and L. Bruzzone, “An automatic method for subglacial lake detection in ice sheet radar sounder data,” *IEEE Transactions on Geoscience and Remote Sensing*, 2018.

-
- [47] A. Moussessian, R. Jordan, E. Rodriguez, A. Safaeinili, T. Akins, W. Edelstein, Y. Kim, and S. Gogineni, “A new coherent radar for ice sounding in Greenland,” in *IGARSS 2000. IEEE 2000 International Geoscience and Remote Sensing Symposium. Taking the Pulse of the Planet: The Role of Remote Sensing in Managing the Environment. Proceedings (Cat. No. 00CH37120)*, vol. 2, pp. 484–486, IEEE, 2000.
- [48] L. Carrer, C. Gerekos, F. Bovolo, and L. Bruzzone, “Distributed radar sounder: A novel concept for subsurface investigations using sensors in formation flight,” *IEEE Transactions on Geoscience and Remote Sensing*, pp. 1–19, 2019.
- [49] F. Sauro, R. Pozzobon, M. Massironi, P. De Berardinis, T. Santagata, and J. De Waele, “Lava tubes on earth, moon and mars: A review on their size and morphology revealed by comparative planetology,” *Earth-Science Reviews*, p. 103288, 2020.
- [50] R. Sood, H. J. Melosh, and K. Howell, “Lunar advanced radar orbiter for subsurface sounding (laross): Lava tube exploration mission,” in *AAS/AIAA 26th Space Flight Mechanics Meeting*, 2016.
- [51] G. E. Cushing, C. H. Okubo, and T. N. Titus, “Atypical pit craters on Mars: New insights from THEMIS, CTX, and HiRISE observations,” *Journal of Geophysical Research: Planets*, vol. 120, pp. 1023–1043, 6 2015.
- [52] M. A. Richards, *Fundamentals of radar signal processing*. McGraw-Hill Education, 2014.
- [53] L. Bruzzone, J. Plaut, G. Alberti, D. Blankenship, F. Bovolo, B. Campbell, A. Ferro, Y. Gim, W. Kofman, G. Komatsu, W. McKinnon, G. Mitri, R. Orosei, G. Patterson, D. Plettemeier, and R. Seu, “RIME: Radar for Icy moon Exploration,” in *International Geoscience and Remote Sensing Symposium (IGARSS)*, pp. 3907–3910, 2013.
- [54] F. Russo, M. Cutigni, R. Orosei, C. Taddei, R. Seu, D. Biccari, E. Giacomoni, O. Fuga, and E. Flamini, “An incoherent simulator for the sharad experiment,” in *2008 IEEE Radar Conference*, pp. 1–4, May 2008.
- [55] L. Carrer and L. Bruzzone, “Solving for ambiguities in radar geophysical exploration of planetary bodies by mimicking bats echolocation,” *Nature communications*, vol. 8, no. 1, p. 2248, 2017.
- [56] A. Ferro, A. Pascal, and L. Bruzzone, “A novel technique for the automatic detection of surface clutter returns in radar sounder data,” *IEEE transactions on geoscience and remote sensing*, vol. 51, no. 5, pp. 3037–3055, 2012.

-
- [57] K. Yee, "Numerical solution of initial boundary value problems involving Maxwell's equations in isotropic media," *IEEE Transactions on Antennas and Propagation*, vol. 14, no. 3, pp. 302–307, 1966.
- [58] M. S. Haynes, "Surface and subsurface radar equations for radar sounders," *Annals of Glaciology*, pp. 1–8, 2020.
- [59] C. Abeynayake and M. Tran, "Ground penetrating radar applications in buried improvised explosive device detection," in *2016 International Conference on Electromagnetics in Advanced Applications (ICEAA)*, pp. 564–567, IEEE, 2016.
- [60] J. A. Avila-Olivera and V. H. Garduño-Monroy, "A gpr study of subsidence-creep-fault processes in morelia, michoacán, mexico," *Engineering Geology*, vol. 100, no. 1-2, pp. 69–81, 2008.
- [61] J. Lai, Y. Xu, X. Zhang, L. Xiao, Q. Yan, X. Meng, B. Zhou, Z. Dong, and D. Zhao, "Comparison of dielectric properties and structure of lunar regolith at chang'e-3 and chang'e-4 landing sites revealed by ground-penetrating radar," *Geophysical Research Letters*, vol. 46, no. 22, pp. 12783–12793, 2019.
- [62] L. E. Besaw and P. J. Stimac, "Deep learning algorithms for detecting explosive hazards in ground penetrating radar data," in *Detection and Sensing of Mines, Explosive Objects, and Obscured Targets XIX*, vol. 9072, p. 90720Y, International Society for Optics and Photonics, 2014.
- [63] G. Picardi, D. Biccari, R. Seu, J. Plaut, W. T. K. Johnson, R. L. Jordan, A. Safaeinili, D. A. Gurnett, R. Huff, R. Orosei, O. Bombaci, D. Calabrese, and E. Zampolini, "MARSIS: Mars Advanced Radar for Subsurface and Ionosphere Sounding," in *Mars Express: the Scientific Payload* (A. Wilson and A. Chicarro, eds.), vol. 1240 of *ESA Special Publication*, pp. 51–69, Aug 2004.
- [64] T. Watters *et al.*, "MARSIS radar sounder evidence of buried basins in the northern lowlands of Mars," *Nature*, vol. 444, no. 7121, p. 905, 2006.
- [65] R. Croci, R. Seu, E. Flamini, and E. Russo, "The SHallow RADar (SHARAD) Onboard the NASA MRO Mission," *Proceedings of the IEEE*, vol. 99, pp. 794–807, May 2011.
- [66] J. Plaut, A. Safaeinili, J. Holt, R. Phillips, J. Head, R. Seu, N. Putzig, and A. Frigeri, "Radar evidence for ice in lobate debris aprons in the mid-northern latitudes of Mars," *Geophysical research letters*, vol. 36, no. 2, 2009.

- [67] R. Phillips, M. Zuber, S. Smrekar, M. Mellon, J. Head, K. Tanaka, N. Putzig, S. Milkovich, B. Campbell, J. Plaut, *et al.*, “Mars north polar deposits: Stratigraphy, age, and geodynamical response,” *Science*, vol. 320, no. 5880, pp. 1182–1185, 2008.
- [68] B. Campbell, L. Carter, R. Phillips, J. Plaut, N. Putzig, A. Safaeinili, R. Seu, D. Biccari, A. Egan, and R. Orosei, “SHARAD radar sounding of the Vastitas Borealis Formation in Amazonis Planitia,” *Journal of Geophysical Research: Planets*, vol. 113, no. E12, 2008.
- [69] W. Kofman, A. Hérique, Y. Barbin, V. Barriot, J-Pand Ciarletti, S. Clifford, P. Edenhofer, C. Elachi, C. Eyraud, J.-P. Goutail, *et al.*, “Properties of the 67P/Churyumov-Gerasimenko interior revealed by CONSERT radar,” *Science*, vol. 349, no. 6247, p. aab0639, 2015.
- [70] E. Heggy, E. Palmer, W. Kofman, S. Clifford, K. Richter, and A. Hérique, “Radar properties of comets: Parametric dielectric modeling of Comet 67P/Churyumov-Gerasimenko,” *Icarus*, vol. 221, no. 2, pp. 925–939, 2012.
- [71] O. Grasset, M. Dougherty, A. Coustenis, E. Bunce, C. Erd, D. Titov, M. Blanc, A. Coates, P. Drossart, L. Fletcher, H. Hussmann, R. Jaumann, N. Krupp, J. P. Lebreton, O. Prieto-Ballesteros, P. Tortora, F. Tosi, and T. Van Hoolst, “JUperiter ICy moons Explorer (JUICE): An ESA mission to orbit Ganymede and to characterise the Jupiter system,” *Planetary and Space Science*, vol. 78, pp. 1–21, 2013.
- [72] D. Blankenship, W. Moore, D. Young, and M. Peters, “Radar Imaging of Europa’s Subsurface Properties and Processes: The View from Earth,” in *AGU Fall Meeting Abstracts*, 2007.
- [73] R. Saunders, G. Pettengill, R. Arvidson, W. Sjogren, W. Johnson, and L. Pieri, “The Magellan Venus radar mapping mission,” *Journal of Geophysical Research: Solid Earth*, vol. 95, no. B6, pp. 8339–8355, 1990.
- [74] R. Simpson, G. Tyler, B. Häusler, R. Mattei, and M. Pätzold, “Venus Express bistatic radar: High-elevation anomalous reflectivity,” *Journal of Geophysical Research: Planets*, vol. 114, no. E9, 2009.
- [75] M. Peters, D. Blankenship, and D. Morse, “Analysis techniques for coherent airborne radar sounding: Application to West Antarctic ice streams,” *Journal of Geophysical Research: Solid Earth*, vol. 110, no. B6, pp. n/a–n/a, 2005. B06303.
- [76] R. Bell *et al.*, “Influence of subglacial geology on the onset of a West Antarctic ice stream from aerogeophysical observations,” *Nature*, vol. 394, no. 6688, p. 58, 1998.

-
- [77] M. Peters, D. Blankenship, D. Smith, J. Holt, and S. Kempf, “The distribution and classification of bottom crevasses from radar sounding of a large tabular iceberg,” *IEEE Geoscience and Remote Sensing Letters*, vol. 4, no. 1, pp. 142–146, 2007.
- [78] E. Heggy, A. Fadlilmawla, T. Farr, and M. Al-Rashed, “Probing Shallow Aquifers in Northern Kuwait Using Airborne Sounding Radars,” in *AGU Fall Meeting Abstracts*, 2011.
- [79] E. Heggy, P. Rosen, R. Beatty, T. Freeman, and Y. Gim, “Orbiting Arid Subsurface and Ice Sheet Sounder (OASIS): Exploring desert aquifers and polar ice sheets and their role in current and paleo-climate evolution,” in *2013 IEEE International Geoscience and Remote Sensing Symposium-IGARSS*, pp. 3483–3486, IEEE, 2013.
- [80] D. Young, D. Schroeder, D. Blankenship, S. D. Kempf, and E. Quartini, “The distribution of basal water between Antarctic subglacial lakes from radar sounding,” *Philosophical Transactions of the Royal Society A: Mathematical, Physical and Engineering Sciences*, vol. 374, no. 2059, p. 20140297, 2016.
- [81] D. Schroeder, D. Blankenship, and D. Young, “Evidence for a water system transition beneath Thwaites Glacier, West Antarctica,” *Proceedings of the National Academy of Sciences*, vol. 110, no. 30, pp. 12225–12228, 2013.
- [82] R. Seu, D. Biccari, R. Orosei, L. Lorenzoni, R. Phillips, L. Marinangeli, G. Picardi, A. Masdea, and E. Zampolini, “Sharad: The mro 2005 shallow radar,” *Planetary and Space Science*, vol. 52, no. 1-3, pp. 157–166, 2004.
- [83] T. Ono and H. Oya, “Lunar radar sounder (lrs) experiment on-board the selene spacecraft,” *Earth, planets and space*, vol. 52, no. 9, pp. 629–637, 2000.
- [84] L. Bruzzone, J. J. Plaut, G. Alberti, D. D. Blankenship, F. Bovolo, B. A. Campbell, D. Castelletti, Y. Gim, A. M. Ilisei, W. Kofman, G. Komatsu, W. McKinnon, G. Mitri, A. Moussessian, C. Notarnicola, R. Orosei, G. W. Patterson, E. Pettinelli, and D. Plettemeier, “Jupiter icy moon explorer (juice): Advances in the design of the radar for icy moons (rime),” in *2015 IEEE International Geoscience and Remote Sensing Symposium (IGARSS)*, pp. 1257–1260, July 2015.
- [85] D. Blankenship, T. Ray, J. Plaut, A. Moussessian, W. Patterson, A. Romero-Wolf, C. Grima, D. Young, K. Soderlund, Y. Gim, *et al.*, “Reason for europa,” *cosp*, vol. 42, pp. B5–3, 2018.
- [86] E. Heggy *et al.*, “Radar probing of jovian icy moons: Understanding subsurface water and structure detectability in the JUICE and Europa missions,” *Icarus*, vol. 285, pp. 237–251, 2017.

-
- [87] E. Donini, S. Thakur, F. Bovolo, and L. Bruzzone, "Assessing the Detection Performance on Icy Targets Acquired by an Orbiting Radar Sounder," in *IGARSS 2019-2019 IEEE International Geoscience and Remote Sensing Symposium*, pp. 997–1000, IEEE, 2019.
- [88] J. Li, J. Paden, C. Leuschen, F. Rodriguez-Morales, R. D. Hale, E. J. Arnold, R. Crowe, D. Gomez-Garcia, and P. Gogineni, "High-altitude radar measurements of ice thickness over the Antarctic and Greenland ice sheets as a part of operation Icebridge," *IEEE Transactions on Geoscience and Remote Sensing*, vol. 51, no. 2, pp. 742–754, 2012.
- [89] D. Bekaert, N. Gebert, C.-C. Lin, F. Heliere, J. Dall, A. Kusk, and S. S. Kristensen, "Multichannel surface clutter suppression: East antarctica p-band sar ice sounding in the presence of grating lobes," *Annals of glaciology*, vol. 55, no. 67, pp. 9–21, 2014.
- [90] K. C. Jezek, S. Gogineni, X. Wu, E. Rodriguez, F. Rodriguez-Morales, A. Hoch, A. Freeman, and J. G. Sonntag, "Two-frequency radar experiments for sounding glacier ice and mapping the topography of the glacier bed," *IEEE transactions on geoscience and remote sensing*, vol. 49, no. 3, pp. 920–929, 2010.
- [91] P. Choudhary, J. W. Holt, and S. D. Kempf, "Surface clutter and echo location analysis for the interpretation of sharad data from mars," *IEEE Geoscience and Remote Sensing Letters*, vol. 13, pp. 1285–1289, Sep. 2016.
- [92] Y. A. Ilyushin, R. Orosei, O. Witasse, and B. Sánchez-Cano, "CLUSIM: A synthetic aperture radar clutter simulator for planetary exploration," *Radio Science*, vol. 52, no. 9, pp. 1200–1213, 2017.
- [93] D. Castelletti, D. Schroeder, S. Hensley, C. Grima, G. Ng, D. Young, Y. Gim, L. Bruzzone, A. Moussessian, and D. Blankenship, "Clutter detection using two-channel radar sounder data," in *2015 IEEE International Geoscience and Remote Sensing Symposium (IGARSS)*, pp. 1052–1055, July 2015.
- [94] R. Raney, "Radar sounder: Cross-track polarimetric selectivity," in *7th European Conference on Synthetic Aperture Radar*, pp. 1–4, VDE, 2008.
- [95] G. Lewis, E. Osterberg, R. Hawley, B. Whitmore, H. P. Marshall, and J. Box, "Regional Greenland accumulation variability from Operation IceBridge airborne accumulation radar," *The Cryosphere*, vol. 11, no. 2, pp. 773–788, 2017.

-
- [96] H. Cane, “Spectra of the non-thermal radio radiation from the galactic polar regions,” *Monthly Notices of the Royal Astronomical Society*, vol. 189, no. 3, pp. 465–478, 1979.
- [97] F. Hélière, C.-C. Lin, H. Corr, and D. Vaughan, “Radio echo sounding of pine island glacier, west antarctica: Aperture synthesis processing and analysis of feasibility from space,” *IEEE Transactions on Geoscience and Remote Sensing*, vol. 45, no. 8, pp. 2573–2582, 2007.
- [98] A.-M. Ilisei, J. Li, S. Gogineni, and L. Bruzzone, “Estimation of ice sheet attenuation by using radar sounder and ice core data,” in *Image and Signal Processing for Remote Sensing XXII*, vol. 10004, p. 1000416, International Society for Optics and Photonics, 2016.
- [99] O. Brandt, K. Langley, A. Giannopoulos, S.-E. Hamran, and J. Kohler, “Radar response of firn exposed to seasonal percolation, validation using cores and ftd modeling,” *IEEE transactions on geoscience and remote sensing*, vol. 47, no. 8, pp. 2773–2786, 2009.
- [100] O. Eisen, F. Wilhelms, U. Nixdorf, and H. Miller, “Revealing the nature of radar reflections in ice: Dep-based ftd forward modeling,” *Geophysical research letters*, vol. 30, no. 5, 2003.
- [101] J. A. MacGregor, J. Li, J. D. Paden, G. A. Catania, G. D. Clow, M. A. Fahnestock, S. P. Gogineni, R. E. Grimm, M. Morlighem, S. Nandi, *et al.*, “Radar attenuation and temperature within the greenland ice sheet,” *Journal of Geophysical Research: Earth Surface*, vol. 120, no. 6, pp. 983–1008, 2015.
- [102] K. Matsuoka, J. A. MacGregor, and F. Pattyn, “Predicting radar attenuation within the Antarctic ice sheet,” *Earth and Planetary Science Letters*, vol. 359, pp. 173–183, 2012.
- [103] K. H. Kjær, N. K. Larsen, T. Binder, A. A. Bjørk, O. Eisen, M. A. Fahnestock, S. Funder, A. A. Garde, H. Haack, V. Helm, M. Houmark-Nielsen, K. K. Kjeldsen, S. A. Khan, H. Machguth, I. McDonald, M. Morlighem, J. Mouginot, J. D. Paden, T. E. Waight, C. Weikusat, E. Willerslev, and J. A. MacGregor, “A large impact crater beneath hiawatha glacier in northwest greenland,” *Science Advances*, vol. 4, no. 11, 2018.
- [104] J. A. MacGregor, W. F. Bottke Jr., M. A. Fahnestock, J. P. Harbeck, K. H. Kjær, J. D. Paden, D. E. Stillman, and M. Studinger, “A possible second large subglacial

- impact crater in northwest greenland,” *Geophysical Research Letters*, vol. 46, no. 3, pp. 1496–1504, 2019.
- [105] K. Christianson, R. W. Jacobel, H. J. Horgan, R. B. Alley, S. Anandakrishnan, D. M. Holland, and K. J. DallaSanta, “Basal conditions at the grounding zone of whillans ice stream, west antarctica, from ice-penetrating radar,” *Journal of Geophysical Research: Earth Surface*, vol. 121, no. 11, pp. 1954–1983, 2016.
- [106] J. G. Paren and G. d. Q. Robin, “Internal reflections in polar ice sheets,” *Journal of Glaciology*, vol. 14, no. 71, p. 251–259, 1975.
- [107] S. Fujita, T. Matsuoka, T. Ishida, K. Matsuoka, and S. Mae, “A summary of the complex dielectric permittivity of ice in the megahertz range and its applications for radar sounding of polar ice sheets,” in *Physics of ice core records*, pp. 185–212, Hokkaido University Press, 2000.
- [108] E. Pettinelli, F. Cosciotti, Band Di Paolo, S. Lauro, E. Mattei, R. Orosei, and G. Vannaroni, “Dielectric properties of Jovian satellite ice analogs for subsurface radar exploration: A review,” *Reviews of Geophysics*, vol. 53, no. 3, pp. 593–641, 2015.
- [109] N. Holschuh, K. Christianson, and S. Anandakrishnan, “Power loss in dipping internal reflectors, imaged using ice-penetrating radar,” *Annals of Glaciology*, vol. 55, no. 67, pp. 49–56, 2014.
- [110] M. Haynes, E. Chapin, and D. Schroeder, “Geometric power fall-off in radar sounding,” *IEEE Transactions on Geoscience and Remote Sensing*, vol. 56, no. 11, pp. 6571–6585, 2018.
- [111] S. Xiong *et al.*, “A new method for automatically tracing englacial layers from MCoRDS Data in NW Greenland,” *Remote Sensing*, vol. 10, no. 1, p. 43, 2017.
- [112] E. J. MacKie, D. M. Schroeder, J. Caers, M. R. Siegfried, and C. Scheidt, “Antarctic Topographic Realizations and Geostatistical Modeling Used to Map Subglacial Lakes,” *Journal of Geophysical Research: Earth Surface*, vol. 125, no. 3, p. e2019JF005420, 2020. e2019JF005420 10.1029/2019JF005420.
- [113] P. S. Tan, J. Paden, J. Li, J.-B. Yan, and P. Gogineni, “Robust adaptive MVDR beamforming for processing radar depth sounder data,” in *2013 IEEE International Symposium on Phased Array Systems and Technology*, pp. 622–629, IEEE, 2013.
- [114] I. Howat, A. Negrete, and B. Smith, “The Greenland Ice Mapping Project (GIMP) land classification and surface elevation data sets,” *The Cryosphere*, vol. 8, no. 4, pp. 1509–1518, 2014.

-
- [115] K. Matsuoka, A. Skoglund, and G. Roth, “Quantarctica”, url=<https://doi.org/10.21334/npolar.2018.8516e961>,” 2018.
- [116] I. Howat, “MEaSURES Antarctic Boundaries for IPY 2007-2009 from Satellite Radar, Version 2. Boulder, Colorado USA. NASA National Snow and Ice Data Center Distributed Active Archive Center..” Accessed:2019-09-12.
- [117] E. Rignot, S. Jacobs, J. Mouginot, and B. Scheuchl, “Ice-Shelf Melting Around Antarctica,” *Science*, vol. 341, no. 6143, pp. 266–270, 2013.
- [118] A. Wright and M. Siegert, “A fourth inventory of Antarctic subglacial lakes,” *Antarctic Science*, vol. 24, no. 6, pp. 659–664, 2012.
- [119] D. Blankenship, S. Carter, J. Holt, D. Morse, M. Peters, and D. Young, “Antarctic subglacial lake classification inventory,” *Boulder, Colorado USA, National Snow and Ice Data Center*, 2009.
- [120] M. Studinger, R. Bell, G. Karner, A. Tikku, J. Holt, D. Morse, T. Richter, S. Kempf, M. Peters, D. Blankenship, *et al.*, “Ice cover, landscape setting, and geological framework of Lake Vostok, East Antarctica,” *Earth and Planetary Science Letters*, vol. 205, no. 3-4, pp. 195–210, 2003.
- [121] A. Kendrick, D. Schroeder, W. Chu, T. J. Young, P. Christoffersen, J. Todd, S. Doyle, J. Box, A. Hubbard, B. Hubbard, *et al.*, “Surface meltwater impounded by seasonal englacial storage in West Greenland,” *Geophysical Research Letters*, vol. 45, no. 19, pp. 10–474, 2018.
- [122] W. Chu, D. M. Schroeder, and M. R. Siegfried, “Retrieval of Englacial Firn Aquifer Thickness From Ice-Penetrating Radar Sounding in Southeastern Greenland,” *Geophysical Research Letters*, vol. 45, no. 21, pp. 11,770–11,778, 2018.
- [123] H. A. Fricker, S. Popov, I. Allison, and N. Young, “Distribution of marine ice beneath the amery ice shelf,” *Geophysical Research Letters*, vol. 28, no. 11, pp. 2241–2244, 2001.
- [124] H. Liu, K. C. Jezek, B. Li, and Z. Zhao, “Radarsat antarctic mapping project digital elevation model, version 2,” 2015.
- [125] M. K. Shepard, B. A. Campbell, M. H. Bulmer, T. G. Farr, L. R. Gaddis, and J. J. Plaut, “The roughness of natural terrain: A planetary and remote sensing perspective,” *Journal of Geophysical Research: Planets*, vol. 106, no. E12, pp. 32777–32795, 2001.

-
- [126] J. A. Ogilvy and H. M. Merklinger, “Theory of wave scattering from random rough surfaces,” 1991.
- [127] C. Porter, P. Morin, I. Howat, M.-J. Noh, B. Bates, K. Peterman, S. Keeseey, M. Schlenk, J. Gardiner, K. Tomko, M. Willis, C. Kelleher, M. Cloutier, E. Husby, S. Foga, H. Nakamura, M. Platson, J. Wethington, Michael, C. Williamson, G. Bauer, J. Enos, G. Arnold, W. Kramer, P. Becker, A. Doshi, C. D’Souza, P. Cummens, F. Laurier, and M. Bojesen, “ArcticDEM, Polar Geospatial Center, Harvard Dataverse, V1, 2018.” Accessed:2021-02-02.
- [128] I. M. Howat, C. Porter, B. E. Smith, M.-J. Noh, and P. Morin, “The reference elevation model of Antarctica,” *The Cryosphere*, vol. 13, no. 2, pp. 665–674, 2019.
- [129] C. J. van der Veen, Y. Ahn, B. M. Csatho, E. Mosley-Thompson, and W. B. Krabill, “Surface roughness over the northern half of the Greenland Ice Sheet from airborne laser altimetry,” *Journal of Geophysical Research: Earth Surface*, vol. 114, no. F1, 2009.
- [130] D. Yi, H. J. Zwally, and X. Sun, “ICESat measurement of Greenland ice sheet surface slope and roughness,” *Annals of Glaciology*, vol. 42, pp. 83–89, 2005.
- [131] M. G. Cavitte, D. D. Blankenship, D. A. Young, D. M. Schroeder, F. Parrenin, E. Lemeur, J. A. Macgregor, and M. J. Siegert, “Deep radiostratigraphy of the East Antarctic plateau: connecting the Dome C and Vostok ice core sites,” *Journal of Glaciology*, vol. 62, no. 232, p. 323–334, 2016.
- [132] H. Miyamoto, J. Haruyama, T. Kobayashi, K. Suzuki, T. Okada, T. Nishibori, A. P. Showman, R. Lorenz, K. Mogi, D. A. Crown, J. A. P. Rodriguez, S. Rokugawa, T. Tokunaga, and K. Masumoto, “Mapping the structure and depth of lava tubes using ground penetrating radar,” *Geophysical Research Letters*, vol. 32, p. L21316, Nov. 2005.
- [133] A. S. Arya, P. R. Rudravaram, G. Thangjam, A. Prof, and k. k. Seelin, “Detection of potential site for future human habitability on the Moon using Chandrayaan-1 data,” *Current science*, vol. 100, pp. 524–529, Feb. 2011.
- [134] G. Hulme, “The interpretation of lava flow morphology,” *Geophysical Journal International*, vol. 39, no. 2, pp. 361–383, 1974.
- [135] S. E. Braden, J. D. Stopar, M. S. Robinson, S. J. Lawrence, C. H. van der Bogert, and H. Hiesinger, “Evidence for basaltic volcanism on the Moon within the past 100 million years,” *Nature Geoscience*, vol. 7, pp. 787–791, Nov. 2014.

-
- [136] S. J. Robbins, G. Di Achille, and B. M. Hynek, “The volcanic history of mars: High-resolution crater-based studies of the calderas of 20 volcanoes,” *Icarus*, vol. 211, no. 2, pp. 1179–1203, 2011.
- [137] J. J. Papike, G. Ryder, and C. K. Shearer, “Lunar samples,” *Reviews in Mineralogy and Geochemistry*, vol. 36, pp. 5.1–5.234, Jan. 1998.
- [138] S. Kempe and M. S. Werner, “The kuka’iau cave, mauna kea, hawaii, created by water erosion: A new hawaiian cave type,” *Journal of Cave and Karst Studies*, vol. 65, no. 1, pp. 53–67, 2003.
- [139] C. R. Rowell, A. Pidlisecky, J. D. Irving, and R. J. Ferguson, “Characterization of lava tubes using ground penetrating radar at craters of the moon national monument, usa.,” *Tech. rep. CREWES Research Report*, vol. 22, pp. 1–18, 2010.
- [140] D. M. Blair, L. Chappaz, R. Sood, C. Milbury, A. Bobet, H. J. Melosh, K. C. Howell, and A. M. Freed, “The structural stability of lunar lava tubes,” *Icarus*, vol. 282, pp. 47–55, Jan. 2017.
- [141] A. E. Theinat, A. Modiriasari, A. Bobet, J. Melosh, S. Dyke, J. Ramirez, A. Maghareh, and D. Gomez, “Geometry and Structural Stability of Lunar Lava Tubes,” in *2018 AIAA SPACE and Astronautics Forum and Exposition*, (Reston, Virginia), American Institute of Aeronautics and Astronautics, 9 2018.
- [142] H. Benaroya, “Lunar habitats: A brief overview of issues and concepts,” *REACH*, vol. 7, pp. 14–33, 2017.
- [143] G. Cushing, “Candidate cave entrances on Mars,” *Journal of Cave and Karst Studies*, vol. 74, pp. 33–47, 4 2012.
- [144] F. Horz, “Lava tubes-potential shelters for habitats,” in *Lunar bases and space activities of the 21st century*, pp. 405–412, 1985.
- [145] P. Boston, R. Frederick, S. Welch, J. Werker, T. Meyer, B. Sprungman, V. Hildreth-Werker, and S. Thompson, “Extraterrestrial subsurface technology test bed: Human use and scientific value of martian caves,” in *AIP Conference Proceedings*, vol. 699, pp. 1007–1018, American Institute of Physics, 2004.
- [146] D. Rapp, “Radiation effects and shielding requirements in human missions to the moon and mars,” *The Mars Journal*, vol. 2, pp. 46–71, 01 2006.
- [147] R. J. L evell e and S. Datta, “Lava tubes and basaltic caves as astrobiological targets on Earth and Mars: A review,” *Planetary and Space Science*, vol. 58, pp. 592–598, 3 2010.

-
- [148] A. Z. Miller, J. L. Gonzalez-Pimentel, S. Stahl, S. Castro-Wallace, F. Sauro, R. Pozzobon, M. Massironi, M. Maurer, L. Bessone, and J. Martinez-Frias, “Exploring possible mars-like microbial life in a lava tube from lanzarote: preliminary results of in-situ dna-based analysis as part of the pangaea-x test campaign,” *EGUGA*, p. 1258, 2018.
- [149] D. P. Cruikshank and C. A. Wood, “Lunar rilles and Hawaiian volcanic features: Possible analogues,” *The moon*, vol. 3, pp. 412–447, Mar. 1972.
- [150] A. G. Taylor and A. Gibbs, “Automated search for lunar lava tubes in the clementine dataset,” in *New Views of the Moon: Integrated Remotely Sensed, Geophysical, and Sample Datasets*, p. 70, 1998.
- [151] S. J. Lawrence, J. D. Stopar, B. R. Hawke, B. T. Greenhagen, J. T. Cahill, J. L. Bandfield, B. L. Jolliff, B. W. Denevi, M. S. Robinson, T. D. Glotch, *et al.*, “Lro observations of morphology and surface roughness of volcanic cones and lobate lava flows in the marius hills,” *Journal of Geophysical Research: Planets*, vol. 118, no. 4, pp. 615–634, 2013.
- [152] R. V. Wagner and M. S. Robinson, “Distribution, formation mechanisms, and significance of lunar pits,” *Icarus*, vol. 237, pp. 52–60, July 2014.
- [153] D. Wyrick, D. A. Ferrill, A. P. Morris, S. L. Colton, and D. W. Sims, “Distribution, morphology, and origins of martian pit crater chains,” *Journal of Geophysical Research: Planets*, vol. 109, no. E6, 2004.
- [154] G. E. Cushing, T. N. Titus, J. J. Wynne, and P. R. Christensen, “THEMIS observes possible cave skylights on Mars,” *Geophysical Research Letters*, vol. 34, p. L17201, 9 2007.
- [155] L. Chappaz, R. Sood, H. J. Melosh, K. C. Howell, D. M. Blair, C. Milbury, and M. T. Zuber, “Evidence of large empty lava tubes on the Moon using GRAIL gravity,” *Geophysical Research Letters*, vol. 44, pp. 105–112, 1 2017.
- [156] T. Kaku, J. Haruyama, W. Miyake, A. Kumamoto, K. Ishiyama, T. Nishibori, K. Yamamoto, S. T. Crites, T. Michikami, Y. Yokota, R. Sood, H. J. Melosh, L. Chappaz, and K. C. Howell, “Detection of Intact Lava Tubes at Marius Hills on the Moon by SELENE (Kaguya) Lunar Radar Sounder,” *Geophysical Research Letters*, vol. 44, pp. 155–160, 10 2017.
- [157] T. Kobayashi, J.-H. Kim, S. R. Lee, and K.-Y. Song, “Nadir detection of lunar lava tube by kaguya lunar radar sounder,” *IEEE Transactions on Geoscience and Remote Sensing*, 2020.

-
- [158] E. Donini, F. Bovolo, C. Gerekos, L. Carrer, and L. Bruzzone, “An Approach to Lava Tube Detection in Radar Sounder Data of the Moon,” in *IGARSS 2018-2018 IEEE International Geoscience and Remote Sensing Symposium*, pp. 8424–8427, IEEE, 2018.
- [159] A. K. Theinat, A. Modiriasari, A. Bobet, H. J. Melosh, S. J. Dyke, J. Ramirez, A. Maghareh, and D. Gomez, “Lunar lava tubes: Morphology to structural stability,” *Icarus*, vol. 338, p. 113442, 2020.
- [160] D. Strangway and G. Olhoeft, “Electrical properties of planetary surfaces,” *Philosophical Transactions of the Royal Society of London. Series A, Mathematical and Physical Sciences*, vol. 285, no. 1327, pp. 441–450, 1977.
- [161] L. Carrer, C. Gerekos, and L. Bruzzone, “A multi-frequency radar sounder for lava tubes detection on the Moon: Design, performance assessment and simulations,” *Planetary and Space Science*, vol. 152, pp. 1–17, 2018.
- [162] F. J. Harris, “On the use of windows for harmonic analysis with the discrete fourier transform,” *Proceedings of the IEEE*, vol. 66, no. 1, pp. 51–83, 1978.
- [163] S. Esmaceli, S. Kruse, S. Jazayeri, P. Whelley, E. Bell, J. Richardson, W. Garry, and K. Young, “Resolution of lava tubes with ground penetrating radar: The tubex project,” *Journal of Geophysical Research: Planets*, vol. 125, no. 5, p. e2019JE006138, 2020.
- [164] P. Martin Larsen, “Industrial applications of fuzzy logic control,” *International Journal of Man-Machine Studies*, vol. 12, pp. 3–10, Jan. 1980.
- [165] D. Chung, W. Westphal, and G. Simmons, “Dielectric properties of apollo 11 lunar samples and their comparison with earth materials,” *Journal of Geophysical Research*, vol. 75, no. 32, pp. 6524–6531, 1970.
- [166] S. Lawrence, J. D. Stopar, R. B. Hawke, B. W. Denevi, M. S. Robinson, T. Giguere, and B. Jolliff, “LROC Observations of Geologic Features in the Marius Hills,” *AGU Fall Meeting Abstracts*, Dec. 2009.
- [167] R. Greeley, “Lava tubes and channels in the lunar Marius Hills,” *Earth Moon and Planets*, vol. 3, pp. 289–314, Jan. 1971.
- [168] R. Sood, L. Chappaz, H. Melosh, K. Howell, and C. Milbury, “Detection of buried empty lunar lava tubes using grail gravity data,” in *Lunar and Planetary Science Conference*, p. 1509, 2016.

-
- [169] J. Haruyama, K. Hioki, M. Shirao, T. Morota, H. Hiesinger, C. H. van der Bogert, H. Miyamoto, A. Iwasaki, Y. Yokota, M. Ohtake, T. Matsunaga, S. Hara, S. Nakanotani, and C. M. Pieters, “Possible lunar lava tube skylight observed by SELENE cameras,” *Geophysical Research Letters*, vol. 36, p. L21206, 11 2009.
- [170] B. E. Walden, T. L. Billings, C. L. York, S. L. Gillett, and M. V. Herbert, “Utility of lava tubes on other worlds,” in *Using in situ Resources for Construction of Planetary Outposts*, p. 16, 1998.
- [171] W. S. Kiefer, “Gravity constraints on the subsurface structure of the marius hills: The magmatic plumbing of the largest lunar volcanic dome complex,” *Journal of Geophysical Research: Planets*, vol. 118, no. 4, pp. 733–745, 2013.
- [172] J. Haruyama, T. Kaku, R. Shinoda, W. Miyake, A. Kumamoto, K. Ishiyama, T. Nishibori, K. Yamamoto, K. Kurosawa, A. Suzuki, S. Crites, T. Michikami, Y. Yokota, R. Sood, J. Melosh, L. Chappaz, and K. Howell, “Detection of lunar lava tubes by lunar radar sounder onboard selene (kaguya),” in *Lunar and Planetary Science Conference*, p. 1711, 2017.
- [173] T. Kobayashi, J.-H. Kim, S. R. Lee, A. Kumamoto, H. Nakagawa, S. Oshigami, H. Oya, Y. Yamaguchi, A. Yamaji, and T. Ono, “Synthetic aperture radar processing of kaguya lunar radar sounder data for lunar subsurface imaging,” *IEEE Transactions on Geoscience and Remote Sensing*, vol. 50, no. 6, pp. 2161–2174, 2012.
- [174] M. M. Bennett and N. F. Glasser, *Glacial geology: ice sheets and landforms*. John Wiley & Sons, 2011.
- [175] R. E. Bell, M. Studinger, C. A. Shuman, M. A. Fahnstock, and I. Joughin, “Large subglacial lakes in east antarctica at the onset of fast-flowing ice streams,” *Nature*, vol. 445, no. 7130, p. 904, 2007.
- [176] O. Alemany, J. Chappellaz, J. Triest, M. Calzas, O. Cattani, J. Chemin, Q. Desbois, T. Desbois, R. Duphil, S. Falourd, *et al.*, “The subglacier drilling probe: concept and design,” *Annals of Glaciology*, vol. 55, no. 68, pp. 233–242, 2014.
- [177] Q. Schiermeier, “Speedy antarctic drills start hunt for earth’s oldest ice,” *Nature News*, vol. 540, no. 7631, p. 18, 2016.
- [178] C. Panton and N. B. Karlsson, “Automated mapping of near bed radio-echo layer disruptions in the greenland ice sheet,” *Earth and Planetary Science Letters*, vol. 432, pp. 323–331, 2015.

-
- [179] C. F. Dow, N. B. Karlsson, and M. A. Werder, “Limited impact of subglacial supercooling freeze-on for greenland ice sheet stratigraphy,” *Geophysical Research Letters*, vol. 45, no. 3, pp. 1481–1489, 2018.
- [180] A.-M. Ilisei, M. Khodadadzadeh, E. Dalsasso, and L. Bruzzone, “Automatic detection of subglacial lakes in radar sounder data acquired in Antarctica,” in *Image and Signal Processing for Remote Sensing XXIII*, vol. 10427, p. 1042718, International Society for Optics and Photonics, 2017.
- [181] M. Schäfer, T. Zwinger, P. Christoffersen, F. Gillet-Chaulet, K. Laakso, R. Pettersson, V. A. Pohjola, T. Strozzi, and J. C. Moore, “Sensitivity of basal conditions in an inverse model: Vestfonna ice cap, nordaustlandet/svalbard,” *The Cryosphere*, vol. 6, pp. 771–783, 2013.
- [182] S. P. Carter, H. A. Fricker, and M. R. Siegfried, “Antarctic subglacial lakes drain through sediment-floored canals: theory and model testing on real and idealized domains,” *The Cryosphere*, vol. 11, no. 1, p. 381, 2017.
- [183] L. C. Sime, R. C. Hindmarsh, and H. Corr, “Automated processing to derive dip angles of englacial radar reflectors in ice sheets,” *Journal of Glaciology*, vol. 57, no. 202, pp. 260–266, 2011.
- [184] M. L. Goldberg, D. M. Schroeder, D. Castelletti, E. Mantelli, N. Ross, and M. J. Siegert, “Automated detection and characterization of antarctic basal units using radar sounding data: demonstration in institute ice stream, west antarctica,” *Annals of Glaciology*, pp. 1–7, 2020.
- [185] J. Long, E. Shelhamer, and T. Darrell, “Fully convolutional networks for semantic segmentation,” in *Proceedings of the IEEE conference on computer vision and pattern recognition*, pp. 3431–3440, 2015.
- [186] O. Tasar, Y. Tarabalka, and P. Alliez, “Incremental learning for semantic segmentation of large-scale remote sensing data,” *IEEE Journal of Selected Topics in Applied Earth Observations and Remote Sensing*, vol. 12, no. 9, pp. 3524–3537, 2019.
- [187] V. Badrinarayanan, A. Kendall, and R. Cipolla, “Segnet: A deep convolutional encoder-decoder architecture for image segmentation,” *IEEE transactions on pattern analysis and machine intelligence*, vol. 39, no. 12, pp. 2481–2495, 2017.
- [188] R. Girshick, J. Donahue, T. Darrell, and J. Malik, “Rich feature hierarchies for accurate object detection and semantic segmentation,” in *Proceedings of the IEEE conference on computer vision and pattern recognition*, pp. 580–587, 2014.

-
- [189] O. Ronneberger, P. Fischer, and T. Brox, “U-net: Convolutional networks for biomedical image segmentation,” in *International Conference on Medical image computing and computer-assisted intervention*, pp. 234–241, Springer, 2015.
- [190] L.-C. Chen, G. Papandreou, I. Kokkinos, K. Murphy, and A. L. Yuille, “Deeplab: Semantic image segmentation with deep convolutional nets, atrous convolution, and fully connected crfs,” *IEEE transactions on pattern analysis and machine intelligence*, vol. 40, no. 4, pp. 834–848, 2017.
- [191] O. Oktay, J. Schlemper, L. L. Folgoc, M. Lee, M. Heinrich, K. Misawa, K. Mori, S. McDonagh, N. Y. Hammerla, B. Kainz, *et al.*, “Attention u-net: Learning where to look for the pancreas,” *arXiv preprint arXiv:1804.03999*, 2018.
- [192] P. Guo, X. Su, H. Zhang, M. Wang, and F. Bao, “A multi-scaled receptive field learning approach for medical image segmentation,” in *ICASSP 2020-2020 IEEE International Conference on Acoustics, Speech and Signal Processing (ICASSP)*, pp. 1414–1418, IEEE, 2020.
- [193] H. Kamangir, M. Rahnemoonfar, D. Dobbs, J. Paden, and G. Fox, “Deep hybrid wavelet network for ice boundary detection in radra imagery,” in *IGARSS 2018-2018 IEEE International Geoscience and Remote Sensing Symposium*, pp. 3449–3452, IEEE, 2018.
- [194] M. Yari, M. Rahnemoonfar, J. Paden, I. Oluwanisola, L. Koenig, and L. Montgomery, “Smart tracking of internal layers of ice in radar data via multi-scale learning,” in *2019 IEEE International Conference on Big Data (Big Data)*, pp. 5462–5468, IEEE, 2019.
- [195] M. Rahnemoonfar, J. Johnson, and J. Paden, “Ai radar sensor: Creating radar depth sounder images based on generative adversarial network,” *Sensors*, vol. 19, no. 24, p. 5479, 2019.
- [196] Y. Cai, S. Hu, S. Lang, Y. Guo, and J. Liu, “End-to-end classification network for ice sheet subsurface targets in radar imagery,” *Applied Sciences*, vol. 10, no. 7, p. 2501, 2020.
- [197] G. Oswald and S. Gogineni, “Recovery of subglacial water extent from greenland radar survey data,” *Journal of Glaciology*, vol. 54, no. 184, pp. 94–106, 2008.
- [198] I. Goodfellow, Y. Bengio, and A. Courville, *Deep learning*. MIT press, 2016.
- [199] J. Schlemper, O. Oktay, M. Schaap, M. Heinrich, B. Kainz, B. Glocker, and D. Rueckert, “Attention gated networks: Learning to leverage salient regions in medical images,” *Medical image analysis*, vol. 53, pp. 197–207, 2019.

-
- [200] F. Yu and V. Koltun, “Multi-scale context aggregation by dilated convolutions,” *arXiv preprint arXiv:1511.07122*, 2015.
- [201] T. Shen, T. Zhou, G. Long, J. Jiang, S. Pan, and C. Zhang, “Disan: Directional self-attention network for rnn/cnn-free language understanding,” *arXiv preprint arXiv:1709.04696*, 2017.
- [202] D. Erhan, A. Courville, Y. Bengio, and P. Vincent, “Why does unsupervised pre-training help deep learning?,” in *Proceedings of the thirteenth international conference on artificial intelligence and statistics*, pp. 201–208, JMLR Workshop and Conference Proceedings, 2010.
- [203] A. Kanazaki, “Unsupervised image segmentation by backpropagation,” in *2018 IEEE international conference on acoustics, speech and signal processing (ICASSP)*, pp. 1543–1547, IEEE, 2018.
- [204] J. Serra, *Image Analysis and Mathematical Morphology*. USA: Academic Press, Inc., 1983.
- [205] D. P. Kingma and J. Ba, “Adam: A method for stochastic optimization,” *arXiv preprint arXiv:1412.6980*, 2014.
- [206] A.-M. Ilisei and L. Bruzzone, “A model-based technique for the automatic detection of earth continental ice subsurface targets in radar sounder data,” *IEEE Geoscience and Remote Sensing Letters*, vol. 11, no. 11, pp. 1911–1915, 2014.
- [207] M. Rahnemounfar, M. Yari, J. J. L. Koenig, and O. Ibikunle, “Deep multi-scale learning for automatic tracking of internal layers of ice in radar data,” *Journal of Glaciology*, pp. 1–10, 2020.
- [208] W. J. Leong and H. J. Horgan, “Deepbedmap: a deep neural network for resolving the bed topography of antarctica,” *The Cryosphere*, vol. 14, no. 11, pp. 3687–3705, 2020.
- [209] X. Xia and B. Kulis, “W-net: A deep model for fully unsupervised image segmentation,” *arXiv preprint arXiv:1711.08506*, 2017.
- [210] J. Lin, “Divergence measures based on the shannon entropy,” *IEEE Transactions on Information theory*, vol. 37, no. 1, pp. 145–151, 1991.
- [211] N. Otsu, “A threshold selection method from gray-level histograms,” *IEEE transactions on systems, man, and cybernetics*, vol. 9, no. 1, pp. 62–66, 1979.

-
- [212] F. Chollet, “Xception: Deep learning with depthwise separable convolutions,” in *Proceedings of the IEEE conference on computer vision and pattern recognition*, pp. 1251–1258, 2017.
- [213] J. Shi and J. Malik, “Normalized cuts and image segmentation,” *IEEE Transactions on pattern analysis and machine intelligence*, vol. 22, no. 8, pp. 888–905, 2000.
- [214] S. Saha, F. Bovolo, and L. Bruzzone, “Unsupervised deep change vector analysis for multiple-change detection in vhr images,” *IEEE Transactions on Geoscience and Remote Sensing*, vol. 57, no. 6, pp. 3677–3693, 2019.
- [215] D. Schleher, “Radar detection in weibull clutter,” *IEEE Transactions on Aerospace and Electronic Systems*, no. 6, pp. 736–743, 1976.
- [216] A. Papoulis and S. U. Pillai, *Probability, random variables, and stochastic processes*. Tata McGraw-Hill Education, 2002.
- [217] J. A. Greenwood and D. Durand, “Aids for fitting the gamma distribution by maximum likelihood,” *Technometrics*, vol. 2, no. 1, pp. 55–65, 1960.
- [218] M. Roth, *On the multivariate distribution*. Linköping University Electronic Press, 2012.
- [219] J. H. Gove and S. E. Fairweather, “Maximum-likelihood estimation of weibull function parameters using a general interactive optimizer and grouped data,” *Forest Ecology and Management*, vol. 28, no. 1, pp. 61–69, 1989.
- [220] K. He, H. Fan, Y. Wu, S. Xie, and R. Girshick, “Momentum contrast for unsupervised visual representation learning,” in *Proceedings of the IEEE/CVF Conference on Computer Vision and Pattern Recognition*, pp. 9729–9738, 2020.
- [221] A.-M. Ilisei and L. Bruzzone, “A method for automatic three-dimensional reconstruction of ice sheets by using radar sounder and altimeter data,” *IEEE Journal of Selected Topics in Applied Earth Observations and Remote Sensing*, vol. 11, no. 2, pp. 401–415, 2018.

List of Abbreviations

ARS airborne radar sounder.

ASI Agenzia Spaziale Italiana.

CONSERT Comet Nucleus Sounding Experiment by Radiowave Transmission.

EFZ echo-free zone.

EM electromagnetic.

EORS Earth-Orbiting Radar Sounder.

ESA European Space Agency.

GPR ground penetrating radar.

GRAIL Gravity Recovery and Interior Laboratory.

IRH Internal Reflecting Horizons.

JAXA Japan Aerospace Exploration Agency.

JUICE JUpter ICy moons Explorer.

KL Kullback-Leibler.

LROC Lunar Reconnaissance Orbiter Camera.

LRS Lunar Radar Sounder.

MARSIS Mars Advanced Radar for Subsurface and Ionosphere Sounding.

MCoRDS Multi-channel Coherent Radar Depth Sounder.

MRO Mars Reconnaissance Orbiter.

NASA National Aeronautics and Space Administration.

NPLD North Polar Layered Deposits.

OASIS Orbiting Arid Subsurface and Ice Sheet Sounder.

pdf probability density function.

PRF pulse repetition frequency.

PRI pulse repetition interval.

RADAR RAdio Detection And Ranging.

REASON Radar for Europa Assessment and Sounding: Ocean to Near-surface.

RIME Radar for Icy Moons Exploration.

RS radar sounder.

RTT round trip time.

SAR Synthetic Aperture Radar.

SCAR Scientific Committee on Antarctic Research.

SCR signal-to-clutter ratio.

SELENE Selenological and Engineering Explorer.

SHARAD Shallow Radar.

SNR signal-to-noise ratio.

SPLD South Polar Layered Deposits.

SRPs Scientific Research Programmes.

SRS Subsurface Radar Sounder.

STRATUS SaTellite Radar sounder for eArTh sUbsurface Sensing.

SVM support vector machine.

WCRP World Climate Research Programme.

List of Symbols

General symbols

$k_{Boltzmann}$	Boltzmann constant
c	Speed of light in vacuum
v_{medium}	Speed of light in the medium
ϵ_0	Dielectric permittivity of free-space
μ_0	Dielectric permeability of free-space
δ	Loss Tangent
ϵ_r	Relative dielectric permittivity
μ_r	Relative dielectric permeability
ϵ_r^{void}	Relative dielectric constant in free-space
ϵ_r^{rock}	Relative dielectric constant of the rock
δ_{rock}	Loss tangent of the rock
Re{ }	Real part of the complex term in the braces
Im{ }	Imaginary part of the complex term in the braces

Symbols related to the electromagnetic wave

P_r	Received by the radar antenna
P_t	Received by the radar antenna
$P_{r,A}(r_A, a_A)$	ARS received power radargrams
$P_{r,E}(r_E, a_E)$	Simulated EORS received power radargrams
f_c	Central frequency
BW	Bandwidth of the signal
λ	Wavelength

h	Height of the platform
A_{ill}	Parameter related to the geometric properties of the target
σ^0	Backscattered coefficient
G	Radar system gain
B_D	Doppler focusing bandwidth
L_a	Length of the synthetic antenna
V_x	Velocity of the moving platform
T_i	Integration time defined as the time interval that the radar illuminates a point on the ground
D_F	Diameter of the first Fresnel zone

Symbols related to the radargrams

ρ_x^f	Radargram along-track focused resolution
ρ_x^{uf}	Radargram along-track unfocused resolution
ρ_y	Radargram across-track resolution
ρ_y^{flat}	Radargram across-track resolution for a flat surface
ρ_y^{rough}	Radargram across-track resolution for a rough surface
ρ_z	Radargram range resolution
R_C	Complex power radargram
R , $R(a, r)$	Real part of the power radargram
$R_I(a, r)$	Imaginary part of the power radargram
$A(a, r)$	Amplitude radargram
$\Phi(a, r)$	Phase radargram
$R_{pred}(a, r)$	Predicted radargram
$R_{dB}(a, r)$	Power radargram in decibel

Symbols related to the distance

x	Distance in the along-track direction
y	Distance in the cross-track direction
z	Distance in the nadir/range direction representing the depth below the surface

$z(r, a)$ Depth of the echo sample at index position (r, a) from $r = 1$

Symbols representing indices and numbers

(r, a) Indices for the range and the along-track/azimuth coordinates

r_A Row index of reference analog (ARS) radargram

r_E Row index of simulated Earth-orbiting (EORS) radargram

N_S Number of rows (samples) in the radargram

a_A Column index of the reference analog (ARS) radargram

a_E Column index of simulated Earth-orbiting (EORS) radargram

N_T Number of columns (radar traces) in the radargram

Symbols related to the RS performance assessment

$\gamma_A(z)$ ARS target propagation factor

$\gamma_E(z)$ EORS target propagation factor

$\hat{\gamma}_A(z)$ ARS estimated target propagation factor

$\hat{\gamma}_E(z)$ EORS estimated target propagation factor

H_A ARS platform altitude

H_E EORS platform altitude

G_A ARS one-way antenna gain

G_E EORS one-way antenna gain

λ_A ARS wavelength

λ_E EORS wavelength

$P_{t,A}$ ARS transmitted signal power

$P_{t,E}$ EORS transmitted signal power

$G_{r,A}$ ARS range processing gain

$G_{r,E}$ EORS range processing gain

$f_{c,A}$ ARS central frequency

$f_{c,E}$ EORS central frequency

$\Gamma_A(r_A, a_A)$ ARS target propagation factors

$\Gamma_E(r_A, a_A)$ EORS target propagation factors

n_+	labels assigned by the classifier to the basal interface samples corresponding to lakes
n_-	labels assigned by the classifier to the basal interface samples corresponding to non-lakes
c_{RBF}, γ_{RBF}	kernel parameters of the subglacial lakes SVM classifier
ℓ_{ARS}	predicted labels of the basal interface obtained by applying the SVM classifier to the ARS data
ℓ_{EORS}	predicted labels of the basal interface obtained by applying the SVM classifier to the EORS data
ξ_{ARS}	vectors representing correct prediction of the nature of the basal interface in the ARS data
ξ_{EORS}	vectors representing correct prediction of the nature of the basal interface in the EORS data
T_{cmb}	Galactic noise temperature, where CMB stands for Cosmic Microwave Background
$\rho(z, a_A)$	target reflectivity profile for the frame a_A as a function of depth z
$\alpha(z)$	target attenuation profile independent of the frequency
$\hat{\alpha}(z)$	estimated target attenuation profile independent of the frequency
L	label corresponding to the geographical zone (geolabel)
N_E^L	total number of frames corresponding to the label L
a_E^L	frame index corresponding to the label L
b	simulation index corresponding to each hypothesis of the variable design parameter
N_b	total number of hypotheses of the variable design parameter
SNR_b	hypotheses values of the variable design parameter – SNR budget
$\theta_b(a_E)$	IRH detection performance metric estimated as the probability of IRH detection for the EORS frame a_E corresponding to the simulation index b
θ	IRH detection probability threshold
$\chi_b^L(\theta)$	cumulative fraction of frames with probability of IRH detection greater than θ for the geolabel L and simulation index b
$\beta_b(a_E)$	basal interface detection metric for each frame a_E and simulation index b

$\Lambda_b(c_E)$	lake detection metric comparing the accuracy of the subglacial lake detection for the EORS and ARS radargrams
β_b^L	cumulative basal interface detection metric, i.e. fraction of frames for which the basal interface detection metric is equal to 1 for the geolabel L and simulation index b
θ_{min}^L	minimum required per-frame probability of IRH detection for the geolabel L
χ_{min}^L	requirement on the cumulative fraction of frames satisfying the per-frame probability of IRH detection for the geolabel L
β_{min}^L	requirement on the basal interface detectability for the geolabel L
SNR_{min}	minimum required SNR budget for a given set of mission requirements and estimated for each geolabel
SNR_{design}	best design parameter that maximizes the performance for all geolabels for a given set of mission requirements

Symbols related to the data analysis

Ω_C	Set of the labels
N_C	Number of classes
ω_c	Label of the c -th class
ω_g	Label indicating the surface class
ω_{LT}^c	Label indicating the ceiling class
ω_{LT}^f	Label indicating the floor class
ω_n	Label indicating features that are related neither to buried cavities nor to the surface but probably generated by the surface topography and other volcanic structures
ω_1	Label for the englacial layer class
ω_2	Label for the basal ice class
ω_3	Label for the bedrock class
ω_4	Label for the thermal noise and echo-free zone and signal perturbation class
ω_4^R	Label for the thermal noise and the EFZ class
ω_B	Label for the background class

ω_T	Label for the target class
$\omega_c^{a,r}$	Predicted label for pixel (a, r)
$\omega_{gt}^{a,r}$	Reference label for pixel (a, r)
$\mathbf{M}, M(a, r)$	Segmentation map

Symbols related to the fuzzy-logic data analysis

d_{LT}	Lava tube depth
$2r$	Lava tube diameter
α	Crossing angle between the longitudinal axis of the lava tube and the moving direction of the radar platform
S	Index of the surface reflection
C	Index of the lava tube ceiling reflection
F	Index of the lava tube floor reflection
a_C	Average amplitude of the lava tube ceiling reflection
a_F	Average amplitude of the lava tube floor reflection
l_C	Length of the lava tube ceiling reflection
l_F	Length amplitude of the lava tube floor reflection
$\mathcal{F}, \mathbf{F}_i$	Candidate lava tube features
N_F	Total number of features
i, j	Index of the features and reflections
N_{AV}	Dimension of the incoherent averaging filter
th_{line}	Threshold for the amplitude of the pixels in the best path
$\mathcal{L}, \mathbf{L}_k$	Lines extracted by the line detection algorithm
k	Index of the segments extracted by the line detection algorithm
L_{min}	Minimum length of the features
O_a	Overlap in the azimuth direction
O_r	Overlap in the range direction
\mathbf{R}_i	Reflection related to the i -th feature
l_i	Length of the i -th feature
z_i	Average depth of the i -th feature

b_i	Barycenter coordinates of the i -th feature
a_i	Average amplitude of the i -th feature
ϕ_i	Average phase of the i -th feature
l_a^k	Azimuth coordinate of the k -th line
N_L^i	Number of segments of the i -th reflection
l_r^k	Range coordinates of the k -th line of the i -th reflection
b_a^i	Azimuth coordinate of the barycenter
$A(l_a^i, l_r^i)$	Amplitude radargram at the azimuth and range coordinates of the lines in the i -th reflection
r_p^i	Range coordinate of the signal peak
$W_{hann}(r)$	Function of the Hann window
T	Length of the considered Hann window
θ_i	Average phase value of the i -th reflection
θ_i^{path}	Phase contribution from the length of the EM wave propagation path
ρ_S	Average depth of the ground reflection
ρ_C	Average depth of the ceiling reflection
ρ_F	Average depth of the floor reflection
F_g	Reflection of the surface
F_c	Reflection of the lava tube ceiling
F_f	Reflection of the lava tube floor
μ_C	Crisp membership function of rule 1 (presence of at least 3 features)
r_G	Attribute of rule 2 (surface length of the candidate feature)
μ_G	Membership value of rule 2
l_R	Length of the considered radargram
a_G, c_G	Parameters of the sigmoid membership function for rule 2
M_G	Overall membership function for the surface reflection
Th_G	Threshold for detecting the
r_L	Attribute of rule 3 (equivalence of lengths)
a_L, c_L	Parameters of the sigmoid membership function for rule 3

μ_L	Membership value of the rule 3
r_P	Attribute of rule 4 (proportionality)
a_P, c_P	Parameters of the sigmoid membership function for rule 4
μ_P	Membership value of rule 4
L_a	Number of pixels with the same azimuth coordinate in the candidate features
r_{al}	Attribute of rule 5 (alignment of barycenters)
a_{al}, c_{al}	Parameters of the sigmoid membership function for rule 5
μ_{al}	Membership value of the rule 5
m	Orientation of the range direction
r_A	Attribute of rule 6 (amplitude comparison)
a_A, c_A	Parameters of the sigmoid membership function for rule 6
μ_A	Membership value of the rule 6
r_ϕ^1	Attribute of rule 7 (phase inversion)
r_ϕ^2	Attribute of rule 7 (phase inversion)
a_ϕ, c_ϕ	Parameters of the sigmoid membership function for rule 7
μ_ϕ^1	Membership value of the rule 7
μ_ϕ^2	Membership value of the rule 7
M_{cf}	Overall membership for a candidate lava tube
t_{tube}	Threshold for detecting lava tubes
lat	Latitude coordinate
$long$	Longitude coordinate
h_{roof}	Thickness of the roof
h_{lt}	Lava tube height
w_{lt}	Lava tube width
N^{FA}	Number of false alarm
N^{LT}	Number of detected candidate lava tubes
ξ_{FA}	False alarm rate
N_{FA}^a	Number of rangelines (traces) covered by the candidate lava tubes (false alarms)

N_{TOT}^a Total number of traces being processed

Symbols related to the deep-learning data analysis

N_p Total number of patches

t Index of the patch

x_p Range dimension of a patch

y_p Azimuth dimension of a patch

H_i^l output of the l -th layer of the neural network

l Index of the neural network layers

i Type of layer or activation function: c stands for convolutional layer, b for batch normalization layer, r ReLU activation function, m for max-pooling, and d for deconvolutional layer, and g

N_L Downsampling/Upsampling blocks of the neural network

M_l Number of features extracted from the l -th layer

(x_k, y_k) range and azimuth dimension of the kernel of the convolutional and deconvolutional layers

W^l Number of parameters of the neural network

$mathdsW$ Set of the parameters of the neural network

M_0 Number of channel of the input of the neural network (for radar sounder, $M_0 = 1$)

μ_t, σ_t Parameters of the batch normalization layer

x_m^l, y_m^l Dimension of the max pooling operation for the l -th block

h^l, w^l Range and azimuth dimension of the output at the l -th layer

d Dilation rate parameter

y'_k, x_k Dimension of the kernel of the dilated convolution filters

N_{ASPP} Number of dilated convolution operations

H_{ASPP} Feature set in output at the ASPP module

M^{ASPP} Number of features of H_{ASPP}

g_i Output features of the next lowest layer used as input of the Attention Gates

α_i^l Attention coefficients from the l -th attention AG

H_{AG}^l	Output of the l -th AG
$H_{out}(a, r, k)$	Features in output at the neural network
$M^{out} = 1$	Number of features in output
$\ell_t(a, r)$	Loss function for pixel (a, r)
\mathcal{L}_t	Loss function term for the radargram
$\mathbf{M}, M(a, r)$	Segmentation map
$s(a)$	Range coordinates of the surface
$P_s(a)$	Power of the surface for each azimuth column a
ℓ_r	Learning rate
\mathcal{E}	Numbers of epochs for the training
\mathcal{J}	Dataset of all the patches, including those from data augmentation
\mathcal{J}_{tr}	Dataset of the patches for the training
N_{train}	Number of patches in the training set
\mathcal{J}_{te}	Dataset of the patches for the test
N_{test}	Number of patches in the test set
N_{tot}	Total number of pixels analyzed with the proposed semantic segmentation method in the inference phase
TP^c	Number of true positive pixels for the c -th class
TN^c	Number of true negative pixels for the c -th class
FP^c	Number of false-positive pixels for the c -th class
FN^c	Number of false-negative pixels for the c -th class
OA	Overall accuracy
\mathcal{D}	Dataset of patches
$\mathcal{D}_{\mathcal{B}}$	Dataset of patches imaging only the background
$\mathcal{D}_{\mathcal{T}}$	Dataset of patches mostly imaging the target
$p_R(A)$	Rayleigh probability density function
$p_N(A)$	Nakagami probability density function
$p_{\Gamma}(A)$	Gamma probability density function
$p_K(A)$	K probability density function

$p_W(A)$	Weibull probability density function
p_1 and p_2	Generic distributions
p_{best}	Best-fitting probability density function
θ_{best}	Parameters of the best-fitting probability density function
μ_z, β_K	Parameters of the K probability density function
$\alpha_\Gamma, \beta\Gamma$	Parameters of the Gamma probability density function
$\tilde{\theta}_{best}$	Estimated parameters of the best-fitting probability density function
$\tilde{\Theta}$	Vector of the $\tilde{\theta}_{best}$ for all the patches
T_θ	Otsu's threshold for separating D_B and D_T patches
$P(r, a)$	Input patch of the neural network
$P_{out}(r, a)$	Output patch of the neural network
L_{rec}	Reconstruction loss between the input and output of the W-Net
$\mathcal{E}(a, r)$	Normalized error radargram
N_{FL}	Number of layers from which the features are extracted
N_G	Total number of features extracted by the network
\mathcal{G}	Concatenated features
g^k	Feature extracted from the neural network
k^*	Most informative feature
R_k	Index based on the Hamming distance between two discretized features

